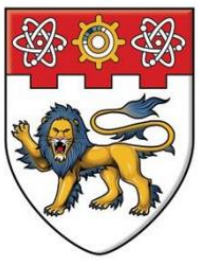

NANYANG TECHNOLOGICAL UNIVERSITY

BORON NITRIDE CARBON FOAMS FOR VARIOUS THERMAL APPLICATIONS

MANUELA LOEBLEIN

SCHOOL OF ELECTRICAL AND ELECTRONIC ENGINEERING

2017

Boron Nitride Carbon Foams for various thermal applications

Manuela Loeblein

School of Electrical & Electronic Engineering

A Thesis submitted to the Nanyang Technological University

in fulfillment of the requirement for the degree of

Doctor of Philosophy

2017

Dedicated to K

Acknowledgements

I would like to express my sincere gratitude to my Thesis supervisor Asst. Prof. Teo Hang Tong Edwin for his guidance throughout the course of my PhD. He provided me with invaluable advice over the years, taught me the essential skills in carrying out and presenting research and gave me countless encouragement to strive for greater achievements. Besides being my academic advisor, he also became a good friend whom I truly cherish. Thank you for taking me in as your student and your willingness in sharing your experience and knowledge with me.

Also, I would like to thank CINTRA and its directors, Prof. Philippe Coquet and Prof. Dominique Baillargeat for hosting me and providing me with this scholarship. I would like to express my sincere gratitude to the colleagues from Soreq NRC in Yavne, Israel, especially Dr. Asaf Bolker, Ms. Nurit Atar and Dr. Ronen Verker, as well as Dr. Cecile Uzan-Saguy from Technion, for their countless and invaluable hours of help, input and helping hands in experiments. I would also thank our collaborators from LIMMS in Tokyo, Japan (especially Prof. Yasuyuki Sakai and Prof. Dominique Collard for hosting me) and IEMN in Lille, France (especially Prof. Emiliano Pallecchi and Mr. Theo Levert) for the fruitful collaborative work.

I thank Dr. Siu Hon Tsang for his constant input, his countless hours and patience to go through my work and his advice on my research. He gave me many ideas for exploration and provided in-depth discussions in my area of research. Thank you for also being a close friend and making my PhD journey a truly enjoyable and memorable one.

Many thanks go to Dr. Matthieu Pawlik, Dr. Annalisa Bruno, Dr. Liu Ming and Dr. Jason Cheah for their guidance and willingness in sharing their experimental expertise with me, especially to Dr. Hongling Li, whom I truly cherish and thank for all her efforts and the time spent teaching me the essentials and skills of Chemistry. Thank you for your friendship and your constant encouragements.

I would also like to thank my group colleagues, especially Dr. Roland Tay, Mr. Olivier Commeto, Ms. Fei Ni Leong and Mr. Jing Lin for their input on my research and especially for their friendship. You have made these years an unforgettable experience. Also, I would like to thank all my juniors, FYP, DIP and JC students, especially Ms. Zhi Lin Ngoh, Mr. Juehan Liau, Mr. Zhi Kai Ng, Ms. Ranjana Shivakumar, Mr. Jinjun Lin and Ms. Lanxin Li, for their hard work and the amenable hours spent together in the lab.

I highly appreciate the help of Mr. Hasman Bin Hassan, the heart of Nanoelectronics Lab 1 for teaching me the experimental skills and knowledge of the various lab-equipment and for always providing helpful technical input, as well as the help of Mr. Eric Phua on teaching and helping me with the Laser Flash measurements.

Very special thanks to my parents and my brother who supported me unconditionally during this entire work and stay far abroad. Thank you for all your love and support and for always having an open ear for me – at any time and any place. It was always reassuring to know you were there and I could count on you at any time.

Last but not least, thank you Salvo, thank you for always taking care of me, being there for me, supporting me in everything I take on and helping me to push through. You definitively made this entire experience much more pleasant and enjoyable.

Table of Content

Abstract

Three-dimensional graphene and hexagonal-boron nitride structures (3D-C and 3D-BN) have recently attracted attention due to their enhanced mechanical, handling and surface area properties, while maintaining the well-reported properties of their two-dimensional constituents. In this Thesis, we developed a new three-dimensional hexagonal-boron nitride carbon (3D-BNC) structures, a hybridized of the two, using chemical vapor deposition (CVD) of CH_4/Ethanol and ammonia borane to further widen their application areas. Through the ability to specifically control the compositions of C and BN (demonstrated through Raman, X-ray photoelectron and energy dispersive X-ray spectroscopy), a highly tunable electrical conductivity (0 – 0.6 Scm^{-1}, measured using the Van-der-Pauw technique), controllable EMI shielding properties (0 – ~50 dB, measured through microwave network analyzer), while maintaining a high and stable thermal conductivity (0.84 – 1.2 $Wm^{-1}K^{-1}$, from laser flash measurements) is obtained.

One of the key advantages of such 3D materials is for thermal management in electronics. The stable thermal conductivity, compressibility and temperature stability of the 3D-foams are ideal conditions to achieve improved thermal management performance. Through compression of the foams, a high cross-plane thermal conductivity of 62 – 86 $Wm^{-1}K^{-1}$, as well as excellent surface conformity is demonstrated. These values are among the highest cross-plane conductivities of freestanding graphene or h-BN structures, and in the same range of eutectic metal foils. Evaluation of the thermal extraction efficiency on a state-of-the-art 2.5D electronic platform along with state-of-the-art thermal interface materials (TIMs) reveals 3D-foam's improved performance of cooling by 20 – 30%, which means a temperature decrease by ΔT of 44 – 24°C. This is colder than any of the commercially available TIMs tested on the same platform (i.e. Sn/Au) and among the highest temperature

decrease of hot spots on actual chips reported so far (e.g. highest values for alternative heat spreaders currently under research range around $\Delta T \sim 13°C$ for CVD-graphene and $\Delta T \sim 20°C$ for exfoliated few-layer graphene). This is a significant decrease, since it is known that the decrease of hot spot temperature by 20°C extends the transistors lifetime by one order of magnitude.

In addition, the interconnected structure of these 3D-foams is also ideal as filler material for insulative polymeric film to enhance its electrical and thermal behaviour as the 3D structure prevents inhomogeneous distribution and aggregation commonly faced when using typical nanofillers. To further unveil its potential, we investigate the enhancement in flexible electronics, space shielding materials and as well as thermo-mechanical actuation in shape memory polymer (SMP).

In flexible electronic, we incorporated 3D-C and 3D-BN with the currently state-of-the-art flexible platform for flexible electronics, polyimide (PI), an improved thermal dissipation by 25-times ($5 – 6\ Wm^{-1}K^{-1}$) is obtained, while preserving full flexibility and toughness of the PI. It is shown that these hybrid films can be directly used as printable substrates and can dissipate heat more efficiently from hot spots, which in turn allows increasing the maximum power applicable by at least 50%. In addition, by incorporating 3D-C into PI, also the electrical conductivity is improved, which can be used for other applications, such as space shielding. In the current space shielding materials there is always a coating of conductive material to prevent the build-up of electrostatic charge, however, these are prone to cracks and failure. Since the hybrid of 3D-C with PI has an electrical sheet resistance of 3 Ω/□, which fulfills the antistatic-criterion to dissipate the build-up of electrostatic charge, it is further developed and space-qualified according to European Space Standards, which requires to test its outgassing properties, as well as Gamma Ray, atomic oxygen (AO) and thermal cycling resistance. Through monitoring

electrical, weight and optical properties it is shown that it withstands and keeps a stable performance throughout various thermal cycles (from -100°C to +160°C), as well as the oxidative and aggressive environment of ground-based simulated space environments (Gamma ray doses equivalent to 15 years in geosynchronous equatorial orbit, and AO exposure equivalent to 8 months in low Earth orbit).

Lastly, the utilization of 3D-fillers in SMP has also been demonstrated. SMPs, despite their easiness in shaping, ultra-light weight and customizability, are limited in their applicability for mechanical actuation, as they are prone to cracks (due to poor thermal conductivity resulting in large thermal gradients across the material leading to internal stress). To target this issue, 3D-BNC foams of varying concentrations are infused with SMPs. Thanks to the homogeneous distribution of the foam within the polymer, a uniform spread of heat is obtained, demonstrated in this work through thermal camera imaging, thus leading to an even transformation of shape. It is demonstrated that through this technique, bigger sample sizes are attainable (maximum sizes without 3D-foam infusion are 3 cm in length, while with the 3D-foam infusion up to 7 cm in length are demonstrated to transform without any cracking). It is shown that the 3D-foams speed up the transformation process by three times, reduce the required energy to initiate the transformation process by 20% and in addition, thanks to the tunability of electrical conductivity of 3D-BNC, a self-heating and timed actuation can be incorporated to the polymer.

List of Figures

List of Tables

List of Abbreviations

2D	two-dimensional
3D	three-dimensional
3D-C	three-dimensional graphene
3D-BN	three-dimensional boron nitride
3D-BNC	three-dimensional boron nitride carbon
AFM	atomic force microscopy
AO	atomic oxygen
APS	(3-aminopropyl) trimethoxysilane
BN	boron nitride
BNC	boron nitride carbon
CNT	carbon nanotube
CVCM	collected volatile condensable material
CVD	chemical vapor deposition
DMA	dynamic mechanical analyzer
DSC	differential scanning calorimetry
EDX	energy dispersive X-ray spectroscopy
EM	electromagnetic
EMI	electromagnetic interference
EMI SE	electromagnetic interference shielding efficiency
ESD	electrostatic discharge
FIB	focused ion beam
GEO	geosynchronous orbit
GO	graphene oxide
h-BN	hexagonal boron nitride
IC	interconnected circuit
IR	infrared
ITO	indium tin oxide

LEO	low Earth orbit
LP	localization parameter
MLI	multilayer insulation
MMOD	micrometeoroid/orbital debris
PDMS	polydimethylsiloxane
PI	polyimide
PMMA	poly(methyl methacrylate)
ppi	pores per inch
RF	radio frequency
RGO	reduced graphene oxide
RML	recovered mass loss
SAM	self-assembled monolayer
SEM	scanning electron microscopy
SMA	shape memory alloy
SMP	shape memory polymer
TEC	thermoelectric cooler
TEM	transmission electron microscopy
TGA	thermogravimetric analysis
TIM	thermal interface material
TRL	Thru, Reflect, Line
TSV	through silicon via
UHV	ultra-high vacuum
UV	ultraviolet
VdP	Van der Pauw
VRH	variable range hopping
XPS	X-ray photoelectron spectroscopy

Introduction

Two-dimensional (2D) materials are materials typically comprised of one-atom-thick crystals with remarkable advantages over conventional bulk materials and very different properties from those encountered in their three-dimensional (3D) counterparts.[1] The first and most prominent reported 2D material is graphene, which contrasting to bulk graphite is a zero-overlap semimetal, with excellent electron mobility and extremely high thermal conductivity.[2-5] In the past decade, the family of these materials has grown to include metals (e.g. $NbSe_2$)[6], semiconductors (e.g. MoS_2, black phosphorous)[7, 8], and insulators (e.g. hexagonal boron nitride h-BN)[9]. Nevertheless, these materials have limited themselves from advancing beyond microscopic electronic needs, due to their current available sizes and quality. Major challenges faced are achieving a defect-free growth which can yield controlled grain size in large area (beyond cm size) and controlling the number of layers and stacking order of the 2D films,[10] since bilayer and multilayer 2D materials exhibit different properties compared to monolayer films.[11] In addition, most of the reported growth parameters require metal foils as catalytic substrate, which in turn requires a transfer process that degrades the quality of the films.[10] Furthermore, high production cost, health and safety concerns regarding potential toxicity also still have to be resolved prior to further commercialization.[12]

While many are still continuing to strive towards perfecting the 2D crystal growth technique,[13-16] recently (since 2011), there has been an upward trend of up-scaling these 2D materials into freestanding 3D spaces (often also referred to as foam-like structures).[17, 18] The basic principle of this technique is to use metal foam as catalytic substrate instead of metal foil, such that during growth, instead of growing into flat sheets, the 2D material adapts to the interconnected structure of the foam template. After

removing the template via chemical etching, the now freestanding 2D material remains stable in the foam-like interconnected configuration. This has become of great interest owing to the ultra-light weight (99.6% porosity, density of 1 – 5 mg cm^{-3}), enhanced mechanical and surface area properties of the obtained structures while keeping their well-reported 2D-structural properties.[19] For example, in the case of graphene, studies have shown that its 3D counterpart has comparable high thermal conductivity,[20] high electrical conductivity,[17] chemical and thermal stability and EMI shielding properties.[21]

1.1 Motivation

Thanks to this up scaling of atomically thin 2D materials into the 3D macroscale, new ways of integration into devices and applications have become possible.[22, 23] The 3D-foams also enable easier large-scale fabrication, since overall the control of defects, domain size and layer number has become less crucial, as the interconnected structure could compensate for any defects that may occur, (i.e. the phonon/electron transport mechanisms take place through multiple parallel paths within the interconnected foam).

Thus far, the main characteristics exploited for application are the high surface area and the interconnection within the foam. The high surface area has been mainly used for battery and supercapacitor applications,[24-27] since it enables a significant increase of stored energy; as well as for sensing and biological applications,[28-31] as it increases the sensitivity and interaction-sites with gases, particles or cells. Due to the interconnected structure, the 3D-foams have also been praised to be superior fillers for polymers,[32] which can bypass the common issues encountered with other nano-filler materials such as agglomeration and high filling fractions.[33]

These two (structural) characteristics alone have demonstrated to boost performance and efficiency within the few application fields implemented thus far. Nevertheless, no

work has looked into exploring and implementing other inherent advantages of the interconnected foam-like structure, or to use its interconnectivity more actively, such as for improved phonon and electron transport. For example, one very compelling advantage of 3D-foams is their compressibility, which would allow exploring a new range of applications that requires enhanced surface conformity. Furthermore, the foam-like configuration is appealing for hybridization of different types of 2D materials, since on the large surface area available, several domains of different materials could be combined. This is especially interesting for integrating two (or more) completely opposed materials into one single platform, as this would enable exploring a new variety of tunable properties and could thus serve applications requiring specific fine-tuning of properties. In addition, replacing the empty free space pores within the structure with other matrices, besides standard polymers, would increase the versatility of the foams and increase their applicability.

As can be seen, there is still a huge potential of unexplored characteristics, which potentially can be implemented to explore new applications, besides the ones reported up until now.

1.2 Objectives and scope

Overall, this Thesis will contribute to the community working in the field of up scaling 2D materials into the macroscopic realm with new insights by investigating new tunable foams, explore characteristics beyond the typically reported structural properties and demonstrate new application areas.

This is done through creating a new up-scaled 2D material based on 3D-graphene (3D-C) and 3D-BN. Due to their intrinsic excellence in thermal conductivity, thermal and chemical stability, as well as their complimentary opposing behavior in electron

conductivity and electromagnetic properties,[34-36] hybridization of these two 3D materials provides a full spectrum of tunable properties. This creates an extremely versatile material that is able to improve performance in various application areas, such as electronic packaging and thermal management.

In order to further extend the bandwidth of 3D-foams, the integration into several matrices, thus far unexplored in literature, is developed, such as thermal conductive adhesives, solder, polyimide and shape memory polymer.

Finally, a few proofs of concept applications in thermal management, flexible electronics and space shielding are demonstrated. This will proof the usefulness of the new characteristics of 3D-foams implemented herein and potentially demonstrate increased performance in the three application areas.

The key objectives are summarized as follows:

- To develop and optimize growth of 3D-C and its electrically opposite 3D-BN
- Combine both into a hybridized foam (3D-BNC) to obtain tunable characteristics
- Optimize properties and fine-tune the recipe to precisely control BN and C concentrations
- Develop recipes for the integration of the foams into different matrices (adhesives, solder, polyimide, shape memory polymer)
- Confirm quality and performance of these new hybrid films
- Explore new applications areas in thermal management, flexible electronics and space shielding
- Benchmark performance and assess the reliability of the materials following the standards required for each application field

1.3 Major contributions of this Thesis

In this Thesis, the first synthesis of novel 3D-BNC (which is a hybrid structure of 3D-BN and 3D-C) is demonstrated by chemical vapor deposition (CVD) growth process and the ability to specifically control the compositions of C and BN. This opens up many new customizable options such as for electronics packaging and thermal interface materials (TIMs) as 3D-BNC offers a highly tunable electrical conductivity (0 – 0.6 Scm^{-1}), controllable EMI shielding properties (0 – ~50 dB), while maintaining a high and stable thermal conductivity (0.84 – 1.2 $Wm^{-1}K^{-1}$). In a next step, the integration of the 3D-foams into new matrix materials, such as adhesives, solders, polyimide and shape memory polymer is investigated. Finally, to demonstrate the versatility of the 3D-foams, the following new application areas are investigated:

1) Thermal management of electronics

Thanks to the precise control of electrical conduction, the 3D-foams are shown to offer a closed solution for electrical packaging needs. Due to their intrinsically interconnected structure, the thermal transport behavior is superior to other comparable structures, reaching thermal conductivity values between 62 – 86 $Wm^{-1}K^{-1}$, (for comparison, graphene and h-BN paper only reach 1 – 5 $Wm^{-1}K^{-1}$), and does not require any supporting additional materials, since they are free standing. Due to their high thermal stability beyond 700°C, they are capable of withstanding the new high demands of IC packaging. The improved thermal conductivity is shown to help to efficiently extract the heat (20% colder than other commercial TIMs). Due to the interconnected structure, the heat is not spread along the area of the chip, but is directly extracted upwards into the heat sink. Higher surface conformity allows a nearly perfect interface without low conducting air gaps.

Through tailored chemical functionalization, adhesion can also be added to the 3D-foams. This further improves the thermal heat extraction capability and renders a strong mechanical bond. In addition, a method to obtain more mechanically robust 3D-foams with preserved electrical and thermal properties is developed in order to also cater for larger gaps and harsh environment thermal application. For this, a new infiltration method with PDMS is developed, called the "hairy" method. In a final step, the reliability and stability of all these materials is tested and evaluated to cater for the requirements imposed by electronic devices.

2) Substrate for flexible electronics

Polyimides (PIs) are known for their ease of fabrication and moldability, high thermal stability, high modulus of elasticity and tensile strength, which makes them currently the standard choice for substrate of flexible electronics. However, their poor thermal conductivity of 0.2 $Wm^{-1}K^{-1}$ has caused limitations to thermal management, which causes creation of hot spots even at low power inputs. Contrasting to current methods used to improve thermal conductivity of PI (by using high filling fractions of nano-fillers), the use of 3D-foam fillers is shown to achieve a drastic 25-fold thermal conductivity improvement to 5 – 6 $Wm^{-1}K^{-1}$, with merely 0.3 vol% (0.35 wt%) filling fraction. This low filling also completely preserves the flexibility of the polymer. It is demonstrated that this new hybrid film can be directly used as a substrate for flexible electronics and yields an increase of applicable power input by at least 23%.

3) Space Blanket application

PIs are currently also the standard choice for space shielding as it renders high temperature and UV stability and toughness. However, its electrical insulating characteristic has caused limitations, such as spacecraft electrostatic charging. In order

to target this issue, the PI is hybridized with 3D-C. It is demonstrated that this composite renders the necessary electrical conductivity (increase by 10 orders of magnitude) to avoid electrostatic discharges and that it withstands and keeps a stable performance throughout various bending and thermal cycles, as well as the oxidative and aggressive environment of ground-based simulated space environment. In order to make the film readily applicable for space blanket application, it is space qualified according to European Space Standards, which include outgassing tests, atomic oxygen exposure, gamma ray exposure and thermal cycling from -100°C to +160°C.

4) Thermo-mechanical application

Shape memory polymers (SMPs) are a polymeric smart material that can register two or more temporary shapes and transform to one another through an external stimulus, such as heat. Due to its easiness in shaping, ultra-lightweight and customizability, SMPs have much potential in applications that require miniaturization and compacting, especially in aerospace industries. However, the major drawback for SMP is its poor thermal and electrical conductivity. As the transformation of shape is initiated by heat, the poor thermal conductivity of the material often leads to a large thermal gradient across the material and inhomogeneous distribution of heat. This results in non-uniform transformation of shapes and can even lead to cracks. Many have attempted to improve their thermal performance through the incorporation of filler based nanomaterials, such as metal nanoparticles, carbon nanotubes and graphene. However, the outcome is always ineffective as the spatial dispersion of fillers within the SMP is often inhomogeneous as these fillers tend to agglomerate and bundle with one another. As such, in this Thesis the 3D-foam fillers are demonstrated to be a good choice of filler for SMPs. It is shown that its networked structure helps to achieve a more efficient heat flow. It is demonstrated that the infusion of 3D-material into SMP can improve the

overall thermal conductivity by 3 times and successfully speed up the shape transformation of SMP without any cracking, shape memory loss and even reduce the energy required to trigger the transformation by 20%. In addition, the tunability of the 3D-foams by using 3D-BNC of different concentrations renders the SMP a self-heating capability that can be timed, thus achieving a multi-step SMP behavior.

1.4 Organization of this Thesis

Chapter 1 provides the motivation and scope as well as the major contributions of this Thesis. Chapter 2 introduces the concept of foam-like materials, including their different fabrication techniques and applications. Chapter 3 presents the basic experimental setup and intrinsic properties of the 3D-foams studied in this Thesis. Chapter 4 summarizes the experimental procedures used for further tuning and optimization of the 3D-foams. Chapters 5 to 8 describe examples of applications explored during the course of this Thesis, ranging from thermal management of electronics to flexible substrate and space applications. Finally, Chapter 9 concludes with a summary of the work accomplished in this Thesis and recommendations for further research on related topics.

2 Literature Review

In order to have a platform to easily integrate 2D nanomaterials into practical applications and devices on a larger scale, it is imperative to develop a new strategy to produce these materials on a sizeable scale. To grow these materials into a 3D macro porous structure has shown to be a viable approach, since it allows to tailor properties, create complex structures, with disregard of minor defects during growth.[37] For graphene for example, this approach has demonstrated to achieve high flexibility, high electrical and thermal conductivity.[17, 20, 21, 38, 39] CVD of graphene on open celled reticulated Ni foam is typically performed to synthesize these 3D-C structures.

3D-BN is 3D-C's atomically analogous but electrically opposite.[2] It's elemental constituent, h-BN domains, has an extremely high thermal conductivity (~1700 – 2000 $Wm^{-1}K^{-1}$),[40] high mechanical strength and hardness (breaking strength of 15.7 and elastic constant of 503 N m^{-1}),[41] chemical inertness and temperature stability of up to 1000 °C,[42] and a dielectric wide band gap of ~6 eV.[43] BN-based ultralight materials appear to be promising for novel applications but remained challenging to fabricate thus far, which is why the uptake into third dimension could enable easier handling and integration of this material.

2.1 Fabrication of 3D-materials

Several different methods have been reported to obtain foam-like graphene and h-BN structures. The first classification for these fabrication methods is into the size of the pores they yield.[27] They can be classified either as micro- and meso-porous or macro-porous. The IUPAC (International Union of Pure and Applied Chemistry) defines this based on the pores' diameter, in which "micro-pores" are defined as pores smaller than

2 nm in diameter, "macro-pores" as larger than 50 nm, and "meso-pores" are pores with diameters in between those two values.[44] The focus of this work is on macro-porous size. This group can be further subdivided into template-type used for fabrication:

2.1.1 Template free

The most common functional groups appearing on the surface of graphene are O-containing groups. These can lead to very useful graphene-like structures (i.e. "graphene-derivatives"), such as GO (graphene oxide) and RGO (reduced graphene oxide). The O-groups on these structures can offer active binding sites for inorganic nanoparticles. These sites in turn can provide linkage points for other graphene sheets and lead to the buildup of macro-porous structures. This processes is known as self-assembly.[45] Besides GO and RGO, recently tannic acid was also reported to induce self-assembly of 3D-C.[46] Commonly, self-assembly is followed by chemical reduction to remove the oxide from the GO.[47] Alternatively, a combination of self-assembly and chemical reduction can also yield 3D-C; it was found that gel-like structures with 3D macro-porous features could be obtained via direct chemical reduction of GO in water with a variety of different reducing agents, (e.g. vitamin C, sodium hydrogen sulfite, hydrogen iodide, sodium sulfide,).[48, 49] A green alternative of such a reduction process was proposed with the use of glutathione.[50] Another alternative for a two-step reduction process for 3D-C was reported with L-ascorbic acid and hydrazine hydrate.[51]

Two other ways to obtain template-free 3D-C are the in-situ polymerization of organic monomers with graphene sheets,[52, 53] and filtration through a membrane filter. Such a filtration process can yield graphene membranes ("paper-like" or "foil-like" graphene), which in turn can be used as building blocks for 3D-C papers.[54, 55]

Another very common technique reported is solution processing: through creating air bubbles within a GO solution, layers of GO sheets settle around the bubbles due to the presence of the gas–liquid interface, which is followed by a solidification process and high temperature annealing.[56, 57] Similarly, such processes were reported for 3D-BN structures, where B_2O_3 and h-BN powder were mixed in acetone, dried and subsequently sintered at 1000°C.[58, 59] Similar to the principle used in the solution processing, gas-foaming process with h-BN ceramic material can yield 3D-BN foams as well. For this, BN precursor gases are mixed and held under high pressure at 1200°C for 2 hr.[60] In another report, polyborazine was used instead for the foaming.[61]

Finally, a technique getting more popular is the use of natural resources, whereby the natural resource is completely converted into 3D-C without remainders, and is thus grouped under the substrate-less techniques. Some examples are sugar, bread and CO_2. Blowing sugar results in the complete conversion into a 3D-C network, which the authors called "strutted graphene (SG)".[62] Similarly to the use of sugar, the use of flour has been proposed for the preparation of 3D-C, whereby yeast and flour are mixed and slowly kneaded until cohered to a paste, followed by fermentation to form the porous structures, drying and finally, carbonization of the bread.[63] A recent report has also shown the possibility of directly converting CO_2 into a 3D-C structure by mixing liquid Na and CO_2 under high pressure for 24 h at 600°C.[64]

2.1.2 Soft template

In a typical soft-template approach, amphiphilic molecules (a chemical compound possessing both hydrophilic and lipophilic properties) and graphene are mixed together in aqueous solution to form 3D hydrogels. Once the water is removed (typically through freeze-drying), the result is a sponge-like structure with highly cross-linked graphene

sheets (denominated as "aerogel").[65] Other structures frequently used to build 3D-C are biomolecules (e.g. DNA,[66] hemoglobin (Hb),[67] and vitamin C[68]), since they offer multiple functional groups on their surface which can chemically interact with graphene sheets through a variety of modes, such as hydrogen bonding, π–π and ionic forces. Another soft template reported is the use of soft metal monoliths; 3D-C was obtained from a dextran/metal salt gel (Co, Ni, Cu, Fe). After annealing the gel, a metal oxide foam is obtained, which afterwards can be used for CVD with CH_4.[69]

2.1.3 Hard template

For hard-templates, the basic principle is to deposit graphene layers on either inorganic or organic particles or to in-situ grow graphene on metallic porous sacrificial layers, with subsequent complete removal of the template. The major classes of hard templates reported are metal foams and metal powder. For the former one, the most common sacrificial template used is Ni foam and the most common deposition technique is CVD, with ethanol or CH_4 as the most common carbon sources,[17, 31, 39, 70] which is also applicable for 3D-BN with sublimation of a powder as precursor.[18, 71] A recent report also showed the possibility of using Ni foams obtained through electro-less plating as hard template in CVD for 3D-C.[72] Alternatively, metal foams can also be obtained from powder metallurgy (i.e. hybrid metal powders are pressed into pellets and then heat treated).[73] Recently, 3D-C was also reported to be fabricated on Ni foam via radio frequency magnetron sputtering at low temperature.[74] For metal powder, a similar principle takes place, but the powder is first pressed/sintered into pellets and then used to grow on using CVD. The obtained structures are of smaller diameter pores.[75, 76]

Similar to the metal version, also microspheres of polymers (e.g. polystyrene and polymethyl methacrylate, PMMA) can be used as hard templates.[77, 78] Such a method

was also reported to obtain 3D-BN, whereby precursor powder was infiltrated in solution inside highly porous polymers. Pyrolysis under an ammonia atmosphere at 1150°C for 90 minutes was then performed afterwards.[79]

Besides CVD, electro deposition is another alternative that can be used to fabricate 3D-C on the abovementioned hard templates. The charged nature of graphene derivatives (such as GO) makes them also alterable through electric fields, and thus electro deposition is another technique that can be used with macroporous hard templates.[80, 81]

Finally, rapid freezing of amphiphilic polymers (e.g. PVA, chitosan) in water is another technique used to obtain 3D-C.[82-84] In such a process, the mixture of ice crystals with amphiphilic polymers are considered hard templates.[85]

2.1.4 Comparison of methodologies

Table 2-1 summarizes all abovementioned fabrication methods of 3D-foams and enlists advantages and disadvantages of each. It must be noted that, even though all these structures are labeled as macro-porous "3D-foams", there are inherent differences between each of them. The main difference relies in the type of interface between single domains. Most structures are composed of single 2D material domains merely stitching/gluing next to each other, without a strong chemical bond, frozen into a 3D build up. Such structures are often also denominated as "aerogels" in literature. This work on the contrary will focus on structures that are built up by a covalent assembly of single domains, which compose a continuous structure ("true 3D-foams"), since such a strong chemical bond between domains will provide a better performance in terms of phonon and electron transport. In Table 2-1 the techniques yielding such "true 3D-foams" are marked with an *.

Table 2-1. Comparative chart of fabrication methods of macroporous 3D-foam

	Method	Advantages	Disadvantages	Ref.
Template-less	Self-assembly	Simple process, that usually can be carried out at room temperature	Often leaves dangling oxidized functional groups; residues of inorganic nanoparticles within 3D-structure	45-47
	Chemical reduction	Has potential to be a green method	Requires multiple steps in solution	48-51
	Polymerization	Usually non-toxic organic monomers; does not require addition of other reactants	Residue of organic monomers within 3D-structure	52, 53
	Filtration	Simple process, carried out at room temperature without complicated chemical reactions	Does not directly yield 3D-structure, requires post-processing	54, 55
	Solution processing	Easy to implement for both, 3D-C and 3D-BN	Requires 3 steps (gassing, solidification, high temperature annealing)	56-59
	Gas-foaming	Easy to implement for both, 3D-C and 3D-BN	Requires high pressure and high temperature annealing	60, 61
	Natural resources*	Very green, especially if CO_2 is used as carbon source	Requires high temperature (sometimes also high pressure); only applicable to 3D-C structures	62-64
Soft template	Hydrogels	Simple process, that usually can be carried out at room temperature	Residues of amphiphilic molecules within 3D-structure	65
	Biomolecules	Use of non-toxic chemicals	Only applicable to 3D-C	66-68
	Soft metal monoliths*	Easy to implement for both, 3D-C and 3D-BN	Requires a second step (CVD)	69
Hard template	Metal foams*	Easy to implement for both, 3D-C and 3D-BN; precise control of growth parameters and morphology; process can be adapted to a low temperature deposition	Requires high temperature (at times also pressure); removal of template required via chemical etching	17, 31, 39, 70-74
	Metal powder*	Easy to implement for both, 3D-C and 3D-BN; precise control of growth parameters and morphology	Requires a pre-step (pressing/sintering of powder); requires high temperature (at times also pressure); removal of template required via chemical etching	75, 76
	Polymers	Easy to implement for both, 3D-C and 3D-BN	Requires high-temperature	77-79
	Freezing	Non-toxic and simple process	Residues of amphiphilic molecules within 3D-structure	82-85

Among the marked techniques, differentiation must still be made based on the degree of control of the final structure during fabrication and the quality of the 2D material in the final structure. For this work, a high control over the outcome is preferred, which can be obtained through the use of metal foams and to some extent also by natural resources. Nevertheless, since the use of natural resources is mainly based on "burning"

the source into carbon, its final quality is difficult to control and might yield carbonaceous structures that are not pristine graphene. For the following review of applications, only controlled "true 3D-foam" structures will be considered.

2.2 Common applications

As mentioned in Chapter 1, thus far the main focus in literature is to use the large surface area of 3D-foams to increase energy output of electrochemical energy storage and conversion devices, as well as to increase the sensitivity of sensors. A brief overview of typical applications reported thus far is given below:

2.2.1 Energy applications

The majority of scientific publications using 3D-C structures for application focus on research of electrode materials for supercapacitors[31, 39, 62, 86-88] and lithium ion batteries.[86-88] This is due to the highly open porous structure of the 3D-foam that allows easy flow of electrolytes with a drastic increase in surface area, which in turn offers a higher storage capacity.

High surface area combined with the good surface hydrophilicity, and well-defined porosity of 3D-C has also driven research towards counter electrodes in solar cells (and especially in dye-sensitized solar cells, DSSC). 3D-C in this case helps to enhance electrolyte–electrode interaction and electrolyte–reactant diffusion which in turn increases performance of such devices.[89-94]

There have been several review papers focusing on 3D-C research for these energy applications.[24, 95]

2.2.2 Sensing applications

The increase in surface area also renders an increased active area for sensing applications, which in turn leads to higher sensitivity and faster response time. Some examples highlighting the drastic increase of sensitivity are the reports on gas detection by Yavari et al.[28], Glucose detection by Dong et al.[31] and carcinoembryonic antigen sensing by Liu et al.[96]

When reinforcing the porous high surface area structure of 3D-C with polymer, an electrically conductive film is obtained with very high sensitivity to mechanical changes. This has driven a lot of research into mechanical sensing of pressure and strain with 3D-C films.[97-102]

2.2.3 Environmental applications

The high surface area and porosity of 3D-foams is also vastly being used for environmental applications, which include absorption and separation of pollutants from water. Thanks to the high porosity, the water can freely flow through the foams; the hydrophobic surface of 3D-C/3D-BN attracts contaminants (such as dyes[50, 103] and other pollutants[58, 60]). This has been extensively reviewed by Shen et al.[104]

2.3 3D-C and 3D-BN in thermal applications

Since the selection of 3D-foam fabrication has been narrowed down in the previous section to those with covalent bonding only, the obtained freestanding 3D-C and 3D-BN structures provide a superior thermal transport path in both the vertical and horizontal plane. The following section provides an overview of recent work published exploring these structures in terms of thermal applications:

For 3D-C, Pettes et al.[20] reported thermal conductivity values at room-temperature depending on growth time and etchant used. The values ranged between 0.26 and 1.7 $Wm^{-1}K^{-1}$. This work showed the benefit of the continuous 3D-C structures that achieve elimination of internal contact thermal resistance. Zhang et al.[105] reported a very low thermal contact resistance of 3D-C, via testing it in a sandwich structure between two Cu blocks (between Si and Al). At maximum compression, the values obtained are of 0.07 cm^2KW^{-1} (0.04 ± 0.02 cm^2KW^{-1}). Sun et al.[106] measured the temperature dependence of 3D-C and revealed that the thermal conductivity ranges from 0.3 $Wm^{-1}K^{-1}$ to 1.5 $Wm^{-1}K^{-1}$ depending on the temperature, whereby the higher value is obtained at 440 K, the lower at 310 K. Hu et al.[107] revealed the efficient flame-retardant properties of 3D-C, which are able to outperform traditional flame retardant materials, such as polymers, metallic oxide, and metal hydroxide. Ahn et al.[108] revealed a new boiling heat transfer phenomenon, by assembling 3D-C-like structures on a heater. With such an assembly it is possible to avoid the sudden increase of wall temperature experienced at critical heat fluxes. And finally, Thiyagarajan et al.[109] proposed 3D-C as a potential candidate for thermoelectric application. Through optimization of thermal conductivity (to reach lower values) and electrical conductivity (to reach higher values), they were able to show efficient thermoelectric performance.

3D-BN was proposed by Cao et al.[61] to be used for high-temperature radomes and thermal insulation.

There are also some reports on the intermixing of 3D-foam structure with an external matrix for thermal applications: 3D-C was mixed with polymer (i.e. polydimethylsiloxane, PDMS) to improve their thermal conductivity; Zhao et al.[110] achieved a 300% increase of thermal conductivity (0.56 $Wm^{-1}K^{-1}$) with a loading of 0.7 wt%, Liu et al.[111] reached 1.52 $Wm^{-1}K^{-1}$ with a 5 wt% loading and Zhao et al.[112] reported

a 440% increase in thermal conductivity (1.08 $Wm^{-1}K^{-1}$) with a combination of 0.2 vol% 3D-C with 2.7 vol% multilayer graphene flakes. In a recent work, Zhao et al.[113] measured the thermal resistance of 3D-C/PDMS composites using the laser flash method and obtained 14 mm^2KW^{-1}, which is only 19% of the value of commercial filled epoxy TIM. Another type of matrix was used by Zhou et al.[38] who infused 3D-C in ceramic for heat transfer and thermal energy storage. A thermal conductivity of 8.28 $Wm^{-1}K^{-1}$ was reported in this work for the 3D-C/ceramic compound. Finally, another common matrix for 3D-C fillers are phase change materials (PCMs). PCMs are considered an efficient heat storage, whereby through phase change from solid to liquid, or vice versa, heat is absorbed and released. Fedden et al.[114] used 3D-C inside the PCM to increase its thermal conductivity in order to improve the transport of heat within the material, Yang et al.[115] infused hybrid graphene aerogels (consisting of 0.45 wt% graphene oxide and 1.8 wt% graphene nanoplatelets) and obtained an improvement of 361% of thermal conductivity (1.43 $Wm^{-1}K^{-1}$), Yang et al.[116] used graphene nanoplatelets to create 3D-C, which they infused with PCM and obtained a 463% increase in thermal conductivity (1.35 $Wm^{-1}K^{-1}$), and finally, Zhang et al.[117] created a 3D-C/PCM composite for solar thermal conversion and for thermal energy storage. The 3D-C within the PCM helps to enable the solar-thermal conversion, increase thermal conductivity and to render the structure form stability.

The surfaces of a foam-like mixture of boron–carbon–nitrogen were reported by Paul et al.[118] for thermal physisorption applications, which could be used for heat pumping and thermal storage. Depending on the achieved crystallinity of the compound, the thermal stability and thermal conductivity can be tuned.

3 Development of foams and basic intrinsic properties

3.1 Introduction

In this Thesis, metal foam templates (i.e. Ni and Cu) are chosen as sacrificial templates for fabrication since they allow full control over the final structure of the 3D-foams (i.e. thickness, pore distribution and pore size). Additionally, these metals are the common metals for 2D CVD growth of graphene and h-BN and their growth mechanisms have been well studied and optimized to obtain high quality films.

This chapter describes the recipes developed to obtain the 3D-foams (3D-C, 3D-BN and 3D-BNC), along with an assessment of their morphology, chemical composition and their intrinsic properties.

3.2 Experimental setup

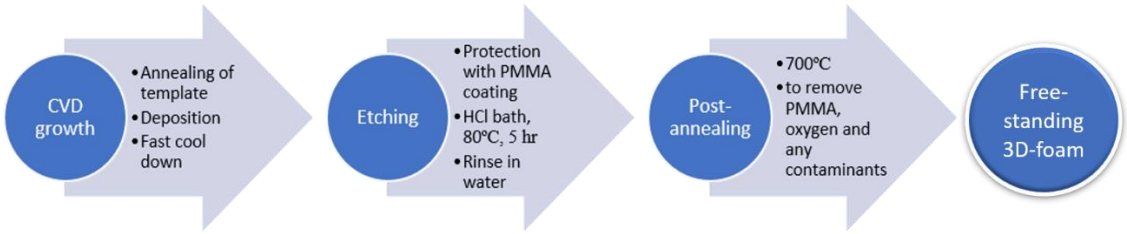

Figure 3-1. Process flow of the required three steps to obtain 3D-foams

To obtain the 3D-foams, a three-step process is required, which involves (1) the CVD growth of the 3D-material on a metallic sacrificial layer, (2) etching of this sacrificial template and (3) post-annealing (Figure 3-1). For each of the 3D-foams, a slightly different CVD recipe is required. Details on the recipes used are as follows:

3.2.1 Growth of 3D-C

Growth of 3D-C is carried out in a split tube furnace using Ni foam (Latech Scientific Supply Pte. Ltd.) as a catalytic substrate; the setup within the furnace is schematized in Figure 3-2. Prior to the growth process, the Ni foam is annealed for 5 min at 1000°C in ambient pressure, under a mixture of Ar and H_2 flow (200:50 sccm), to remove any potential contaminants and oxides. Subsequently, either ethanol or CH_4 is lead into the tube to start the deposition. In the case of ethanol, the Ar and H_2 mixture (2000:50 sccm) is redirected to an ethanol bubbler, which will create bubbling of ethanol and transport it towards the growth area. 10 min are sufficient to obtain full coverage of the Ni foam. For the case of CH_4, a flow of 10 sccm is added to the mixture of Ar and H_2 (200:50 sccm) for 10 min for complete coverage of graphene. After growth, the lid of the furnace is lifted for fast cooling. The cooling time will depend on the type and size of furnace used, but usually takes 30 min.

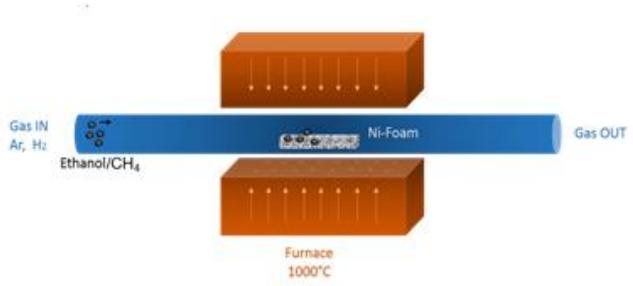

Figure 3-2. Schematic of 3D-C growth setup

3.2.2 Growth of 3D-BN

Growth of 3D-BN is carried out similarly to 3D-C in a split tube furnace using Ni foam as a catalytic substrate. Instead of a gaseous precursor for growth, sublimation of a precursor powder is required, as well as a constant connection to a pump. Figure 3-3 shows the different setup within the furnace, whereby the precursor powder borazane (NH_3-BH_3) is placed in a separate alumina container within the same tube, but away

from the heating area of the furnace. Prior to the growth process, the Ni foam is annealed for 2 hr at 1000°C in 50 Pa of H_2. Subsequently, the growth is started by wrapping an external heating source of 100 – 120ºC around the tube area where the powder is located, which will immediately start the sublimation of borazane. For a 10 cm x 2 cm sample ca. 0.5 g of powder are required. During growth, the flow rate of H_2 is adjusted according to the suction power of the pump and must maintain a pressure of 60 Pa. 1 hr is sufficient to obtain full coverage of the Ni foam. Also in this case, after growth, the lid of the furnace is lifted for fast cooling.

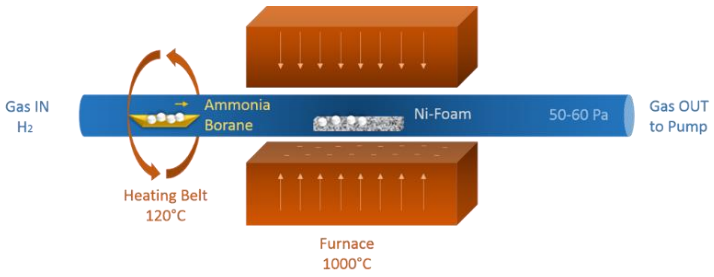

Figure 3-3. Schematic of 3D-BN growth setup

3.2.3 Growth of 3D-BNC

The synthesis of 3D-BNC is done similarly, following the same procedures as for pure 3D-C/BN via a two-step process, whereby the growth of BN is carried out first, quenched at the required %-coverage and then immediately followed by the growth of C using ethanol. This allows to achieve good controllability of C:BN composition.[119]

3.2.4 Post-growth etching and annealing

Once the growth of the material is finalized and the furnace reached a temperature below 180ºC, the as-grown 3D-material/Ni sample can be taken out. To proceed with the removal of the Ni foam, the samples are first coated with PMMA to protect the 3D-material layers. After the PMMA has been cured, the sample is then immersed into hydrochloric acid (HCl) of a concentration of 3M at 80ºC until the Ni is completely

etched away. This will take around 5 hr which was determined via XPS and EDX, which showed no trace of Ni in their survey spectra. The obtained structure is a free-standing 3D-foam coated in PMMA. Finally, to remove the PMMA, the sample is annealed under ambient pressure in Ar and H_2 mixture (2000:50 sccm) at 700ºC for 1 hr. After this, the obtained pure 3D-material structure remains stable without collapsing. Figure 3-4 schematizes the step-wise post-growth procedure.

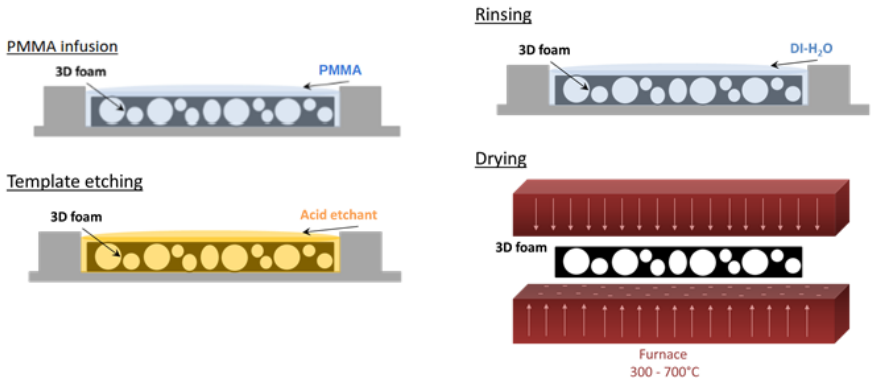

Figure 3-4. Schematic of post-growth experimental setup

3.2.5 Standard characterization techniques

3.2.5.1 For optical imaging

Scanning electron microscopy, SEM (LEO 1550 Gemini and JEOL JSM 5600LV at 15 keV) is used to investigate the morphology of the 3D-foam structure.

Transmission electron microscopy, TEM (Tecnai F20) is used to investigate the structure in the nm-regime and determine the number of layers. For this, carbon coated Cu grids were prepared by dispersion.

3.2.5.2 For compositional analysis and structural analysis

Energy dispersive X-ray spectroscopy, EDX (Oxford Instruments INCA x-act integrated with JEOL JSM 5600LV at 15 keV) is used to determine and map the elemental composition of the 3D-foams.

Raman spectroscopy (WITec CRM200 Raman with an Nd:YAG 532 nm laser as excitation source) is performed at room temperature to determine the crystalline configuration of the 3D-foams.

Surface analysis of the samples is carried out using VG ESCALab 220i-XL Imaging X-ray photoelectron spectroscopy, XPS (last calibration in Sep 2014). Monochromatic Al Ka X-ray (hν = 1486.7eV) was employed for analysis with a photoelectron take-off angle of 90° with respect to the surface plane. The maximum analysis depth lay in the range of 4 – 8 nm. Survey spectra are acquired for elemental identification while high-resolution spectra are acquired for chemical state identification and surface composition calculation. The charge correction is based on C 1s in sp^2 C=C carbon at 284.5 eV. For chemical state analysis, a spectral deconvolution is performed by a curve-fitting procedure based on Lorentzians broadened by Gaussian using the manufacturer's standard software. The error of binding energy is estimated to be within ±0.2eV.

3.2.5.3 Thermal measurement

Thermal conductivity measurements are performed through the laser flash technique (NETZSCH LFA 467 HyperFlash and LINSEIS XFA 500).[120] The basic principle is depicted in Figure 3-5: a short laser pulse is sent through the bottom side of the free-standing sample and on its top side, an IR-detector records the temperature rise caused by the laser.

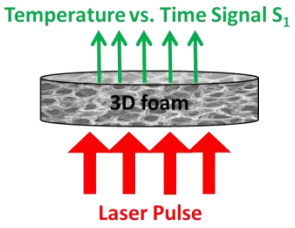

Figure 3-5. Schematic of the laser flash method for thermal conductivity measurement

With the relation of temperature rise and time, the thermal diffusivity a (mm^2s^{-1}) can be extracted using the empirical formula [120]

$$\alpha(T) = 0.1388 \frac{d^2}{t_{1/2}} \quad (3\text{-}1)$$

with d (cm) thickness of the sample and $t_{1/2}$ (s) the time to the half of maximum temperature rise. The thermal diffusivity in turn can be used to calculate the thermal conductivity κ ($W\ m^{-1}K^{-1}$) by using [120]

$$\boldsymbol{\alpha(T) = \frac{\kappa(T)}{c_p(T)\cdot\rho}} \quad (3\text{-}2)$$

with c_p ($kJ\ kg^{-1}K^{-1}$) specific heat and ρ ($kg\ m^{-3}$) density of the sample. The thermal conductivity is in cross-plane, meaning that it goes through the thickness-direction of the film.

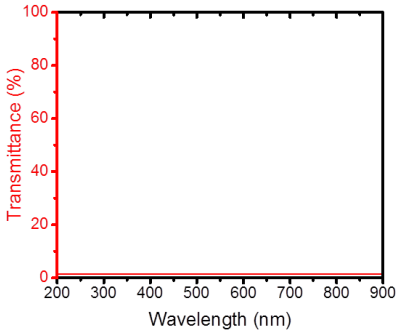

Figure 3-6. UV-vis spectroscopy results for transmittance of 3D-foam

For the use of the laser flash technique on porous materials (i.e. to verify the validity of Formula 3-1 for such structures), it must be ensured that the laser penetration depth remains much smaller than the total thickness of the sample (i.e. thickness of sample >> optical penetration depth of laser). In order to verify this, direct measurements of the transmission of the sample were conducted. Since the LINSEIS XFA 500 laser flash uses a Xenon lamp as shot source, which covers almost the complete wavelength range from visible to invisible, in the following, the complete range from 200 nm to ca. 1000

nm is considered. Transmission measurement of an uncompressed 3D-foam of same thickness and ppi as used for the laser flash measurement was performed via UV-vis spectroscopy (Shiimadzu UV-2450 Spectrophotometer). The measurement was repeated on several different spots, all obtained curves displayed the same behaviour. A representative curve is shown in Figure 3-6. It can be seen that the 3D-foam has a negligible transmittance of 1.3%, thus there is no through-hole light transmission. This makes it clear that no light passes through the samples, i.e. the penetration depth remains much lower than the sample thickness.

3.2.5.4 Electrical measurement

Electrical conductivity was measured on a four-probe Karl SUSS 200 Micro-Prober by using the Van-der-Pauw (VdP) method. This method is applicable to structures with irregular geometry.[121] The measurement is based on the induction of current along one edge of the sample, while on its opposite side the voltage is measured, and this is repeated 4 times with alternating positioning of current and voltage measurement (Figure 3-7).

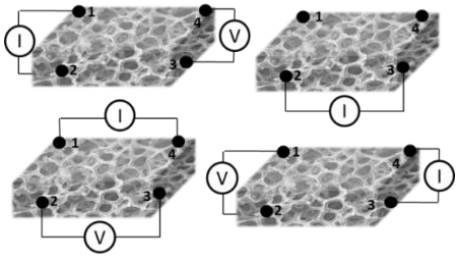

Figure 3-7. Schematic of the modes of the 4-point Van-der-Pauw method for measuring electrical resistivity

3.2.5.5 EMI SE measurement

EMI SE was measured in the range of 10 MHz (μ-Processor) to 18 GHz (X-band) using an Agilent N5230A PNA-L microwave network analyzer which is calibrated using the TRL (Thru, Reflect, Line) calibration method.

3.3 Obtained structures

3.3.1 Morphology

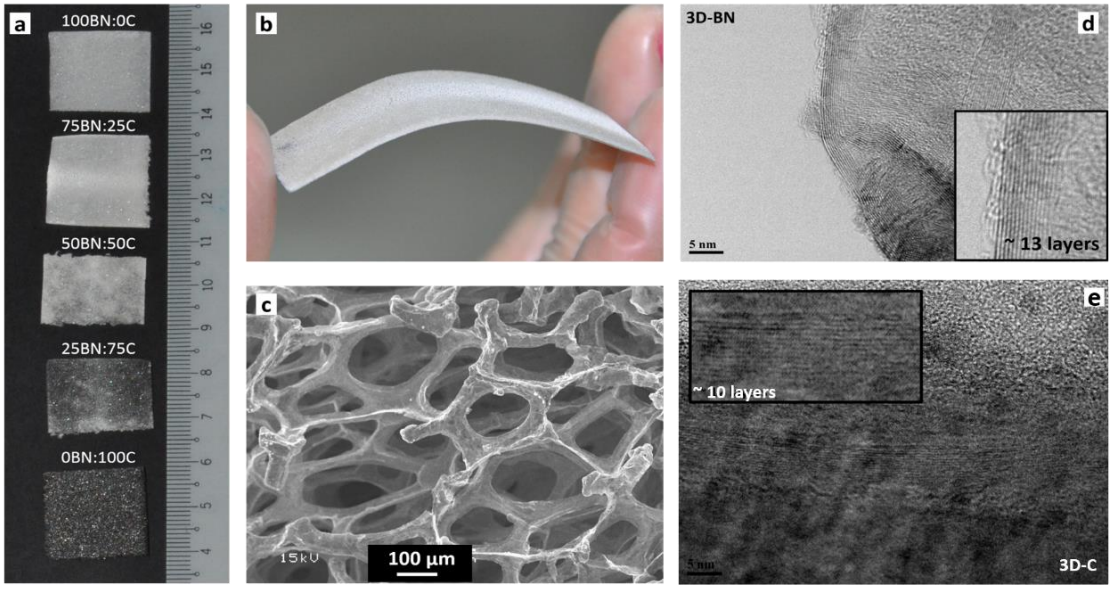

Figure 3-8. (a) Images of 3D-BNC with different BN:C ratios after the removal of Ni foam and PMMA; **(b)** demonstration of the flexibility of the freestanding 3D-BNC structure; **(c)** top view SEM image of the foam-like architecture; **(d-e)** TEM images of 3D-BN and 3D-C, respectively, to show their layered structure

Figure 3-8a shows the obtained free-standing 3D-BNC (i.e. after removal of Ni and PMMA) at different C:BN concentrations. Pure 3D-BN is seen to be white in color while pure 3D-C is seen as black. A distinct transition can be seen on the 3D-BNC as the C:BN concentration varies. A higher concentration of C in the 3D-BNC will result in a denser distribution of darker patches and vice versa. The obtained freestanding lightweight 3D-BNC composite also displays flexibility as seen in Figure 3-8b. The highly porous 3D-BNC network duplicates the structure of the Ni foam templates, which is interconnected throughout the configuration. The SEM image in Figure 3-8c shows the top-view of the 3D architecture. It is observed that the pores are distributed homogenously within the structure and have a mean diameter of ≈250 µm. This highly porous structure allows the BNC hybrid foam to achieve ultra-low density (≈1 to 5 mg cm^{-3}) and ultra-light weight while retaining its structural integrity with flexural toughness. TEM images in Figure

3-8d and e show the edges of graphene foam and h-BN foam, respectively and the layering structure can be clearly seen. The number of layers shown in these TEM images are representative of the typical samples used for applications tested in this Thesis. The number of layers can be controlled from very few layers up to 30 layers, depending on precursor gas flow rate and growth time. Some examples of such control are shown in Figure 3-9.

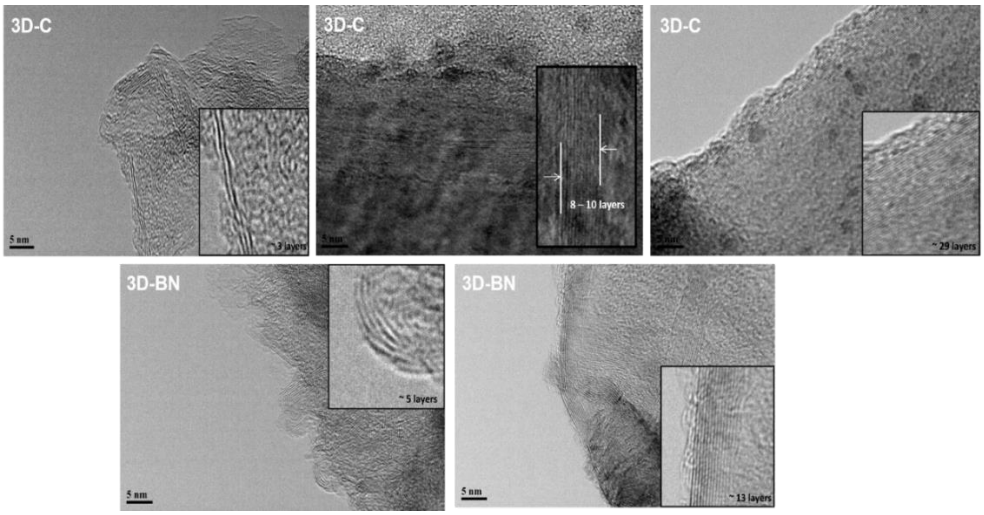

Figure 3-9. TEM images demonstrating sample structures of 3D-foam with tailored layer numbers. The total amount of layers of graphene or h-BN can be tailored during the growth by adjusting the precursor gas flow rate and growth time

3.3.2 Nature of composition

Figure 3-10 shows the proposed growth mechanism and the formation of 3D-BNC. The Ni foam is represented as a 3D porous cube which is built up by stacked sheets of porous Ni. The growth mechanism is illustrated as follows: BN growth is first initiated on the Ni foam as borazane is sublimed at 120°C producing aminoborane (NH_2BH_2) and borazine ($B_3H_6N_3$). The BN precursor diffuses into the Ni and nucleation occurs on the Ni surface. Subsequently, random patches of multi-layer h-BN were obtained as the neighboring BN domains coalesce together. However, the BN growth is quenched prematurely before a continuous layer of BN is formed throughout the Ni foam, leading

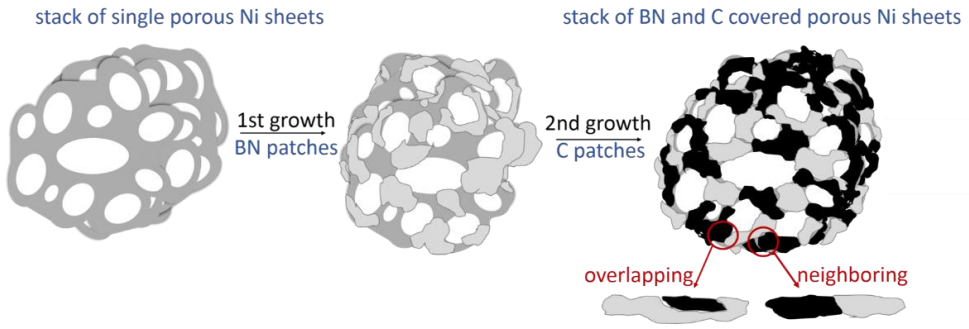

Figure 3-10. Schematic of the 2-stage synthesis process of 3D-BNC: first, patches of h-BN are grown on Ni foam with CVD process. Second, graphene is grown on the empty patches of the uncovered Ni foam, with some etches overlapping the BN patches and forming the stacking/overlapping junctions

to partial coverage of 3D-BN. The process of obtaining partial coverage 3D-BN patch is similar to its 2D counterpart, in which, various parameters that could control the growth have already been well studied.[122-124] Typically, BN growth takes ≈60 min to cover the Ni foam completely. After BN growth is terminated, ethanol is introduced into the quartz tube for C growth. The graphene domains nucleate and grow over the uncovered Ni regions continuously and attaching or overlapping with the existing BN, forming hybridized BNC layers which cover the entire Ni template.

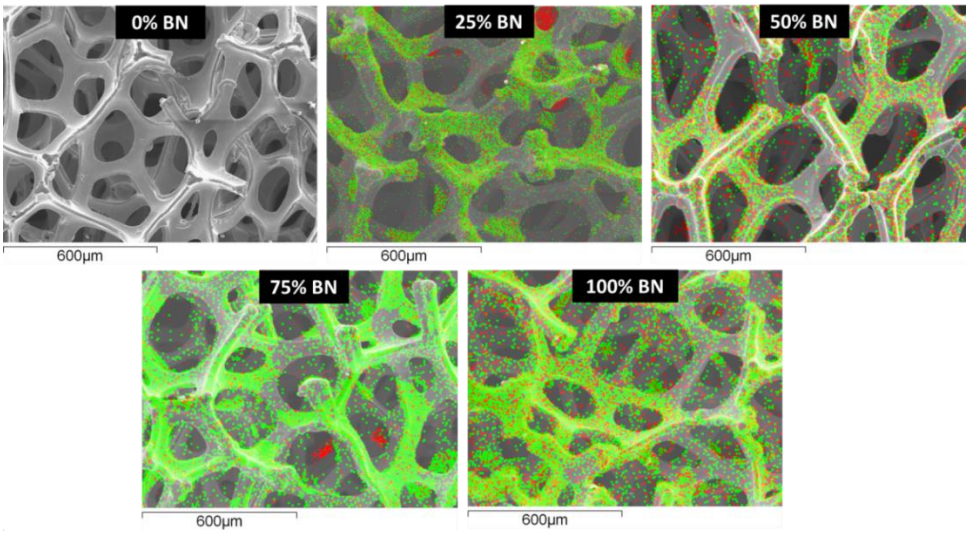

Figure 3-11. EDX result of the 1st step of 3D BN-C synthesis (growth of 3D-BN) at different growth times. The mapping (green and red correspond to B and N) shows the obtained h-BN coverage of each sample, from left to right a. 0%, b. 25%, c. 50%, d. 75% and e. 100% respectively. The evolution of the BN clusters supports the proposed mechanism of patches. The patches increase gradually and cover the entire Ni scaffold as time increases

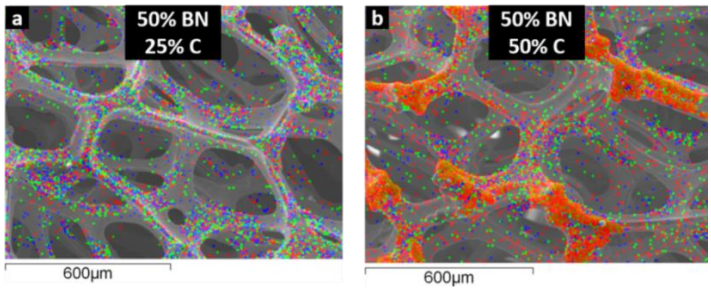

Figure 3-12. EDX mapping of the 2nd step of 3D BN-C synthesis, with **(a)** 25% C (red) on 50% BN and **(b)** 50% C (red) on 50% BN. This shows that 3D-C grows on exposed Ni surface and forms patches. The coverage of C on Ni scaffold gradually increases when growth time is increased

This is similar to the synthesis of patched and stacked graphene and h-BN 2D structure reported recently.[125] (The EDX mapping of the growth process of 3D-BNC at different stages is shown in Figure 3-11 and Figure 3-12). In this way, it is possible to effectively control the composition of C:BN by varying the growth time in sequence (Table 3-1).

Table 3-1. Growth time – concentration relation for the synthesis of 3D-BNC

Time Bubbler [min]	Concentration %C	Time Precursor [min]	Concentration %BN
10	100	0	0
9	90	4	10
8	75	10	25
6	50	23	50
3.5	25	38	75
3	20	42	80
0	0	60	100

To have a better understanding of the distribution for the C- and BN-domains on the as-grown BNC hybrid foam, EDX spectroscopy and mapping was carried out. Figure 3-13a–c presents the SEM images with integrated EDX mapping of the three obtained BN:C concentrations (25:75, 50:50 and 75:25), respectively. The K shell emission line for carbon peaks (0.22 keV) is mapped in red, nitrogen peaks (0.392 keV) in blue and

boron peaks (0.183 keV) in green. It is observed that clusters of C, N and B are distributed randomly, yet evenly across the entire 3D architecture, corresponding to the photographs in Figure 3-8b. The corresponding EDX spectra of different concentration of C:BN are plotted in Figure 3-13d–f, and the B/C/N wt% distribution are listed in the inset of each plot.

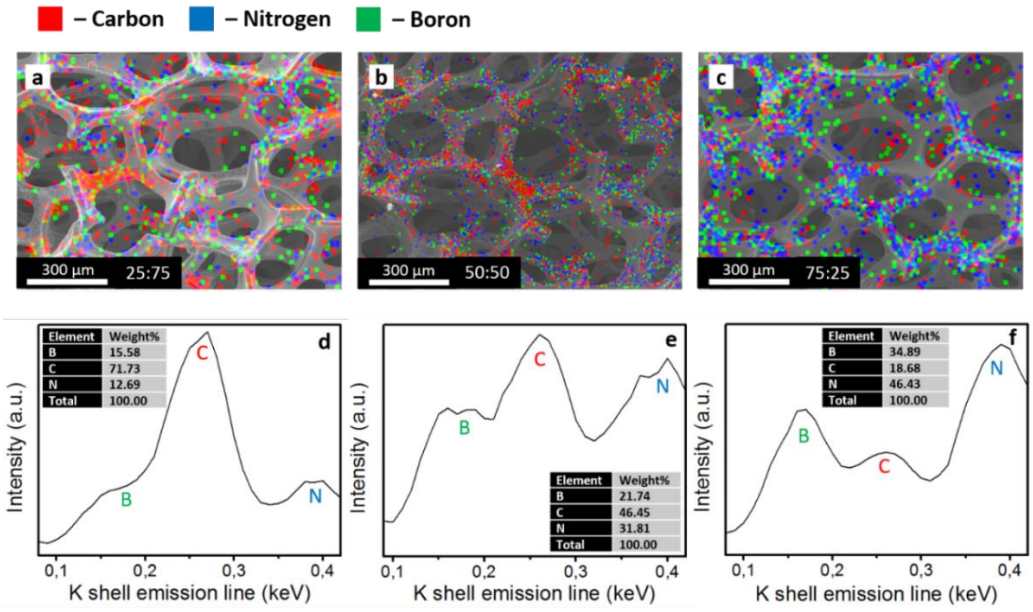

Figure 3-13. (a–c) EDX mapping of 3D-BNC with different BN:C ratio (25:75, 50:50 and 75:25), with red (color) corresponds to carbon, blue (color) to nitrogen and green (color) to boron-peaks; **(d-f)** are the respective K shell emission line plots where boron K emission line is at 0.183 keV, carbon at 0.277 keV and nitrogen at 0.392 keV. Insets are the estimated content (%) of the elements B, C and N

To determine the crystalline configuration of the as-grown BNC, Raman spectroscopy was used. Figure 3-14a shows the Raman spectra of BNC-foam for different concentrations, comparing them with a spectrum of pure 3D-C sample (top curve). It is observed that the absence of D peak in the pure 3D-C sample indicates the presence of high quality pristine graphene. The second-order Raman band (2D band) can be used to estimate the number of layers of CVD-grown graphene according to its relative intensity with respect to the G band (I_{2D}/I_G).[126] The intensity of the G band is about 4 times higher than the intensity of the 2D band ($I_{2D}/I_G \approx 0.25$), indicating multi-

layer graphene.[127] The Raman spectra for 3D-BNC with different compositions show three distinct peaks corresponding to D, G and 2D band of graphene, respectively.[126] The evolution of D peak at ≈1360 cm^{-1} arises with increasing BN concentrations due to a combination of the E_{2g} phonon mode of h-BN ≈1370 cm^{-1} and defect peak of graphene (D peak ≈1350 cm^{-1}).[128, 129] This suggests stacked structures of BN and C layers, where Raman peaks are originated independently from BN and graphene, respectively. Furthermore, a shoulder at the G peak, which is another disorder induced band (D′ peak ≈1620 cm^{-1}) is observed when BN concentration is increased to 50%. This further confirms the in-plane stitching of BN and C domains. [130, 131]

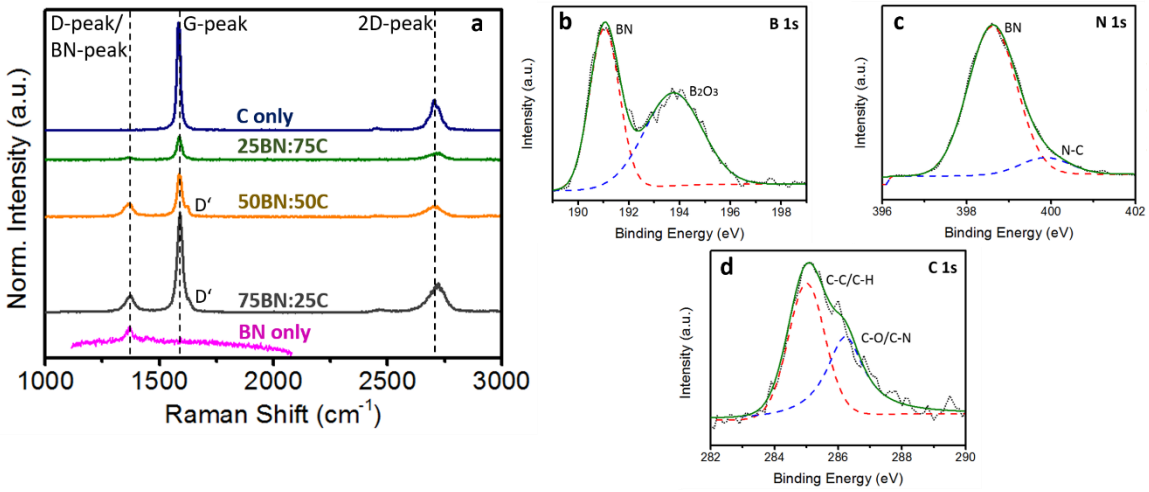

Figure 3-14. (a) Raman signal of 3D-BNC of different BN:C ratio. The peak at 1360 cm^{-1} is contributed by h-BN [128] and D peak from disordered graphene. The other two peaks at 1580 cm^{-1} and 2700 cm^{-1} are the signature G and 2D peaks from graphene, respectively [126]; **(b–d)** XPS result of the bonding nature in 3D-BNC. The core levels of B, N and C 1s are displayed respectively

The nature of the chemical bonding structure of the 3D-BNC was analyzed with XPS and the spectrum of B, C and N are shown in Figure 3-14b-d. The position of the spectra of all three elements are very similar to the previously reported XPS studies for 2D BNC.[130] The main peak of the B 1*s* is at 191 eV, close to the B 1*s* peak reported for h-BN (190.75 eV), indicating B-N bonding.[132] A second peak located at 194 eV

corresponds to B_2O_3 bonding, originating from the O contained in ethanol during graphene growth. The N 1*s* peak located at 398.5 eV further confirms the presence of a B-N bond. This is similar to the reported N 1*s* peak of h-BN (398.2 eV).[132] The C 1*s* main peak is located at 285 eV, which is close to the value observed in graphite. This suggests that the C-C bonds also coalesce towards graphene/graphitic domains. The shoulder in the spectrum at ≈400 eV indicates bonding between C and N. This arises from the boundaries between C and BN domains. It should be noted that no B-C bond was observed due to the low atomic resolution of B, corresponding to the case of h-BNC.[131]

3.4 Intrinsic properties

3.4.1 Thermal conductivity

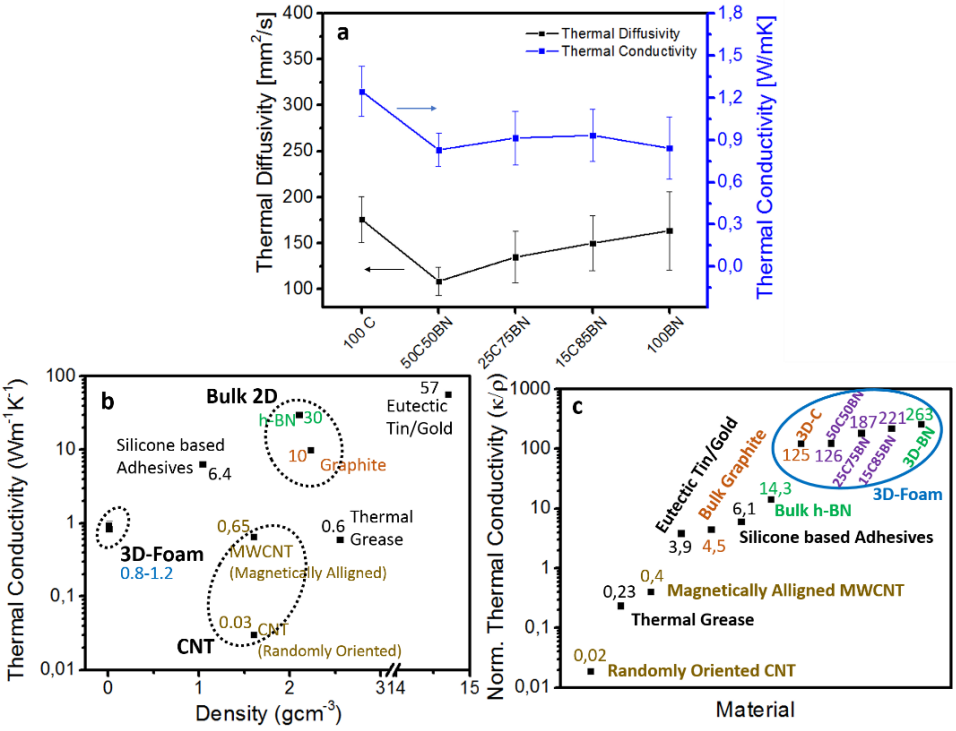

Figure 3-15. (a) Measured thermal diffusivity and the calculated thermal conductivity of the 3D-BNC at different BN:C ratio; **(b)** comparison of the cross-plane thermal conductivity between 3D-BNC with the current state-of-the-art TIMs and other carbon-based nanomaterials (CNT and graphene); **(c)** Normalized thermal conductivities of the stated materials with respect to their densities

Bulk graphite and bulk BN are known to have very high cross-plane thermal conductivities of around 10 $Wm^{-1}K^{-1}$ [11, 133] and 30 $Wm^{-1}K^{-1}$,[134] respectively. The highest cross-plane thermal conductivity measured on 3D-C is only 1.7 $Wm^{-1}K^{-1}$ [20] due to its high porosity and low density. However, compared to composite polymer/nano-carbon (such as carbon nanotubes (CNTs) and graphene) at the same loading fraction, the thermal properties of 3D-C are actually several times higher.[135, 136] The reason for this is due to the 3D interconnected nature of 3D-C compared to dispersed nano-fillers such as CNTs and graphene. As 3D-BNC is a composite of 3D-C and 3D-BN, its cross-plane thermal performance should be comparably high as well. Figure 3-15a shows the thermal characteristics of the 3D-BNC foam.

The 3D-C sample is found to have a thermal conductivity of 1.25 ± 0.18 $Wm^{-1}K^{-1}$ which is comparable to the previous reported value at 1.7 $Wm^{-1}K^{-1}$.[20] For 3D-BN, it is found to be 0.84 ± 0.22 $Wm^{-1}K^{-1}$. The thermal conductivities of 3D-C and 3D-BN are comparable since graphene and h-BN both have high thermal conductivities due to their similar phonon spectrum.[40, 137] For 3D-BNC, their thermal conductivities are measured to be between 0.9 ± 0.18 and 0.84 ± 0.22 $Wm^{-1}K^{-1}$. It is lower as compared to 3D-C due to the presence of interface between C and h-BN domains.[138, 139] Additionally, bulk thermal conductivities κ_{BULK} of the 3D-BNC for varying concentrations are calculated with Schuetz and Glicksman approach for open-celled metal foams at low loading[140]

$$\kappa_{BULK} = \left(3/\varphi \right) \cdot \kappa \qquad (3\text{-}3)$$

where φ is the volume fraction of the material. The volume fraction φ for 3D-C is about 0.4%, 0.1% for 3D-BN and about 0.2% for their hybrid BNC forms. Results are tabulated in Table 3-2 and are comparable to the reported value of ≈2000 $Wm^{-1}K^{-1}$ and 360 $Wm^{-1}K^{-1}$ for graphene and BN, respectively.[141-143]

Figure 3-15b shows a comparative chart between 3D-BNC with other state-of-the-art commercial thermal conductive materials (thermal grease, eutectic tin/gold, Si based adhesive)[144, 145] used for thermal interfacing and as well as other carbon-based nanomaterials that are in the research frontier (CNTs[135] and graphene[136]). To truly highlight the exceptional advantages of low-density foam-like materials, the respective material thermal conductivities are normalized with their density and are shown in Figure 3-15c. Clearly, these 3D-BNC foam-like structures have a significantly higher performance (2 – 3 orders of magnitude higher) than other current thermal materials when the density (and thus weight) of the materials is considered.

Table 3-2. Comparison between measured thermal conductivity of the foam materials κ and as calculated bulk materials κ_{BULK}, with $\kappa_{BULK} = (3/\varphi)\kappa$, where φ is the volume fraction

Sample	Therm. Conductivity Foam [$Wm^{-1}K^{-1}$]	Therm. Conductivity Bulk [$Wm^{-1}K^{-1}$]
100C	1.25	934.14
50C:50BN	0.83	995.94
25C:75BN	0.92	1568.62
15C:85BN	0.93	1931.54
100BN	0.84	2526.98

3.4.2 Electrical conductivity

BN is known to be highly insulating with a wide band gap of ≈6 eV,[43] whereas graphene is highly conductive with carrier mobility surpassing the 10 000 $cm^2 V^{-1}s^{-1}$.[2] Hence, a compositional variance of the two (such as BNC) is expected to enable electrical tuning with an ultra-wide spectrum. Figure 3-16a shows the electrical conductivity and resistivity plots of the 3D-BNC foams with respect to different BN:C concentrations. It is observed that the electrical conductivity σ, decreases with

increasing BN concentration. The decrease of σ per %-amount can be divided into three regions: I the very high electrical conductivity of pure 3D-C followed by a sudden drop into region II with a linear decrease according to the increasing concentration of BN:C. Region III comprises of very low σ, which is almost completely insulating due to the effects of BN dominating the structure.

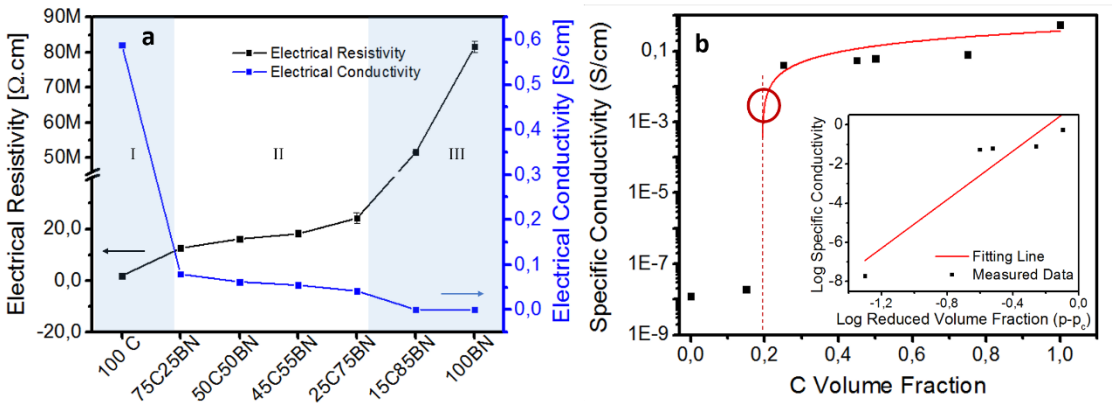

Figure 3-16. (a) Electrical measurement results of 3D-BNC at different C:BN ratios. Region I corresponds to the highly conductive (low resistive) range, region II to the linear change of the electrical conductivity according to the BN:C concentrations, region III is the highly insulating. **(b)** Plot of electrical conductivity as a function of C volume fraction. The inset shows the log-log plot of the electrical conductivity of 3D-BNC as a function of (p-p_c) with a linear fit

The divisions (region I, II, III) are dependent on the varying BN:C concentrations. In region I (pure 3D-C), charge carriers can move freely and rapidly through the continuous graphene network, resulting in a very high measured σ of 0.6 Scm^{-1}. In region II, a sharp decline in σ is observed (0.08 Scm^{-1}) and it decreases almost linearly with increasing amount of BN concentration. These BN domains can be perceived as resistive barriers within a 3D-C network causing a higher resistive path, which hinders the flow of electrons. As the BN concentrations increases to ≈85% in region III, the 3D hybrid network is dominated with BN domains. This causes even more discontinuity within the block impeding charged carrier flow through the material and thereby resulting in an exponential increase in resistivity (from ≈24 Ω.cm at 25:75 C:BN to ≈52 MΩ.cm at

15:85 C:BN). This observation matches with the percolation threshold theory for composite materials.[146, 147] When a certain composition of graphene inside the mixed material matrix is reached, the conductivity rises sharply, transforming into a conducting material. The conductivity of the composites can be further rationalized in terms of modified classical percolation theory,[146]

$$\sigma = \sigma_0 \cdot (p - p_c)^t \qquad (3\text{-}4)$$

where σ represents the conductivity of the composite, σ_0 the scaling factor, p the volume fraction of the filler (in this case C is denominated as such), p_c the volume percolation concentration, and t the critical exponent. Figure 3-16b shows a plot of electrical conductivity of BNC as a function of C volume fraction. From the fitted curve, the percolation threshold is ~0.2. This means that from C:BN 20:80 onwards, 3D-BNC starts to become a conductive material. The inset is a log-log plot of the electrical conductivity as a function of reduced volume fraction (p-p_c) and from the linear fit, a critical exponent t of 6.2 ± 1.3 is calculated. The high value of t corresponds to the steep transition between insulating and conducting mode.

3.4.3 EMI shielding effectiveness

The shielding and its efficiency is measured in terms of shielding effectiveness (SE) and it is defined by IEEE standard[148] as "the ratio of the signal received (from transmitter) without the shield to the received signal inside the shield", and can be formulated as the logarithmic ratio of incoming power P_i to transmitted power P_t of an electromagnetic wave, expressed in decibel (dB). The higher the dB-level of EMI SE, the lesser electromagnetic wave is transmitted through the shielding material. Figure 3-17a and Figure 3-17b show the plots of EMI SE transmittance (S12) and reflectance (S11) measurements, for five different samples (3D-C, 75BN:25C, 50BN:50C, 25BN:75C and

3D-BN), respectively. The incident and transmitted waves can be represented by complex scattering parameters (S-parameters): S11 (or S22) and S12 (or S21) which can be correlated with reflectance, *R*, and transmittance, *T*, through formula (3-5) and (3-6),[35]

$$R = |S_{11}|^2 = |S_{22}|^2 \quad (3\text{-}5)$$

$$T = |S_{12}|^2 = |S_{21}|^2 \quad (3\text{-}6)$$

The absorbance, *A*, can be calculated through the relation $A + R + T = 1$.[35] 3D-C, due to its highly conductive properties, exhibits high EMI shielding performance (≈50 to 55 dB within the frequency range of 8 to 13 GHz),[35, 36] and BN on the other side is highly insulating, and thus is completely transparent to electromagnetic waves and presents no barrier to them (comparable to air). For 3D-BNC, it is observed that with increasing amount of C concentration in the hybrid structure, S12 increases correspondingly and these observations are in strong agreement with the electrical conductivity measurement. When comparing the electrical measurement (Figure 3-16a) with EMI SE (Figure 3-17) measurements, it is obvious that S12 enhances with increasing electrical conductivity. Region I (high content of C) is of high conductivity and expectedly corresponds to high shielding effectiveness while region III (poor electrical conductivity due to high content of BN) corresponds to a much lower shielding effectiveness. In region II the electrical conductivity decreases linearly in tandem with the shielding effectiveness. A higher decrease from 50:50 to 25:75 is also observed as it is closer to the percolation threshold. Hence, by carefully controlling the concentration of BN and C, the EMI SE properties of the 3D-BNC can be tuned for specific applications needs. This is non-trivial since different application systems have finite tolerances towards both over and under-shielding in the EM regime (Table 3-3 tabulates some applications needs). A good

example would be microprocessors (500 MHz – 1.5 GHz) where both over-shielding and under-shielding should be avoided.[149]

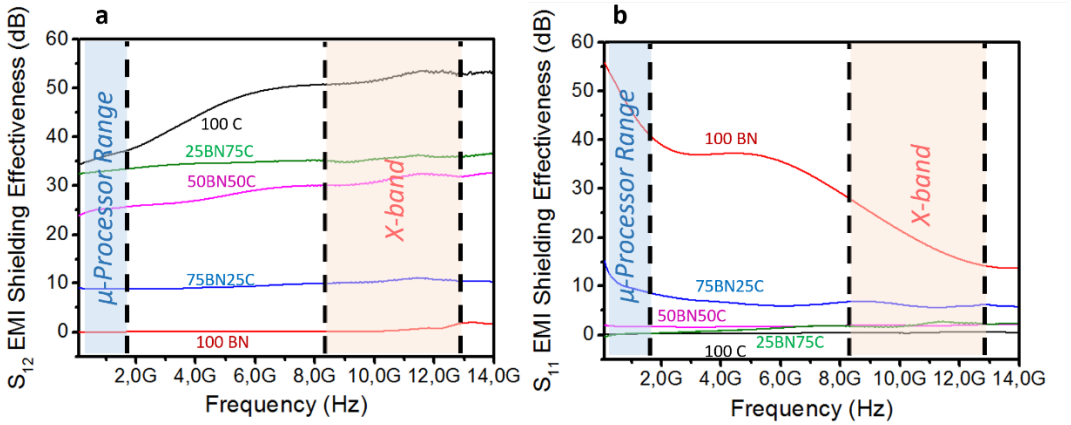

Figure 3-17. (a) and **(b)** are the S12 and S11 measurement of the 3D-BNC with different composition from 100 MHz to 14 GHz. Depending on the ratio of BN:C, the EMI shielding effectiveness of 3D-BNC can be tuned from 0 – 50 dB for S12 and 0 – 40 dB for S11. The two highlighted regions correspond to the microprocessor range (500 MHz – 1.5 GHz, blue) and X-band (8.2 GHz – 12.4 GHz, red)

Table 3-3. Each device has a specific requirement of shielding which should be taken into account in the final design in order to avoid over shielding and under shielding[149]

Typical Application	Required Shielding
Notebook Computer	15 – 20 dB
Desktop Computer	12 – 20 dB
Cell Phone	70 – 90 dB
Cable Tap	70 – 90 dB
Workstation/Server	30 – 40 dB

3.5 Summary

In summary, in this chapter the basic recipes for growth of 3D-C and 3D-BN were developed, as well as the growth sequence and parameters of BN and C in order to achieve a novel hybrid and tunable material. After obtaining the structure, a systematic study on its tunable characteristics was carried out, namely thermal conductivity, electrical characteristics and EMI SE.

4 Tuning of foams

4.1 Introduction

In this chapter, recipes to precisely modify the 3D-foams according to application needs are developed. One such requirement for example is to be able to increase the density, since the current recipes yield a material that is comprised of merely 0.3% of 2D material, the rest being open pores. In addition, 3D-foams are praised as superior filler materials for polymers due to their interconnected structure. Thus, recipes to integrate the foams with matrix parent materials will be developed. For this purpose, new matrix materials, such as thermally conductive adhesives and thus far unreported polymers are explored. In the following chapter, these newly developed recipes will be presented, along with first assessment of obtained quality.

4.2 Characterization tools

Besides the characterization tools described in 3.2.5, further characterization to determine the successful integration of the 3D-foam skeleton into an external matrix is necessary:

4.2.1 Wetting properties

Contact angles were measured to determine the wettability of obtained structures. Contact angle occurs at liquid–vapor interfaces, in this case where water meets a solid surface. Water contact angles smaller than 90° stand for hydrophilic surfaces, water contact angles larger than 90° stand for hydrophobic surfaces.[150] Here, it is measured using a video contact analyzer (Dataphysics OCA) and analyzed with the software SCA 20.

4.2.2 Polymer integrity

Thermogravimetric analysis (TGA, TA Instruments Q500 and Shimadzu Scientific Instruments DTG-60H) is performed to study the decomposition profile of polymer – 3D-foam composites. This method investigates the stability of the material at elevated temperatures by heating them up to ~1100°C while monitoring their weight.[151, 152] This way, any changes in physical and chemical properties of the material tested are measured as a function of increasing temperature.

Differential scanning calorimetry (DSC, TA Instruments Q100) is a thermal measurement that determines the difference in the amount of heat required to increase the temperature of a sample as a function of temperature.[153] This technique can detect thermal transitions within a polymer (such as the glass transition temperature).

4.3 Tuning density

For some applications, such as biological scaffold or thermal,[20, 154] it is important to be able to tune the number of layers comprising the foam, or more drastically, increase the density, since 99.6% of the volume of a bare foam is air/free space.

Typical 3D-foam has between 8 and 10 layers. The number of layers can be tuned by the growth parameters; above 10 layers, the 3D-foam starts to resemble graphitic or bulk h-BN structures. To increase the density of the 3D-foams, two approaches can be used; namely, (1) prolonging the growth duration and (2) compressing the 3D-foam with an applied force. The difference between the two is mainly that in (1), the thickness of the walls increases while the pore distribution remains unchanged. As for (2), it decreases the pore size but the thickness of the walls remains unchanged.

To verify the quality of both methods, Raman spectroscopy was performed on both types of samples. The results in Figure 4-1a show a stable quality throughout the

varieties of 3D-foams. The typical peaks for a high quality multi-layer graphene, together with their ratio, are well preserved in all three graphs (G-peak at 1580 cm^{-1}, 2D-peak at 2700 cm^{-1}, absence of D-peak at 1350 cm^{-1} and a ratio of G:2D-peak intensity of 0.25).[126] As an example of denser foams achieved through compression, Figure 4-1b shows a SEM image of a sample 90 times denser than the standard 3D-foams and it can be seen clearly that the size of the pores decreased accordingly. Figure 4-1c shows the maximum density achievable, whereby all pores have been closed and only the outline of the walls are still visible.

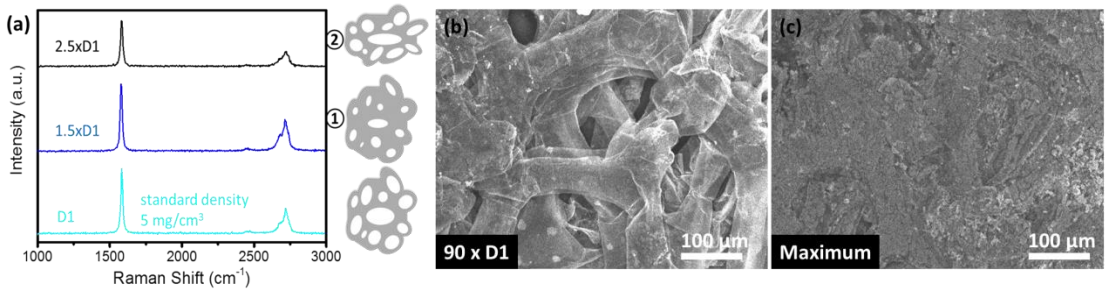

Figure 4-1. (a) Raman spectroscopy on the 3D-foams with different density obtained through the two different methods to increase layer numbers. **(b)** SEM image of a 3D-foam compressed down to 90 times its original density D1, **(c)** SEM image of a maximum compressed 3D-foam

4.4 Infusion of 3D skeletal structure in Thermal Adhesives

4.4.1 Metals

3D-foams are incorporated into metals through chemical functionalization. Since metals are electrically conducting, only 3D-C is used for this experiment. Conventionally, methods to adhere metals on 3D-C comprise evaporation,[155] electrochemical deposition[39, 70] and hydrothermal procedure,[31] which do not allow covalent bonding and are mainly used to add metals on the outer layers of the 3D-C. This does not provide a continuous thermal or electrical conduction path and upon

heating beyond the metal's reflowing point, the metals detach and form single clusters, without intermixing with the 3D-C.

Typical metals used in electronics are Sn, Cu, Au (and Sn/Au). For functionalization with these metals two chemical steps are required, which are namely the oxidation of 3D-C, followed by a chemical reduction with the respective metal salt in order to obtain a covalent bonding between metal and 3D-C. The schematic in Figure 4-2 summarizes the necessary steps.

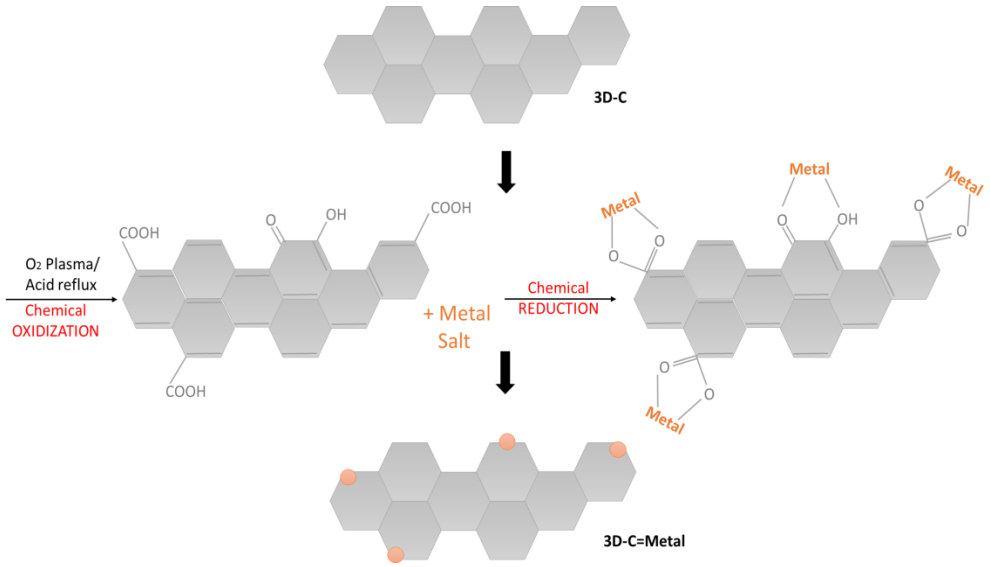

Figure 4-2. Schematic of the steps required for obtaining metal-infused 3D-C (3D-C=Metal)

4.4.1.1 Oxidization of 3D-C

This can be obtained via O_2 plasma of 3D-C, or via acid reflux. For the first case, the samples are placed inside an O_2 chamber. Typically, after treatment of one side, samples need to be flipped over and the treatment repeated. Since for this type of oxidization the functionalization is inhomogeneous (higher on the outer surface than inside the foam), acid reflux is usually preferred as oxidization method. For this, samples are immersed in sulfuric acid (H_2SO_4)/nitric acid (HNO_3) 3:1 v/v for at least 20 hours at room

temperature. Afterwards, the solution is diluted with DI-H_2O and filtered. Samples need to be washed and dried at 90 – 110 °C. This yields a spatially more uniform distribution of functionalization.

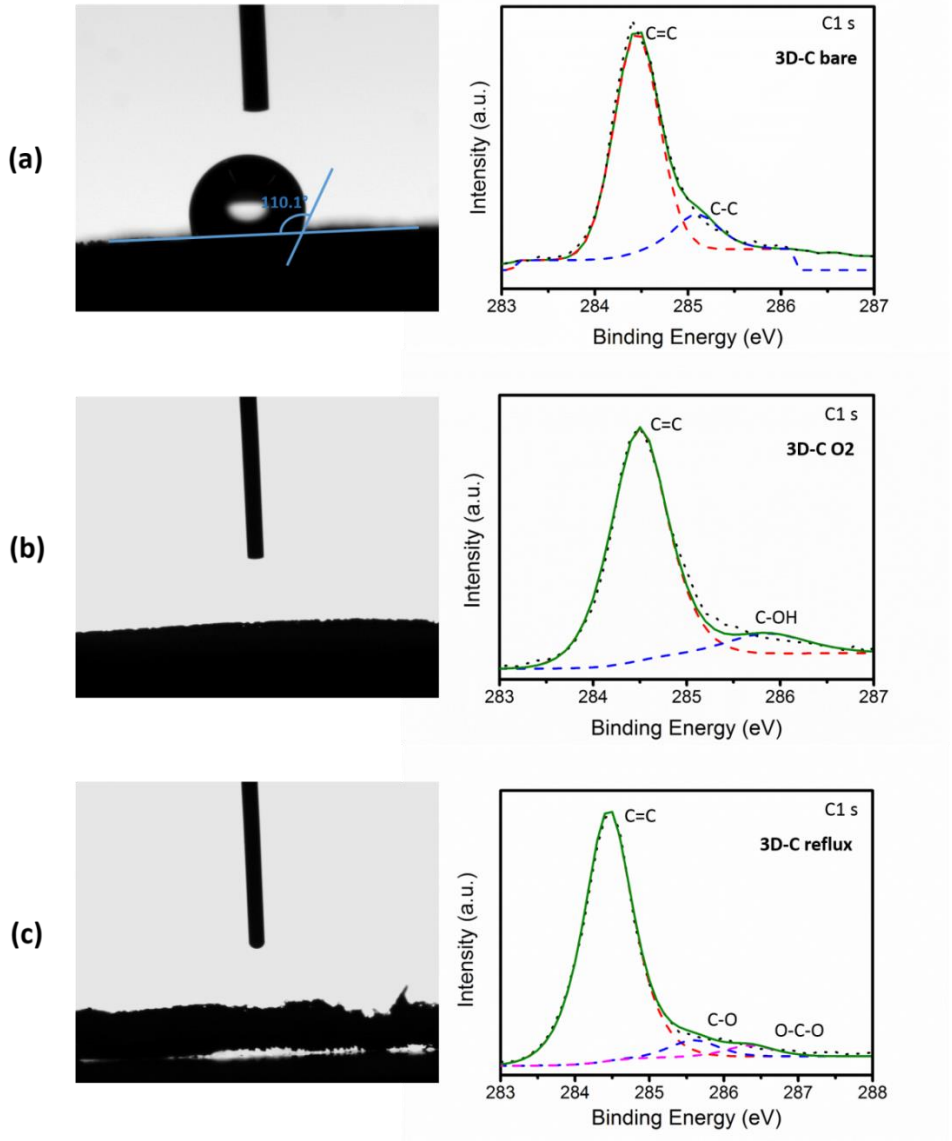

Figure 4-3. Measurements to determine successful oxidization of 3D-C surface through contact angle and XPS on **(a)** unmodified 3D-C, **(b)** O_2 plasma treated 3D-C and **(c)** 3D-C after acid reflux

O_2 plasma mainly attaches –OH (hydroxyl) terminated groups on the surface of 3D-C,[156, 157] acid reflux mainly –COOH (carboxyl) terminated groups.[158] Both groups are suitable for the functionalization with metals. In order to determine the success of

oxidization of 3D-C, contact angle measurements and XPS were carried out and results are shown in Figure 4-3. The peaks obtained for the C1s spectra are in accordance with the previously stated functional groups obtained with each method. Contact angle shows that untreated 3D-C is hydrophobic and the water droplet remains floating on top of the 3D-C. Both O_2 plasma and acid reflux yield immediate adsorption of the water droplet due to the hydrophilicity rendered.

4.4.1.2 Chemical functionalization of 3D-C with metal

In order to enable reflow between 3D-C and the metal/solder, metal functionalization on the surface of 3D-C is required. This is achieved via chemical reduction of the oxidized 3D-C with the respective metal salt. This chemical reduction is exemplified for the case of Sn:

The process is adapted from a previous report on Sn-functionalized graphene oxide sheets.[159] For synthesis of 3D-C=Sn (Sn-functionalized 3D-C), for each mg of 3D-C, 2 – 5 ml aqueous solution of $SnCl_2.2H_2O$ (2 – 5 mg) and citric acid (2 – 5 mg) as buffer are mixed. Instead of citric acid, also other buffers such as trisodium citrate dihydrate or tetrahydrofuran can be used. Afterwards, 2 – 5 ml $NaBH_4$ (10 – 20 mg) aqueous solution is carefully added to the mixture. This is to reduce Sn^{2+} to Sn and oxidize 3D-C back to pure 3D-C. The samples have to be stirred/shaken in ice bath for at least 3 h (or until the solution turns into clear transparent color). The resultant products are separated by filtration and washed with DI-water and then dried.

The structure and morphology of 3D-C=Sn was analyzed by SEM with integrated EDX and XPS. The results are shown in Figure 4-4. In both cases it can be seen that Sn was successfully attached due to the Sn-C bonds detected. The EDX maps show a homogeneous distribution of the metal on the 3D-C.

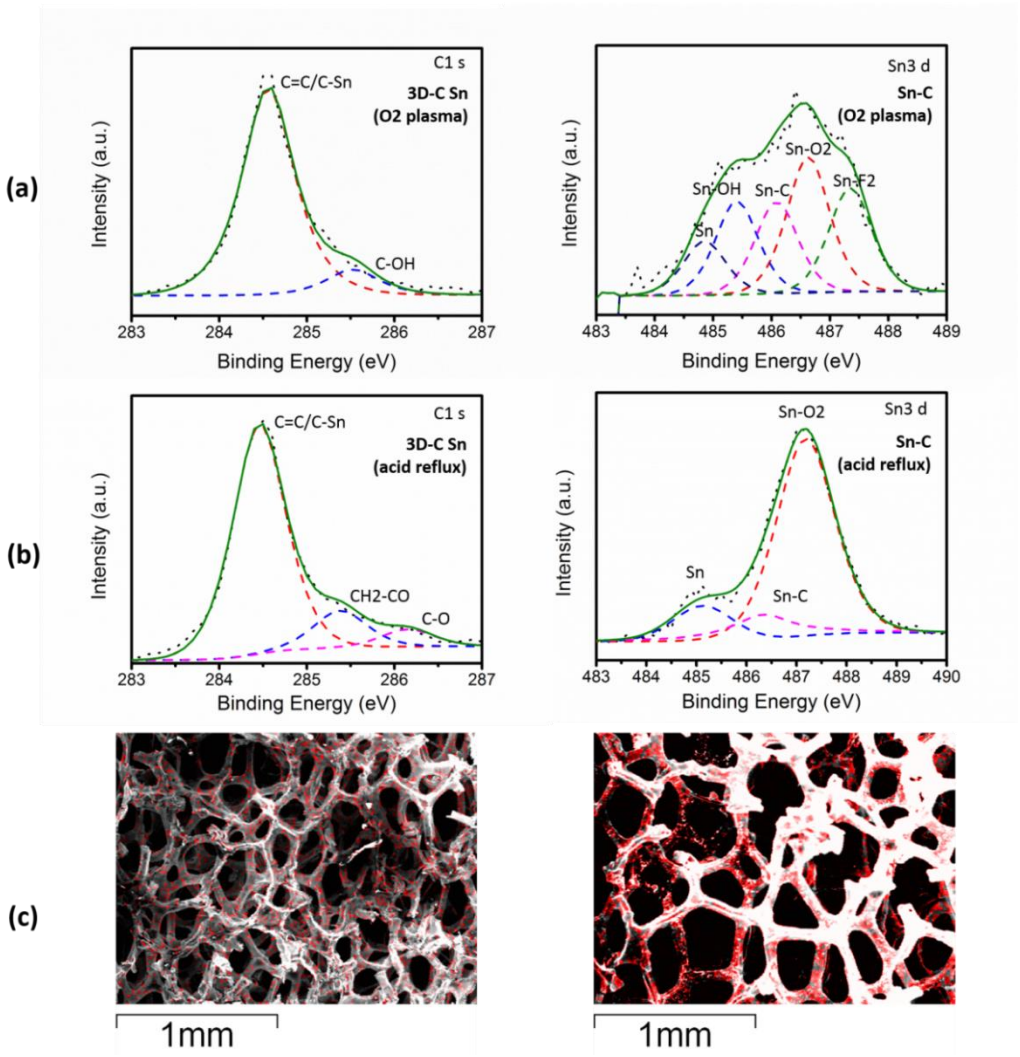

Figure 4-4. Characterization of attached Sn-particles. **(a)** XPS of C1s and Sn3d using O_2 plasma as surface pre-treatment; **(b)** XPS of C1s and Sn3d using acid reflux as surface pre-treatment; **(c)** their corresponding EDX maps with Sn mapped in red

The reduction can be adapted to the different metal salts. For example for Au, $AuCl_4^-$ is used;[160] for Cu, $CuSO_4.5H_2O$.[161] For the Cu case, also copper(II) acetate monohydrate (20 – 30 ml, 1 – 5 g) with NaOH (5 – 10 ml of 2M) can be used for the reduction.[162]

To visualize the successful functionalization and to highlight its effect on metal reflow, Sn powder was spread onto 3D-C and 3D-C=Sn foam and heated up above its melting temperature. The results in Figure 4-5 show that on untreated 3D-C (Figure 4-5a), the Sn is not able to attach, whereas for the functionalized case (Figure 4-5b) it can be clearly seen that Sn attached onto the foam and started forming bigger clusters

embedded within the 3D-C. Also, when squashing the foam while the sample is heated up (Figure 4-5c), it can be seen that the foam uniformly intermixes with the metal and is able to fill the pores with re-solidified Sn.

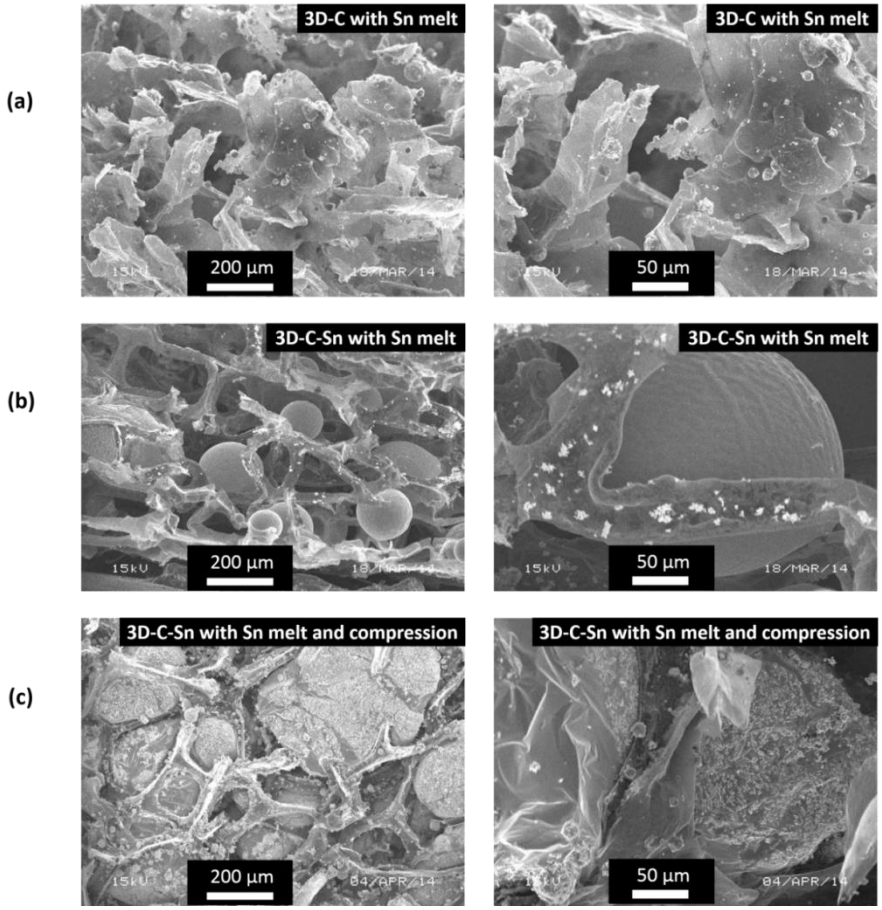

Figure 4-5. Results of Sn powder melting and compressing. **(a)** 3D-C without previous Sn infusion treatment; **(b)** 3D-C-Sn with attached molten balls of Sn; and **(c)** 3D-C-Sn with attached molten Sn powder after compression at high temperature

4.4.2 Silane

Silanes (i.e. amino-silanes) are a thermally conductive liquid "paste" and typically used as adhesion promoters between surfaces.[163-165] Typical silane compounds are aminopropyl-trialkoxy-silane, APTES (3-aminopropyl) triethoxysilane, APS (3-aminopropyl) trimethoxysilane, 3-(Trimethoxysilyl) propylamine for bonding to Al, Cu or Si, and cysteamine complexes for attachment onto gold surfaces.[166]

The hybridization method can be adapted according to final application, ranging between (1) submerging the foam in the paste and then placing onto the final surface, (2) placing the foam on the final surface and then dripping the paste onto it, (3) dripping the paste onto the final surface, and then placing the foam onto it. After each method, the structure must be dried, which can be fastened up via heating at 120°C. Further optimization can be obtained through pre-annealing of the solution to 70°C. This yields a more structured and ordered silane film, with far less unreacted ethoxy groups.[167] The post-annealing temperature (i.e. the temperature used for drying the samples) has no effect on the final film quality. For all methods, either 3D-BN or 3D-C can be used, since both will turn into electrically insulating foam with $\rho = 770 \pm 10$ Ω.cm. Figure 4-7 shows XPS survey spectra of 3D-C before and after silane functionalization (the silane used in this case is (3-aminopropyl) trimethoxysilane with the chemical formula shown in Figure 4-6). The additional presence of N 1*s*, O 1*s*, Si 2*p* and Si 2*s* for the latter case corroborates the successful hybridization of the amino-silane with the 3D-C.

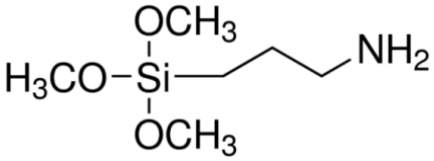

Figure 4-6. Chemical formula of (3-aminopropyl) trimethoxysilane (APS)

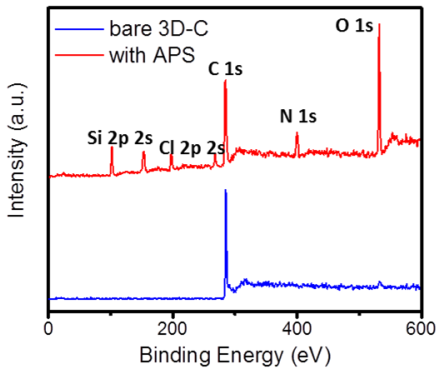

Figure 4-7. XPS survey spectra of 3D-C functionalized with APS

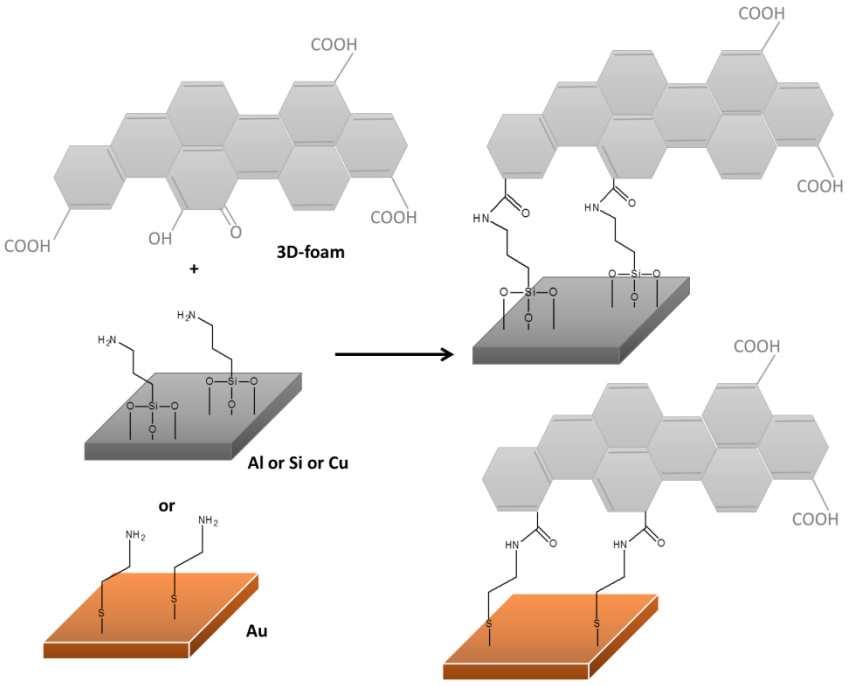

Figure 4-8. Schematic of chemical bonding between 3D-foam, silane and substrate

Figure 4-8 schematizes the chemical bonding present between paste and 3D-foam. The paste has binding sites, which are able to bind covalently to the 3D-foam and to the substrate underneath, typically Si, Al, Cu and Au surfaces. Thanks to this covalent link, an overall stronger bond and direct conduction path between substrate and 3D-foam is achieved.[85, 87-89] The attachment preferably occurs on the O-containing groups of the foam. Nevertheless, further forced induction of additional O-groups into the foam (e.g. as described in 4.4.1.1) will decrease overall performance for this case.

4.5 Infusion of 3D skeletal structure in Polymer

4.5.1 PDMS

Polydimethysiloxane (PDMS, Sylgard® 184) is a silicone polymer an it is a very common polymer often used to infuse with 3D-C.[17, 21, 168, 169]

For "conventional" 3D-foam/PDMS preparation, the PDMS resin (10:1 base:curing agent) is dripped onto the entire foam, which can be either bare or still with Ni, and then

cured for 1 hr at 130°C. For the case of Ni still being inside the sample, the Ni is etched away after the polymer has been fully cured. Figure 4-9a shows an optical image of 3D-C infused in PDMS, Figure 4-9b,c SEM images of a sample's top and cross-section view.

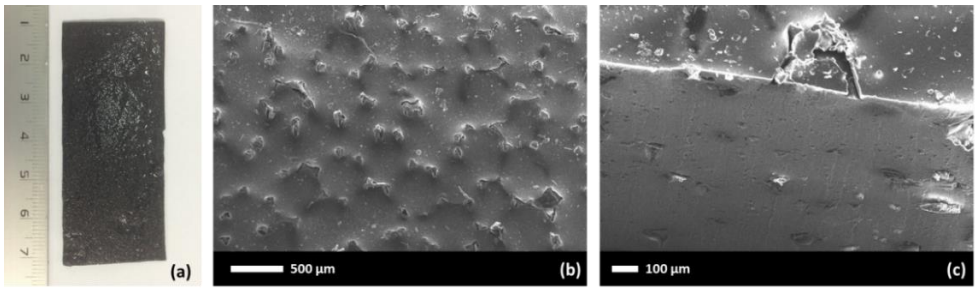

Figure 4-9. (a) Optical image of 3D-C infused with PDMS using conventional method. SEM imaged of 3D-foams infused with PDMS using conventional method. **(b)** top view and **(c)** tilted view of the edge revealing the cross-section

4.5.2 "Hairy" PDMS

Structures prepared with the "conventional" PDMS infusion suffer from loss of electrical conductivity and thermal properties, as well as additional layers of bare polymer below its structure, which further lowers the performance. This is why a new method is developed that yields 3D-foam that is infused with PDMS only in its central layer, with the bottom and upper layers still freely exposed – the "hairy" method.

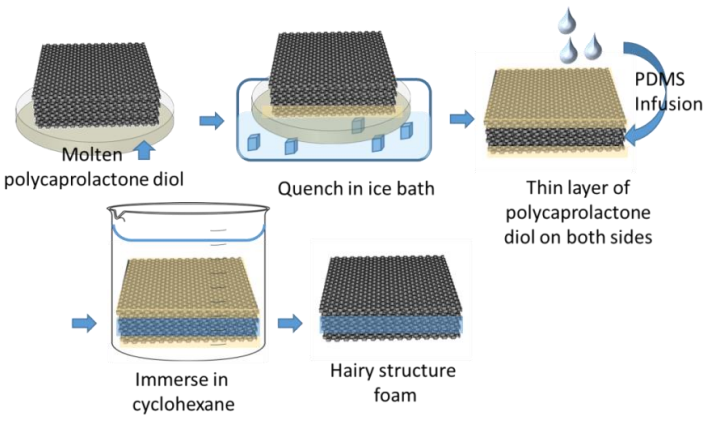

Figure 4-10. Schematics experimental procedure to obtain "Hairy" PDMS infusion

To prepare these "hairy" structures, 3D-foams still containing the metal foam template are used. Then, a thin layer of polycaprolactone diol is melted at 80 °C in an aluminum pan and the 3D-C/BN coated Ni foam dipped into the melt to coat the edge with a thin layer of it. The height of the molten polycaprolactone diol inside the pan determines the thickness of the later exposed part of 3D-foam. Subsequently, the pan with the foam inside is quenched in ice bath to solidify the polycaprolactone diol layer on the surface of the 3D-foam. The same procedure is repeated for the other side. This yields a porous 3D-foam sandwiched between two thin layers of polycaprolactone diol. PDMS is subsequently infused into the remaining uncoated layers of the foam to obtain a uniform coating of PDMS within the porous structure. Degassing is carried out during infusion process to remove air bubbles and ensure a uniform coating throughout the 3D-foam. The PDMS coated foam is then left in the oven at 60 °C for 24 hours. Then, polycaprolactone diol is dissolved and rinsed a few times in cyclohexane to fully remove traces of it in the system, exposing the hairy structure of the original foam. Once the samples are completely dry, the Ni is etched away through chemical etching with HCl. After all the Ni is removed, samples are washed in DI-H_2O and subsequently dried. Figure 4-10 schematizes the steps required. The process can be adapted to obtain "hairy" layers on both sides or on one side only (i.e. skipping the second polycaprolactone diol coating step). Figure 4-11a and Figure 4-11b show optical images of the obtained samples with and without the PDMS infusion. It can be seen that the process does not change the overall physical appearance of the 3D-foams. In Figure 4-11c and Figure 4-11d the flexibility of the structures is demonstrated, as they are able to completely conform to the curvature of a 6.5 mm diameter rod and fully return back to their original shape without breaking. This is in big contrast to bare 3D-foams, which beyond a bending angle of 15° immediately break (Figure 4-12).

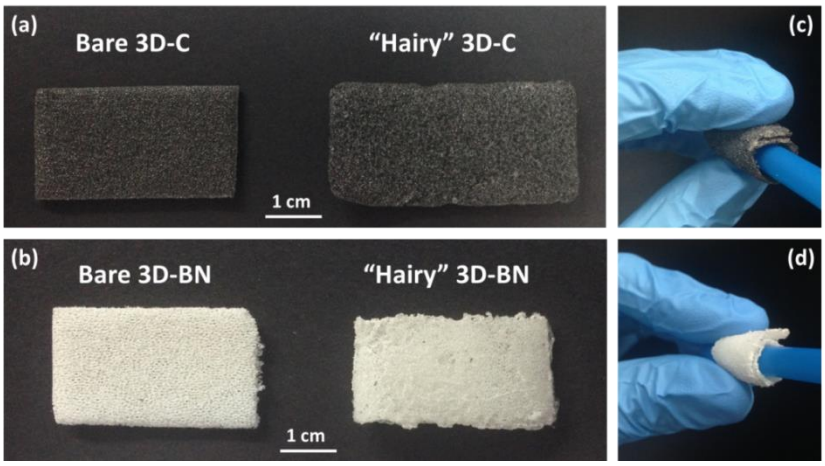

Figure 4-11. Optical images without and with the "hairy" infusion **(a)** of 3D-C and **(b)** of 3D-BN. Demonstration of flexibility **(c)** of "hairy" 3D-C and **(d)** of "hairy" 3D-BN

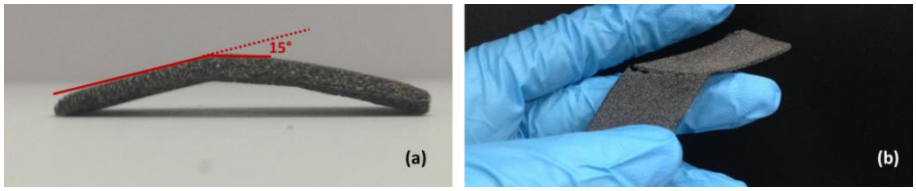

Figure 4-12. Bending studies on bare 3D-foam. **(a)** Point of break at 15°, **(b)** broken sample

Cross-sectional SEM images of the 3D-foams without and with the "hairy" infusion are shown in Figure 4-13a and Figure 4-13b, respectively. It can be clearly seen that the infusion yields a single thin layer of PDMS in the center of the foam without causing any contamination, and without causing any structural changes to the 3D-foams (i.e. their structure outside the infusion layer remains intact, exactly like the 3D-foam's bare morphology).

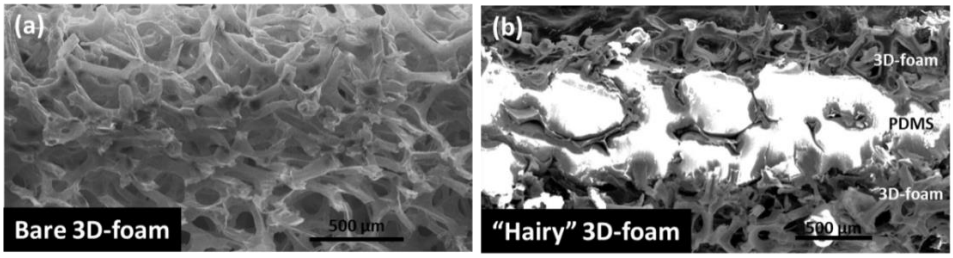

Figure 4-13. Cross-sectional SEM images of **(a)** bare and **(b)** "hairy" 3D-foam

Further corroboration of the non-invasiveness (i.e. no changes in quality) was assessed through Raman spectroscopy, and results are shown in Figure 4-14. As evident from the graphs, the infusion step does not alter the crystal structure of the 3D-foams (i.e. fully preserved peak position and width).

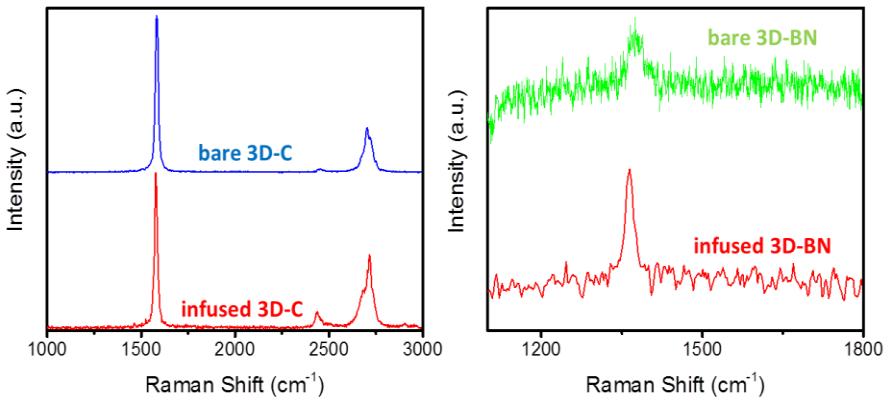

Figure 4-14. Raman spectroscopy results on 3D-foams with and without "hairy" infusion

4.5.3 PI

For infiltration with PI, pyromellitic dianhydryde-oxydianiline (PMDA-ODA) PI precursor was used. Its chemical structure is shown in Figure 4-15.

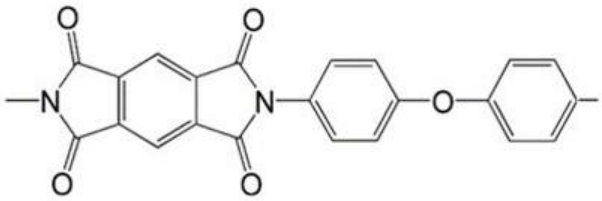

Figure 4-15. Chemical structure of PMDA-ODA polyimide monomer

Since residual stress is a serious issue that arises in infiltration of PI with fillers,[170] mainly due to solvent evaporation, a process to target this problem was carefully developed: instead of using the conventional two-step poly(amic acid) process,[171, 172] the infiltration process was divided into several steps with diluted polyamic acid solution,

thus enabling enhanced penetration of the solution. This prevents the build-up of strain within the film and at the interface between PI and 3D-foam during the curing stage. This process is particularly suitable for 3D-foam structures, due to the three-dimensional skeleton, as the total volume required to obtain a full-film can be calculated a-priori. The schematic of the infiltration process is shown in Figure 4-16. First, a diluted polyamic acid (PAA) solution is poured onto the 3D-foam and cured, using a SiO_2 substrate as mold. After curing, a thin PI film forms at the bottom of the 3D-foam and this serves as a limit for subsequent steps, where each layer will be built on top of the previous one. Next, an additional layer of diluted PAA solution is poured onto the composite and cured. This step is repeated until the cured PI thickness is close to that of the bare 3D-foam. The dilution level and the amount of PAA solution are determined by the porosity and volume of the 3D-foam prior to the infiltration. The final free-standing flexible 3D-foam/PI films are then obtained by peeling the nanocomposites from the Si substrate. The peeling off is enabled due to reduced adhesion between the PI and the Si substrate as a result of the oxide layer deposition on the Si wafer.[173]

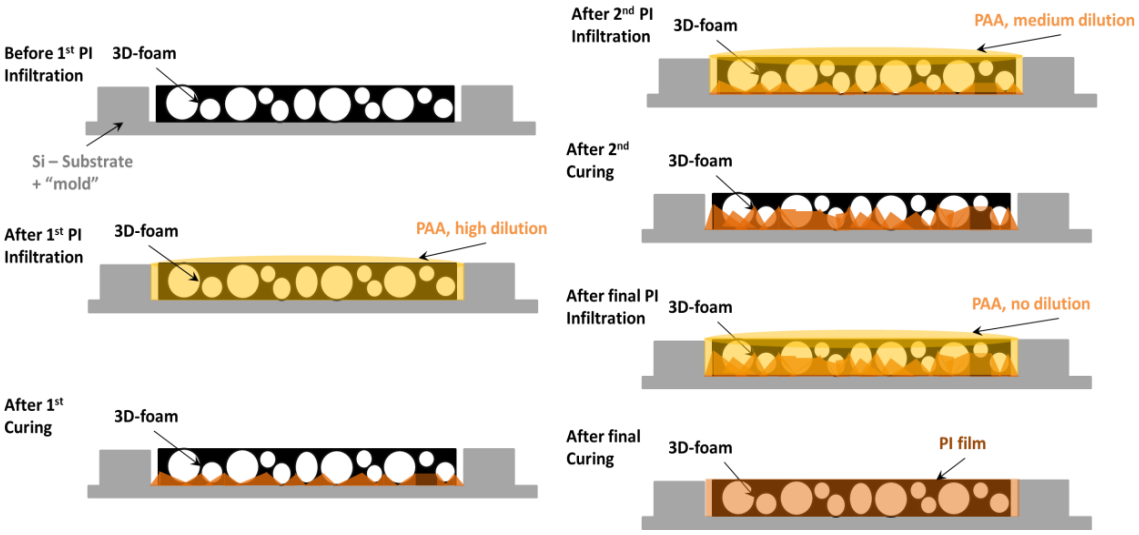

Figure 4-16. Schematic of the infiltration process of PI into 3D-foam

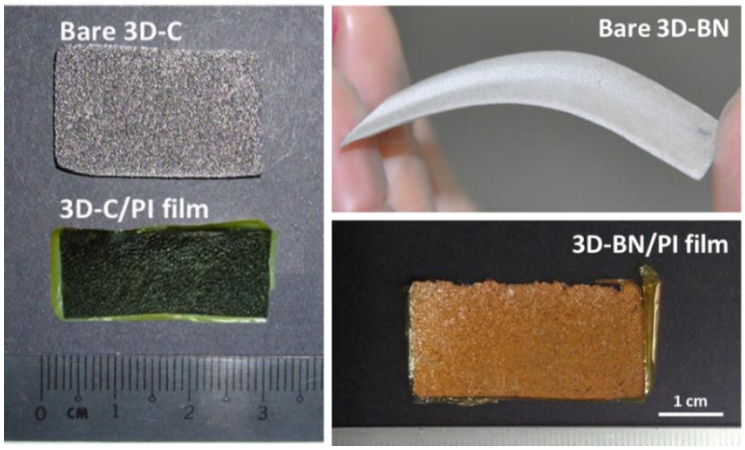

Figure 4-17. Optical images of the bare 3D-foams and their respective PI films

Optical images of both bare 3D-C and 3D-C/PI composite and bare 3D-BN and 3D-BN/PI composite are shown in Figure 4-17, indicating a homogeneous distribution of PI along the 3D-foams. Figure 4-18 shows the cross-section SEM of 3D-foam and PI infiltrated 3D-foam. It can be clearly seen that the entire highly porous structure of the 3D-foam has been completely infused with PI and no air pockets are observed.

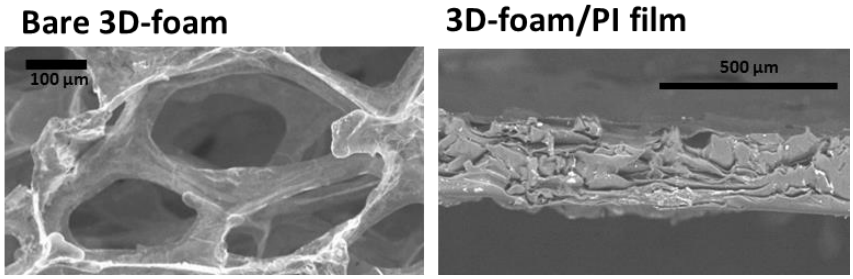

Figure 4-18. Cross-section SEM images of bare 3D-foam and 3D-foam/PI film

Raman spectroscopy was performed to verify the quality of the foams and the spectra are shown in Figure 4-19. The bottom (blue) graph shows the bare 3D-C spectrum, the bottom green bare 3D-BN. The two distinctive graphene peaks at 1580 cm^{-1} (corresponding to the G-peak) and 2700 cm^{-1} (corresponding to the 2D-peak) can be detected,[126] as well as the h-BN peak at 1370 cm^{-1}.[129] For the 3D-C/PI and 3D-BN/PI composites (red), all these peaks are preserved with the appearance of an additional

small D-peak (at ~1350 cm^{-1}) for the 3D-C case, indicative of the 3D-C/polymer interface. The fact that its intensity is minimal indicates that the infiltration of PI into 3D-C scaffold does not significantly change the crystalline structure of it.[174]

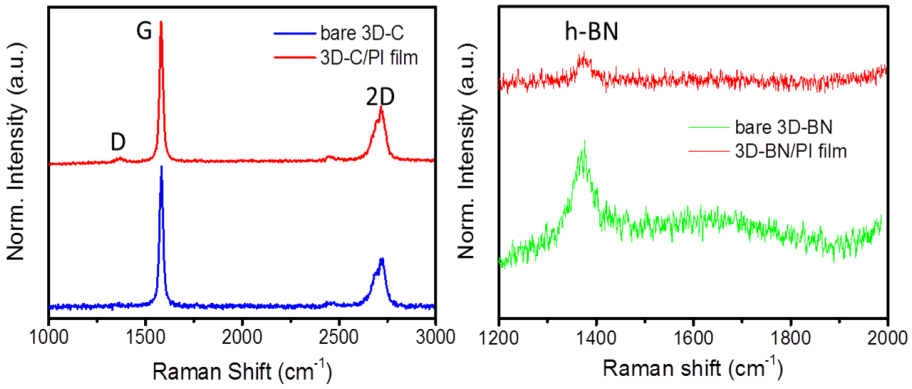

Figure 4-19. Raman spectroscopy before and after infusion with PI

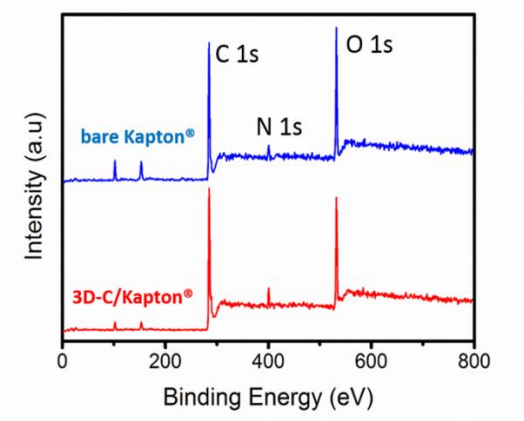

Figure 4-20. XPS survey spectra of bare PI and infused PI

To verify the chemical integrity of the PI inside the 3D-foam/PI hybrid, XPS measurements were carried out. As described by Grossman et al.,[175] the molecular structure of Kapton® PI consists only of C 1*s*, N 1*s* and O 1*s*. Figure 4-20 compares the obtained survey spectra for bare PI and infused PI, and it can be seen that both match, which means the chemical integrity of the PI is preserved inside the nanocomposite film. The two small Si peaks seen in both spectra at around 100 and 150 eV originate from the Si substrate used during fabrication process of the films.

Further optimization of the film smoothness and thickness can be obtained through improving the mold used during curing (i.e. using a stamp-like approach).

4.5.4 Epoxy SMP

For the synthesis of SMP and the infusion of SMP with 3D-foams, a similar approach to a previously reported epoxy SMP case was adopted.[176] In brief: 3 chemicals are prepared, namely EPON 826 as the resin that is responsible for the shape memory performance in epoxy, Jeffamine D-230 and NGDE, as curing agents to stabilize the polymer upon heating. EPON is first heated to 75 °C for 15 minutes. Afterwards, Jeffamine D-230, and NGDE are added and mixed with a mole ratio of 1.3:1.0:0.7 (EPON:NGDE:Jeffamine). After thoroughly stirring, the mixture is added drop-wise to the 3D-foam fillers. For the shaping of SMP, Al molds are used. The samples are then inserted in a vacuum chamber for 15 minutes to degas the remaining air bubbles. Afterwards, the samples are cured for 1 hour at 100 °C and post-cured for another hour at 130 °C. Subsequently, the samples can be removed from the Al molding and cut into desired shapes. In Figure 4-21, a cross-sectional SEM view of foam infused with SMP is shown. It can be seen that the process yields bubble free samples. The shadow structures inside the polymer block correspond to parts of the foam. It can be seen that the foam spreads homogenously throughout the entire cross-sectional area of the SMP. It is worth mentioning that even though the foam expands uniformly throughout the entire structure, it requires only a volume (weight) fraction of 0.3 vol% (0.35 wt%) and due to the ultra-light density of the foams, the overall material does not change in weight or original density through the infusion step. These small filling fractions are also orders of magnitude smaller than current fillers used (such as talc with 30 vol% filling factor, carbon nanotubes with 2 vol%, and aluminum nitride with 40 wt%).[177]

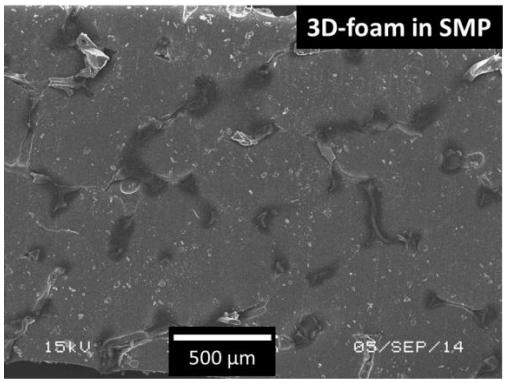

Figure 4-21. Cross-sectional SEM image of SMP infused with 3D-foam

In order to evaluate whether the infusion with the 3D-foams changed the intrinsic properties of the polymer, decomposition temperature and glass transition temperature (T_g) of the composites were measured. For this, TGA was used to study the decomposition profile of bare SMP and 3D-foam infused SMPs; and DSC for T_g determination.

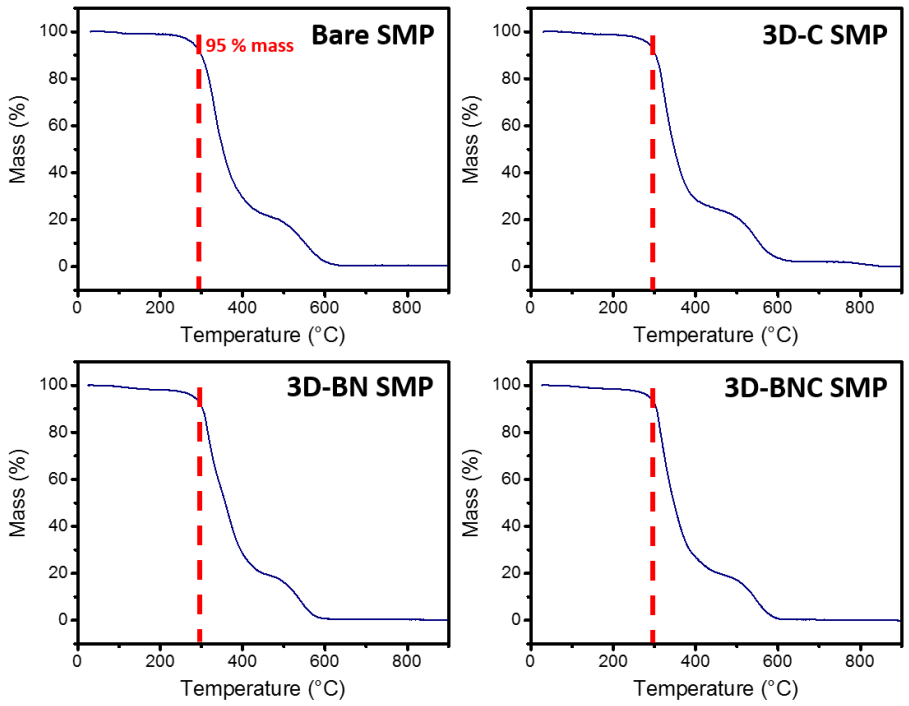

Figure 4-22. TGA results to determine decomposition temperature of all 4 types of SMP studied. The decomposition temperature is determined at the 95% of weight point, marked with the red dashed line

Figure 4-22 shows the decomposition profile of bare SMP and 3D-C, 3D-BN and 3D-BNC infused SMP. The temperature at the point of 5% mass loss determines the decomposition temperature. It can be seen that all results show identical curves and the point of 5% mass loss is in a similar range of 283 ± 3.5°C for all four materials. This indicates that the infusion of 3D-foam does not affect the structure of the cured SMP.

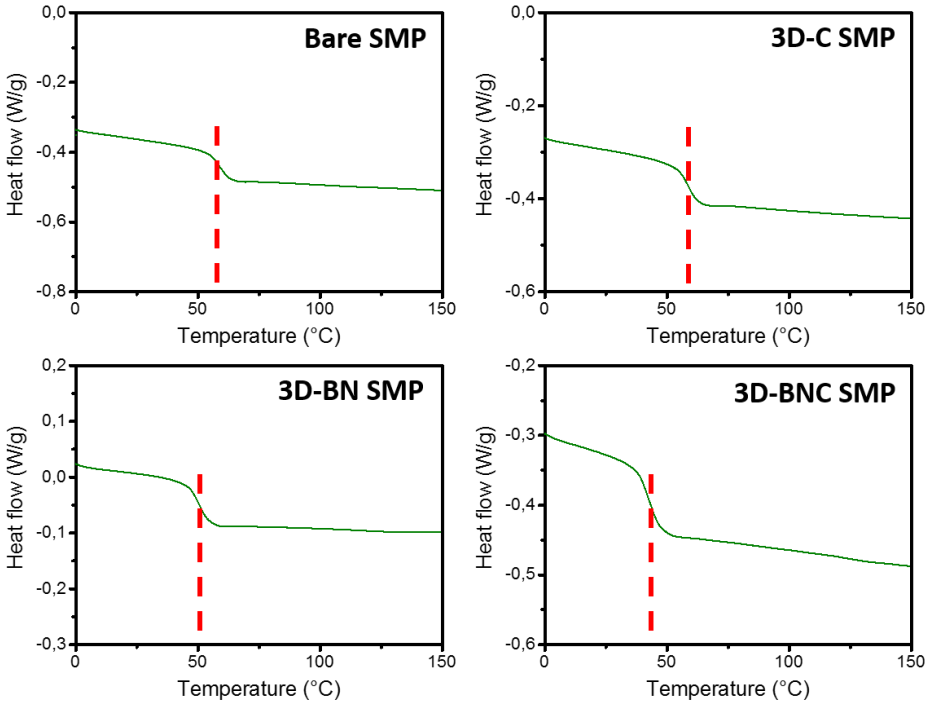

Figure 4-23. DSC results to determine glass transition temperature (T_g) of all 4 types of SMP studied. The glass transition temperature was determined by the central point of the slope, marked in red

For DSC, a temperature sweep up to 280°C was carried out and results are shown in Figure 4-23. It can be seen that glass transitional temperatures of 58.4°C, 56.7°C, 50.6°C and 52.6°C were obtained for bare SMP, 3D-C/SMP, 3D-BN/SMP and 3D-BNC/SMP, respectively. Taking into consideration possible experimental error, it can be thus stated that the infusion with 3D-foams has no effect on the T_g of SMP.

These results oppose previous results reported for 3D-C/epoxy composites,[178] in which the glass transition temperature was affected after infiltration. The difference of these works relies in the fact that in the present case, the epoxy SMP is infused after etching off the Ni template, and direct bonds between polymer resin and 3D-foam become unlikely. This is an important characteristic, since any structural changes would also affect the shape memory performance of the SMP.

4.6 Summary

In summary, this chapter provides the recipes for further enhancement and tuning of the 3D-foams properties. This includes the increase in density, the addition into thermally conductive matrices such as metals and silane, and to enhance the mechanical properties via hybridizing with different polymers.

For all recipes, an assessment of quality was performed and it was shown that the 3D-foams retain all their properties and structure throughout the different processes.

5 Application in thermal management of electronics

5.1 Introduction

The advancement of semiconductor technology in the era of "more-than-Moore"[179] has led to an increasing challenge in thermal management. ICs are so densely packed that they heat up within milliseconds,[1,180, 181] resulting in an extreme increase of generated heat[182] (e.g. current power electronics modules can go up to 200 Wcm^{-2})[183]. In order to mitigate this problem, the conventional way of extracting the heat through the substrate has been improved via adding heat sinks either on top or below the electronic device. The contact to these heat sinks is further enhanced through TIMs[180] and these TIMs are essential to reduce the thermal boundary resistance between the chip's active area and the heat sink.[184] Typical TIMs can be classified into electrically conductive and insulative types. For the former class, metal alloys containing In, Bi, Sn, Au are the common materials used. Although their thermal conductivities are usually high (i.e. ~50 $Wm^{-1}K^{-1}$), the use of these TIMs is sometimes limited, due to their electrical conducting nature that can interfere with RF components and their limited integration ability with other-non-metal materials due to their wetting properties. Additionally, for miniaturization of devices, the TIMs utilized have to shrink in size and weight correspondingly as well. Thus only the use of very thin metal foil is allowed which decreases the effective thermal conductivity by several orders.[185] Also, the use of metallic TIMs require high temperatures for reflow in order to achieve good surface conformity, which can range between 90°C to 450°C[186] limiting its usage. For electrically insulating TIMs, typical materials include greases, phase change materials, gels, adhesives and polymers.[182, 187, 188] These TIMs are able to achieve good surface conformity at low temperature and are relatively easy to apply. Nevertheless, their

thermal conductivities remain in the lower regime (0.1 – 0.3 $Wm^{-1}K^{-1}$).[182] Many have improved these materials by infiltrating them with high thermally conducting fillers, such as metals (i.e. Ag, Au, Ni, Cu)[189] and ceramics (i.e. Al_2O_3, AlN, BN).[190, 191] This strategy increases the thermal conductivity of commercially available TIMs to 5 – 10 $Wm^{-1}K^{-1}$.[192] Despite this, it is still much lower than typical metallic TIMs and electronics materials, which creates a bottleneck in the thermal extraction channels (i.e. typical solder materials have a thermal conductivity ranging between 20 – 60 $Wm^{-1}K^{-1}$ at room temperature).[33, 193, 194] Although one could increase the loading fraction of the fillers to increase the thermal conductivity, large filling ratios would also affect its viscosity and other parameters defining the applicability, such as curing temperature, dry-out and pump-out.

Today, the demand in performance for modern ICs has already pushed the current TIMs beyond their limit.[195] As a consequence, the performance of new generation chips has to be lowered at times to avoid over-heating[196] (which means adjusting their frequency according to the temperature)[197]. This is obviously undesirable.[198] As such, it is of importance to overcome this heat dissipation challenge[199, 200] and many have begun to explore various nanomaterials as next generation nano-thermal interface materials.[201]

Since it has been reported that the interconnected nature within the 3D-foams could drastically overcome the internal contact thermal resistance, as single graphene domains within the 3D-foam form a continuous graphitic structure through covalent bonding,[20] and it has been shown that such foam-like structures have superior thermal interfacial characteristics to other surfaces due to the increased contact surface area,[145] it is believed that the 3D-foams would serve as a new TIM with an overall thermal extraction performance that would far exceed the thermal performance of the current TIMs. Thus, in this chapter, the application of 3D-foams as ideal TIM candidates is studied in order

to overcome current thermal management challenges. Characteristics that are critical to TIMs have been investigated, which include cross-plane thermal conductivities, interface and, most importantly, evaluation of the thermal extraction efficiency. To further improve the bonding strength and applicability, in a next step, electrically conducting and insulating means of thermal adhesion have been added to the foams and analyzed. In a last step, mechanical robustness of the foams has been enhanced in order to also cater for harsher environment and large-gap application. Reliability and thermal stability of all methods have also been assessed.

5.2 Thermal characterization methods

Since this chapter describes different modes of thermal interface application, which require different methods of assessment of thermal performance, the following gives an overview of different methodologies used:

For adhesion-less samples, the traditional single layer laser flash method is used, since the thermal performance is mainly dependent on the structure itself. Additional assessment of the boundary properties is also done.

Since in the case of adhesive materials the advantage of thermal performance is due to the bonding with the boundary surface, the actual benefit can only be assessed in such a configuration. As such, instead of measuring the thermal conductivity of the single layer TIM, thermal conductivity is measured using the laser flash method on sandwiched structures. The TIM is bonded between two Si wafers, roughened Si wafer (Si,r), Cu foil and Al foil, and then measured as a single layer structure. This way, an effective thermal conductivity of the stack is obtained, which then is compared to the ideal value of a single Si/Cu/Al layer. This way, the effectivity of the TIM layer in transferring the heat from the bottom to the top layer is quantified.

5.3 Adhesion-less thermal management

5.3.1 Material preparation and characterization

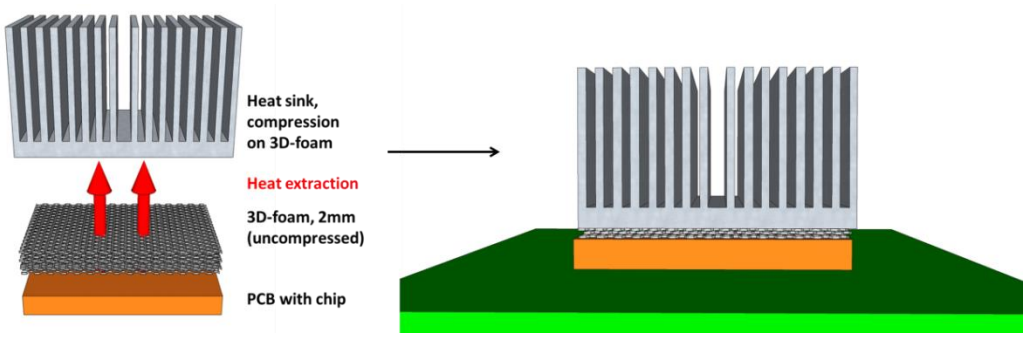

Figure 5-1. Schematic of adhesion-less application of the 3D-foams in thermal management of electronics

For an adhesion-less application, the compressibility of the foams is exploited. By placing the foam in its uncompressed state and then compressing it down via the weight of for example a heat sink or another chip. Figure 5-1 schematizes the typical setup without adhesion for thermal management of electronics. For this type of application, 3D-C may be used for electrically conducting needs; 3D-BN for electrically insulating requirements.

5.3.1.1 Thermal contact resistance characterization

Measurements are conducted according to ASTM 5470 on a commercial TIM Tester (AnalysisTech, model 1400). The principle of this method is based on imposing a one-dimensional heat flow across the sample and measure the resulting temperature difference. The sample thermal resistance, R_{th}, is then defined as the ratio of the temperature difference to the heat flow. According to the Standard, the 3D-foams are considered Type II materials (low contact resistances, elastic and plastic deformations combined with an elasticity increase with deformation), so a controlled contact pressure

is applied. Sample size is of 33 mm diameter disks, test temperature is of 50°C. Used pressure is of 10 psi, which yields full compression.

5.3.2 Thermal conductivity

The biggest constrain for the effective thermal conductivity of the 3D-foams is the very low volume fraction (0.4%),[20] hence, if the density of the 3D-foam could increase, the thermal conductivity will rise by several orders.

To investigate the correlation between the density of the 3D-foams and their respective thermal conductivities, the cross-plane thermal conductivity was measured using the laser flash method[202] since the z-plane heat spread is more crucial for the effectiveness of heat extraction for TIMs.[33, 136] Obtained thermal conductivity measurement results are shown in Figure 5-2, in which the thermal conductivity (red curve) was plotted along with their corresponding densities (blue curve) of each measured sample. Closed squares represent results for 3D-C and open squares for 3D-BN. The base thermal conductivities of the pristine 3D-foams are of 1.2 $Wm^{-1}K^{-1}$ and 0.84 $Wm^{-1}K^{-1}$, for 3D-C and 3D-BN respectively. As the density increases, the highest thermal conductivity values achieved are at 86 ± 10 and 62 ± 10 $Wm^{-1}K^{-1}$ for 3D-C and 3D-BN (error deviation due to the non-perfect surface flatness), respectively. It must be noted that 3D-BN has a slightly lower thermal conductivity than 3D-C, due to the cumulative effect of the following structural differences: (1) h-BN and graphene have a different phonon dispersion, especially in their flexural modes (which leads to increased phonon-phonon scattering),[203-205] (2) higher isotopic impurity in h-BN (i.e. BN has a larger isotope mixture of 19.9% ^{10}B and 80.1% ^{11}B than graphite with 98.9% ^{12}C and 1.1% ^{13}C, which leads to an increase in phonon-isotope scattering. This in turn reduces the thermal conductivity in BN),[205, 206] (3) the difference in mass of B and N (since phonon frequency depends on the mass, and thus in BN local fluctuations in the natural

frequency appear which leads to additional phonon scattering)[204, 207] and (4) intrinsic phonon-phonon scattering due to lattice anharmonicity (also caused by the dual-character of BN, as compared to graphene).[205, 208] The results show that there is a proportional relation between density and thermal conductivity for both types of 3D-foam. In addition, it is also worth mentioning that the two methods of obtaining high-density 3D-foam (i.e. prolong growth time and compression of the 3D-foam) have been compared and their thermal conductivities are comparable. The reason is that both these methods do not change the internal configuration of the 3D-foam and thus the internal thermal contact resistance remains low.[20]

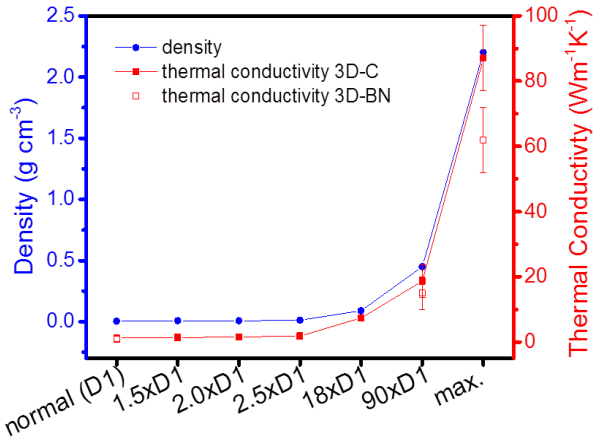

Figure 5-2. Measured density and thermal conductivity of 3D-C and 3D-BN

The cross-plane thermal conductivities for 3D-C and 3D-BN are 14-fold and 30-fold increased over typical multilayer graphene and h-BN (i.e. graphene has a thermal conductivity of 6 and h-BN of 1.5 – 2.5 $Wm^{-1}K^{-1}$ in the z-plane).[209, 210] This is due to the isotropic interconnected structure of the 3D-foam: while in 2D graphene (or h-BN), phonon transport is anisotropic (i.e. only along the in-plane direction, and for out-of-plane propagation between the layers only weak Van der Waals forces are present that do not enable efficient phonon transport), in 3D-foams, the graphene or h-BN sheets are stitched to each other covalently and follow an isotropic structure, which is preserved

Table 5-1. Comparison of cross-plane thermal conductivities among graphene and h-BN structures

Material	Cross-plane thermal conductivity [W $m^{-1}K^{-1}$]	Remarks	Ref.
Graphene	6	Weak Van der Waals forces limit conductivity between layers	[210]
h-BN	1.5 – 2.5	Same as graphene	[209]
Graphene paper	max. 1 – 5	Anisotropic behavior and alignment of the G particles, which becomes evident in the layered structure under SEM	[211, 212]
h-BN paper/BN-polymer nanocomposites	n.a. (only in-plane)	Similar to G paper, h-BN paper is extremely layered Pure BN has weak strength and is difficult to obtain as freestanding film, thus needs support from another material	[213-216]
Commercial Silver epoxy TIM	1.76 (pristine) 9.9 (5 vol% graphene filler)	Stable in working temp range of epoxy, which is only 5 – 75 °C	[193]
Graphene nanocomposite epoxy	5.1 (10 vol%)	Stable only at 5 – 75 °C	[136]
Graphene laminate on PET	40 – 90	Strongly dependent on flake size due to the amount of single flakes required not freestanding	[217]
Multilayer graphene in epoxy	5	Temperature dependence of values, not freestanding	[218]
3D BN nanosheet networks in epoxy	2.4 (9.29 vol%)	Infiltrated in epoxy anisotropic	[219]
h-BN in polyimide	7 (60 vol%)	Not freestanding and requires high volume fractions	[220]
3D-foam	62 ± 10 (BN) 86 ± 10 (C)	Freestanding and compressible, stable up to 700 – 900 °C	This work

even when density is increased. This way, in 3D-foams the phonon transport can be directed into all directions in an isotropic manner. Also, these maximum values of thermal conductivity are among the highest cross-plane conductivities of free-standing graphene or h-BN structures. For comparison, the closest structure to the 3D-foams studied here is graphene and h-BN paper. For this type of structures, thermal conductivity at the out-of-plane direction is difficult to improve further due to the anisotropic behavior and alignment of the graphene or h-BN particles (maximum values reported are of 1 – 5 $Wm^{-1}K^{-1}$).[211] This becomes very evident when observing their cross-sectional SEM images, whereby the layered structure can be clearly seen.[212, 213] Further comparison to other structures is given in Table 5-1.

In addition, for actual application, it is challenging to obtain freestanding graphene or h-BN structures that can be applied directly without the need of supportive materials (such as polymers), which further hinders the phonon transport. For 3D-foams, besides their outstanding thermal conductivity, these 3D-foams do not require additional mixing with supporting materials and are fully freestanding.

5.3.3 Interface characteristics

For TIMs, besides thermal conductivity, the quality of the interface between the chip and sink play a major role in the quality of heat transfer. Some of the important considerations include: (1) thermal properties of the interface, (2) optimization of the interface, since due to the very bad conduction of heat in air (thermal conductivity of 0.026 $Wm^{-1}K^{-1}$ at room temperature) any presence of free space void in the joint area would increase significantly the thermal resistance, (3) surface roughness of the contact, (4) any possible stress occurring due to coefficient of thermal expansion (CTE) mismatches.[221] To investigate these properties, measurements according to ASTM5470 are performed. The value obtained is of R_{th} = 0.197 KW^{-1} (0.262 in^2KW^{-1}), which is considered a very low thermal contact resistance. This is due to the very high surface conformity of the 3D-foam and shows that the 3D-foam is able to decrease the interface resistance of two mating surfaces. This value is in a similar range as reported previously in a comparable test where 3D-C foam was placed between two Cu blocks (between Si and Al) and pressed down, which gave a thermal resistance of 0.45 KW^{-1} (0.26 KW^{-1}).[145] For comparison, the thermal interface resistance of commercial grease is around 6 times higher, at 2.71 KW^{-1}, and silicone based adhesive is 3 times higher, at 1.35 KW^{-1}.

To observe the morphology of compressed 3D-foam, Focused Ion Beam (FIB) and SEM have been used to measure the thickness of the branches of the 3D-foam and the

3D-foam itself after a compression step between two Si wafers. For this, a window has been cut through the compressed 3D-foam in order to access the 3D-foam within the sandwiched structure (Figure 5-3a). It can be seen that on average, each branch is between 1.1 and 1.3 µm thick (Figure 5-3b). Since the porosity of the Ni template used is between 100 and 110 ppi, and with an initial thickness of 1.67 mm of the 3D-foam, the number of vertical pores inside the structure is between 6 and 7. Since samples comprised of 10 layers are used for this application, which are supposed to be non-compressible, then the minimum thickness the 3D-foam can reach is 6.6 µm. The SEM image also reveals that there is still free space present between the branches. This is due to the fact that there was a gap between the Si wafers due to its warpage,[222, 223] which is larger than the minimum thickness of the 3D-foam, thus the 3D-foam does not require full compression in order to fill this gap.

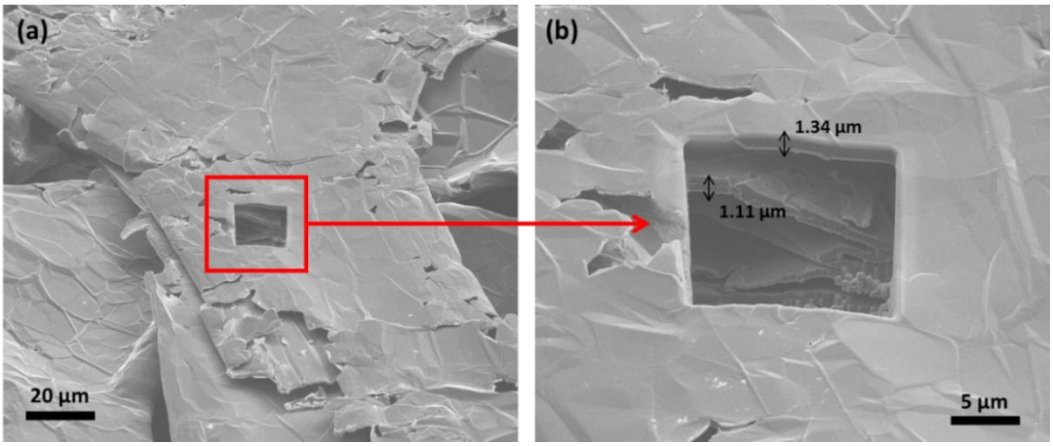

Figure 5-3. SEM studies of the compressed 3D-foam. **(a)** FIB cut has been performed to measure the thickness of the graphite inside the 3D-foam; **(b)** zoom into the cut with measurement

In order to quantify the compressibility of the 3D-foams, a study of the relationship between applied force and compression level is shown in Figure 5-4. The measurement was performed by placing uncompressed 1.67 mm thick samples centralized on the parallel plate compression clamps of a dynamic mechanical analyzer (DMA Q800) with

a resolution of 1 nm. Used parameters were a force ramp from 0.001 N to 18 N at 0.1 N min^{-1} for compression, followed by a force ramp from 18 N to 0.001 N at 0.25 N min^{-1} for release. Due to the system's limitations, the force could only be ramped up to 18 N, which did not achieve the full compression of the 3D-foams down to ~6.6 µm. It can be seen that 18 N yields a compression down to 25.4 µm for 3D-C and down to 36.4 µm for 3D-BN. From the graph, it can be extrapolated that in order to reach 6.6 µm, a force of ~22.8 N is required for 3D-C and of ~24.6 N for 3D-BN. This could be achieved by compression with a weight of 2.3 – 2.5 kg without applying any additional external forces. After release, a slight decompression in the range of 40 – 50 µm is visible, which for application as heat spreader would not be the case since the weight of the heat sink will not be removed.

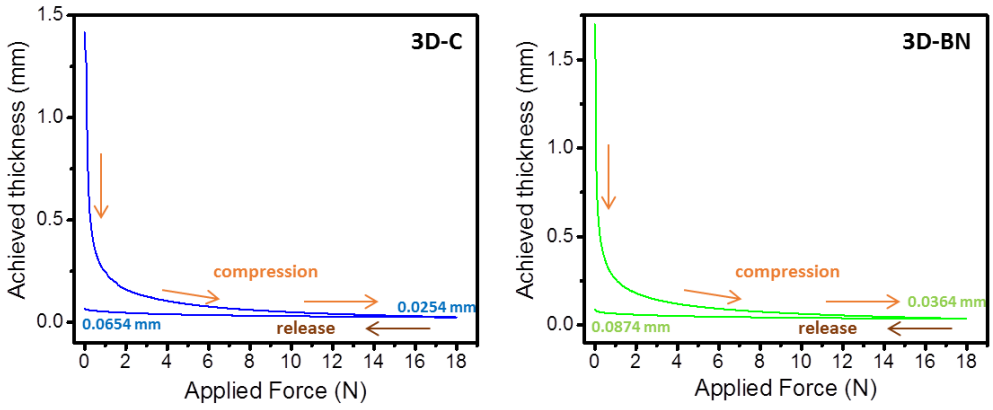

Figure 5-4. Relationship applied force – achieved compression for 3D-C and 3D-BN

To further demonstrate that the 3D-foam would fit into most surface roughness and thus improve the thermal interface between the two, various artificial trenches of different aspect ratio were fabricated on a Si wafer as a test platform for extreme cases and compressed with the 3D-foam. The cross-section of the Si–3D-foam configuration was observed under SEM and Figure 5-5 shows two examples of the trench-arrays before and after compression with the 3D-foam. Figure 5-5a,b show the case of 20 µm

deep, 2 µm wide trenches; Figure 5-5c,d of the 40 µm deep and 25 µm wide section. For both cases, it can be seen clearly that the 3D-foam is able to completely fill up all the gaps. The good fitting of the 3D-foam into all the trenches are due to the fact that the structure of the 3D-foams is very refined, and it is several orders smaller than the usual surface roughness or unevenness/warpage.

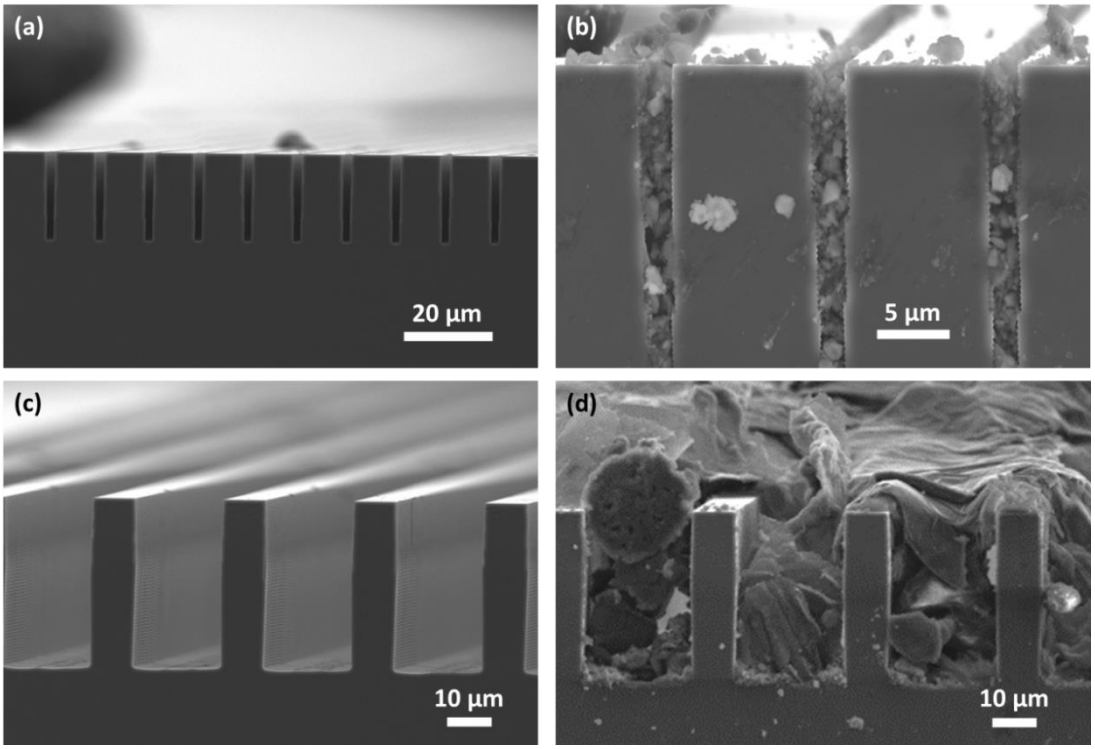

Figure 5-5. SEM studies of the surface conformity of 3D-foam after compression on varying surface roughness. **(a)** Cross-sectional view of the 20 µm deep and 2 µm wide trench before compression with 3D-foam and **(b)** after compression with it; **(c)** cross-sectional view of the 40 µm deep and 25 µm wide trench before compression with 3D-foam and **(d)** after compression with it

5.3.4 Device level testing

To access the heat extraction performance of 3D-foams on electronic devices, evaluation was carried out on a 2.5D electronic test platform.[224] 2.5D packages refer to the packaging of multiple dies on a Si interposer with Cu-filled Through Si Vias (TSVs) as electrical interconnects. Dissimilar dies with different functions can be assembled together to fulfill faster operation through shortened interconnects. Nevertheless, even

though the shortened interconnect lengths reduce the power consumption, the power dissipation for each die tends to remain unchanged. This results in unfavorable heat density within the packages. Thus, thermal management is a key challenge to be addressed in 2.5D packages and system designs,[225, 226] whereby the TIMs performance can play a key role in 2.5D packages cooling.

The 2.5D thermal test chip used herein is shown (without any overmold) and schematized in Figure 5-6. It consists of a thermal test die (5.08 mm × 5.08 mm) along with two dummy dies (7.6 mm × 10.9 mm and 8 mm × 8 mm), which represent the logic and memory chips in a typical 2.5D integration. The thermal test die consists of four heating unit cells (which cover over 85% of the chip area to provide uniform heating), and six diodes for die temperature sensing. For the molded test vehicle, additional molding process was conducted on the wafer level with epoxy mold encapsulation on the chip package. The thermal diodes were calibrated in the air-convection oven with data taken at room temperature, 60°C, 100°C, and 140°C to obtain the proportionality factor (K-factor). The six diodes on the thermal test chip have excellent linearity with R-squared value ≥ 0.9999, with almost identical K-factor of 517 KV^{-1} ±1.2 KV^{-1} based on four calibrated packages on board. During the test, a power supply from Xantrex (XHR 150-7) is used to supply electrical power to the thermal chip, the temperature reading is attained by activating the diodes with 1 mA current from a Keithley 2400 source meter. For temperature increase test, the package is first placed in still air for 10 – 15 minutes without power input. Then the diode voltage (V_{diode}) and the ambient temperature ($T_{a,0}$) are recorded as initial readings. A J-type thermocouple with factory calibration is used to measure the ambient temperature. The power input is then applied, and the corresponding junction temperatures and ambient temperature recorded after

reaching thermal equilibrium. The corresponding junction temperature T_J is then calculated as follows: [227]

$$\boldsymbol{T_J = \Delta V * K + T_{a,0}} \quad (5\text{-}1)$$

where $T_{a,0}$ is the ambient temperature before the power is input and ΔV the average of the diode voltage difference before the power input.

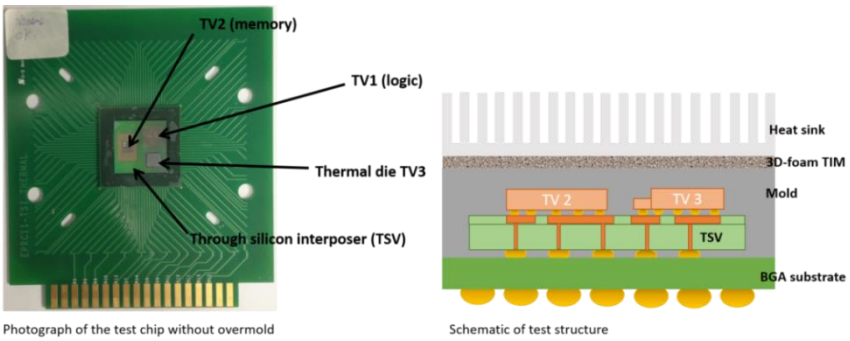

Figure 5-6. Test device used to assess the material's performance under real conditions. **(a)** Photograph of the chip without any overmold; **(b)** schematic of the cross-sectional view of the test setup. TV1 stands for a dummy logic unit, TV2, dummy memory unit and TV3 for the thermal die array (source of the hot spot)

Figure 5-7a shows a photograph of the complete setup used, in which the 3D-foam is compressed directly between the test chip and the heat sink (marked here with an arrow). The 3D-foams were first placed in their uncompressed state onto the chip and then compressed down via the weight of the heat sink. Two types of test chip where used, one where the heating element is exposed (denominated as "no overmold", Figure 5-7b) and another where the heating source is covered with a mold (denominated as "with overmold", Figure 5-7c). The difference between the two is that in the former case, the performance only depends on the material itself (thus a direct evaluation of the heat spreading capabilities of the material), whereby for the latter, it is a more application-related situation where the performance is also affected by the low conducting overmold material, since the heat has to first go through it before being transferred to the TIM and

then to the heat sink. As such, measurement with overmold would result in an overall reduction of the heat extraction performance. Besides the 3D-foams, other standard TIMs were evaluated in order to benchmark the performance.

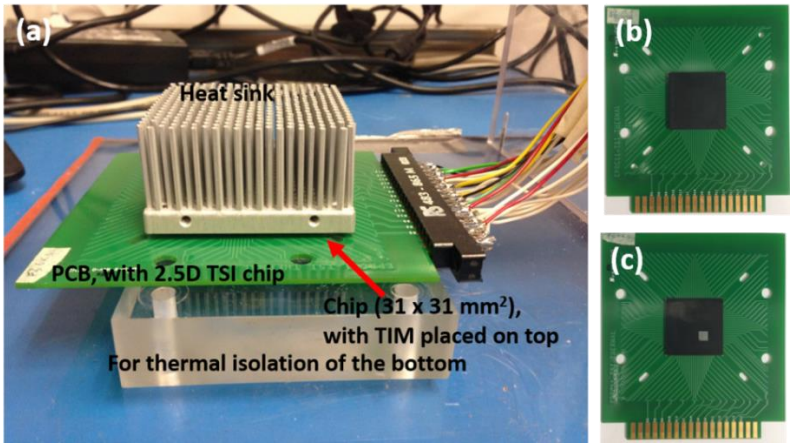

Figure 5-7. (a) 2.5D test setup used; **(b, c)** top view of the chip used, with and without overmold on the heater section, respectively

Figure 5-8 shows the obtained results, 3D-BN is being compared directly with other electrically non-conducting TIMs and 3D-C with other electrically conducting TIMs. The graphs show the increase in temperature at the junction of the chip to the ambient as a function of applied power. All materials tested have a linear character, whereby the slopes drastically change between materials. Comparison of the curves shows that the 3D-foams perform with higher efficiency: the change in temperature measured shows that 3D-foams are able to maintain the device at a lower operating temperature. The slopes of the graphs are enlisted in Table 5-2 together with the achieved improvement over the standard TIMs tested. It can be seen that in all these cases, the 3D-foams achieve a significant decrease in its temperature differential; for instance, 3D-BN is able to maintain the chip 10% and 25% cooler than its commercial electrically insulating counterparts with and without overmold, respectively (this is equivalent to 15.06°C and 23.6°C less heat at the point of maximum power applied during the test), and 3D-C achieves 12% and 42% improvement over its electrically conducting counterparts,

equivalent to 12.56°C and 39.85°C less heat at 4.4W, for the overmold and non-overmold case, respectively.

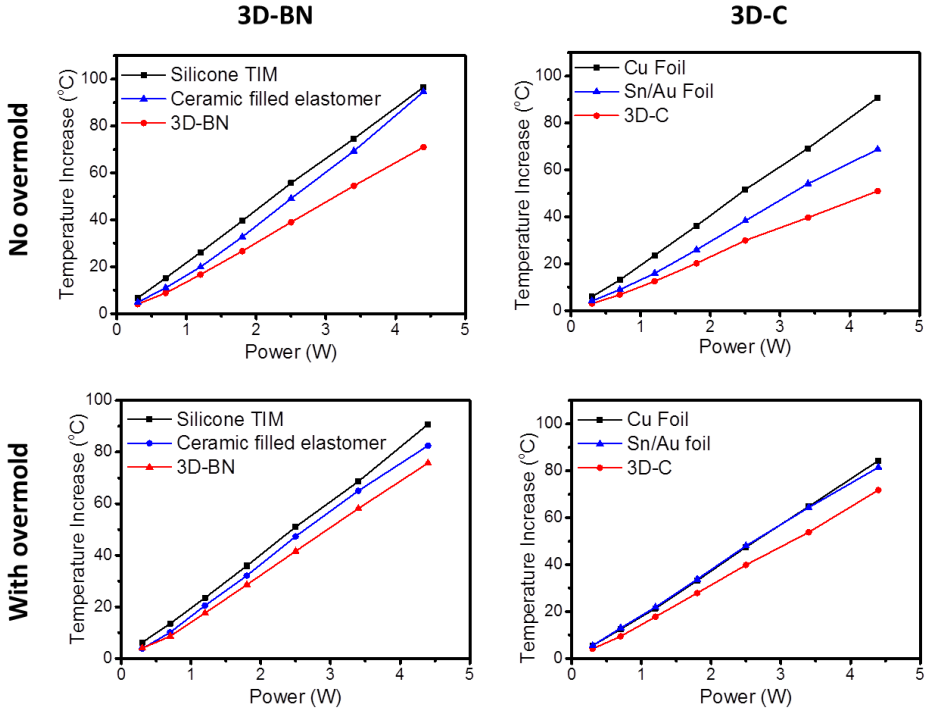

Figure 5-8. Obtained results, grouped according to device used and electrical conductivity characteristic, mean error deviation ±0.19°C

Table 5-2. Temperature increase slopes for various materials tested with the 2.5D platform

		Material	Slope [°C W^{-1}]	Improvement [%]
No overmold	Electrically insulating	3D-BN	16.6	-
		Silicone TIM	22	25
		Ceramic filled elastomer	22	25
	Electrically conducting	3D-C	12	-
		Cu-foil	16.2	26
		Sn/Au-foil	20.8	42
With overmold	Electrically insulating	3D-BN	17.8	-
		Silicone TIM	19.6	10
		Ceramic filled elastomer	20.6	14
	Electrically conducting	3D-C	16.6	-
		Cu-foil	18.8	12
		Sn/Au-foil	18.8	12

Table 5-3 compares the obtained results with values reported by other thermal management materials tested on different test-platforms from literature. It must be noted that the reported values in these examples were obtained without the use of overmold on top of the hot spot. It can be seen that for such cases, the 3D-foams outperform other materials, paired with better applicability (e.g. one of the alternative approaches which achieved the highest temperature decrease of 20°C, using exfoliated graphene quilts,[228] is still 4°C lower than 3D-BN and 24°C lower than 3D-C, and it requires a precise control over layer number, exfoliated size and location, which is difficult to achieve).

Table 5-3. Comparison of hot spot temperature decrease of different materials

Material	Achieved temperature decrease of hot spot	Remarks	Test platform	Ref.
CVD-Graphene heat spreader	ΔT~ 13°C at 0.0156 to 0.624 W	Application of graphene not very practical (requires PMMA transfer to platform, then hot acetone to remove PMMA)	Pt micro-heater, temperature determined from measured resistance	[229]
Graphene paper	ΔT ~ 24-18°C (from thermal camera image)	Orientation of films only parallel to platform	Samples suspended above an iron head, temperature recorded through IR camera	[212]
Exfoliated graphene quilts (few-layer graphene)	ΔT = 20°C[b)]	Layer number, exfoliated size and location are difficult to control through exfoliation	AlGaN/GaN HFETs, ΔT determined from temperature-dependent shifts in Raman peak positions	[228]
Layered h-BN film	ΔT = 20°C	Not freestanding, requires acetate cellulose support, polycrystalline BN	Micro-heater configuration, temperature recorded through IR camera	[230]
Graphene-based film with addition of silane-functionalized molecules	ΔT ~ 6-12°C[b)] at 2.52 W	Material only oriented in parallel	Pt micro-heater, temperature determined from measured resistance	[231]
3D-foam	ΔT ~ 15°C[a)b)]/24°C[b)] (3D-BN) ΔT ~ 23°C[a)b)]/40°C[b)] (3D-C) at 4.4 W	Orientation of structure isotropic, improved thermal conductivity out of plane, thus heat is extracted, rather than spread along the film	Thermal test die, temperature determined through internal diode voltage	This work

[a)]Use of overmold on top of the hot-spot
[b)]Use of heat sink on top of the hot-spot

The compression with the heat sinks is sufficient to compress down the 3D-foam to conform to the surface profile, but it does not yield maximum compression.

Nevertheless, this is sufficient enough to obtain enhancement of heat extraction. Besides showing the outstanding performance of the 3D-foams, these results also highlight that heat-spreading performance not only depends on the thermal conductivity of the material used, but also on the surface conformity. For example, the metal foil's performance was comparable to the ceramic filled elastomer, even though their thermal conductivities differ by more than 50 $Wm^{-1}K^{-1}$ (i.e. the thermal conductivity of the elastomer is of 3.3 $Wm^{-1}K^{-1}$, Sn/Au foil is of 57 $Wm^{-1}K^{-1}$). Moreover, since the purpose of the TIM is to displace any micro and/or macroscopic free space voids in between interfaces to improve heat conduction, any inclusions beyond the size of these gaps would be redundant and eventually lower the overall interface thermal conductivity.

To further analyze the correlation between surface roughness and the optimized thickness for TIMs, tests with 3D-foams of varying thickness were performed on the mold and heat sink with different surface roughness**.** The same setup of Figure 5-7 was used, with heat sinks of different surface roughness, namely R1, R2 and R3, being applied. A total of three heat sinks (the surface profile of each heat sink is shown in Figure 5-9a-c) were tested and for each heat sink, 4 different initial thicknesses of 3D-C were tested (i.e. initial thickness of 1 mm, 2 mm, 5 mm and 10 mm before being compressed and conformed to the interface).

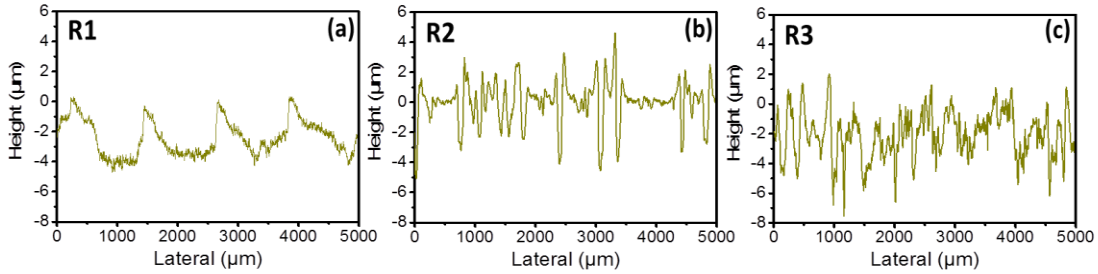

Figure 5-9. Surface roughness profile of the three heat sinks used

Figure 5-10 shows the obtained graphs of temperature increase and Figure 5-11a shows the obtained results plotted as a function of initial thickness of the 3D-foam.

Interestingly, it can be seen that an initial thickness of 2 mm is enough for all cases to achieve an effective heat extraction (i.e. in the most roughened heat sink, the 2 mm result is nearly identical with the 5 mm and 10 mm result).

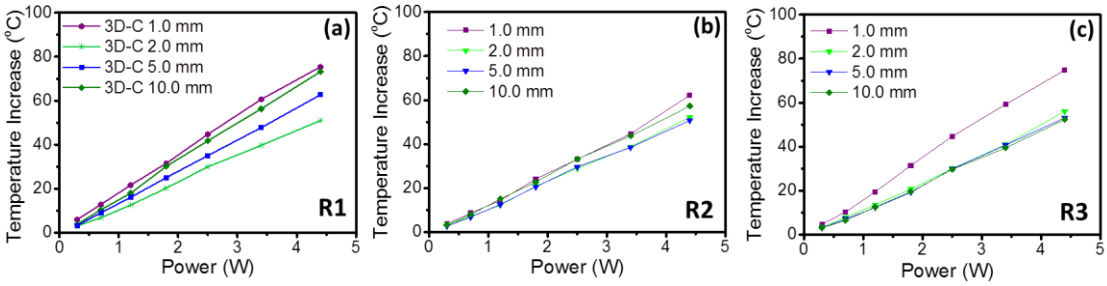

Figure 5-10. Corresponding results obtained using the test setup from Figure 5-7, mean error deviation ±0.21˚C

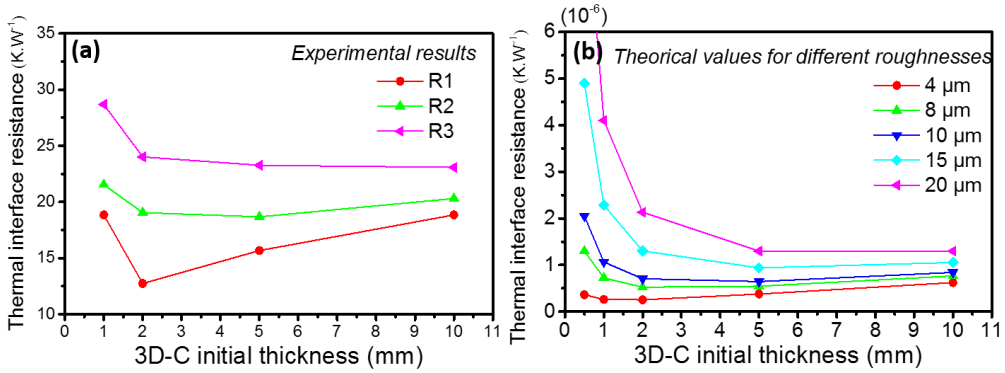

Figure 5-11. (a) Experimental results for different surface roughness measured at 4 W as a function of starting thickness of the 3D-foam; **(b)** theoretical results for different surface roughness and trend of the temperature increase measured at 4 W

This can be explained as follows: as mentioned previously, the 3D-foam will fill all free space gaps between the mold and the heat sink. The resistance of the interface is thus the bulk resistance of the 3D-foam R_{3D} given by: [232]

$$\boldsymbol{R_{3D}} = \frac{\boldsymbol{t_e}}{\boldsymbol{k_{3D}(t_e)}} \qquad (5\text{-}2)$$

where t_e is the effective thickness of the 3D-foam between the heat sink and the mold, k_{3D} is the thermal conductivity of the 3D-foam which is also dependent on the effective

thickness. The Bruggeman assumption gives the relation between the thermal conductivity and the porosity, which also depends on the thickness: [232]

$$\boldsymbol{k_{3D} = k_G(1 - f(t_e))^{3/2}} \quad (5\text{-}3)$$

with f the porosity and k_G the thermal conductivity of bulk 3D-foam (i.e. 86 $Wm^{-1}K^{-1}$ according to the value obtained previously at maximum compression). When the heat sink compresses the 3D-foam on the mold, it fills all the free space gaps between the two mating surfaces; however, unlike the previous case with Si–Si, the mold is soft and will compensate the non-flatness of the heat sink, which means that the thermal interface resistance is only affected by the surface roughness and the minimum thickness of the 3D-foam t_{min}. Due to this, it is possible to correlate the impact of the 3D-foam's effective thickness with the behavior of the thermal resistance for a given surface roughness: by combining relations (5-11) and (5-12), the calculation of the thermal resistance of the interface is computed in Figure 5-11b according to the initial 3D-foam thickness for 5 different roughness t_r (4, 8, 10, 15, 20 µm). The values of the effective thickness t_e = t_{min} + t_r (addition of the minimum thickness reachable by the film with the surface roughness) used are summarized in Table 5-4.

Table 5-4. Calculation of the thickness for the study of the evolution of the interface thermal resistance of 3D-C

Initial thickness of the 3D-foam t_{init} (mm)	Minimum thickness t_{min} (µm) (cf thermal boundary section for the calculation method)	t_e for an example roughness of 4 µm (t_e = t_{min} + t_r)
0.5	2	6
1	4	8
2	8	12
5	21	25
10	43	48

With this relation, it can be observed that for very thin thickness the thermal resistance is very high, which then continues to decrease until an optimal thickness is reached. This optimal thickness point is schematized in Figure 5-12, whereby the 3D-foam nicely fills in the free space gaps without creating any additional spacing between the heat sink and the mold (thickness/gap width $\delta \approx 0$). This optimal value is achieved with an initial thickness of 2 mm for the three cases of surface roughness tested here. Beyond this optimal thickness, compression of thicker 3D-foams leads to two simultaneous effects, namely the compression of material at the edge of the grooves (which leads to the addition of extra-material between the two mating surfaces, $\delta >> 0$) and to a higher compression level of the 3D-foam inside the gap (as can be seen by comparing the SEM images in Figure 5-12). Since a higher compression level inside the grooves leads to lowered thermal interface resistance, but at the same time the addition of material between the surfaces increases it, the two opposing effects sum up to an overall less linear increase of thermal interface resistance. This becomes evident in the case for R2,

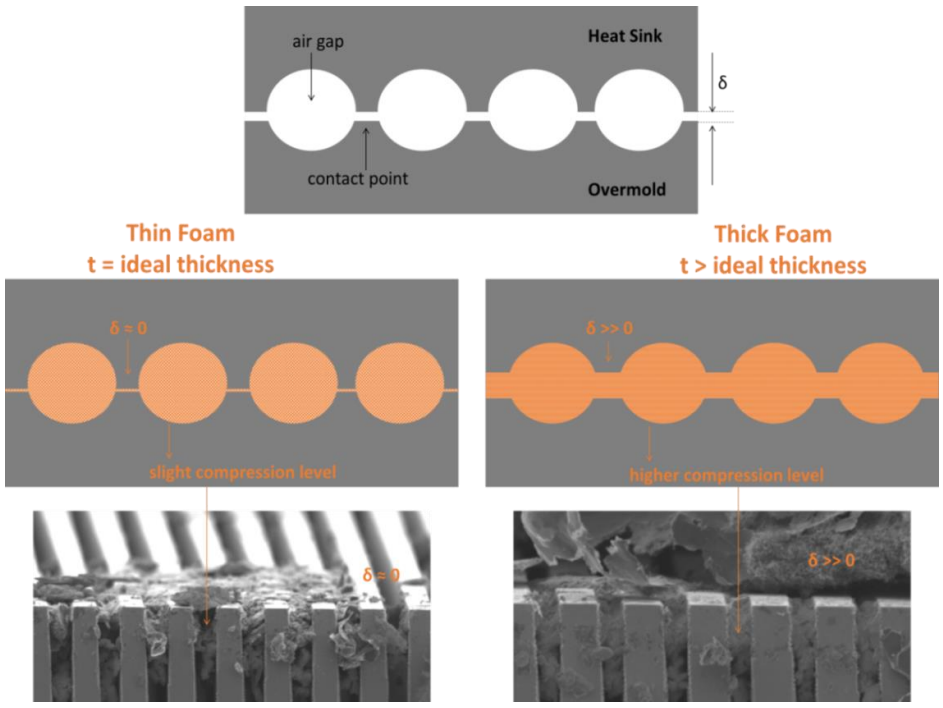

Figure 5-12. Schematic of the gap adaptability of the 3D-foams to illustrate the effect of using 3D-foams with ideal thickness and larger thickness

where the 5 mm 3D-foam achieves a similar performance as the 2 mm 3D-foam, since the slight addition of extra material between the surfaces is balanced off with an increased level of compression inside the gaps. The same applies to the case for R3 sample with the 10 mm thick 3D-foam. This is why in Figure 5-11, the 2 mm 3D-foam achieves optimal thermal interface resistance results up to a surface roughness of 10 um and slightly thicker 3D-foams do not change this performance. It must be noted that experimental and theoretical values match, and the optimal thickness for each surface roughness can be reliably predicted.

5.4 Electrically insulating adhesion

For the case of TIM with adhesion, the hybridization of 3D-foam with silanes (short covalently bonded organic molecules) is used. The silane molecules form a self-assembled monolayer (SAM) onto the 3D-foam and the substrate. These SAMs consist of a head group, molecular backbone and a terminal end group. The head is the one with the affinity towards the substrate and can be tailored according to specific metals, oxides, and semiconductors.[233] Since it is known that the phonon heat transport across an interface is directly controlled by the strength of the bonding layer,[234, 235] as well as the phonon spectra match (acoustic match) of the materials at the interface,[236, 237] SAMs are the "thermal glue of choice" as they have shown to achieve covalent bonds (stronger than Van der Waals bonds).[238] Covalent bonds have been proven to increase the efficiency of heat transfer between interfaces since they introduce additional thermal pathways through their functionalized molecules.[239] Within the class of SAMs, silanes are the gold-standard for thermal bonding purposes, due to their simple chemistry and multifunctional nature, which make them able to easily bind two different substrates.[239] The advantage of using silanes for thermal bonding was reported for the following cases:

Liquid interface – acting as bridge for the vibrational mismatch between gold and polymer and thus enabling efficient resonance-like thermal transport.[236] Gaseous interface – it was shown that SAMs maximize the heat exchange between solid and gas interface, which is important since single phase gas cooling is the dominant thermal management technology.[240] Solid interface – prominent examples for this case are other materials of the carbonaceous family, since for them, despite their high thermal conductivity values, their great promise as thermal material has been difficult to translate into actual high performance heat extraction.[166] The most prominent example are CNTs – CNT interfaces bridged with covalent linkers exhibit drastically increased thermal transport and mechanical interface adhesion over unmodified CNT adhesion to metals through only van der Waals interactions.[166, 241, 242] In one example, the paste was used to adhere vertically aligned multi-walled CNT forests to Cu oxide. This functionalization achieved a 9-fold reduction of thermal contact resistance over the non-functionalized contact. This lead to CNT-based TIMs with thermal resistances of 4.6 ± 0.5 mm^2KW^{-1} which is comparable to conventional metallic solders.[243] Another example of the carbonaceous family is graphene – for which functionalization was shown to constrain the cross-plane phonon scattering. This in turn recovered the flexural phonon lifetime and enhanced in-plane heat conduction of bonded graphene.[239] Other examples of successful bonding between solid interfaces relevant for thermal management are dielectrics – through introducing a strongly bonding organic layer at the metal/dielectric heterointerface enhanced interfacial thermal conductance was achieved. This leads to strong interfacial bonding (i.e. values as high as 430 $MW\,m^{-2}\,K^{-1}$) and changes in the vibrational density of states near the interface. This was shown for Cu-silica, Au–titania and Au–SiO_2.[244] And finally, organo-silanes were also successfully used to bond TIMs to their release layer.[245]

5.4.1 Material preparation and characterization

For electrically insulating TIM with adhesion, both 3D-C and 3D-BN can be used, since in both cases the silane renders the foam an electrically insulating coating ($\rho = 770 \pm 10$ Ω.cm).

Adhesion is added via silane hybridization (described in section 4.4.2). The silane (3-aminopropyl) trimethoxysilane (APS) is used for all the herein described tests, since it contains three pure $–OCH_3$ groups without any additional functional groups and would thus provide an efficient bonding without dangling side-bonds.

5.4.1.1 Bonding test

In order to quantify the bonding strength of the materials, a sandwich of Si–3D-foam–Si (Al–3D-foam–Al, Cu–3D-foam–Cu) pasted onto the parallel holders of an Instron® mechanical tester is used. A tensile strain force ramp is then applied to tear apart the Si wafers. For sample preparation, the 3D-foam is first placed on one of the Si wafers, the electrically insulating paste is then dripped onto the foam. Subsequently the second piece of Si is placed on the (still wet) foam. Afterwards, the sandwich structure is dried, while compressed down to its minimum thickness. Similarly, samples with only paste were prepared by applying the same compression force.

5.4.2 Thermal Performance

Table 5-5 summarizes obtained results in terms of efficiency drop. The measurement of two bare stacked Si wafers clearly demonstrates the importance of the middle layer: the presence of air in between the layers tremendously decreased the overall thermal conductivity by more than 70%, even though the surface roughness was minimal and only a small fraction of air was trapped at the interface. This decrease even further

increased to 87% when the air gap was bigger (i.e. the roughened Si case). The results clearly show the obtained improvements with 3D-foam TIMs over commercial TIMs; even without adhesion, the thermal conductivity of Si is preserved by more than 80%, while the commercial TIM loses almost 60% of the thermal conductivity. The adhesion further improves the performance of 3D-foams and achieves full preservation of the Si thermal conductivity. This is even applicable for the roughened Si case, since the 3D-foams are able to conform to the surface roughness, as already shown in section 5.3.3. The measurements performed with the different metal foils demonstrate the versatility of the adhesion towards different types of surface. The affinity towards the metal can be further enhanced by using silanes with different head groups, with higher affinity towards the specific metal. It must be noted that also here, the 3D-BN case is generally lower than its 3D-C counterpart (due to the difference in phonon modes, impurity levels, etc.) and also due to its higher chemical inertness, which leads to less binding sites between silane and 3D-BN than for 3D-C. Contrastingly to previous work on silane-

Table 5-5. Thermal efficiency for electrically insulating adhesive 3D-foams

Structure	Efficiency decrease (i.e. deviation from ideal single layer case)
Si-air-Si	-71.5%
Si- 3D foam TIM-Si (non-adhesive)	-17.7%
Si-commercial adhesive TIM-Si	-57.5%
Si-adhesive 3D foam TIM-Si	-15.4% – 0% (BN – C)
Si,r-air-Si,r	-87%
Si,r-adhesive 3D foam TIM-Si,r	-0.07 – 0%
Cu-air-Cu	-99%
Cu-adhesive 3D foam TIM-Cu	-50% – -15%
Al-air-Al	-99%
Al-adhesive 3D foam TIM-Al	-40% – -20%

carbonaceous material, due to the interconnection of the foam, the results for 3D-foam are isotropic (e.g. aligned compressed graphene papers were reported to suffer from a huge anisotropy, even when incorporating the SAM, with $k_{\parallel}/k_{\perp}$ = 69.3 at 25 °C)[246]. It must be also noted that the silane layers are not suitable to be used as stand-alone interfacial SAM between solid-solid junctions, as they are a class of interfaces with very low thermal conductance.[247] Even though it is still being debated on how the chain length changes the overall conductance (i.e. theoretical calculations in 2003 by *Segal et al.* reported an independent conductance for chain length of N>15, while for N=2-4 an unexpected rise was seen,[248] in 2006 *Wang et. al.* measured experimentally no dependence on chain length at all,[247] in 2010 *Hu et al.* using molecular dynamics simulations saw indications that interfaces with longer chains have higher conductance,[235] in 2013 *Markussen et al.* reported phonon interference as a function of SAM thickness obtained through calculations,[249] and finally, there was a measured length dependence by a factor of 3, with an optimum of ~25 pW/K with 4 carbon atoms, by *Meier et al*. in 2014[250]), it can be concluded that overall, when used as the linking point between TIM and substrate, the temperature gradient inside the SAM is negligible, since it consists of highly aligned short (i.e. only long enough to provide a covalent bond between TIM and substrate) chains, which provide a quasi-one-dimensional thermal transport in each chain.[236] If the SAM chains become longer, the overall interface thermal conductance increases, since long SAM chains (N>12) are more flexible and would start to bend and become disordered and thus have a finite thermal resistance.

5.4.3 Bonding strength

Figure 5-13 shows the force that is required to yield detachment for each sample. Pure 3D-foam does not stick on any surface in general. Pure APS is a strong adhesion

promoter, which will only detach at a force of 31.44 N. When used in conjunction with 3D-foams, the force decreases to 10.2 N for Si, 17.6 N for Al, 12.1 N for Cu, which is due to the foam itself, since even though it is reinforced by APS, it is still able to tear apart. Nevertheless, the strength achieved is much higher than for usual TIMs (e.g. the adhesive TIM described in[251] detaches at ~6N, and the one in[166] at ~4 N) .

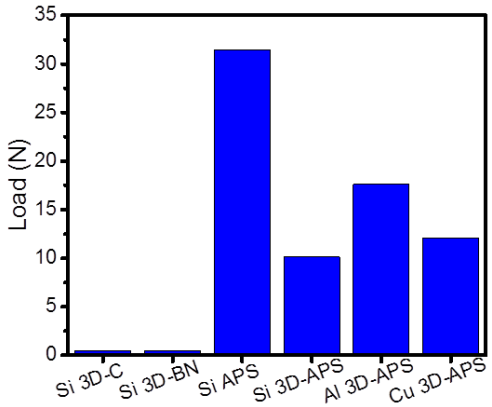

Figure 5-13. Mechanical detachment of 3D-foam TIMs with electrically insulating adhesion

5.5 Electrically conducting adhesion

Conventional metal TIMs ensure high thermal conductivity and exhibit good solder and wetting properties after reflow, which leads to low thermal interface resistance.[180] Thus, the incorporation of metals into the 3D-foam is the chosen method to add electrically conducting adhesion.

5.5.1 Material preparation and characterization

Only 3D-C is used for electrically conducting TIM with adhesion. To obtain a homogeneous hybrid of solder and foam, the process of metal hybridization described in 4.4.1 is used. For the following experiments, Sn was used as intermixing metal. The process is also applicable to other metals and metal alloys. It must be noted that the

hybrids CTE only depends on the metal chosen, thus for final application, the CTE requirement can be fulfilled by adapting the metal.

Similar to the electrically insulating case, important parameters evaluated are thermal performance and bonding strength. Sample preparation for the bonding test is modified as follows: 3D-C=Sn foam is sandwiched between Sn foil, which in turn is sandwiched between the Si. This is then heated up beyond the soldering temperature of Sn while applying compression. Samples with only Sn (of same thickness) are prepared using the same method for comparison.

5.5.2 Thermal performance

Table 5-6. Thermal efficiency for electrically conducting adhesive 3D-foams

Structure	Efficiency decrease (i.e. deviation from ideal single layer case)
Si-air-Si	-71.5%
Si- 3D foam TIM-Si (non-adhesive)	-17.7%
Si-commercial adhesive TIM-Si	-57.5%
Si-reflown Sn-Si	-15.4%
Si-reflown 3D C=Sn-Si	-0%
Si-reflown 3D C-Si	-61.5%

Results of the efficiency drop of the electrically conducting adhesion are shown in Table 5-6. It can be seen that pure reflowed Sn solder is not able to fully preserve the thermal conductivity, while the hybrid of functionalized 3D-C=Sn with reflowed Sn is able to provide a lossless transfer of heat. It must be noted that the same amount of Sn foil was used for the pure sample and the 3D-C=Sn sample. Also, for comparison, a normal 3D-C was reflowed with Sn foil, which resulted in a decrease of more than 60% of the ideal thermal conductivity with no adhesion. These results highlight, firstly, the

need of the chemical functionalization step of 3D-C in order to have a good thermal pathway from solder to 3D-foam; secondly, the achieved improvement over bare 3D-foam when adhesion is added and lastly, the superior TIM qualities of the hybrid 3D-C=solder even over pure solders. Latter observation is due to an increase in surface conformity properties.

5.5.3 Bonding strength

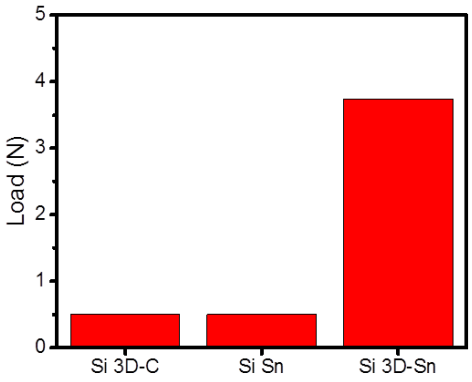

Figure 5-14. Mechanical detachment of 3D-foam TIMs with electrically conducting adhesion

Figure 5-14 shows the force that is required to yield detachment for each sample. It can be seen that pure reflowed Sn solder does not provide good adhesion. Sn intermixed with 3D-C on the other side, increased the strength from 0.5 N to 3.74 N. This is due to the refined structure of the 3D-materials (nm regime),[20] in which it is few orders smaller than the surface roughness of the Si wafer, which allows an increase in contact area and thus better adhesion (i.e. pure Sn is too flat). This is also the reason for the improved performance in the previous thermal test. Contrasting to the APS case, here the solder provides a solid backbone to the 3D-C, which prevents it from tearing apart.

5.6 Extension to gap-filling applications

Similarly to consumer electronics,[181, 183] electronics in the automotive environment (ambient temperatures from -40° to +200°C)[252, 253] and other harsh environment

electronics, such as the downhole oil and gas industry (with operating temperatures up to +150°C and +200°C, respectively) and avionics industry (with ambient temperatures from -55°C to +200°C)[254] are experien cing a higher demand in performance (i.e. faster processors, more functions, higher bandwidths) while becoming more compact and smaller.[255, 256] This leads to a drastic increase in power densities and heat dissipation rates (e.g. values as high as 100 Wcm^{-2} for commercial and 1000 Wcm^{-2} for military high power electronics are soon to be reached).[257] With this, also the thermal management problem in harsh environment application has become increasingly severe.[255] Despite the improvement achieved for thermal management solutions in consumer electronics,[182, 187, 201] those thermal solutions cannot be directly applied for harsh environment applications, since the gaps to be filled are thicker (in the order of millimeters, which is much larger than that for TIMs used in electronic device applications), sometimes complexly wound in random directions,[258] the ambient and operating temperatures are higher and additional exposure to shock, vibration and sometimes even spillage are common additional difficulties encountered.[253-255]

Due to the compressibility of the 3D-foams, the final thickness achievable after the compression step is limited and in the µm range and can thus not be directly applied for gap filling applications. One way to achieve increased thickness is by infusing the 3D-foams with polymers. The polymer backbone provides a robust support for the 3D-foam, enhances flexibility and handling, and prevents the 3D-foam from total compression.[17, 21] Even though there have already been reports on the infiltration of 3D-foams with polymers for thermal-related applications,[110-112] their achieved electrical conductivity and thermal properties are drastically decreased (i.e. none of the reported values is nearly the 60 $Wm^{-1}K^{-1}$ of the bare compressed foam). More compelling, additional layers of bare polymer below the structure are inevitable using usual polymer-infusion

techniques, which further lowers the performance and does not allow good surface conformity properties.[180] Mitigating this problem by increasing the filling fraction of the foam is often not successful, since the achieved further increase in thermal conductivity is minimal[259] and it can yield to loss of flexibility of the polymer.[260]

In order to address all these issues and to obtain a high performance thermal gap filler material, we developed a new way of infusion of 3D-foams with polymer: the "hairy" method. It combines the advantages of both – the infusion process provides mechanical support, but at the same time, the intrinsic properties of the 3D-foam are fully preserved as well as its surface conformity. This is obtained through infusing only the central layer of the foam, as schematized in Figure 5-15. Since in automotive applications elastomeric polymers of silicone (such as PDMS) are already used in mountings around motor coils of electric vehicles,[258] PDMS is the choice of polymer for this work.

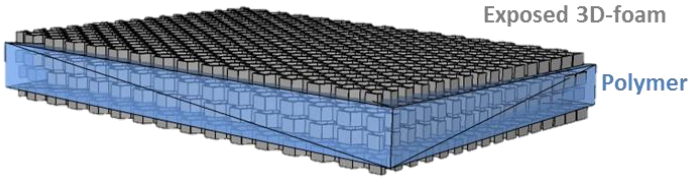

Figure 5-15. Schematic of the "hairy" structure of infused 3D-foam with polymer

5.6.1 Material preparation and characterization

Preparation of samples for this application uses 3D-C for electrical conducting and 3D-BN for electrical insulating needs, followed by the infusion process described in section 4.5.2. For measurements, foams of initial thickness of 2 mm were used, with a PDMS coating of 1 mm thickness. Since the more stringent requirement for this application is the resilience to vibration, additional Instron® 5567 mechanical tests were used in the tensile and compression mode at room temperature to assess the dampening properties of the material.

5.6.1.1 INSTRON mechanical tester

For tensile testing, samples of known dimensions were clamped into the mechanical tester and then a strain rate of 1 mm/min applied. Tensile stress and strain are determined from the applied tensile force over the original specimen cross-sectional area and elongation of the sample over its original length, respectively. For compression testing, the sample with a specified dimension was loaded at the center of the lower platen, a compression rod with 50 mm diameter was then applied onto the sample with a controlled speed, and all the compressions were conducted within the confinement of the small upper platen. Compressive strain and stress were calculated using the displacement of the compression rod divided by the original height of the sample and the applied compressive force over the cross-sectional area of the samples, respectively. Recoverability of the sample is defined as the displacement recovered over applied displacement. The uniaxial compression experimental data was acquired at a loading–unloading rate of 0.04 mm/min at a strain of 60%. For the "hairy" sample, the exposed bare 3D-foam was already pre-compressed, since this is the configuration in the final application of gap filler. A total of 100 compression cycles were performed for the "hairy" 3D-foam, 10 cycles for the bare 3D-foam.

5.6.2 Enhanced mechanical properties

Figure 5-16a shows the tensile stress-strain curves of bare and "hairy" 3D-foam and it can be observed that all the samples follow similar trajectories, i.e. linear mechanical behavior until an abrupt breaking point. The inset in Fig. 5a shows an enlarged graph of the bare 3D-foam tensile stress-strain curve. It can be seen that there are several peaks and valleys along the curve, which was previously assigned to the alignment of single graphene branches within 3D-C towards the direction of the tensile load.[261] Here, this

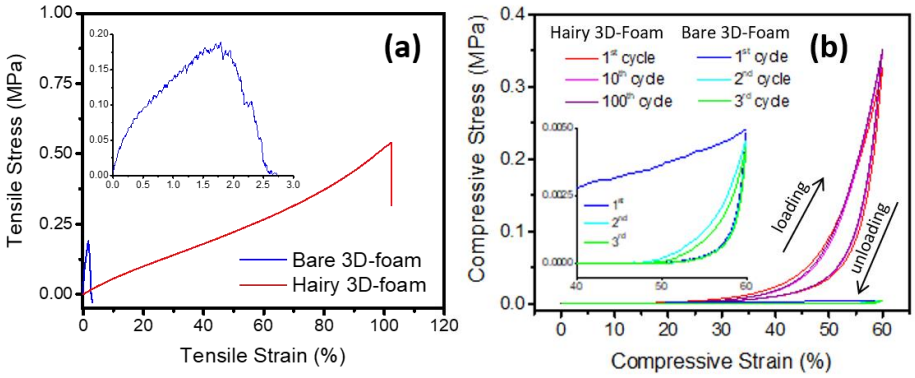

Figure 5-16. (a) Stress-strain curves resulting from tensile stress measurements, **(b)** cyclic stress-strain curves resulting from compressive stress measurements (inset: zoom into the 40 to 60% compressive strain region of bare 3D-foam)

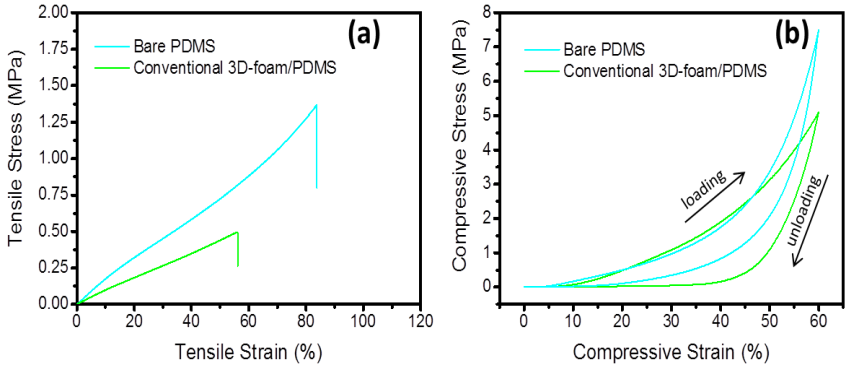

Figure 5-17. Mechanical results of bare PDMS and conventional 3D-foam/PDMS composite **(a)** tensile, **(b)** compression

was also observed for the tensile curves of 3D-BN. The hairy 3D-foam performs with much higher breaking elongation as compared to the bare 3D-foam. The as prepared bare 3D-foam exhibits high Young's modulus of 10.5 MPa on account of the intrinsically strong graphene domain (graphene has a Young's Modulus of 1050 GPa)[262], while it breaks at the strain as low as 1.8%, which is due to the weak van der Waals stacking between the domains[119] that uncouples easily upon tensile loading. While for the hairy 3D-foam, the almost two orders increased breaking elongation at 102% is quite outstanding, which is even higher as compared to the bare PDMS and conventional 3D-foam/PDMS (Figure 5-17). This large increase in strain-at-break is not only attributed to the highly crosslinked PDMS chains within the structure which can endure high

tensile load,[263] but also due to additional free interactions (frictions) between the PDMS chains and the graphene domains, which lead to timely dissipation of energy accumulated during the tensile loading, postponing the stress concentration induced failure. As a result, the well-connected 3D structure and the high intrinsic mechanical structure of the graphene domains[261] contribute to the increases of both tensile strength (from 0.19 to 0.54 MPa, 3-fold increase) and breaking elongation. The remarkable tensile mechanical performance of the hairy 3D-foam indicates its outstanding flexibility and toughness, which are pivotal for its potential applications.

To demonstrate the robustness of the "hairy" 3D-foams for gap filler application, Figure 5-16b shows the cyclic compressive stress-strain curves of the bare 3D-foam and the hairy 3D-foam at an applied strain of 60%. It can be observed that an almost full shape recovery was performed by the hairy 3D-foam after first loading-unloading cycle, which remains consistent over the long-term compression of up to 100 cycles, showing no observable degradations in shape recovery characteristics and properties and compressive strength. With only 50% of the total volume of the sample with PDMS, the "hairy" 3D-foam was able to perform with a comparable shape recoverability as compared to bare PDMS, which makes it capable of providing stable mechanical support when serving as thermal gap filler. Contrastingly, the bare 3D-foam deformed almost plastically upon continuous compression with only 16% shape recoverability (inset of Figure 5-16b) after first compression at a 60% strain, which is followed by minute elastic recovery during subsequent cycles as a result of the reversible compressions of the compressed portion. The poor resilience of bare 3D-foams is owed to the fact that the main effect of compression on 3D-foams is branch and sheet bending, in which the excellent in-plane strength of graphene/h-BN is not fully utilized.[261] Furthermore, the weak van der Waals intermolecular interactions at the sheet junctions

are unable to produce a reversible recovery of the foam after the release of compression loading. These effects lead to the low compressive strength measured. The excellent shape recoverability of the "hairy" 3D-foams could be attributed to the excellent compressive resilience of the infused PDMS portion and also the bridge-effect of the PDMS between separated graphene sheets which strengthens the whole structure.[264] During the compressive loading and unloading, the restacking and agglomeration of the graphene domains are hindered due to the existence of the PDMS component, which serves as a lubricant that has both glidant and anti-adherent properties. In addition, the more effective and efficient load transfer performance of this hybrid structure and the elasticity of the PDMS portion collectively contribute to the 70-fold increase in compressive strength as compared to the bare 3D-foam (from 0.005 MPa to 0.33 MPa). The overall enhancement in compressive mechanical performance of the hairy 3D-foam ensures its structural stability upon serving as gap filler (i.e. withstand possible shock or vibration). Table 5-7 summarizes all mechanical test results for the bare 3D-foam and "hairy" 3D-foam. As mentioned previously, under tensile loading, the bare 3D-foams better utilize the high in-plane properties of their constituent 2D-sheets as it aligns towards the direction of the load, and thus the tensile strength is orders of magnitude larger than the compressive strength.

Table 5-7. Measured mechanical properties

	Bare 3D-foam	Hairy 3D-foam
Tensile strength (MPa)	0.19	0.54
Elongation at break (%)	1.8	102
Young's Modulus (MPa)	10.5	0.53
Compressive strength (MPa)	0.005	0.33
Recoverability (%)	~16	~90

5.6.3 Electrical and thermal conductivity

With regard to the "hairy" foam's electrical conductivity, since the outer layers are completely exposed, they completely retain their electrical characteristics (i.e. 3D-C remains conductive with ρ = 1.7 Ω.cm and 3D-BN remains insulating with ρ = 16.0 x 10^6 Ω.cm), even during and after bending. This exceeds current best performing 3D-filler/PDMS composites, for example graphene aerogel in PDMS could maximally retain 80% of its electrical conductivity at different bending conditions.[265] This also applies to the thermal properties of the "hairy" 3D-foams: measurements carried out with the "hairs" compressed on both sides of the polymer layer (i.e. after being compressed with a force of ca. 24 N) achieved same values as bare compressed 3D-foams (i.e. ~86 $Wm^{-1}K^{-1}$ for 3D-C and ~62 $Wm^{-1}K^{-1}$ for 3D-BN). This is more than two orders improvement over previously reported 3D-C/graphene-sheet mixtures (0.7 wt%) in PDMS with 0.56 $Wm^{-1}K^{-1}$,[110] and a ca. 50-fold and 60-fold increase over 3D-C in epoxy with 1.52 $Wm^{-1}K^{-1}$[1111] and 3D-C/graphene flakes in PDMS with 1.08 $Wm^{-1}K^{-1}$,[112] respectively. The hairy method is also able to surpass other high-performance fillers, for example a mixture of PDMS with diamond particles and boron nitride platelets yield 6.1 $Wm^{-1}K^{-1}$,[258] 10-times smaller than the 3D-BN "hairy" foam.

These results are evidence that the infused PDMS layer in the center of the sample does not affect the electrical and thermal transport. This is because the interconnection of the foams is maintained within this layer and the outer bare foam layers are not altered at all. Thanks to this non-invasive method, the phonon and electron transport still takes place on a seamless network and thus the main contribution to the thermal conductivity comes from the 3D-foam. Hence, when the foam is in its compressed state (with the "hairs" fully compressed), the main contribution to the thermal conductivity comes from the bare hairs, and thus the overall thermal conductivity is close to the thermal

conductivity of the fully compressed bare foam. This is extremely important for thermal gap filling applications, since this means that the generated heat which is in direct contact with the bottom layer of the foam can be directly transferred through a larger gap into the top layer of the foam which can then be in contact with a cooling section or the ambient to release the heat.

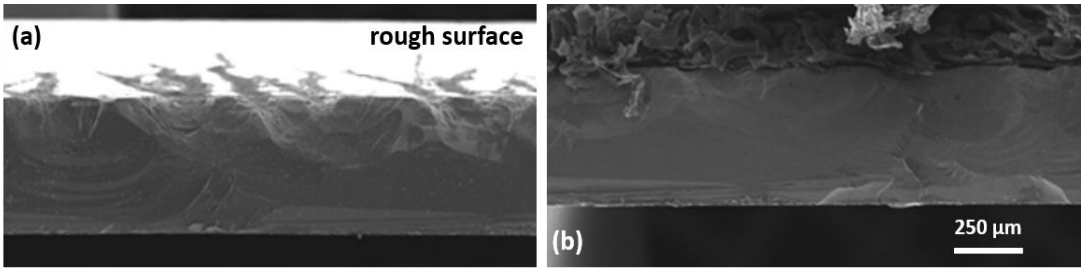

Figure 5-18. Surface conformity of the "hairy" 3D-foam: rough surface **(a)** before and **(b)** after compression with the foam

Thanks to the exposed hairs, also the same surface conformity as reported for the bare foams is achieved. The amount of exposure of hairs can be tuned in accordance to the surface roughness of the mating surfaces to achieve a seamless contact. Figure 5-18a,b show SEM images of a sample rough surface before and after compression with a "hairy" 3D-foam on its outer layer, respectively. It can be clearly seen how the foam closely follows the contour of the rough substrate.

5.7 Stability and reliability

Since the 3D-foams are used as TIMs for electronics, it is important to assess their applicability within the entire life span of a device (typical life expectancy of electronic equipment is given in Table 5-8). A low-quality TIM would start degrading with time and cause an increase in thermal interface resistance and junction temperature of the device, and might even lead to failure. This is why it is important to determine the stability and reliability performance of the 3D-foam TIMs and to evaluate its life

expectancy. In order to provide comprehensive screening, a variety of accelerated stress tests are performed. This is to closely represent the possible settings the TIM might be exposed to. The three most common stress categories for TIMs are the temperature and humidity stress test, temperature/power cycling stress test and high temperature storage/bake/soak test.[151]

Table 5-8. Life expectancy of electronic equipment[266]

Size	Equipment	Life expectancy
Small appliances	Mobile phone MP3 players Irons Hair dryers	2 – 3 years
Medium size appliances	Cleaners Refrigerators/freezers Microwave ovens	3 – 6 years
Large appliances	Electric cookers	5 – 10 years
	Fridge/freezer	3 – 6 years
	Washing machines	3 – 6 years
	Low prices portable TVs	2 – 5 years
	Higher priced non-portable TVs	5 – 8 years
	Low priced Hi-Fi systems	2 – 5 years
	Higher priced Hi-Fi systems	5 – 8 years
IT hardware	Desktops	3 – 4 years
	Laptops	2 – 3 years
	Tablets	2 – 3 years

5.7.1 Tests performed for stability and reliability

The thermal stability (i.e. TIM operational range) of the 3D-foams was studied via TGA (methodology similar to section 4.2.2), which is a method commonly used to evaluate TIM's stability at elevated temperatures.[151, 152] The point of 5% mass loss is considered the starting point of degradation. Further chemical analysis was carried out using XPS. Reliability of the 3D-foams was assessed through temperature cycling and elevated-temperature/humidity tests following JEDEC standards. Since the 3D-foams are of a very fragile nature, different samples were used for each measurement. All samples were cut into the correct size for the measurement, prior to cyclic testing. All

samples were grown concurrently to avoid differences caused by batch fluctuations. For cyclic testing, the samples were placed together in a tray.

5.7.1.1 Temperature cycling

Following JEDEC Standard JESD22-A104D, the 3D-foams ability to withstand alternating high- and low-temperature extremes is assessed. Permanent changes in the material's characteristics could result from these mechanical stresses. A single-chamber stationary setup was used with -40°C – +145°C as minimum and maximum temperatures, with a soak time of 15 min and a ramp rate of 10°C/minute for a total of 1000 cycles. Samples were taken out for evaluation every 250 cycles.

5.7.1.2 Elevated-temperature/humidity testing

Following JEDEC Standard JESD22-4118, the elevated temperature and humidity encountered by electronics hardware is simulated and the 3D-foams reliability under these conditions evaluated. Set parameters are 85°C at 85% relative humidity for a total of 1000 hours. The samples were taken out for evaluation every 250 hours.

5.7.1.3 Evaluation of reliability

In order to evaluate the material's reliability, visual inspection was the first parameter observed (SEM), followed by chemical analysis via XPS (section 3.2.5.2) and physical analysis through TGA (section 4.2.2) and density measurements obtained by weighing a sample of known dimensions with a precision electronic balance (Mettler Toledo).

5.7.2 Bare foam stability and reliability

Thermal stability results of the bare 3D-foams are shown in Figure 5-19. The blue curve corresponds to 3D-C, which shows that it remains unchanged up to 700°C and

that only after this point, it loses 95% of its weight. 3D-BN (green curve) on the other side remains stable up to 900°C, and then increases in weight, which is due to the oxidation of BN to B_2O_3 which is heavier in mass. The initial slight decrease of the 3D-BN mass is due to the loss of hygroscopic water.[267, 268] Both results are in good agreement with literature.[269, 270] It is worth mentioning that typical operating temperatures for electronics is of 65 – 85°C for commercial applications, 110 – 120°C for military electronic systems, and as high as 175°C for automotive ICs and the upper spectrum of military applications (all demarcated in the graph).[271] Evidently, both 3D-foams can withstand all the important operating temperature ranges.

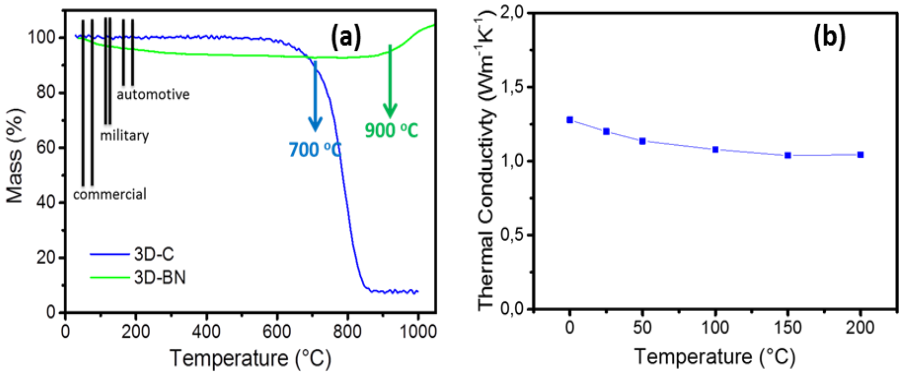

Figure 5-19. (a) Thermal stability of the 3D-foams. measured via TGA curves of 3D-C (blue) and 3D-BN (green); **(b)** thermal stability of 3D-C throughout a temperature range from 0°C to 200°C, measured through laser flash

To ensure that the thermal conductivity of the 3D-foams remains stable throughout the temperature range of electronics, laser flash on uncompressed 3D-C was performed from room temperature to 200°C and Figure 5-19b shows the obtained results. It can be seen that the thermal conductivity remains stable at ± 10%, which corresponds to previously reported values for this type of 3D-foam.[20, 119]

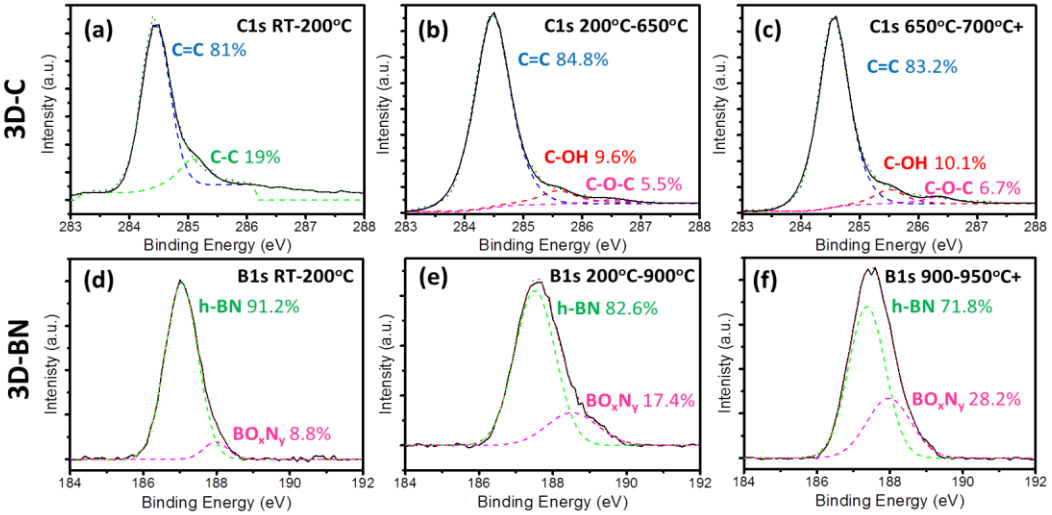

Figure 5-20. (a, b, c) C1s XPS high resolution spectra of 3D-C at different temperature ranges, **(d, e, f)** B1s XPS high resolution spectra of 3D-BN at different temperature ranges

XPS analysis was carried out on the 3D-foams after exposure to different temperatures in air for one hour from 200°C and up to 720 °C for 3D-C and 920°C for 3D-BN. The results are shown in Figure 5-20a-f. For the case of 3D-C, in the range of room temperature to 200°C, only a pure graphitic structure was detected, comprised of only carbon aromatic groups. Starting at 200°C, an oxidation of 5 – 6% is visible, which only slightly increases at 700°C (i.e. the point of mass loss). For the case of BN, a similar behavior can be observed; BN oxidizes slightly with increasing temperature, but the level of oxidization remains in a low regime of 8 – 17%. This very high thermal stability beyond the usual operating temperatures is of great advantage, especially for electronics, where the growth in both compactness and performance has increased heat generation problems. In particular for electrically insulative TIMs, one of the current challenges is their thermal stability beyond temperatures of 120 – 200°C (i.e. polymers degrade under such high temperatures,[272] grease hardens).[163] 3D-foams (i.e. 3D-BN for electrically insulative TIM) on the other hand are capable to withstand the increasing demands for electronics in high temperature environment.

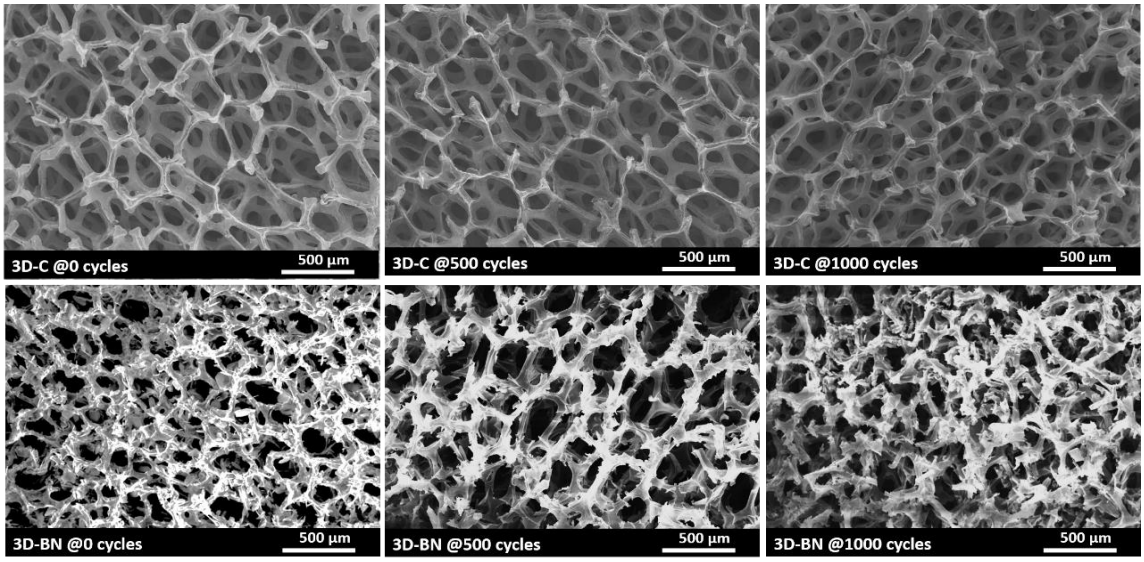

Figure 5-21. SEM images of the 3D-foams after 0, 500 and 1000 thermal cycles from -40°C – +145°C

Representative SEM images of samples after 0, 500 and 1000 cycles of temperature cycling stress test are shown in Figure 5-21. It can be clearly seen that for both cases, 3D-C and 3D-BN, the morphology of the samples did not change at all, as in there are no obvious visible changes observable in the image. The pore size and distribution, as well as the outer surface of the walls remain unchanged.

Table 5-9. Chemical analysis of the 3D-foams after thermal cycling (-40°C – +145°C)

Cycle	3D-C		3D-BN	
	C at%	O at%	BN at%	O at%
0	95.6	4.4	93.6	6.4
250	95.2	4.8	93.4	6.6
500	97.1	2.9	92.7	7.3
750	96.8	3.2	95.1	4.9
1000	95.8	4.2	93.9	6.1

Chemical analysis on the samples after 0, 250, 500, 750 and 1000 cycles also did not reveal any significant changes. As could be seen in the stability tests, the major possible changes occurring to the foams is oxidation, which is why the atomic % composition of C and O, and BN and O were extracted from the XPS surveys of 3D-C and 3D-BN,

respectively and are summarized in Table 5-9. Even though there is no bonding to O detectable in all the C 1*s* high resolution spectra, there is still oxygen present in the 3D-C survey spectra due to normal contamination. For the 3D-BN case, as could be seen in the stability XPS spectra, there is a small BO_XN_Y portion intrinsically available, which is caused by the annealing in air to remove the PMMA. The variation in O content between samples is of maximum -1.5 at% and +0.9 at%, which is within the same fluctuation seen in the B:N stoichiometry (which also varies from the ideal 1:1 by a margin of measurement error of ±1.9 at%), and is therefore negligible.

Analysis of physical properties of the samples are summarized in Table 5-10. It can be seen that the point of mass loss (i.e. degradation) of the 3D-foams measured through TGA remains stable throughout the tested range of samples (3D-C with a measured mean value of 677.1°C ±17.99°C and 3D-BN with 945.985°C ±15.89°C). The values are consistent with typical degradation values reported for such materials[269, 270] and the error deviation is within the acceptable margin reported for TGA/DSC measurements at high temperature.[273] The same is observed for the density of the samples; 3D-C has a mean density of 1.44 ±0.28 mg/cm^3 throughout the range of tested samples, 3D-BN 6.482 ±0.37 mg/cm^3. It can be seen that the values remain consistent without significant changes throughout the thermal cycles.

Table 5-10. Physical analysis of the 3D-foams after thermal cycling (-40°C – +145°)

Cycle	3D-C		3D-BN	
	Point of Mass loss [˚C]	Density [mg/cm^3]	Point of Mass loss [˚C]	Density [mg/cm^3]
0	671.95	1.5	938.725	6.2
250	697.53	1.3	960.16	6
500	694.438	1.3	921.675	6.56
750	663.76	1.2	952	6.8
1000	657.82	1.9	957.365	6.85

The temperature cycling stress tests can be used as a means to test the operational lifetime of the 3D-foams, i.e. how many on-off cycles it can withstand. With these results, it can be seen that the 3D-foams could withstand over 1000 on and off cycles without any loss in material properties.

Representative SEM images of samples after 0, 500 and 1000 hours of elevated-temperature/humidity stress test are shown in Figure 5-22. As in the previous case, the pore size/distribution and outer surfaces remain unchanged (unchanged morphology).

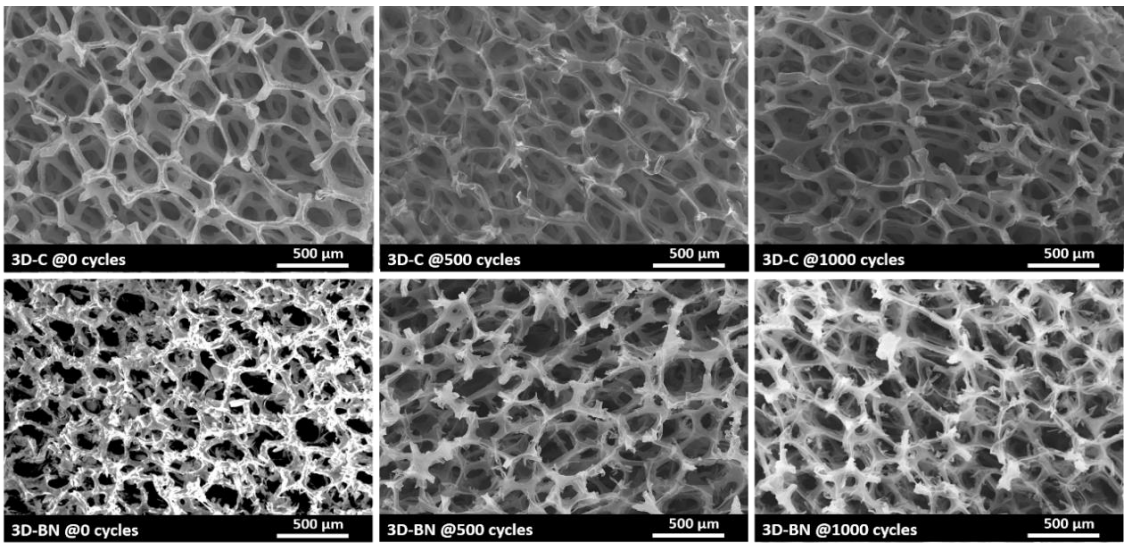

Figure 5-22. SEM images of the 3D-foams after 0, 500 and 1000 hours of 85°C/85% RH exposure

Also in this case, chemical analysis on the samples after 0, 250, 500, 750 and 1000 hours of exposure did not reveal any significant changes (Table 5-11). The variation between samples is maximally of –1.3 at% and +1.0 at%, which is, again, within the acceptable margin (i.e. comparable to the variation seen in the B:N stoichiometry). Results of the physical analysis are summarized in Table 5-12. The measured point of mass loss (i.e. degradation) of 3D-C is at 651.52°C ±15.01°C, for 3D-BN at 922.1°C ±14.38°C. Again, these values are within the usually reported values for these materials[269, 270] and, as mentioned before, within the typical error deviation expected for

such measurements.[273] Similarly to the thermal cycling density results, also in this case the values remained stable throughout the exposure. 3D-C has a mean value of 1.68 ±0.3 mg/cm^3, 3D-BN of 5.882 ±0.45 mg/cm^3.

Table 5-11. Chemical analysis of the 3D-foams after 85°C/85% RH testing

Cycle	3D-C		3D-BN	
	C at%	O at%	BN at%	O at%
0	95.6	4.4	93.6	6.4
250	98.2	3.8	92.9	7.1
500	97.7	4.3	94.9	5.1
750	97.9	5.1	92.6	7.4
1000	97.7	4.3	93.5	6.5

Table 5-12. Physical analysis of the 3D-foams after 85°C/85% R.H testing

Cycle	3D-C		3D-BN	
	Point of Mass loss [˚C]	Density [mg/cm^3]	Point of Mass loss [˚C]	Density [mg/cm^3]
0	671.95	1.5	938.725	6.2
250	657.18	1.7	907	5.3
500	631.59	2.1	909.35	6.21
750	644.2	1.3	920.741	6.2
1000	652.68	1.8	934.684	5.5

The elevated-temperature/humidity stress test is considered as an accelerated stress test. Such tests are necessary to speed up the "aging" of the material to predict the performance at the end of its use (end of life, EOLife, performance). Regression curve fitting based on Arrhenius relationships is used in such cases.[151] It must be noted that the test conditions are artificial and not typical use conditions, to accelerate the degradation (to be able to perform the test in a manageable timeframe). From the results for the 3D-foams it can be concluded that the samples would stay reliable for at least

1000 hr in 85% RH and 85°C. Using formula (5-4), the equivalent time to failure for different conditions are extrapolated and listed in Table 5-13.[274]

$$\frac{t_{tf}\,at\,T_2 and\,RH_2}{t_{tf}\,at\,T_1 and\,RH_1} = \left(\frac{RH_1}{RH_2}\right)^n * exp\left[\frac{\Delta E_a}{k}\left(\frac{1}{T_2}-\frac{1}{T_1}\right)\right] \qquad (5\text{-}4)$$

with t_{tf} time-to-failure, T temperature, RH relative humidity, n an empirical constant = 3, ΔE_a empirically found energy activation for failure mechanism = 0.9 eV and k Boltzmann's constant = 8.62 x 10^{-5} eV/K.

Table 5-13. Equivalent lifetimes to 1000 hr in an 85°C/85 RH test

Temperature [°C]	RH [%]	Time to failure t_{tf} [hr]
85	85	1000 = 6 weeks
25	40	3801600 = 434 years (office conditions)
35	95	89000 = 10.15 years (jungle conditions)
60	40	90000 = 10.3 years (consumer electronics)
130	40	351 = 15 days

With these values, it is possible to estimate the shelf life, as well as operational lifetime of the material if constantly in use. For 3D-foams, the shelf life under normal office conditions would thus be of at least 434 years, under very humid conditions (such as those encountered in Singapore), at least 10.15 years. 3D-foams would withstand an operational lifetime of at least 10.3 years in consumer electronics kept constantly on (which far exceeds the expected lifetime of the electronic itself) and 15 days in military electronics kept constantly on at maximum power.

5.7.3 Adhesive foam stability and reliability

In order to determine the stability of the adhesive types of 3D-foam at high temperatures, Figure 5-23 shows their TGA curves. Also here, the slight decrease at the beginning is due to the loss of hygroscopic water.[267] It can be seen that the electrically

insulating adhesive remains stable up to ~430°C, and the electrically conducting adhesive up to ~380°C. This is still far beyond the limits of current TIMs, which only withstand up to 120 – 200°C.

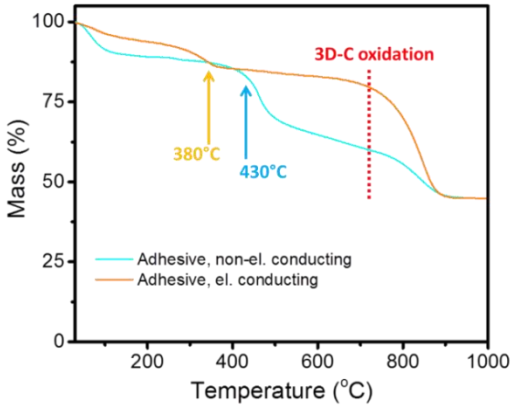

Figure 5-23. TGA curves for adhesive 3D-foam TIMs

Since it has been shown that the 3D-foams have a shelf life of over 10 years under "jungle" conditions as well as at least 10 years of operational life time in consumer electronics, the reliability of the adhesive 3D-foams is mainly constrained by the adhesives themselves. For silane, (e.g. APS), according to the manufacturers website, a shelf life of 5 years under ambient conditions is suggested.[275] Similarly, most manufacturers of solder suggest a shelf life of 2 – 3 years under ambient conditions.[276]

Thermal cycling of silane showed failures in bonding after 50 000 cycles from +4°C to +60°C;[277] aging tests in water at 94°C revealed an increase in resistance to cyclic fatigue which actually strengthened the bond strength.[278]

Temperature cycling of Zn/30Sn, Au/20Sn and Pb/5Sn solder joints was tested for up to 2,000 cycles from -40°C to +125°C,[279] which are considered harsh conditions for electronics equipment. Results showed that Au/20Sn was able to maintain 90% of the initial shear strength after 2,000 cycles; degradation was observed for the other two joints after 500 cycles. The modes of degradation were however very different for the

two: Pb/5Sn failed due to severe cracking inside itself, Zn/30Sn formed cracking inside the intermetallic layer on the substrate side. This indicates that Zn/Sn can be improved through inserting a suitable barrier layer, while this cannot be applied for Pb/5Sn. These results highlight that Au/20Sn is one of the best choices as high-temperature solder and it does not require any barrier coating on the substrate.[280] It must be also noted that for metallic adhesion, moisture absorption is not a significant issue, unless when different metals are directly in contact (galvanic corrosion).[180] For example, exposure of lead free solder Zn-Sn to 85°C/85%RH for up to 1,000 hours showed stable results, even in severe humidity.[279]

5.7.4 PDMS-reinforced foam stability and reliability

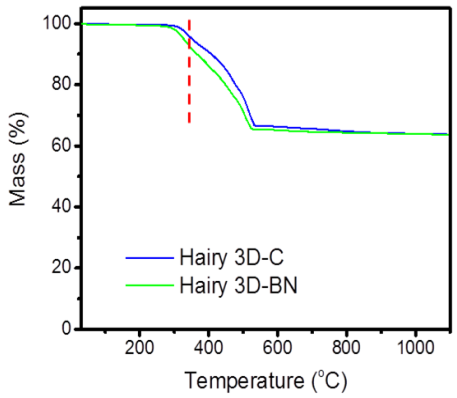

Figure 5-24. Thermal stability measurements of the "hairy" foams through TGA

Even though the 3D-foams can withstand temperatures as high as 700°C and 900°C, polymers are known to be prone to structural changes at elevated temperatures (i.e. above the glass transition temperature T_g, the polymer changes, usually hardens), which could cause CTE and performance problems.[180] In order to corroborate the applicability of the "hairy" foams for harsh environment thermal management needs (i.e. ambient temperatures in the range of 200°C), its thermal stability was assessed. TGA curves of

"hairy" 3D-C and 3D-BN are shown in Figure 5-24. It can be seen that both the curves follow usual decomposition lines of bare PDMS,[281, 282] with a decomposition temperature at around ~330°C. This remains well above current TIM limits[163] and could thus be used for harsher and more demanding environments, such as electric motors. It must be noted that PDMS is a polymer with intrinsic good environmental stability.[283] Thermal cycling tests previously reported[284] revealed that PDMS can survive in air for long periods at 200°C and for short periods at 250°C without degrading. It also retains its flexibility at temperatures down to -45 – -55°C.[285]

5.8 Summary

In this chapter, different variations of 3D-foams were studied for the use of high-performance TIMs. First, the 3D-foams in their bare state have been investigated. Studies were carried out on 3D-C and 3D-BN with varying densities, in order to cater for different electrical conduction application needs. Results for the high-density 3D-foams have shown that high thermal conductivities across the plane direction in the range of 62 – 86 $Wm^{-1}K^{-1}$ are achieved. This is a 14- and 30-fold increase over their 2D counterparts, 300 – 800 times higher than standard TIMs and a 10-fold increase over recent reported TIMs that are comprised of other nanomaterials (such as graphene laminate, graphene and h-BN paper). In addition, due to the compressible nature of the 3D-foams, a superior surface conformity was revealed. Direct comparison of the 3D-foams to other state-of-the-art TIMs has shown improved cooling performance by 20 – 30% (a drastic decrease of chip temperature on a 2.5D test platform from ca. 95°C to 51°C for 3D-C and to 71°C for 3D-BN at an applied power of ~5 W was measured, which is 20% colder than any of the commercially available TIMs tested on the same platform, i.e. Sn/Au). Comparison to other results from literature also revealed the

superior qualities of the 3D-foams (e.g. highest values for alternative heat spreaders currently under research range around $\Delta T \sim 13°C$ for a CVD-graphene heat spreader,[229] $\Delta T \sim 6 – 12°C$ for a graphene-based film with added silane-functionalized molecules,[231] and $\Delta T \sim 20°C$ for exfoliated few-layer graphene[228]). This is a significant decrease, since it is known that the decrease of hot spot temperature on chips by 20°C extends the transistors lifetime by one order of magnitude.[228] It must be also noted that for most alternative materials currently under research, the cooling down of the hot spot is via the distribution of the heat throughout the film in the in-plane direction and not by extracting it upwards (to a heat sink). At equilibrium, such spreading of the heat would keep the entire chip at elevated temperatures and defeats the purpose of maintaining the chip below a safe operating region.[33] Contrastingly, for 3D-foams, their outstanding thermal conductivity in the cross-plane direction and their thin thickness (which will fasten up the heat transfer upwards, rather than lateral), makes them thus ideal candidates for solving current thermal management needs.

These overall enhancements in thermal performances are due to the isotropic thermal behavior given by the initial foam-like, interconnected structure, which is contrasting to usual nano-TIMs, where only weak Van der Waals forces ensure the contact between layers, and thus hindering good phonon transport.

To further provide versatility and applicability to different applications, the 3D-foams were further developed to include adhesion. Also in this case, it was catered for both, electrically insulating and electrically conducting cases through developing two different kinds of adhesion. In order to also develop the 3D-foams for thermal gap filling application in harsh environment, they were further developed to be able to fill larger gaps and withstand vibration. For this, a new way of infusing polymer into 3D-foams was developed which leaves the outer parts of the 3D-foam still exposed. This method

proved to be a very good method to re-enforce the bare 3D-foam structure, since it rendered an increase in tensile strength by ~185%. At the same time, this method allows to fully retain the electrical and thermal characteristics of the foams (electrical resistivity of 1.7 Ωcm for 3D-C and of 16.0 x 10^6 Ωcm for 3D-BN, thermal conductivity of ~86 $Wm^{-1}K^{-1}$ for 3D-C and ~62 $Wm^{-1}K^{-1}$ for 3D-BN), since it is a non-invasive way of infusion which preserves the networked and interconnected structure of 3D-foams. These foams were further characterized according to thermal gap filler needs, which are the compressibility/dampening properties, as well as thermal stability. It was shown that the "hairy" foams provide a restorative force (i.e. can act as a spring), with a performance similar to bare PDMS, which is the material currently being used for such purposes.

In a final step, the reliability and stability of all presented variations of 3D-foam TIMs has been assessed. It was shown that the bare 3D-foams can withstand temperatures up to 700 – 900°C without any chemical changes, which is at least 500°C above current available TIMs, and stay reliable (without any chemical or physical changes) even after 1000 thermal cycles (from -40°C to +145°C) and 1000 hours at elevated-temperature/humidity (85°C/85% RH). For the modified versions of the foams it has been shown that all of them are able to withstand temperatures at least as high as 380°C for a minimum period of 3 years.

The availability in both electrically conducting and insulating mode, combined with the high cross-plane thermal conductivity and excellent surface conformity, lets these 3D-foam combine the advantages of both metallic TIMs (i.e. high thermal conductivity) and polymeric/adhesive-based TIMs (i.e. good surface conformity). These advantages would allow electronics to be driven towards a higher power regime and enable a closed-form solution[33] for future electronics device package.

6 Application as improved flexible substrate

6.1 Introduction

Flexible electronics technology provides a non-rigid and versatile platform that extended many conventional electronics into a large diversity of novel applications through the transfer of the currently available processes and components onto flexible platforms (some examples are the bionic eye,[286] optic nerve,[287] flexible battery,[288] conformable RFID tags,[289] displays[290] and touch screens[291]). Among those platforms, polyimides (PIs), being known for their high thermal stability, high modulus of elasticity and tensile strength, ease of fabrication and moldability, have become the material of choice and demonstrated its application in various organic and flexible electronics, including dielectrics for high speed signal transmission, packaging (encapsulation), membrane materials and shielding materials/coatings.[172, 292] However, PI suffers drawbacks from its low thermal conductivity and electrically insulative nature.[293] For instance, its low thermal conductivity has resulted in a heat dissipation challenge for flexible high power electronics (for comparison, the thermal conductivity of crystalline Si is in the range of 100 $Wm^{-1}K^{-1}$ [294] whereas PI is in the range of 0.24 $Wm^{-1}K^{-1}$ [295]). This drastic difference in their thermal dissipation capability bears heavily on the designers of flexible devices. Inevitably, the performance of these devices will need to throttle down to reduce power consumption in order to decrease the heat generated by their operation.

One way to mitigate this issue is to infuse higher thermal conductivity materials into the polymer matrix to improve its overall conductivity. Recently, there is a growing interest to use highly thermally conductive nanomaterials as nanofillers for infusing into the matrix. Nanomaterials such as graphene,[260, 296] carbon nanotubes[297, 298] and metallic

nanoparticles[299] are common fillers for these purposes. Although improvements of the overall conductivity can be obtained using this approach, there are still considerable challenges, such as inhomogeneous distribution of the nanofiller within the polymer matrix, aggregation and low filling fraction. Another critical concern is the poor long range thermal conduction seen in many of these composites as only a fraction of these individual nanomaterials are coupled together (weakly through Van der Waals forces) and most of the fillers are generally encapsulated entirely by the polymer matrix.[33]

In this chapter, new 3D-foam/PI composites are developed and shown to be a viable substitute for flexible electronics substrates. The 3D-foams serve as effective filler, which can improve the electrical conductivity by 10 orders of magnitude and thermal conductivity by 10 – 25 times with a filling factor of merely 0.3%. In addition, to study its reliability for the use in flexible electronics, temperature dependence of the film's electrical and thermal characteristics and aging effect under various mechanical stressing cycles have been studied. These tests reveal that there is no sign of degradation under strenuous mechanical bending, which is normally a problem with composite films of this nature.

6.2 Material preparation and characterization

Preparation of samples for this application uses 3D-C for the electrically conducting films and 3D-BN for the electrically insulating films, followed by the infusion with PI polymer described in section 4.5.3. Since the major challenge in flexible electronics is the heat dissipation, thermal conductivity, temperature dependent electrical conductivity and proof of concept heat spreading experiments were carried out.

6.2.1 Temperature dependent electrical conductivity

The temperature dependent electrical conductivity measurements are performed in a dedicated 4-point Hall/resistivity system using the VdP method described in section 3.2.4. The sample temperature is controlled using a THMS600 Linkam stage working in N_2 atmosphere. The current is supplied using a Keithley 220 programmable current source and measured using a Keithley 485 picoamper-meter. Each of the four contacts is connected to a very high input impedance Keithley 6514 electrometer. The voltage difference between each of the two electrometers is measured using a Keithley 2000 multimeter. The current source, electrometers, multimeter and sample contacts are connected to a Keithley 7001 switch.

6.3 Conductive flexible substrate (3D-C/PI)

6.3.1 Electrical conductivity

Figure 6-1a shows the results of sheet resistance measurements performed on bare 3D-C (black squares) and 3D-C/PI composite film (red circles) at a temperature range from -160°C to +200°C. Both curves show the same behavior, with the maximum electrical sheet resistance of about 4.8 Ω/□ at -160°C, which decreases proportionally with rising temperature and reaches the minimum of about 3 Ω/□ at +200°C. These results indicate that the PI infiltration into 3D-C does not cause any parasitic effect on its intrinsic electrical conductivity. The average sheet resistance measured for 10 different 3D-C/PI samples of the same thickness (218 ± 22 μm) at room temperature is found to be 4.9 ± 1.16 Ω/□, which is a suitable value for electrically conducting flexible substrates.

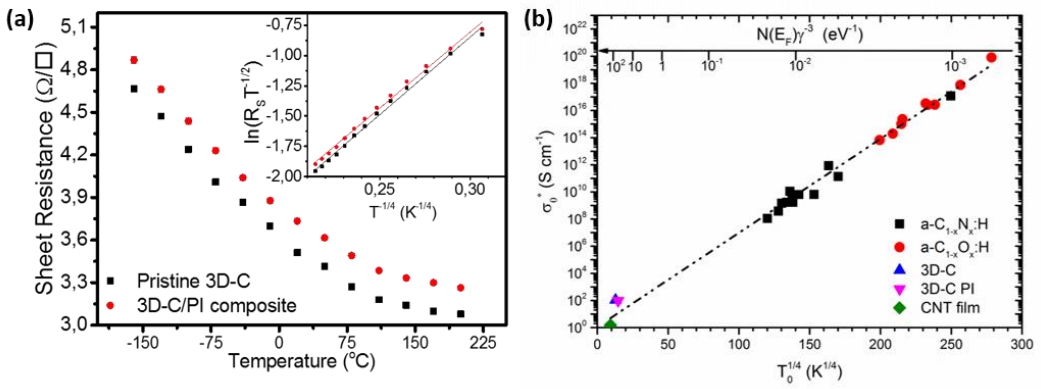

Figure 6-1. (a) Sheet resistance of bare 3D-C and 3D-C/PI at a temperature range of -160°C – 200°C (inset: fit of VRH model, that is ln(R $T^{-1/2}$) vs. $T^{-1/4}$ for both materials); **(b)** the values of the fitted parameters for Godet's band tail VRH model extracted from Figure 6-1 plotted (blue and pink triangles) alongside collected values of the same parameters for different a-C films by Godet et al.[300] (black squares and red circles) and a CNT-PI composite film[173]

In order to have a better understanding of the electrical conductivity behavior, the results have been fitted with several conduction behaviors. Both samples have been found to best fit the Variable Range Hopping (VRH) model by C. Godet,[301] as shown in the inset of Figure 6-1a.[302] The sheet resistance R_s (Ω/□) follows a VRH behavior due to carriers hopping between energy levels within band-tails, described by [301]

$$\boldsymbol{R_s(T) = R_{00}\, T^{\frac{1}{2}} exp\left(\left(\frac{T_0}{T}\right)^{\frac{1}{1+d}}\right)} \qquad (6\text{-}1)$$

where R_{00} is the band tail's resistivity pre-factor, T_0 (K) is the temperature coefficient that contains the hopping parameters, i.e. the density of states and the localization length of the wave-function and d is the hopping space dimensionality. The results fit the VRH model with a $T^{-1/4}$ temperature dependence, d = 3. This indicates a 3 dimensional electronic conductivity in both the bare 3D-C and 3D-C/PI samples.[303] The 3D VRH electronic transport mechanism suggests that the electrical conductivity in the 3D-C skeleton involves carriers hopping between energy levels within band-tails located at the graphene sheets grain boundaries. Similar electrical conduction behavior have been

reported by both C. Godet et al. and Q. Li et al. for CNT bundles, CNT fibers and other carbon based materials.[301, 304]

The temperature-dependence of the films sheet resistivity is compared with other carbon materials according to the VRH model. The prefactor σ_0* and slope $T_0^{1/4}$ are extracted according to equation (6-2), which is the conductivity-equivalent description of equation (6-1): [300]

$$\boldsymbol{\sigma(T) = \sigma_0^* T^{-\frac{1}{2}} \exp\left(-\left(\frac{T_0}{T}\right)^{\frac{1}{4}}\right)} \quad (6\text{-}2)$$

where, σ is related to the conductivity (S cm^{-1}) of the samples. Figure 6-1b shows the extracted prefactor and slope for the pristine 3D-C sample and 3D-C/PI film alongside the previously reported different amorphous carbon films[300, 303] and a sheet composed of bundled CNTs.[173] As clearly seen, the extracted values of prefactor and slope agree well with the previously reported trend for amorphous carbon films (dashed line), as expected from carbon-based materials. The extracted values of the 3D-C/PI film are similar to those of the bare 3D-C sheet, suggesting that the original conductivity mechanism of the 3D-C is preserved after the PI infiltration. In addition, the value of the localization parameter (LP) $N(E_F)\gamma^{-3}$ is calculated according to equation (6-3): [300]

$$\boldsymbol{N(E_F)\gamma^{-3}T_0 = 310} \quad (6\text{-}3)$$

where $N(E_F)$ is the density of states near the Fermi level, $1/\gamma$ is the decay length of the electronic wave function and $T_0^{1/4}$ is the slope extracted from equation (2). The values calculated for the LP in the case of 3D-C and 3D-C/PI are 126 eV^{-1} and 76 eV^{-1}, correspondingly. These large values of LP ($N(E_F)\gamma^{-3} >> 10^{-5}$) indicate a very weak electronic localization.[300] This is expected for a material composed of graphene layers, in which the electrical conductivity is weakly affected by phonon scattering.

6.3.2 Mechanical flexibility

For flexible electronics, the polymeric substrate is required to withstand bending cycles and stretching. It must be guaranteed that the material will preserve its thermal, electrical and mechanical properties over a period of standard life-time of electronics while undergoing bending and stress. In order to account for this, electrical conductivity measurements are carried out after repeated bending cycles. A bending diameter of 3.4 mm results in a strain of 17.6% at the 3D-C/PI composite's outer layer as calculated by Formula 6-4.[173]

$$\boldsymbol{\varepsilon_f = \frac{6Dd}{L^2} \times 100} \qquad (6\text{-}4)$$

where ε_f is the strain at the outer surface (%), D is the maximum deflection at the center of the sample (mm), d is the sample's thickness (mm) and L is the sample's span (mm). This bending diameter, far beyond the usual stress applied typically, was chosen in order to accelerate possible effects on performance. The bending cycle is depicted in the inset of Figure 6-2, which shows the schematics of the film in its straightened state and when it is rolled around a 3.4 mm ceramic cylinder. The change in the sheet resistance of the 3D-C/PI film was monitored throughout 260 bending cycles. The results are shown in Figure 6-2. The sheet resistance increased from 5.9 Ω/□ to 9.37 Ω/□ and no obvious breaking or cracking was observed throughout the cycles. The small increment in the sheet resistance is due to the less elastic structure of 3D-C, which, as a result from bending, slightly disintegrates within the PI matrix. Nevertheless, despite the defects caused by the bending of 260 cycles, the sheet resistance of the 3D-C/PI still remains relatively low, compared to other composites with similar filling fractions without bending stress.[305, 306]

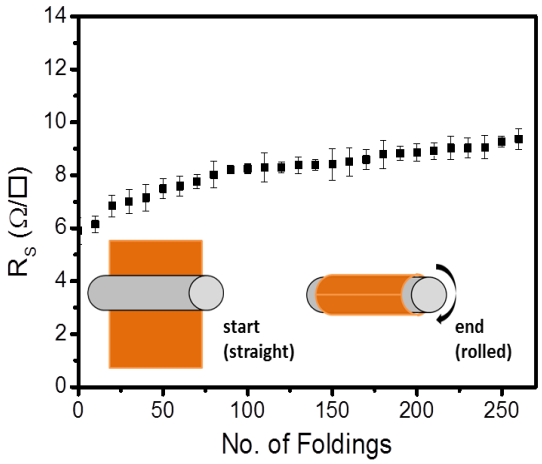

Figure 6-2. Sheet resistance of the composite film for 260 bending cycles (inset shows the start state and end state of the film at a bending cycle)

6.3.3 Thermal performance

Figure 6-3 shows the thermal conductivity results of 3D-C/PI (red, top line) and bare PI (blue, bottom line) over a temperature range of 0 – 200°C, to account for the different operating temperature ranges of electronics.[271] It can be seen that the bare PI has a thermal conductivity of 0.15 $Wm^{-1}K^{-1}$ at room temperature and remains stable at elevated temperatures. With the infusion of 3D-C, the thermal conductivity increased to 1.7 $Wm^{-1}K^{-1}$ at room temperature, more than 1 order of magnitude higher than bare PI and remains stable throughout the temperature range (within the error deviations of ± 0.18 $Wm^{-1}K^{-1}$). The results are in good agreement with previous measurement for bare 3D-C.[20, 119]

For comparison, Table 6-1 tabulates the thermal conductivity enhancement of PI with 3D-C and compares it with other reported fillers, such as graphene,[307, 308] carbon nanotubes[309] and other metal particles.[310-313] For PI, the highest reported thermal conductivity was achieved with 45 vol% of silver particles, yielding 15 $Wm^{-1}K^{-1}$.[310] Taking into consideration that the result obtained here with 3D-C is only through a 0.3

vol% filling fraction, and in order to have a better comparison, the average improvement of the thermal conductivity per filling fraction of various fillers are also presented in the table. For 3D-C/PI, the thermal conductivity improvement per 0.1 wt% (0.1 vol%) is 0.443 (0.5167) times, while for the same wt%, multi-walled carbon nanotubes (MWCNTs) only has an improvement of 0.0023 per 0.1 wt%. Other higher values achieved are 0.033 for 0.1 vol% of silver particles and 0.022 for 0.1 wt% of a three-dimensional hybridized SiC nanowires on graphene.[308]

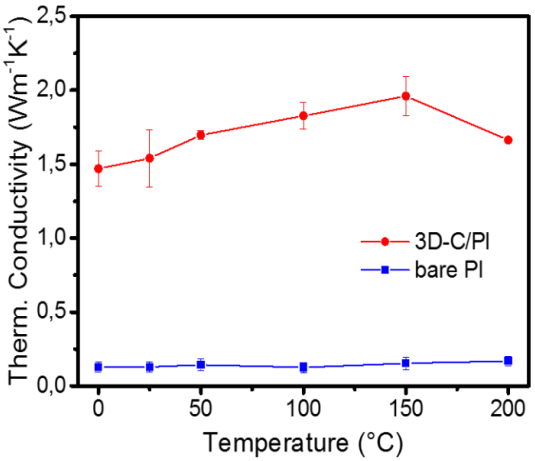

Figure 6-3. Thermal conductivity characterization at a temperature range of 0°C – 200°C for 3D-C/PI film and bare PI

The high efficiency of 3D-C as thermal filler for polymer is due to its interconnected structure. This interconnected structure allows heat to be conducted seamlessly across the entire composite without experiencing any thermal boundary resistance caused by the polymer matrix. This is in contrast to other nanofillers that despite their high intrinsic thermal conductivities, their contribution to thermal conductivity enhancement of the composite is quite poor since they are usually embedded completely within the polymer matrix, resulting in a discontinued path for long range thermal conduction. Therefore, 3D-C achieves better thermal performance, with minimum filling factor.

Table 6-1. Comparison of the thermal conductivity of filler-PI composite film

	Filling Factor		Thermal Conductivity [W $m^{-1}K^{-1}$]		Normalized increase per 0.1% filling factor[a]		Ref.
	wt%	vol%	Bare PI	Filled PI	wt%	vol%	
SiC	7		0.25	0.577	0.0047		307
nanowires on graphene	11		0.25	2.63	0.022		308
MWCNTs	3		0.18	0.25	0.0023		309
BN-c-MWCNTs	3		0.18	0.38	0.0067		309
Silver particles		45	0.2	15		0.033	310
BN	30		0.18	1.2	0.0034		311
Aluminum nitride		30	0.22	0.6		0.0013	312
Nanoparticles		10	0.26	0.32		0.0006	313
3D-C	**0.35**	**0.3**	**0.15**	**1.7**	**0.443**	**0.5167**	**this work**

[a] Calculated as: $\frac{k_{filled\ PI}-k_{bare\ PI}}{\%\ filling\ factor}/10$

Even further improvement is achievable by using better molds, as mentioned in 4.5.3. This way, a thermal conductivity in the range of 6 $Wm^{-1}K^{-1}$ is achievable.

6.3.4 Proof-of-concept

Both the stable thermal conductivity and demonstrated stable electrical conductivity mechanism throughout the tested temperature range has proven the film to be suitable to operate reliably throughout the different operating temperature ranges of electronics. In order to further demonstrate the applicability of the 3D-C/PI film as a conductive flexible substrate and to demonstrate its advantage over conventional films, test structures were deposited on both films. For this, conventional PI film and 3D-C/PI film were first coated with parylene (to avoid short circuits from the conductive 3D-C) and subsequently covered with thin lines of Ni/Au, as shown in Figure 6-4. Subsequently, a

current ramp was lead through the test structures while observing the generated heat under thermal camera.

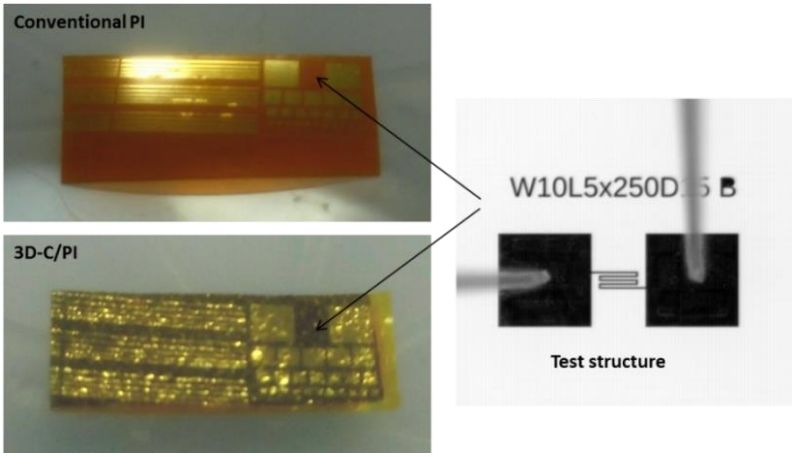

Figure 6-4. Optical images of the used test structures for 3D-C/PI

Figure 6-5 shows the thermal images of both samples at 1.1 V. Beyond this point, the conventional PI sample breaks down, which means the maximum current applicable on PI is of ~180 mA and the maximum power supported is of ~0.2 mW. By direct comparison of the two samples at this point, it can be clearly seen that the heat generation on the conventional PI is significantly higher than on the hybridized film (it reaches up to 180°C).

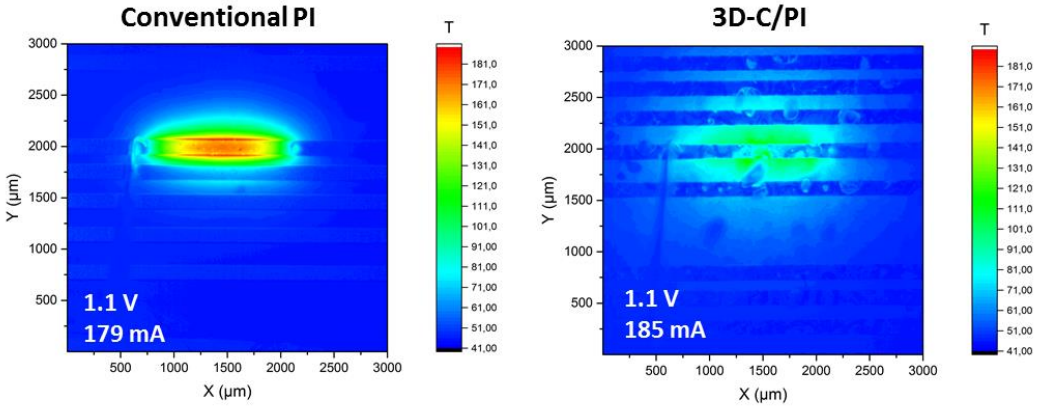

Figure 6-5. Thermal images of the test structures at 1.1 V

The current was further ramped up on the 3D-C/PI sample until reaching its breakdown. Figure 6-6 shows the obtained thermal image at maximum power. At this point, maximum temperatures of 140°C are reached on some spots. The 3D-C/PI helped to increase the maximum current applicable to ~216 mA, which means a maximum power of ~0.3 mW, corresponding to a 50% improvement.

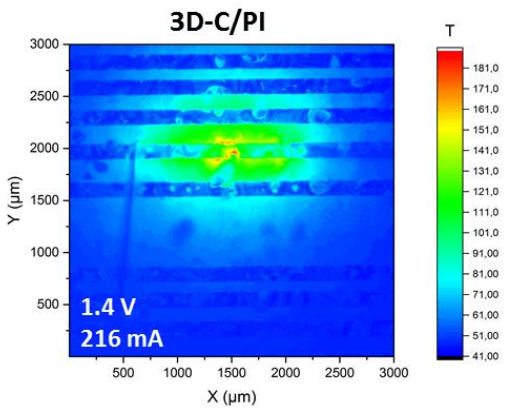

Figure 6-6. Thermal image of the test structure on 3D-C/PI at 1.4 V

It must be noted that the thickness varied between samples (125 µm PI and 160 µm 3D-C/PI), as well as the roughness, which means after further process improvement, 3D-C/PI could even further improve performance.

6.4 Insulating flexible substrate (3D-BN/PI)

The correct choice of insulating filler material for the electrically insulating case is more restricted than for the electrically conducting case, since, besides the intrinsic thermal conductivity of the filler material and the amount of filling required (high filler loading can lead to a decrease of mechanical properties[192]), also the dielectric constant plays a very important role. If the dielectric properties of the PI and the filler differ too much, electric field distortion could occur.

Typical nanomaterials of choice for electrically insulating filler needs are listed in Table 6-2. Among these nanofillers, BN was found to be very suitable filler for highly conductive composites and ideal for electronic packaging application.[192, 220] It has high thermal conductivity, high electrical resistivity, low dielectric constant (matching to that of PI), high temperature resistance and low density.

Table 6-2. Typical filler materials for electrically insulating needs

Filler-type	Remarks	Ref.
Al_2O_3	4.3 W/mK at 60 vol% in epoxy, high dielectric constant	314
SiO_2	Low thermal conductivity at 55-70 vol% in epoxy	315, 316
ZnO	High dielectric constant	317
BeO	High toxicity and cost	192
AlN	11.5 and 11.0 W/mK at 60 vol% in PVF and epoxy, low oxidation resistance and high dielectric constant	318
Si_3N_4	Moderate thermal conductivity	319
SiC	High saturated carrier drift velocity, high dielectric constant	320
GO	4-fold thermal conductivity increase at 5wt% in epoxy, easy to get reduced via low-temperature thermal treatment (which turns it to electrically conducting graphene)	321
Diamond	4.1 W/mK at 68 vol% in epoxy, high cost, no superiority	322
$BaTiO_3$	300% increase of thermal conductivity at 50 wt% in EVA, low thermal conductivity, very high dielectric constant, high density	323
BN	**Found very suitable for filler material with high thermal conductivity**	192

6.4.1 Electrical conductivity

VdP measurement on the film revealed an electrical resistivity of ~1.3 GΩcm, which corresponds to a very insulating sample (for reference, bare PI is ~1.5 GΩcm, which is in the same range as 3D-BN/PI).

6.4.2 Mechanical flexibility

In order to verify the flexibility of the composite PI, a qualitative study was carried out via repetitive bending of the polymer. Figure 6-7 shows an example of such bending. It can be seen that no damage was caused to the PI's initial flexibility. The 3D-BN/PI film can be bent several times without breaking (here shown after 50 times rolling).

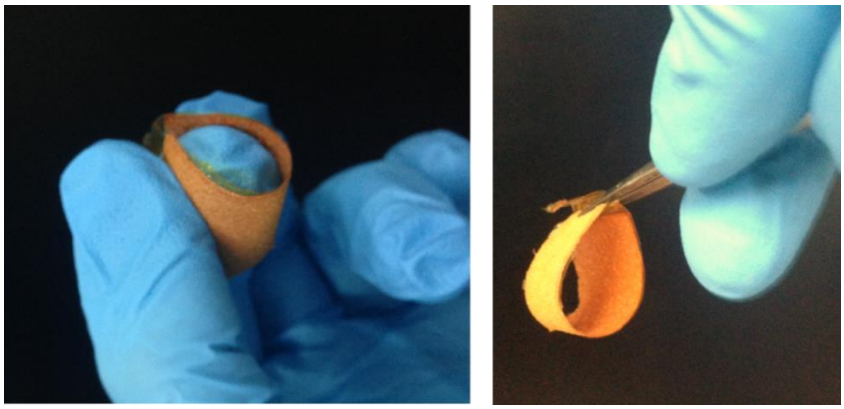

Figure 6-7. Demonstration of the flexibility of the 3D-BN/PI film

6.4.3 Thermal performance

Prior to optimization of the mold, the film achieves a thermal conductivity of 1.3 – 1.4 $Wm^{-1}K^{-1}$. Results after optimization are shown in Figure 6-8, which clearly highlights the extreme increase in thermal conductivity obtained. For reference, the typical thermal conductivity of pure PI is demarcated (0.2 $Wm^{-1}K^{-1}$). The thermal conductivity of hybridized PI with merely a filling fraction of 0.3 vol% (0.35 wt%) of 3D-BN is in the order of 5 W $m^{-1}K^{-1}$ throughout the temperature range, which corresponds to a 25-fold increase. For comparison, other achieved thermal conductivity results of BN-filled PI are shown in Table 6-3. It can be seen that all of them require high filling fractions. This is due to the loss of interconnection of those fillers, such that high loading fractions are necessary in order to obtain a continuous thermal transport

path throughout the PI.[216] This can lead to loss of the PI's mechanical properties, and increases the probability of breaking during bending cycles.

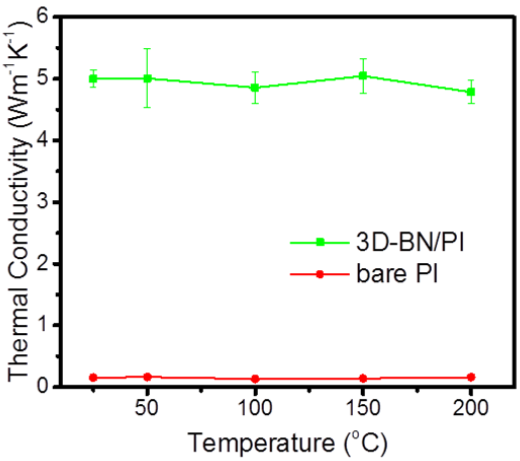

Figure 6-8. Laser Flash thermal conductivity result of 3D-BN/PI

Table 6-3. Comparison of the thermal conductivity of various reported filler-PI composite film

Filler-type	Filling Fraction wol%	wt%	Thermal conductivity [W/mK]	Ref.
h-BN particles	60		7	220
Surface modified BN nanosheets		30	1.2	311, 324
Titanate coupled BN nanosheets		50	0.86	325
Titanate coupled BN nanosheets + graphene		50+1	2.1	326
3D-BN	**0.3**	**0.35**	**5**	**This work**

[a] Through-plane (z-direction)

Similar to its 3D-C counterpart, the robustness of the film at high temperature was tested. For this, TGA was performed in dry air environment, and the obtained mass loss curve is shown in Figure 6-9. The point of 5% mass loss (i.e. the point up to which the material remains stable) is measured to be at ~520°C, which is in agreement to obtained values of pure PI.[327]

To corroborate 3D-BN/PI's stability up to ca. 500°C, its electrical conductivity was measured after heating the sample up to 500°C for one hour. The film remained stable with $\rho \approx 1.3$ GΩcm.

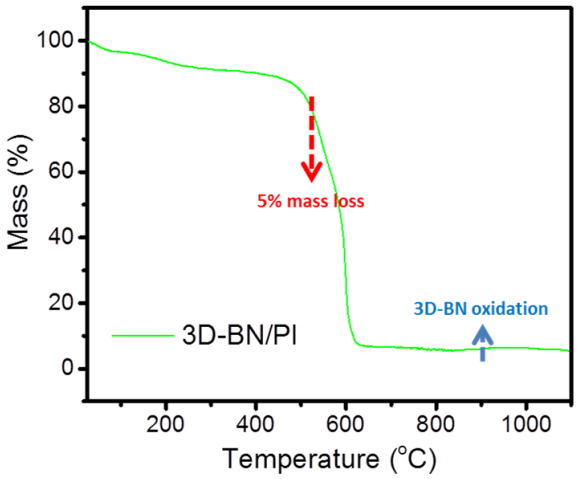

Figure 6-9. TGA thermal stability of 3D-BN/PI

6.4.4 Proof-of-concept

In order to demonstrate its direct applicability as a flexible substrate, an electronic resistor structure was printed using ink jet printing with silver ink. Contrasting to conventional PI film,[328] the 3D-BN/PI film did not require any prior surface modification in order to obtain good adhesion of the ink onto the surface. Figure 6-10 shows the obtained structure on 3D-BN/PI.

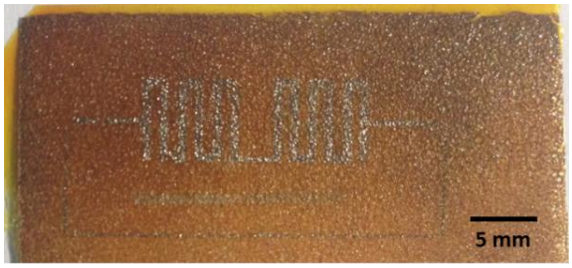

Figure 6-10. Printed electronic resistor on 3D-BN/PI film

In a last step, to demonstrate the improved heat spreading capability of 3D-BN/PI film over conventional PI, a hot spot of 60 °C was created in the center of a 2 cm x 3 cm film of bare PI and hybridized PI of same thickness. The evolution of temperature was observed under thermal camera. Figure 6-11 shows the obtained thermal images after 5 minutes of constant contact with the heat source. It can be clearly seen that for the case of conventional PI, the heat remains confined within its point of generation even after 5 minutes of constant contact with the external heat source. Contrastingly, the 3D-BN/PI film is able to spread the heat along the entire film, in a radial pattern centered towards the hot spot. It must be noted that this was already observable after short exposure to the heat source.

This spread is important, since 1) confined heat in single spots can lead to stress within the sample and thermal management issues,[293] and 2) this will allow fast propagation of heat along the film, thus efficient extraction of unwanted heat towards cooling sections in flexible electronic application.

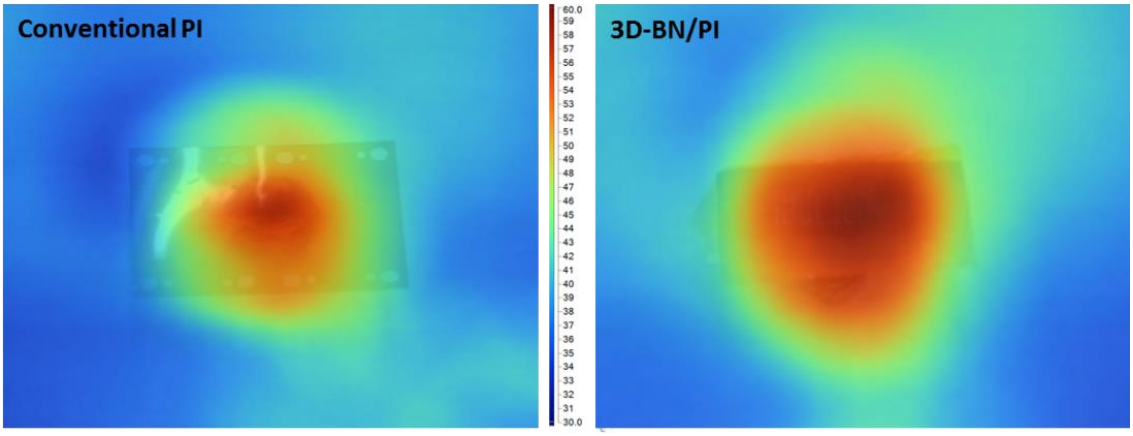

Figure 6-11. Thermal images of the heat spreading capabilities of conventional PI and 3D-BN/PI

6.5 Summary

This chapter demonstrated the applicability of the new 3D-foam/PI films for flexible electronics. Via using 3D-C, an electrically conducting substrate was achieved, while 3D-BN is applicable for dielectric needs. Instead of the typical dis-conjoined fillers, an intrinsically interconnected network of 3D-foam within the PI was obtained. This approach preserves the properties of the foam, while greatly enhancing the PIs electrical and thermal properties, while also keeping flexibility and mechanical strength of the PI.

The proof-of-concept experiments have demonstrated the readiness of the films to directly replace existing polymer films (i.e. printing techniques were compatible to surface roughness and chemical composition). Due to the achieved increase in thermal conductivity, significant improvement in heat spreading capability was demonstrated which led to an increase of applicable power of at least 50%.

7 Application as space blanket

7.1 Introduction

Thanks to its excellent radiation and chemical resistance as well as its thermal stability,[329] PIs (i.e. Kapton®) are also among the few polymers that are space qualified[330-333] and are used in thermal control blankets (multilayer insulator, MLI) for satellites and space exploration mission.[333-335] These blankets are necessary to protect the space vehicle from the harsh space environment (it is noteworthy to mention, that among all the failure modes of the spacecraft, approximately 25% are related to interactions with the space environment).[336]

The different environments in space are namely five: the vacuum, the neutral, the plasma, the radiation and the micrometeoroid/orbital debris (MMOD) environment.[337] In this Thesis, the focus is on LEO (low earth orbit, at 200 – 700 km altitude) and GEO (geosynchronous orbit, at 35800 km altitude) as these are the orbits where most satellites are launched to. In these orbits, exposed materials are constantly suffering degradation from atomic oxygen (AO) (LEO altitudes only),[338] ultraviolet (UV) and ionizing radiation, ultrahigh vacuum (UHV), thermal cycles (±100°C every 90 min.) and impacts from hypervelocity micrometeoroids and orbital debris.[339-342] In particular, AO exposure and radiation effects are known to have a highly reactive nature and cause unwanted chemical interactions. These lead to oxidation, erosion, degradation of materials properties (i.e. mass loss) and are among the greatest concerns for long-term missions.

Despite PI's advantages, its dielectric nature is still a problem in its direct implementation in the outer layer of space thermal blanket. This issue is due to electrostatic discharge (ESD) in some LEO and mostly GEO orbits. ESD is a

consequence of the difference in surface conductivity between conductors and dielectrics, leading to potential charge differences in the presence of plasma. This charging effect would create serious issues ranging from damage to onboard electronic systems[337, 343] long-term degradation of the exterior surfaces coatings, enhance contamination of surfaces,[344] or lead to material damage. In addition, similarly to other polymeric materials, PI films significantly erode under exposure to AO.[345, 346] An electrically-conductive and AO-resistant indium tin oxide (ITO) coating is commonly deposited on the external surfaces of PI films to attain ESD and AO durability for thermal blanket applications.[334] However, such coatings are prone to crack, and they cannot tolerate folding or bending even at small radii.[347] Mechanical robustness tests on ITO-coated films have resulted in immediate fracture of the coating upon bending and thus to loss of sheet conductivity.[348] In addition, micrometeoroid or debris impacts in LEO may compromise the coatings. An opening in a coating allows AO to attack the substrate and undercut the coating, thereby creating an ever-growing region of erosion.[349, 350] Another way to mitigate the PI's ESD problem, while preserving its flexibility, is by adding conductive (electrical/thermal) nanomaterial such as graphene,[260, 296, 351, 352] carbon nanotubes[298, 306, 353] and metallic nanoparticles[299] as nanofillers into it. Nevertheless, there are other considerable challenges, such as the inhomogeneous distribution of these nanofillers, aggregation and limited filling fraction due to the effect on the structural integrity of the polymer matrix, such as curling, bending, displacement, cracking and delamination that usually arises with the incorporation of fillers.[170, 182, 354]

Here, 3D-C/PI composite is applied to demonstrate its applicability to replace current MLI outer layers, as schematized in Figure 7-1.

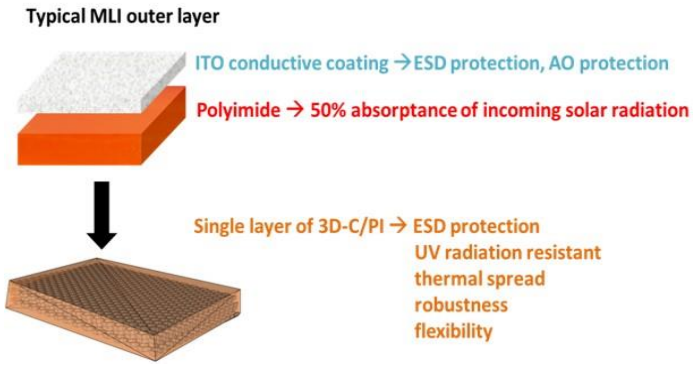

Figure 7-1. Schematic of the 3D-C/PI film to be used as the outer layer of the space protection blanket (multi-layer insulation, MLI)

7.2 Material preparation and characterization

Preparation of samples for this application uses 3D-C foams and the infusion with PI polymer as described in section 4.5.3. The material is characterized according to strict requirements for space environment, which includes thermal cycling, thermo-optical characteristics and exposure to space environment specific environments (Gamma ray and AO exposure and outgassing). To quantify the effect of some of these environments on the film, electrical measurements before and after exposure are carried out, for which the same setup described in 6.2.1 is used.

7.2.1 Thermo-optical characteristics

The thermo-optical characteristics of the films, α_s and ε, are measured at room temperature by an IR/solar reflectometer (TESA 2000, AZ technologies) using an integrating sphere.

7.2.2 Gamma ray exposure

The 3D-C/PI film is exposed to approximately 10 mega Gy (0.1 giga rad). This is equivalent to 15 years in space (GEO orbit electron radiation dose).[336] The exposure to

gamma rays (cobalt 60 source spectral peaks at 1.33 Mev and 1.17 Mev) is conducted at room temperature in atmospheric pressure. This measurement simulates ionizing radiation in GEO space environment, which is dominated by electrons and lower flux of solar protons, with typical total irradiation doses of 0.7 MGy/yr.

7.2.3 AO exposure

The AO source is a RF plasma source (Litmas RPS 1.5-3kW, 1.7-3MHz)[355] connected to a small vacuum chamber in 90º angle, with a sample holder located down the pumping stream. Oxygen (99.999%) is fed to the RF plasma source using a mass flow controller in order to create the oxygen plasma. A PI film is used as reference sample in order to determine the AO fluence in each exposure. The mass loss of the samples is measured using a micro-balance, (Sartorius SE2 readability of 0.1 μg).

7.2.4 Outgassing

The outgassing tests are performed according to a standard test method, ECSS-Q-70-02A (from 26th of May 2000)[356] to approve the composite films as low-outgassing materials for vacuum environment. Samples are held for 24 hours at a temperature of 125 °C and pressure of less than 1×10^{-5} Torr. The mass loss of the specimen itself without the water volatile is denoted as the recovered mass loss (RML, wt%). During the outgassing test, a collecting plate is held at 25 °C to measure the amount of collected volatile condensable material (CVCM, wt%). Mass gain/loss is measured by micro-balance (Sartorius SE2 readability of 0.1 μg).

7.3 Thermo-Optical properties for space

The MLI acts as a radiation barrier to control heat flow to and from the satellite. The MLI is typically composed of multiple (up to 30) layers of thin polymer films (PI or

Mylar, about 25 µm thick) with vapor-deposited metal on one or both sides.[334] Typically, each metal reflector reflects between 90 to 97% of the impingent radiation. The cumulative effect is that of a nearly 100% radiation insulation. Since the MLI is attached to the spacecraft's skeleton with adhesives and connectors that may be damaged due to heat, over-heating of the MLI's outer layer must be strictly avoided. To evaluate materials for this purpose, their equilibrium temperature, T(K) in space must be calculated according to their thermo-optical properties. As radiation is the dominant mechanism for heat transfer in a vacuum environment, the relevant thermo-optical properties are the heat absorbed from the sun, with respect to the solar absorptance, α_s, and the heat radiated to the material's surroundings according to its emittance, ε. The equilibrium temperature can be thus calculated by [337]

$$T = \left(\frac{\alpha_s}{\varepsilon}\right)^{1/4} \left(\frac{SA_n}{\sigma A}\right)^{1/4} \tag{7-1}$$

where S (W/m^2) is the solar flux per unit area at the relevant orbit, A_n (m^2) is the film's surface area normal to the solar flux, A (m^2) is the material's total surface area, and σ (5.67 10^{-8} Wm^{-2}K^{-4}) is the Stefan-Boltzmann constant. With this, it is evident that the use of conducting metal as a coating for ESD protection of the MLI's outer layer is prohibited since metals in space would heat up to T = 500K = 230ºC due to an α/ε ratio as high as 10.[337]

For 3D-C/PI, the calculation was related to samples with sphere geometry (normal area factor of A_n/A=0.25)[357] and a solar flux of 1366.1 Wm^{-2}, which is the average flux value at 1 AU from the sun.[358] The thermo-optical characteristics of the films, α_s and ε, are measured at room temperature by an IR/solar reflectometer using an integrating sphere and are shown in Table 7-1, along with reference values for pure PI (commercial

Kapton®).[337] The composite films demonstrated an increase in α_s by a factor of 2 compared to that of pure PI. This phenomenon has been reported before for previously studied carbon-based composites for space applications.[173, 359, 360]

Table 7-1. Thermo-optical properties of pure PI (i.e. Kapton®) and 3D-C/PI films

Sample	α_s	ε	α_s/ε	T_{max} (°C)
3D-C/PI	0.91	0.79	1.15	15.49
Kapton® [337]	0.48	0.81	0.59	-28.8

According to equation (7-1), the rise of the carbon-based composites' α_s involves an increase in their operating temperatures in space compared to that of pure PI. The maximum temperatures that the 3D-C-PI films are expected to experience in space are calculated to be 15.49°C, compatible with outer-layer thermal blanket applications.

7.4 Electrical conductivity for ESD mitigation

Spacecraft charging occurs due to the build-up of charge on exposed external surfaces, especially in the GEO environment. A spacecraft that is subjected to a space plasma may be charged to high electrical potentials.[337] Because of differences in surface conductivity, conductors and dielectrics will be charged to different potentials in the presence of plasma. If the potential difference is high enough, a breakdown threshold is exceeded and an ESD between the surfaces may occur. The transient generated by this discharge can couple into the spacecraft electronics and cause upsets ranging from logic switching to complete system failure. Discharges can also cause long-term degradation of exterior surfaces coatings and enhance contamination of surfaces.[344]

The anti-static criterion to dissipate electrostatic charge build-up requires surface resistivity in the range of $10^4 – 10^{10}$ Ω/□,[361] which is well above the sheet resistance measured for the 3D-C/PI composite samples of 3 – 4 Ω/□ (section 6.3.1). In addition, unlike the electrical conductivity of the ITO coating, the conductivity of the 3D-C/PI film has been shown to be resilient under bending, as demonstrated in section 6.3.2. Moreover, the entire bulk of the 3D-C/PI film is conductive and not just on the surface. This makes the electrical conductivity of the film durable to damage to the films surface, in contrast to the sensitive ITO surface coating.

7.5 Thermal cycling

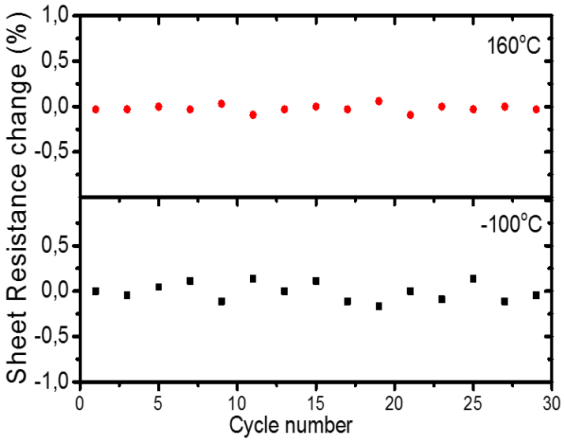

Figure 7-2. Measurement of the change in sheet resistance after thermal cycling

To investigate the resilience of 3D-C/PI towards thermal stress, electrical conductivity measurements were carried out under repeated heating and cooling cycles. The temperature range is chosen according to requirements for vehicles in space. The change in sheet resistance (in %) for 30 repetitions is measured and the results are shown in Figure 7-2. The upper graph (denoted with red dots) shows the change in the sheet resistance measured at 160°C, while the lower graph (denoted with black squares) is the measured changes at -100°C (measured at every two periods). From both of these results,

there is no obvious change in the sheet resistance after 30 thermal cycles with minor fluctuation in the range of +/-0.09%. This shows that the thermal cycling does not have any effect on the electrical conductivity of the 3D-C/PI, which is due to the relatively high thermal stability of the 3D-C network.

7.6 Space qualification

To ensure the PI infiltration into 3D-C does not affect its performance for space applications, accelerated space environment reliability studies of the 3D-C/PI composite are conducted with ground-based space simulation systems, consisting of Gamma ray and AO exposure at different doses, as well as outgassing tests according to European space standards.[362] The changes in electrical behavior are monitored and the structural changes of the material before and after the exposures studied with SEM.[363] The durability of these PI-based composites is not expected to be affected by solar vacuum ultraviolet (VUV) radiation, as the similar polyimide, Kapton®, has been shown to be insensitive to VUV radiation.[364]

7.6.1 Gamma Ray exposure

The exposure to ionizing particle radiation is simulated by exposing the 3D-C/PI film to approximately 10 mega Gy (0.1 giga rad) of gamma radiation (^{60}Co source). This dose is equivalent to 15 years in space (GEO orbit electron radiation dose).[361] The change of temperature-dependent sheet resistance as a result from the gamma ray exposure is shown in Figure 7-3. All of the three curves show the same temperature-dependent sheet resistance characteristic, having its maximum of 5 Ω/□ at -160°C and minimum of 3 Ω/□ at +200°C. No change in the film conductivity and no visible degradation in the film is observed. These observations show that the 3D-C/PI composite is capable of surviving the high doses in GEO.

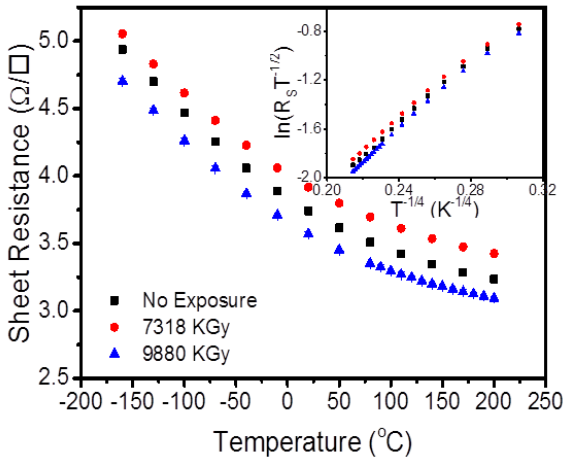

Figure 7-3. Electrical properties after gamma-ray exposure for the 3D-C/PI film at different doses and the measurement of the electrical conductivity at a temperature range of -160°C – 200°C (inset shows the fit of VRH for all three samples)

To further demonstrate that Gamma ray exposure has no effect on the films performance, the films sheet resistance is monitored after thermal cycling and fit with the VRH behavior. The inset of Figure 7-3 shows that the transport mechanism of all the three films remains unchanged after exposure.

7.6.2 AO exposure

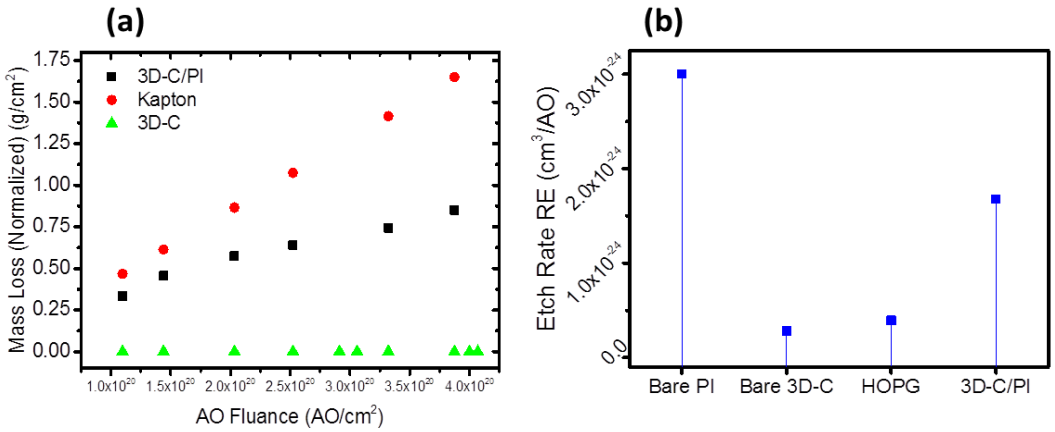

Figure 7-4. (a) Mass loss as a result of AO exposure of the 3D-C/PI, bare PI film, and bare 3D-C at high fluences (4.3×10^{20} AO cm^{-2}, equivalent to 8 months at 500 km LEO altitude; **(b)** comparison of etching rates

Interaction of AO with the spacecraft surfaces can degrade materials, especially organic hydrocarbons and polymers,[20, 21] through either oxidation and erosion (etching). In the case of hydrocarbons, the AO resultant products, such as CO, CO_2, H_2O, and others, are volatile and evaporate from the surface, thereby exposing the interior materials for further reaction with AO. For AO exposure study, bare 3D-C, 3D-C/PI film, and a reference PI film are exposed to AO fluences of up to 4.3×10^{20} AO cm^{-2}, equivalent to about 8 months at a LEO altitude of 500 km,[338] and their mass loss values versus AO fluence are shown in Figure 7-4a.

From the slope of the curves it can be seen that the 3D-C/PI film etch rate is about half of that of bare PI film. It can also be seen that the 3D-C/PI film curve shows two different regions of behavior, whereby the first two dots have a similar slope as the bare PI film, and the next dots show a linear behavior with a lower slope. This is due to the fact that at the beginning the top layer of the film is etched, which has a higher PI to 3D-C ratio (PI rich layer). Subsequently more 3D-C is exposed, which lowers the total etch ratio. From these measured mass loss curves, the reaction efficiency can be calculated using the mass loss of a sample having surface area dA (cm^2) exposed to duration dt (s) as follows: [366]

$$\boldsymbol{dm = \rho R_e \phi dA dt} \tag{7-2}$$

where ρ (g cm^{-3}) is the density of the material, ϕ (atoms $cm^{-2}s^{-1}$) is the AO flux, and R_e (cm^3atom^{-1}) is the material's reaction efficiency. Figure 7-4b shows the etch rates calculated from the mass loss curves for bare PI, 3D-C and 3D-C/PI, derived from the results of Figure 7-4a, together with that of HOPG.[355] It can be observed that both 3D-C and HOPG possess reaction efficiencies in a similar range of 4×10^{-25} cm^3/AO, while that of 3D-C/PI improved by two times over the bare PI film (ca. 1.6×10^{-24} and 3×10^{-24}

cm^3/AO, respectively). It must be noted though, while a two-fold improvement has been achieved for an exposure equivalent to 8 months, the total mission duration typically comprises 4 – 10 years, for which the 3D-C/PI films would require further improvement in etch rate.

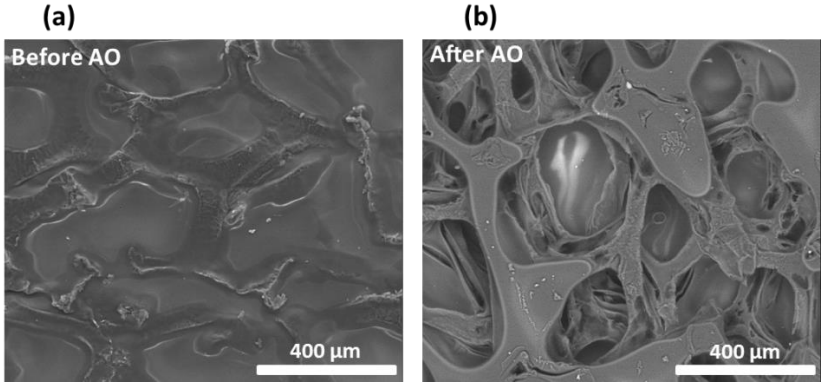

Figure 7-5. (a) and **(b)** SEM image of the surface of the nanocomposite film before and after the AO exposure, respectively

In order to have a better understanding on the behavior of the 3D-C/PI film when exposed to AO, SEM images are taken at the surface before and after the exposure and are shown in Figure 7-5a and Figure 7-5b, respectively. Before the AO exposure, the 3D-C structure is fully infused with PI and only the top-layer of 3D-C can be differentiated from the background. Contrastingly, for the sample after AO exposure, most of the PI at the top surface was etched and revealed more of the 3D-C structures (several layers of 3D-C can be seen). This is in agreement with the lower reaction efficiency calculated for the 3D-C compared to PI. The low R_e for 3D-C is attributed to the extremely strong bonding of the C-atoms within its structure. Polymers on the other side are more susceptible to AO oxidation and erosion effects, resulting in chemical rupture of bonds which leads to byproducts such as CO, CO_2, H_2O. It has been reported that under AO exposure, most polymers show loss of surface gloss and loss of weight together with degradation of mechanical and physical properties.[365]

7.6.3 Outgassing

Outgassing is the release of molecules that were either contained or absorbed by the material. Low outgassing is important to prevent the possible release of molecular contamination that can affect the sensitive neighboring surfaces (such as mirrors and detectors in satellites) and in extreme cases, causes a transformation to its chemical structure, uniformity, volume and/or density. The low-outgassing criterion requires RML of less than 1 % and CVCM lower than 0.1 %. The outgassing parameters obtained for 3D-C/PI are RML = 0.30% and CVCM = 0.06%, these values are close to those of bare PI,[367] well satisfying the outgassing criterion. This shows that the infusion of 3D-C does not change the nature of PI and the composite is acceptable for space deployment.

7.7 Summary

In this chapter, the applicability of 3D-C/PI composite film for space blanket application has been demonstrated. It was shown that it has suitable thermo-optical properties, electrical sheet resistance, as well as robustness against thermal cycling. In addition, simulated space environment exposure test results have shown that gamma radiation has no effect on the composite's electrical conductivity and its outgassing properties are still within the standards of the European Cooperation for Space Standard (ECSS). Further, exposure to AO fluence, revealed that the composite 3D-C/PI film is roughly two times more resistant to etching than bare PI due to the low reaction efficiency of the 3D-C skeleton. The results indicate the films suitability for GEO environments where no exposure to AO is expected; further advancement such as the incorporation of organic/inorganic molecules into the PI solution[359] may increase the AO resistance further for future LEO suitability as well.

8 Thermo-mechanical application

8.1 Introduction

Shape memory polymer (SMP) is a special type of polymer defined as a polymeric smart material that can alter its shape from a deformed shape (temporary shape) back to its original shape (permanent shape) induced by an external stimulus (trigger),[368-370] such as external heating,[371, 372] electro-activated,[373-378] light-induced,[372, 379-381] solution-responsive,[382-385] magnetic-responsive[386-389] and microwave-induced.[390] The advantages of SMPs include their low density, low cost, easy processing, and large recoverable strains.[369] Moreover, it is also light weighted and exhibits high recovery strain compared to similar shape memory performance substances, such as shape memory alloys (SMAs).[391-393] Today, SMP has been applied into many industries, such as in biomedical surgery,[394-398] smart fabrics/wearable technology[399, 400], automobile industry[401-403] and aerospace engineering,[404, 405] mostly because of its ease in shaping and low cost. However, SMPs still suffer from major drawbacks, such as low recovery stress/forces, long response time, low cycle life, and weak material stability.[369, 406] Additionally, similar to other polymers, SMP is a poor conductor for heat with low operational frequency and narrow bandwidth. This hinders its application for large area and raises high potential of cracking and damage to the structure due to non-uniformity of heat spread caused by its low thermal conductivity. In addition, bare SMP is electrical insulating in nature that further limits its potential in other applications for which electrical conduction is preferred. In order to address these issues, many have incorporated fillers (i.e. alumina, aluminum, brass, glass, graphite, magnesium oxide, stainless steel, calcium carbonate, acetylene black)[316] to enhance the properties of SMP, such as to increase the speed and stability of heat transmission and also the mechanical

properties. However, these fillers tend to agglomerate and bundle with one another through Van der Waals forces, causing challenges to acquire highly homogenously dispersed filler infused SMP. Aggravating to this, is the potential of shape memory loss caused by the filler itself and/or their agglomeration.[177]

In this chapter, the integration of 3D-foams into SMP and its effect on thermal conductivity, switching speed and performance, mechanical strength and energy required for transformation will be studied. In a next step, the implementation for large area and self-heating capability will be also explored. In addition, through the use of 3D-BNC, a self-heating capability is added to the SMP, whereby required BNC ratios can be easily tailored according to the design parameters determined by the application. With this and through precise patterning of the BNC positions, a timed actuation can be achieved, as well as render the SMP an internal heating mechanism.

8.2 Material preparation and characterization

The preparation for SMP samples uses all variations of 3D-BNC foams (including bare 3D-C and 3D-BN) and the infusion with polymer is carried out as described in section 4.5.4. Besides standard thermal and electrical measurements (sections 3.2.5.3 and 3.2.5.4), specific measurements to determine the shape memory performance are required. These are carried out through dynamic mechanical analysis (DMA, TA Instruments Q800 DMA), which measures strain, stress and displacement at given force, temperature and time. To quantitatively and qualitatively demonstrate the shape memory actuation, thermal camera imaging is used. For this, samples are connected to a Horizon Electronics DHR3653 (94 Watts) power supply which provides the current for the direct heating of the samples. The samples are imaged using a FLIR A320 IR thermographic camera.

8.3 3D-foam hybridization with SMP

Figure 8-1 shows the obtained hybridized structures along with their respective bare 3D-foam.

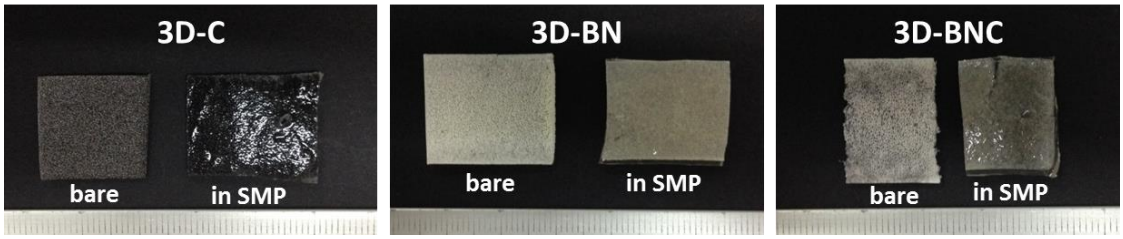

Figure 8-1. Optical images of the bare foams and SMP infused foams

8.3.1 Effect on thermal conductivity

The thermal conductivity of the hybrid films is measured at room temperature and above the glass transition temperature of the SMP at 60°C. The thermal conductivity of bare SMP is found to be 0.09 $Wm^{-1}K^{-1}$ and 0.103 $Wm^{-1}K^{-1}$, while the 3D-C/SMP is measured to be 0.361 $Wm^{-1}K^{-1}$ and 0.341 $Wm^{-1}K^{-1}$, which is a 4 to 3-times improvement over bare SMP. For 3D-BN/SMP, the thermal conductivity is measured to be 0.157 $Wm^{-1}K^{-1}$ and 0.145 $Wm^{-1}K^{-1}$, a ~1.5-times improvement, and for 3D-BNC/SMP (50:50), the thermal conductivity is measured to be 0.21 $Wm^{-1}K^{-1}$ and 0.17 $Wm^{-1}K^{-1}$, which is a 2.3 to 1.6-times improvement over bare SMP. The slightly higher results of 3D-C/SMP over 3D-BN/SMP and 3D-BNC/SMP are in agreement with the previously obtained results of their bare foam state.

8.3.2 Effect of electrical conductivity

The electrical conductivity of the 3D-foam/SMP hybrids can be controlled by precisely choosing the BN and C content. This enables the SMP to cater the whole spectrum: good electrical conductivity with a low sheet resistance of 40 $\Omega\square^{-1}$ is achieved

by using 3D-C, preserved complete insulating behavior of bare SMP with the addition of 3D-BN (63.9 T $\Omega\square^{-1}$), and a tunable conductivity is achieved with the incorporation of 3D-BNC (230 – 24580 $\Omega\square^{-1}$).

8.3.3 Effect on shape memory performance

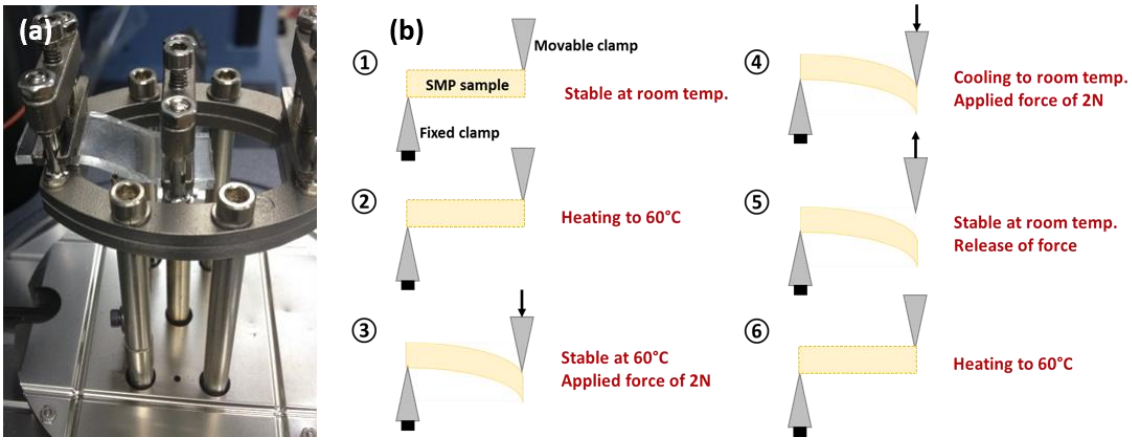

Figure 8-2. (a) Achieved DMA bending setup. Image taken for bare SMP sample, after applying 2 N in 60 °C environment; **(b)** schematics describing each step of the stress-strain test for SMP performance

Shape memory properties are assessed for the different stimuli through cyclic mechanical tests.[407] In this case, data is collected through DMA testing, which monitors the stress, strain and displacement while samples undergo temperature changes and force application. The test is repeated 4 times and 60°C is used as the switching temperature (above glass transition of all samples). The required force for inducing shape transformation is assessed prior to cyclic testing through a force ramp at 60°C inside the DMA. A final force of 2 N is chosen for all samples (Figure 8-2a shows the yielded deformation of SMP upon application of 2 N). The schematics in Figure 8-2b depict the process of this shape-memory performance testing: first, the sample is clamped and stabilized inside the DMA; afterwards the temperature is ramped up to 60°C. After reaching 60°C, the force of 2 N is applied on the sample, which remains

stable while the sample is subsequently cooled down (shape fixing). In the next step, the force is released and the temperature is raised again to 60°C. This leads the SMP to switch back to its original flat state (shape recovery). When the original shape is recovered and stable 60°C reached, the force is re-applied and the process is repeated.

Figure 8-3 illustrates the obtained results as two-dimensional graphs of change of strain and displacement with temperature, force and time; Figure 8-4 shows the same results represented as three-dimensional stress-strain-temperature curves ("shape memory behavior" curves).[408]

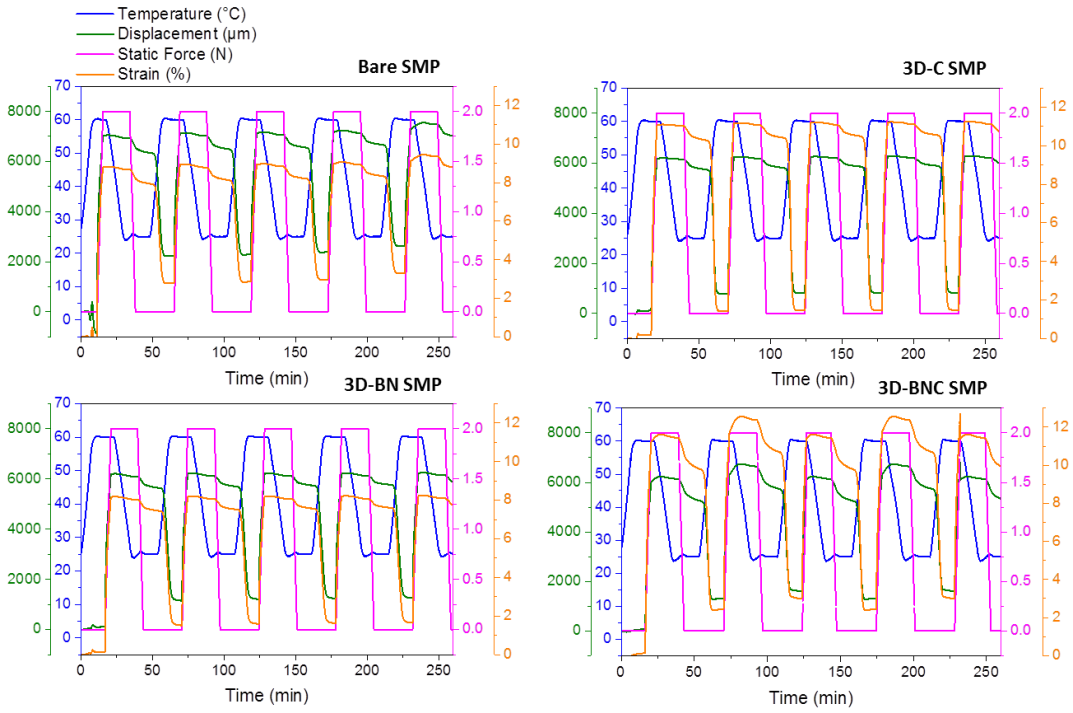

Figure 8-3. 2D shape memory performance test results obtained using DMA. Results for the four types of SMP, bare, 3D-C infused, 3D-BN infused and 3D-BNC infused SMP. It shows the change of strain, displacement with temperature and force and time, for each type of material

These cyclic tests determine the strain fixity rate R_f and the strain recovery rate R_r. For each number of cycles N, R_f quantifies the ability of the material to recover its

permanent shape; R_r quantifies the ability to hold the applied mechanical deformation during the process.[407] These parameters are calculated through the following ratios: [407]

$$R_r(N) = \frac{\varepsilon_m - \varepsilon_p(N)}{\varepsilon_m - \varepsilon_p(N-1)} \times 100 \tag{8-1}$$

$$R_f(N) = \frac{\varepsilon_u(N)}{\varepsilon_m} \times 100 \tag{8-2}$$

with ε_m representing the temporary shape's mechanical deformation, $\varepsilon_p(N)$ the permanent shape's mechanical deformation after N cycles and $\varepsilon_u(N)$ the residual of strain after retraction in the Nth cycle. From equations (8-1) and (8-2), it becomes evident that R_f and R_r ideally should be 100%. For this work, the shape memory parameters are calculated based on the strain values in the third cycle (N = 3).

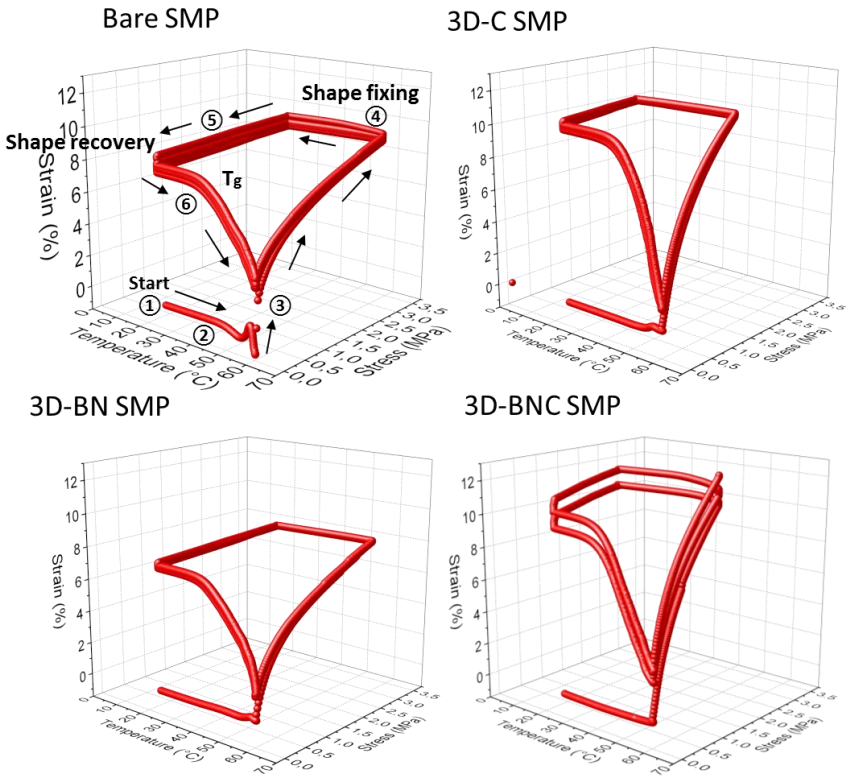

Figure 8-4. 3D stress-strain-temperature data representation for the shape memory performance of bare SMP, 3D-C SMP, 3D-BN SMP and 3D-BNC SMP

Table 8-1. Summary of important characteristics of SMP and 3D-foam infused SMPs

	Bare SMP	SMP-C	SMP-BN	SMP-BNC
Filling factor	-	0.3 vol%	0.3 vol%	0.3 vol%
Decomposition temp.	280.7 °C	280.6 °C	282.3 °C	288.2 °C
Glass transition temp.	58.4 ±3 °C	56.7 ±3 °C	53.6 ±3 °C	52.6 ±3 °C
Thermal conductivity, RT	0.090 ±0.003 $Wm^{-1}K^{-1}$	0.361 ±0.017 $Wm^{-1}K^{-1}$	0.157 ±0.007 $Wm^{-1}K^{-1}$	0.21 ±0.010 $Wm^{-1}K^{-1}$
Thermal conductivity, 60 °C	0.103 ±0.006 $Wm^{-1}K^{-1}$	0.341 ±0.003 $Wm^{-1}K^{-1}$	0.145 ±0.016 $Wm^{-1}K^{-1}$	0.17 ±0.007 $Wm^{-1}K^{-1}$
Sheet resistance	20000 $T\Omega\square^{-1}$	40 $\Omega\square^{-1}$ (bare 3D-C 8.53 $\Omega\square^{-1}$)	63.9 $T\Omega\square^{-1}$ (bare 3D-BN 8.9 $G\Omega\square^{-1}$)	24580-230 $\Omega\square^{-1}$ (bare 3D-BNC 5000-50 $\Omega\square^{-1}$)
Bending deformation ε_m	8.97%	11.21%	8.21%	12.56%
Strain recovery rate R_r	98%	97.1%	99.4%	94.4%
Shape fixity rate R_f	98.5%	98.6%	97.3%	97%

The bare SMP shows a large deformation in the first cycle, which remains stable throughout the subsequent cycles. A viscous plastic deformation of 8.83% is observed when applying stress at high temperature. The third cycle mechanical deformation ε_m is of 8.97%, which results in a strain recovery rate $R_{r,bare}(3)$ of 98% and shape fixity rate $R_{f,bare}(3)$ of 98.5%. For the case of 3D-C/SMP, the viscous deformation increased to 11.1% and the third cycle mechanical deformation is of 11.21%. The strain recovery rate and strain fixity rate remain stable with $R_{r,3D\text{-}C/SMP}(3)$ of 97.1% and $R_{f,3D\text{-}C/SMP}(3)$ of 98.6%. For 3D-BN/SMP, the initial viscous deformation remains in the same range of bare SMP at 8.19%. The third cycle mechanical deformation is of 8.21%, which is lower than 3D-C's case, but similar to the neat SMP. The strain recovery rate and strain fixity rate also remain stable at $R_{r,3D\text{-}BN/SMP}(3)$ = 99.4% and $R_{f,3D\text{-}BN/SMP}(3)$ = 97.3%. For 3D-BNC/SMP the values for $R_{r,3D\text{-}BNC/SMP}(3)$ and $R_{f,3D\text{-}BNC/SMP}(3)$ are equivalent to 94.4 and 97%, respectively. It can be seen that all values remain in a similar range, which indicates that the incorporation of the 3D-foams into SMP does not change/hamper the shape memory performance of the polymer. Additionally, since all values approach the

targeted 100%, and there is no detectable decrease within all 5 cycles, the performance is considered ideal.[409] Usually it is common for filled SMPs to experience shape memory loss.[177] Table 8-1 summarizes all results mentioned thus far for the 3D-foam hybridized SMPs; a comparative study of different filler materials in SMP is shown in Table 8-2. The important parameters for comparison are filling factor, thermal conductivity and shape memory performance (fixity and recovery rate). CNTs and graphene sheets are a good material for direct comparison as they also require low filling fractions.[408, 410] As it can be seen, the increase in thermal conductivity is very low and the shape fixity rate is far from 100%. It was stated that CNTs decrease the mechanical properties of SMPs, rather than enhancing them, which is why they may not be appropriate fillers for incorporation in SMPs.[177] Using graphene sheets may be a better choice in terms of thermal conductivity increase and retention of shape memory performance. However, the single sheets tend to agglomerate which poses difficulties for fabrication. In another study using 3D carbonaceous interconnected material,[259] thermally exfoliated reduced graphene oxide networked ferromagnetic hybrid, an increase of thermal conductivity of the SMP from 0.217 $Wm^{-1}K^{-1}$ to 0.258 $Wm^{-1}K^{-1}$ (0.0041 per filling %), while retaining shape memory performance was reported. Taking into consideration the networked character of the filler and its high filling fraction of 10 vol%, this increase in thermal conductivity is relatively small. Additionally to SMP epoxy, other non-shape memory filled epoxy's are enlisted in Table 8-2 along with their thermal conductivity, such as carbon fibers[411] and graphite foam.[412] The numbers clearly show the high filling fractions usually required for significant increase in thermal conductivity (e.g. 56 and 8.55 vol% for carbon fibers and graphite foam), which is opposed to the herein described 3D-fillers, where even small fractions as small as 0.3 vol% can increase the thermal conductivity by 300%.

Table 8-2. Comparison of thermal conductivity and shape memory performance of different filler materials

	Filling Factor		Thermal Conductivity [W $m^{-1}K^{-1}$]		Shape fixity	Shape recovery	Ref.
	wt%	vol%	Bare SMP	Filled SMP			
Carbon Nanotubes		1-5	0.242	0.251 (@0.3 wt%)	from 56 to 70%	100%	[410]
Graphene sheets	0.5 1			~0.4 ~0.8	from 97% to 95% to 96%	from 89% to 95% to 96%	[408, 413]
3D graphene-ferromagnetic hybrid	10		0.217	0.258			[259]
Nickel zinc ferrite particles		1-20		n.a.	no significant change	no significant change	[414]
Nanoclay	1-5			n.a.	from 96 to 93%	from 100 to 85%	[415]
Glass fiber	10-30			n.a.	n.a.	65%	[416]
Aluminum nitride	40		0.12	0.44	n.a.	From 96 to 70%	[417]
Talc		30	0.27	2.50	n.a.	n.a.	[418]
Carbon fibers		56	0.1	695	n.a.	n.a.	[411]
Graphite foam	8.55		0.34	14.67	n.a.	n.a.	[412]
3D foams	**0.35**	**0.3**	**0.1**	**0.15 – 0.35**	**98.5 ±1**	**98 ±1**	**this work**

8.4 Achieved improvements

8.4.1 Transformation speed

In order to demonstrate the property enhancement brought about by 3D-fillers, two sets of video images were recorded. For the first one, two equally sized SMPs, one bare and one with 3D-C filler, are prepared, deformed into the same shape and placed simultaneously on a heating stage. This way, their temporary to permanent transition speed of transformation is compared. Snapshots of this trial are displayed in Figure 8-5. The first set of images shows the initial state where both samples are deformed into the same shape. Almost immediately after placing the samples on the heating stage, which

is heated above glass transition temperature at 60°C (second row of images), the sample infused with 3D-C starts returning back to its permanent shape. The time stamp marks 15 seconds at this point. Only 45 seconds later (third pair of images), the 3D-C infused SMP returns back to its original shape, while the bare SMP slowly starts to transform back. Almost 2 minutes later, the bare SMP finalizes the transformation process (last row of images). This verifies the three-fold increase of thermal conductivity leading to a three-fold decrease in time required for transformation. In addition, no shape memory loss was observable, since the two structures returned to their fully flat permanent state.

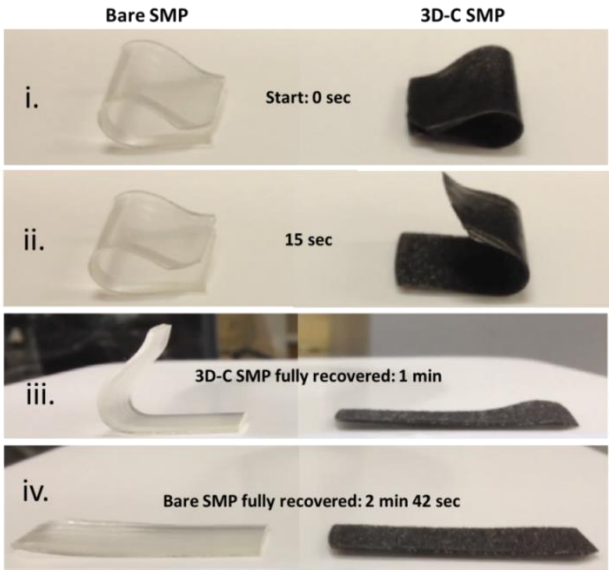

Figure 8-5. Comparison between bare SMP (transparent sample) and infused SMP (black sample) [i.] at 0 sec (both polymers in deformed shape), [ii.] infused SMP returns back faster than bare SMP, [iii.] at 1 min, infused SMP has returned back to its original shape, [iv.] at 2 min 42 sec, bare SMP completed the transformation process

8.4.2 Uniformity of heat spread and energy

The second video images recorded are to assess and quantify the uniformity of heat transfer of 3D-foam infused SMP. 3D-BN/SMP is used in this case and compared to bare SMP. Figure 8-6a shows the final samples used, which is SMP molded into two 1 cm x 7 cm slabs with carbon wires embedded in the sample edges as integrated heating

elements. These carbon wires have a typical resistance of ~4.5 $\Omega\square^{-1}$ for a length of 1 cm, thus enabling their use as heating element. One of the two samples includes a 1.1 cm x 2.4 cm (1.8 mm thick) 3D-BN embedded across the top part of the slab. The 3D-BN is expected to serve as a heat conductor, transferring heat from the carbon fiber heaters embedded at the edges to the center of the SMP slab, potentially reducing the temperature gradient across the sample. The thermal response of the two samples is tested via measuring the temperature gradient across their surface using a thermographic camera. The maximum, minimum and average temperatures in a selected area are extracted from the thermal images, which enables a precise spatial investigation of the temperature gradient across the samples surface. Typical thermographic images of the two samples are shown in Figure 8-6b. The carbon wires used as the heating element are clearly seen in the images in bright yellow, representing the higher end of the measured temperature range. Relevant areas on each of the samples surfaces are selected for analysis: for the SMP reference sample, the area is located at the center of the sample, away from the heater carbon wires (borders of rectangle pointed out by red arrows).

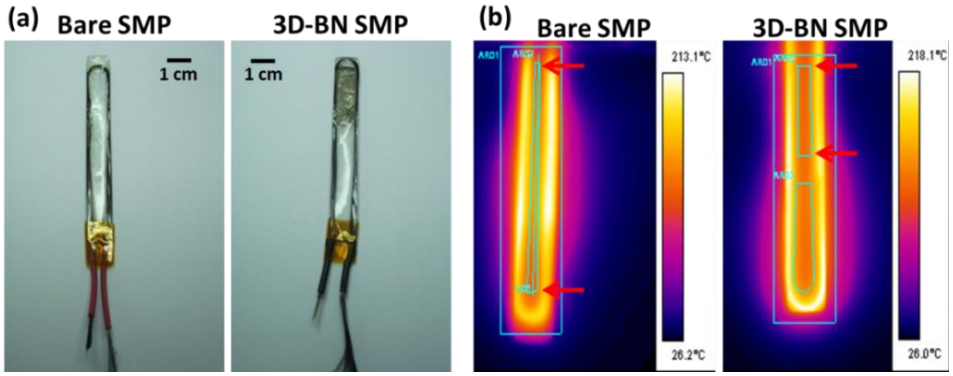

Figure 8-6. (a) images of the bare SMP and 3D-BN SMP sample used in the thermal camera experiment; **(b)** typical thermographic images of the two samples. Temperature gradients on the sample surfaces were measured for the different areas marked in the images with cyan lines (highlighted with red arrows)

The temperature gradient on the 3D-BN/SMP sample is also measured in the center of the sample, in a section with 3D-BN (borders of rectangle pointed out by red arrows). Figure 8-7a shows the average temperature measured for each of the samples as a function of the power used for heating the wires, normalized by the sample mass. Normalizing by the sample mass is required in order to compare the results of the different samples, as heating a larger mass will require more energy and therefore result in higher power consumption. These measurements clearly show that heating the 3D-BN/SMP sample needs measurably less power than heating the reference SMP sample, i.e. the 3D-BN/SMP sample requires ~20% less power (4.89 Wg^{-1}) than the reference sample (6.25 Wg^{-1}) in order to reach an average temperature of 139°C. Moreover, the addition of 3D-BN to the SMP reduces the temperature gradient on the sample surface, thus making the temperature uniform across the sample. This effect is observed in the reduced standard deviation measured for the 3D-BN/SMP sample, as seen in Figure 8-7b, where the difference between the lowest and highest measured temperatures on a sample are plotted as a function of the average surface temperature. The addition of 3D-BN did in fact increase the measured temperature uniformity. This effect can be clearly seen in the reduced maximum temperature difference of 38.2°C measured at an average surface temperature of 139°C, as compared to a temperature difference of 50°C which is measured on the SMP reference sample for the same average surface temperature. It is clear that the SMP reference sample shows relatively poor temperature uniformity, specifically in average temperatures close to the glass transition temperature of the SMP (an example cross-section temperature profile of bare SMP is shown in Figure 8-8a, where the large deviation in temperature can be clearly seen; an example cross-section temperature profile of 3D-foam infused SMP is shown in Figure 8-8b, where uniformity in temperature can be clearly seen).

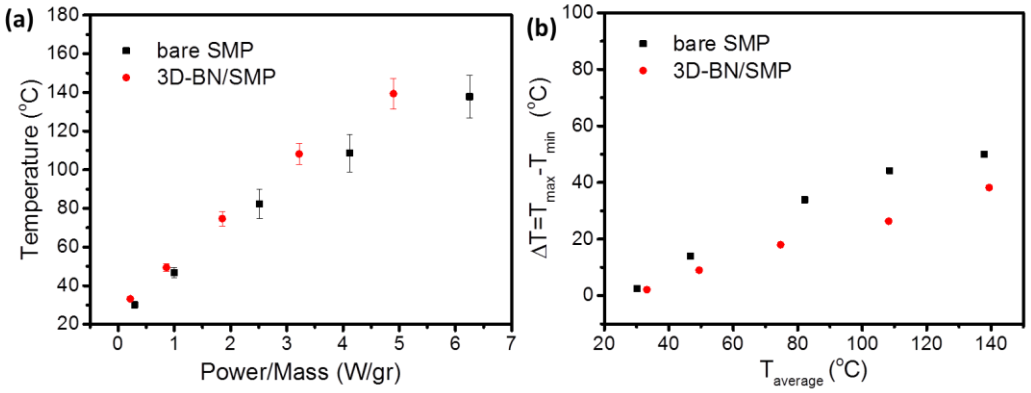

Figure 8-7. Quantitative analysis of the thermal camera results. **(a)** Average temperature measured on the analyzed sample area as a function of the heating power normalized by the sample mass. **(b)** the maximum temperature difference $\Delta T = T_{max} - T_{min}$ as a function of the average surface temperature measured on the SMP reference sample and the 3D-BN SMP sample

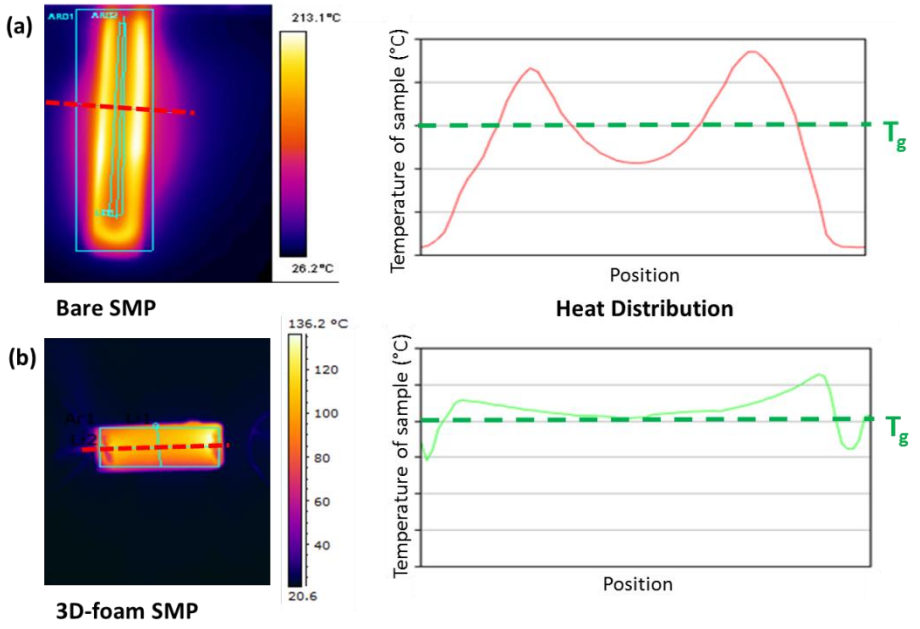

Figure 8-8. Thermal camera and heat distribution across **(a)** bare SMP sample and **(b)** 3D-foam infused SMP sample

It is thus evident that the addition of 3D-BN not only significantly reduced the amount of power needed in order to heat the SMP up beyond its glass transition temperature, but also increased the temperature uniformity in the center of the SMP sample, minimizing the temperature gradient inside the sample.

8.4.3 Increase of actuation area

In a next step, the performance of SMP and infused SMP for larger area applications is assessed. It is known that bare SMP performs well in small area samples, but when large areas are required, its non-uniform heat distribution poses serious problems.[177] This is especially important for practical applications of shape memory materials, as the temperature change has to be spatially uniform to avoid unwanted internal strain. During the heating process, such non-uniformities in temperature may cause parts of the material to have a temperature higher than the glass transition temperature while others remain below it. This will cause parts of the sample material to be in a rubbery state while other parts remain solid, giving rise to internal non-uniform strains that can produce mechanical failure in the form of cracks.

Due to the demonstrated improvements in heat spreading uniformity through the infusion of 3D-foams, it is believed that large area application will now be enhanced and damage and cracks avoided. In order to test this, two larger pieces (7 cm x 1.5 cm) of bare SMP and 3D-C/SMP are prepared with an integrated resistive heating wire throughout their length direction (Figure 8-9a). Both samples are deformed into the same U-bend shape (Figure 8-9b) and heated up by applying a constant current onto the embedded wire. The heat immediately transfers to the whole structure of the 3D-C/SMP which starts transforming back; while in the bare SMP sample the heat is not spreading, since no transformation is visible. This causes stress at the bent area, which leads to a local failure and spreads into a long crack at the bending point (Figure 8-9c and Figure 8-9d). The 3D-C SMP sample returns back to its permanent shape without any damage (Figure 8-9c). This clearly highlights the significant improvement in uniformity of heat spread achieved through the incorporation of 3D-foam materials into SMPs.

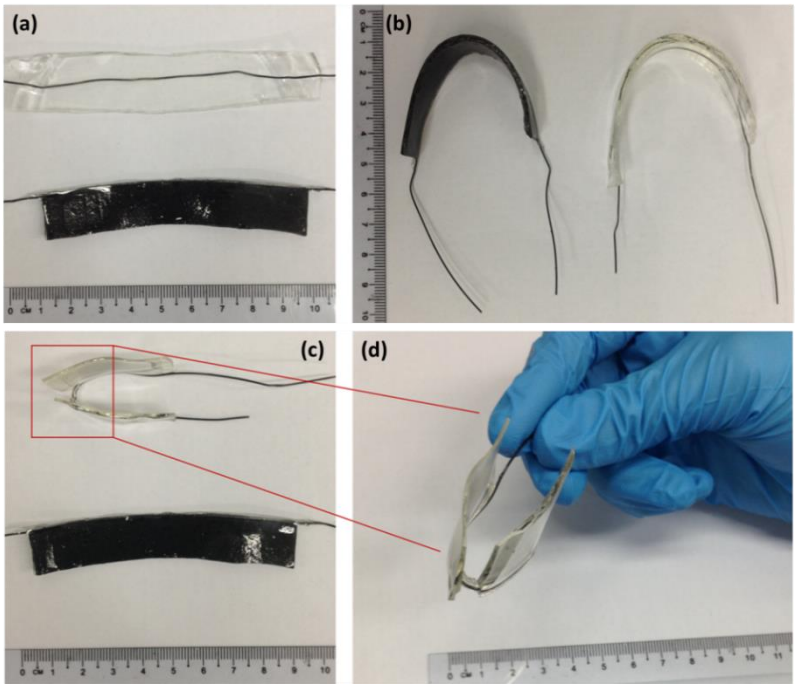

Figure 8-9. Optical images of the trial on larger area application. **(a**) Starting point of the 7 cm long bare SMP and 3D-C SMP; **(b)** both samples were bend into the same U-bend shape with same angle; **(c)** during transformation, the bare SMP cracked at the central bending point, while 3D-C completely returned to its flat state; **(d**) zoom into the crack in bare SMP, which expanded throughout the entire width of the sample

8.5 Self-heating capability and timed actuation

For practical applications, it is evident that external heating is not feasible for most cases. In order to bypass this issue, internal heating is necessary to make SMP more applicable.[370, 419] It is also imperative to use a more spatial uniform configuration as heating medium, replacing the wires usually used. This could be achieved through the use of materials such as 3D-C or 3D-BNC embedded in the polymer matrix (and in addition would not only render an internal heating element, but also improve the SMP's overall performance as shown in the previous sections).

In order to assess 3D-BNC's self-heating properties, first, an 85% BN 15% C sample was connected to a probe-station via two wires attached through silver paint to the foam

and simultaneously monitored under thermal camera. The current running through the samples was gradually ramped up, while monitoring the heat distribution under thermal camera. Before taking the image, the temperature of the sample was measured with a thermocouple to ensure the correctness of the measurement. Throughout the measurement, the sample was kept suspended with minimum contact to other surfaces. Figure 8-10a shows the obtained I/V and temperature curve and thermal images of the sample at 30 mA. The curve shows a steady increase in temperature with increasing current; temperatures reached at 20 mA are 57.6°C, at 30 mA 93.5°C, at 40 mA 161.2°C and at 50 mA as high as 207.4°C. This demonstrates the self-heating capability of the 3D-foam. After this, the experiment was performed with 3D-BNC/SMP hybrid for comparison. The same 85% BN 15% C sample was infused into SMP and the experiment repeated. Figure 8-10b shows the obtained heating curve and a thermal image at 30 mA. It must be noted that the size after SMP infusion slightly increased due to SMP edges of 0.5 mm on each side.

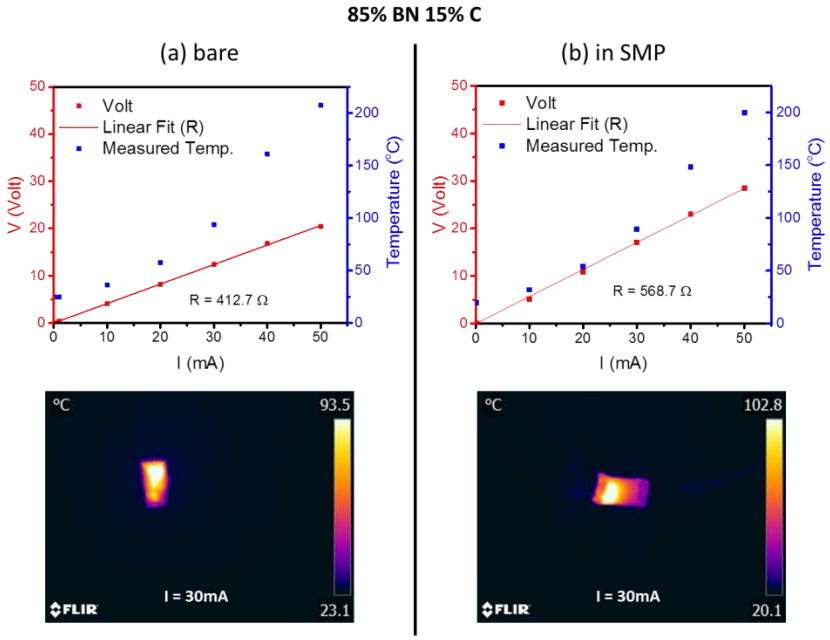

Figure 8-10. Self-heating capability of 3D-BNC/SMP samples. Temperature and voltage as a function of heating current and thermal image at 30 mA for **(a)** bare 85% BN 15% C and **(b)** SMP infused 85% BN 15% C sample

It can be seen that the sample showed increased resistance after SMP infusion. Since the sample and the contacts remained the same before and after the infusion process, it is likely that the infusion and curing process of the SMP produced some structural change to the 3D-BNC that caused this increase. It can be also seen that the SMP infused sample reached similar temperatures than the bare sample for the same current. This indicates that the effect of resistance increase and reduction of surface area in contact with air balanced off the effect of increased mass of the sample on the self-heating. Two more examples of the same experiment with other BN:C ratios are shown in Figure 8-11 (15% BN 85% C and 100% C). It can be seen that both samples experienced a similar relative increase in resistance after SMP infusion and that the samples reached the same temperatures at same current as their bare counterparts. This shows that the self-heating mechanism of 3D-BNC foams can be directly engineered for SMP application; the choice of BN:C concentration can be designed according to application parameters (dimensions, temperature and power input requirements).

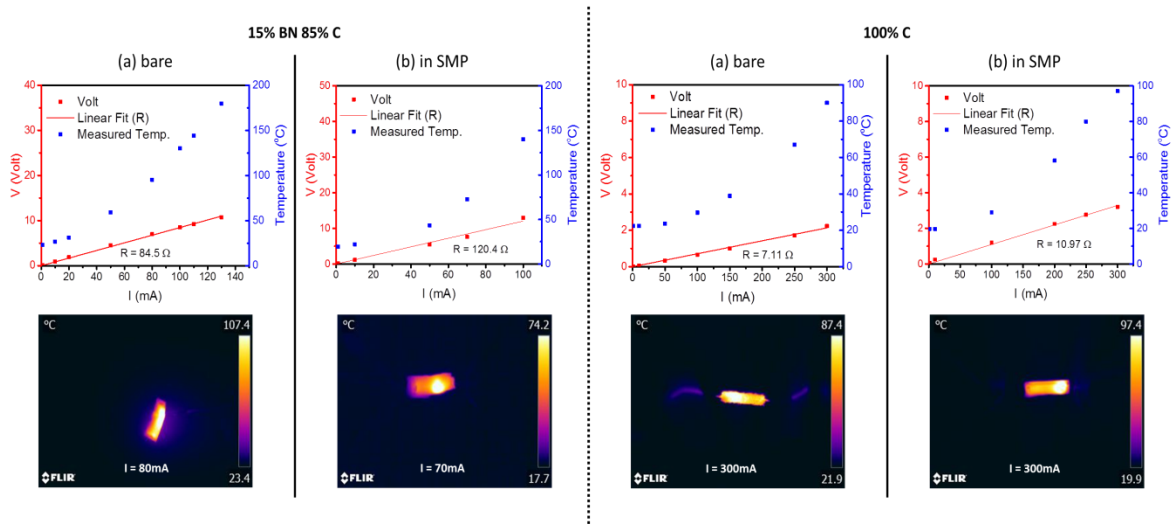

Figure 8-11. Self-heating capability of 3D-BNC/SMP samples. Temperature and voltage as a function of heating current and thermal images for **(a)** bare and **(b)** SMP infused 3D-BNC samples of concentration 15% BN 85% C and 100% C. (same 3D-foam samples were used for bare measurements and infused measurements)

Since 3D-BNC has a complex structure in which it is challenging to directly probe the interaction between filler and SMP, a 3D model in COMSOL Multiphysics is used to determine the relation between sample dimensions, temperature and heating current. For this purpose, first, the obtained results are normalized to eliminate differences occurring from slight deviations in pore distribution, humidity, ambient temperature and heat transfer coefficients *h*: for the bare 3D-BNC case, the convection heat transfer coefficient multiplied by the surface area *h·A* was extracted from the measurements (equation 8-3)

$$\boldsymbol{P = hA\left(T_{sample} - T_{ambient}\right)} \tag{8-3}$$

and normalized per sample volume *V*, assuming that the surface area per volume ratio is the same for all samples and that any changes between the normalized extracted parameters $\frac{hA}{V}$ are due to changes in the heat transfer coefficient between experiments.

Results for the 85%BN 15%C sample are $h_1 A_1 = 5.352 e^{-3} \frac{W}{K} \rightarrow \frac{h_1 A_1}{V_1} = 0.02811 \frac{W}{Kcm^3}$,

for the 15%BN 85%C sample $h_2 A_2 = 7.383 e^{-3} \frac{W}{K} \rightarrow \frac{h_2 A_2}{V_2} = 0.04644 \frac{W}{Kcm^3}$ and for the

100%C $h_3 A_3 = 10.833 e^{-3} \frac{W}{K} \rightarrow \frac{h_3 A_3}{V_3} = 0.09911 \frac{W}{Kcm^3}$. The measured temperature difference (from ambient) as a function of the power used, shown in Figure 8-12a, indicates a linear dependence, as expected from a convection based heat loss process. The results show a different linear slope for each of the experiments. Neglecting radiative heat loss, the main reason for the slope difference is the difference in the total surface area *A* between the different sized samples and the difference between the ambient conditions *h* during the different experiments. Under the assumption that

surface area to volume ratio is roughly equal for all samples, $\frac{A_3}{V_3} = \frac{A_2}{V_2} = \frac{A_1}{V_1}$, the results can be normalized to a surface area corresponding to a specific sample size (normalized to the volume of the 100% C sample). In addition, in order to calculate the appropriate heating power for each sample, the resistance of each sample is calculated. This is done using the measured resistivity and assuming the size of the sample to be 100% C sample size. The results of the normalized ΔT as a function of the normalized power are shown in Figure 8-12b. After normalizing the differences due to surface area and sample size, the differences in the slope represents the differences in the heat transfer coefficient between the experiments (different ambient temperature, humidity and pressure). Assuming the latter, the following ratios for the heat transfer coefficients are obtained $h_1 = 0.282\,h_3$, $h_2 = 0.466\,h_3$. The difference between the three heat transfer coefficients h is acceptable, as the heat transfer coefficient for atmospheric air was measured to be between 5 to 100 $WK^{-1}m^{-2}$, depending on humidity and temperature. Normalizing the results for all samples (h_1 and h_2 to h_3 and all the samples surface area to that of sample 100% C) leads to a linear temperature increase as a function of heat power, as shown in Figure 8-12c. Since the heat loss through convection is only dependent on the surface area, the final temperature has the same dependence on the heating power for all the samples. Thus, for a given current, the samples with higher resistance will reach higher temperatures. This can be seen in Figure 8-12d, where the temperature change as a function of electrical current for samples with normalized dimensions is shown. In this figure, the resistance of samples with dimensions of l = 1.6 cm, w = 4 mm, t = 1.7 mm was calculated using the measured effective resistivity for each sample. The calculated resistivity values were used in order to determine the heat power used, which in turn was used to calculate the temperature difference. Note that these results apply to the

material in atmospheric conditions without any polymer infused. For the 3D-BNC/SMP results, normalization was done similarly and the result is shown in Figure 8-12e. A direct comparison of the normalized results with and without SMP infusion is shown in Figure 8-12f.

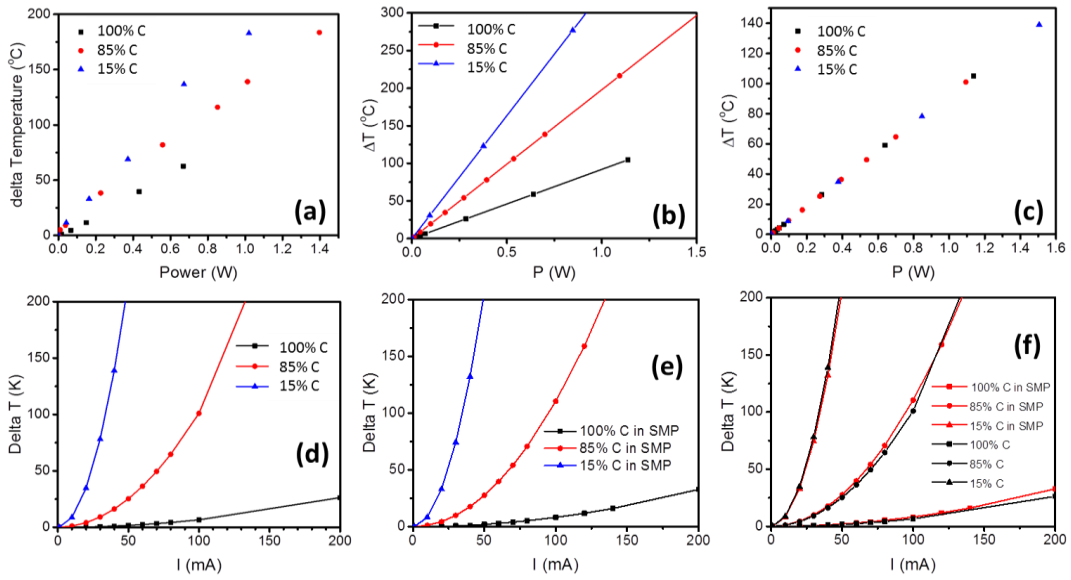

Figure 8-12. Measured $T_{sample} - T_{ambient}$ as a function of **(a)** heating power of bare 3D-BNC samples, **(b)** heating power (normalized to the 100% C sample size/surface area), **(c)** heating power (normalized to the 100% C sample surface area and to the heat transfer coefficient h_3), **(d)** applied current (all samples are normalized to the 100% C sample size). **(e)** Normalized values for the SMP infused case samples. **(f)** Direct comparison of (d) and (e)

The curves from Figure 8-12d are then used to validate the model used in COMSOL for the bare 3D-BNC. In this model, one pore of the foam is represented by a sphere-centered tetrakaidecahedron (such geometry is similar to the foam structure).[420] The foam is supposed to be homogenous, so only one cell build up by one pore infused with a medium is simulated; a scale factor equivalent to the theoretical total number of pores inside the foam is then applied to predict the behavior of the whole structure. The program then uses finite element simulation method with Fourier's law to predict the self-heating behavior. For the bare 3D-BNC case, the model first treats the foam as filler in air. Figure 8-13a shows the direct comparison of simulated results with experimental

results; it can be seen that the model used accurately calculated the self-heating behavior of the three bare foams tested. Thus, in a next step, the air in the model is replaced with measured data for SMP (i.e. measured thermal and electrical conductivity, density and specific heat). Also, these results are compared to the measured normalized results (Figure 8-12e, direct comparison is shown in Figure 8-13b) and it can be seen that also for this case, the model of the 3D-BNC with SMP infusion is in good agreement with the experimental results for several foam compositions and applied power. Thus, this model can be used to design self-heating SMP for given dimensions, temperature and electric input (i.e. those input parameters will determine the resistivity required for the 3D-BNC, which in turn determines the BN:C ratio, as described in section 3.4.2).

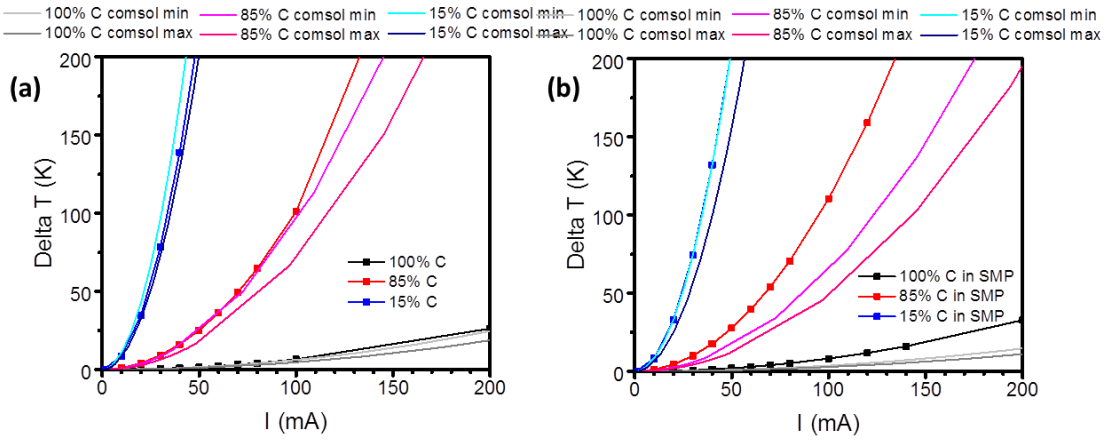

Figure 8-13. Comparison of simulated results with experimentally obtained results for **(a)** bare BNC and **(b)** 3D-BNC/SMP infused samples

The concept of adapting the BN:C concentration according to design parameters can be further developed into designing timed actuation ("4D-SMP"): the use of 3D-BNC infused SMP allows a spatial-selective actuation (i.e. timing of the recovery of the dual SMP in several different steps, resulting in an overall multi-shape behavior).[370] The definition of multi-shape behavior is that at least two or more thermal transitions are independently used in a crosslinked network to fix and recover two or more temporary

shapes, all in one shape memory cycle.[421] Currently, multi-step SMP is achieved via mechanically mixing polymers of different T_g,[422-425] or infiltration of different fillers (such as fibers,[426, 427] CNTs and iron oxide,[428] or inks[429]) in order to elicit different responses to external stimuli.[430] However, similarly to the use of fillers to increase thermal conductivity of the SMP, non-uniformity of filler distribution poses problems for practical applications also in this case.[427] Further challenges for multi-step SMPs is that at least one of the shape recoveries is compromised due to the partial freezing of the polymer chains during the shape-fixing steps;[409] and the realization of a n-step SMP typically requires a (n-1)-step programming instead of only one-step for the dual SMP.[370] To overcome such limitations, a combination of intrinsic and extrinsic multi-SMP concept was proposed.[370] The use of 3D-BNC in SMP is thus such a concept as it combines intrinsic multi-SMP (each section of T_g can be targeted with a different BNC) and extrinsic SMP since it can be timed while using the same polymer in each section. Using such a configuration may allow several transformation steps (quintuple-SMP is the current record[431]) with only one shape-fixing step. Thanks to the COMSOL model previously verified with experimental data, a system can be designed with spatially separated different BNC sections that can cater for different transition temperatures or be triggered at different input power.

8.6 Summary

In this chapter, 3D-C, 3D-BN, and 3D-BNC were synthesized and successfully infused into SMP matrix. These hybrid structures achieve improved thermal conductivity by 1.5 to 4-fold over bare SMP for 3D-BN/3D-BNC infused samples and 3D-C infused samples, respectively. Through cyclic DMA measurements it was shown that the infusion with 3D-foams does not alter the shape memory performance of the

SMP, even after several repetitions. This is mainly owed to the interconnected structure of the 3D-foams and their very light weight, which prevents any agglomeration, renders a homogeneous network within the SMP and does not add any additional weight to the polymer. The improvement in thermal conductivity, paired with the homogeneous distribution within the SMP leads to a more uniform heat spread, which in turn significantly increases the total active area, as it prevents the buildup of internal strains and failures (failure in the form of cracking during the shape memory process is a common challenge in larger scale application due to the poor thermal conduction of bare SMP, which often causes a large thermal gradient across the sample). Adding to these benefits is the reduction by 20% of total energy input required. And finally, the use of 3D-BNC infused SMPs was shown to possess tunable self-heating characteristics, which are directly translated into the SMP configuration. It was demonstrated that with 3D-BNC, heating sections and spreading sections can be integrated in one single material, and that this can be further designed to obtain a timed-SMP effect.

The herein presented SMP hybrid represents a combination of extrinsic and intrinsic multi-SMP properties. Using the 3D-foam as fillers provides a platform of next generation SMP filler, which will be able to render any SMP the ability to work on large scale applications, at faster recovery rates and with less energy requirements while having no constraints of long term loss of shape memory performance.

9 Conclusions and Recommendations for Future Work

9.1 Conclusions

This work has extended the work on upscaling 2D materials into the 3D macroscopic realm by introducing a new class of hybrid 3D-foam as well as studying and using properties beyond the traditionally reported ones. For the first time, this has driven the focus onto 3D-foams as an active material, contrasting to previous work using it merely as a passive material to increase surface area and filler interconnectivity of polymers.

For the first time, hybridization of two different 2D-materials, namely h-BN and graphene, onto one single 3D platform was shown. The obtained lightweight (1 – 5 mg cm^{-3}) 3D-BNC has tunable characteristics, i.e. electrical conductivity of 0 to 0.6 Scm^{-1} and EMI shielding propertied from 0 to ≈50 dB, while keeping a stable thermal performance (0.84 – 1.2 $Wm^{-1}K^{-1}$). It was demonstrated that the 3D-BNC combines the similarity and the opposing properties of both C and BN to create a user configurable macro foam-like material with a large spectrum of electrical and EM tuning options.

It was shown that this material by itself has high potential to be used as a new high-performance TIM with outstanding heat extraction capability. Up until this point, 3D-foams were considered as thermoelectric/thermal storage material, which is owed to their high porosity, but in this work, a complete opposed behavior was demonstrated. This was achieved by turning its perceived “disadvantage” of high porosity into an advantage by compressing the 3D-foam. This has led to a drastic increase in thermal conductivity and in turn improved cooling performance by 20 – 30% over conventional TIMs, with a superior surface conformity, low thermal contact resistance and stability up to at least 500°C higher than current materials. Even further improvement in thermal performance is achieved by intermixing the 3D-foams with a thermal adhesive matrix.

This way, a closed-form thermal solution is obtained that combines the best characteristics of current TIMs (i.e. good surface conformity, low thermal contact resistance, high thermal conductivity, and long-range reliability) and even surpasses their performance (i.e. higher thermal stability and better cooling profile).

The incorporation of 3D-C and 3D-BN into PI demonstrated that the improvement in heat dissipation can be transferred into hybrid films, without altering the inherent mechanical properties of the polymer. This way an improved substrate for flexible electronics was obtained, which fully maintained its robustness and flexibility, but with an increase of thermal conductivity by 25 times. This hybridization could drastically improve heat dissipation, which was demonstrated with proof of concept printed resistors that could be powered up 50% higher on hybridized films than on conventional PI.

Furthermore, the use of 3D-C in PI could increase the resilience of the polymer towards the aggressive environment encountered in space (i.e. atomic oxygen, thermal cycling and gamma ray irradiation), while maintaining its thermo-optical and outgassing properties. In addition, the electrical conductivity rendered to PI through 3D-C mitigated the electrostatic discharge build up problem current thermal space blankets suffer from.

It was also shown that the intermixing of 3D-foams with an active external matrix, such as epoxy SMP, is of great benefit: 3D-BNC speeds up the transformation process by up to three times, reduces required activation energies by 20% and helps to significantly enlarge the total usable active area. Furthermore, the tunability of BN and C concentrations yields a tunable self-heating effect within the SMP, which can be used to design timed actuation. Up until now, SMPs have been very limited in their application fields due to their constrained small sizes and non-uniformity of actuation. Thanks to the incorporation of active 3D-foams, their applications can now be extended.

Above all, this Thesis has demonstrated the great versatility of the 3D-foams achievable when integrating different 2D-constituyents into a single macrostructure and when using their properties in a more active way. This has extended the field of 3D materials and added a new branch of tunable applications, with great potential for commercialization.

9.2 Recommendations for future work

To even further improve the performance of the 3D-foams in the herein investigated thermal applications, the following next steps are suggested for future work:

9.2.1 Further improvement in thermal management

Since the thermal conductivity is dependent on the density of the 3D-foams, it is recommended to test foams with smaller pores. Smaller pores will increase the total volume fraction of material and thus increase the thermal conductivity. However, it must be considered that the decreased porosity might reduce the compressibility (and thus surface conformity) of the foams. A trade off must thus be found between minimizing pore size and compressibility. To help determine the optimum point, more refined COMSOL simulations may be used, for which a more exact 3D-model of the foam has to be developed. The approximation using a sphere-centered tetrakaidecahedron, as in our SMP simulations is a good starting point for such a refined model; further fine-tuning needs to take into account the randomness of pore distribution. In order to incorporate the effect of mechanical compression on the 3D-foam into simulations, the work by Wang et al.[432] is suggested as reference. This work describes how to implement coarse grain molecular dynamics simulations on 3D-C structures to determine mechanical deformations as a function of strain and stress.

Due to its reported drastic increase in thermal performance, this application has huge commercial potential; the development of large-scale fabrication is thus also suggested. Since the final size is mainly restricted by the size of the furnace used during CVD, it is suggested to replace the tube furnace by a chamber furnace, since the diameter and tubular shape greatly restrict the possible shapes and sizes. Further challenges to be addressed prior to commercialization are the scalability for large area manufacturing, which includes (1) ensuring uniformity during growth and yield; (2) find a scalable way to use sublimated ammonia-borane powder for the growth of 3D-BN, as right now relatively large quantities are required with little uniformity for samples larger than 20 cm x 5 cm; (3) adapt the low pressure method of 3D-BN to ambient pressure, as low pressures could hinder the scalability; and (4) make the handling of the foam easier, as due to their light weight and compressibility, at their current stage, the 3D-foams are fragile and can break easily if not handled properly.

9.2.2 Further improvement in flexible electronics application

Also for this application, it is suggested to further explore the upper limit of thermal conductivity achievable. This should be done through a study of filling fraction versus thermal and mechanical properties. Increased filling fraction is bound to improve the thermal performance, but at the same time, it must be ensured that the flexibility of the hybrid PI film is well maintained. Once this optimum point is found, it is suggested to test the heat spreading capabilities under more strenuous conditions, i.e. use actual lithography on the films and test thermal performance of such smaller structures, which will resemble more closely the final commercial application.

9.2.3 Further improvement in space application

Due to the non-invasiveness of the 3D-foam within the polymer matrices shown in the previous chapters (i.e. the intrinsic and mechanical properties of the polymers remain completely unchanged), the infusion process of 3D-foam into any other class of PI or SMP can be easily adopted. This means, that other PI and SMP could be used to cater for specific requirements (e.g. chain length of polymer backbone, transition temperature). As such, it would be very interesting to combine the work on PI and SMP into one: use a PI based SMP for space application. This way the established space qualification could be extended to SMPs as well, increasing their space environment endurance. This will be very interesting, since weight, stowage volume, structural integrity and the reliability of the deployment mechanism of satellites have always been critical considerations in the design of satellites.[433-435] It is thus suggested to replace the conventional moveable metal alloy panels used to support solar arrays and antennas[436] with a single part light material system that is based on 3D-foam infused SMP that has a specific temperature trigger and is durable in LEO environments. This would allow the solar array and antenna to conform to the satellite body and unfold upon deployment, as illustrated in Figure 9-1. Such a continuous and seamless deployment system does not only reduce the weight as compared to the conventional metal alloy panels, it also reduces the complexity for the deployment by removing the need for mechanical joints/locks.[436] This then significantly reduces potential failure points increasing operational reliability.

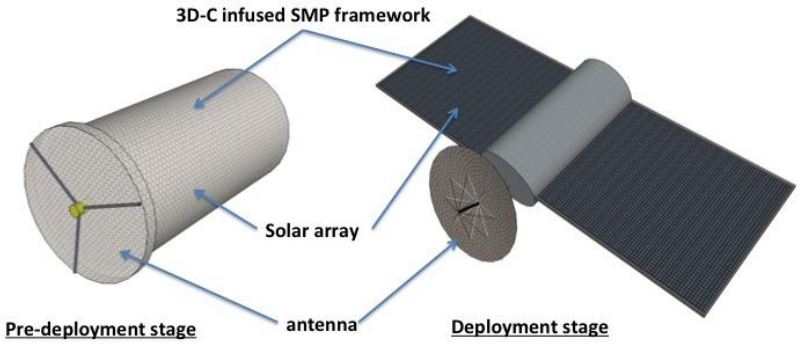

Figure 9-1. Schematic of the satellite at its pre-deployment stage, with the 3D-foam infused SMP solar panel array and antenna conformed to the main body; and at its deployment stage, with the 3D-foam infused SMP solar panel array and antenna transformed into the deployment shape

9.2.4 Other application fields

Due to the interconnected structure of the 3D-foams, their application field is not limited to thermal. A few exploratory studies have been performed to test their applicability in other new areas:

9.2.4.1 Tissue Engineering & Cell Stimulation

Compared to traditional polymer scaffolds, 3D-C's inherent structure combined with its interesting properties, such as (1) high electrical conductivity (while polymeric scaffolds are completely insulating), (2) ultralow density, (3) high porosity and (4) extremely high specific surface area (e.g. for 3D-C 850 m^2 g^{-1}, for polymer ~1 – 10 m^2 g^{-1}),[28, 437, 438] could better mimic the physiological environment conducive for cell growth and additionally (1) allow tissue stimulation, (2) require less non-biological material to degrade for high volumes (i.e. for 3D-C ~5 mg cm^{-3}, for polymer ~88 – 138 g cm^{-3}),[439, 440] (3) enhance the oxygen diffusion and (4) increase the cell density attached on the scaffold. The great potential of 3D-foams in cell culturing has become evident in studies investigating 3D-C's differentiation effects with neural stem cells (NSCs)[29] and human mesenchymal stem cells[30] which both demonstrated the possibility of

differentiation through 3D-C. Moreover, we have demonstrated that 3D-C is biodegradable with a tunable rate, which is further beneficial for its potential use as tissue scaffold.[154] Interestingly, there are also mark differences between 3D- and 2D-carbon as it has been shown recently that 3D-C has anti-inflammation properties against external insults, while graphene has no such effect.[441] It would be thus interesting to further dive into this research field and to combine tissue growth with direct electrical stimulation, which would be unique within the field of tissue engineering, and especially interesting in the field of electrically sensitive cells, such as neurons.

9.2.4.2 Dye-sensitized solar cells

Another research field, which used 3D-C only as supportive structure to enhance the surface area, are dye-sensitized solar cells (DSSCs). Several groups have integrated the foam into current DSSC counter electrodes,[90, 94] as well as anode materials.[93, 442, 443] Despite the achievements reported, ultimately, the performance of DSSCs is still dependent on their standard materials themselves (i.e. dye uptake time, adsorption capacities and charge separation mechanisms). A new approach to directly utilize 3D-C as a stand-alone material for DSSC would take away this dependence on TiO_2. However, 3D-C cannot be used directly due to its lack of band-gap. In an explorative study we reported the utilization of a stand-alone modified 3D-C, oxidized 3D-C (o-3D-C), which can be utilized directly, providing a TiO_2-free approach.[444] This first study already demonstrated improved saturation by 600 times, and adsorption capacity by 7 times, as well as suitable band structure and fluorescence quenching properties. It would be interesting to further optimize these properties and potentially develop an all-carbon 3D-DSSCs.

9.2.4.3 Fiber optics

Through tuning the number of layers to mono-/few-layer foams, 3D-C can be used as a saturable absorber (SA) to mode-lock fiber lasers,[445] which helps overcome the applicability issues encountered with CNTs and 2D graphene (one of the main limitations of CNT-based SAs is the operation wavelength, which is restricted by the diameter of the CNT;[446, 447] and a limiting factor to 2D graphene is its required wet-transfer process),[448] while combining the advantageous properties of graphene, which are large modulation depth, ultrafast recovery time, low mode-locking threshold, wavelength-independent saturable absorption, and high thermal damage threshold.[448-452] Our exploratory study with three-layer 3D-C showed that stable output pulses with a fundamental repetition rate of 9.9 MHz and a pulse width of 1 ps are generated from the fiber laser. Potentially, the saturation absorption strength could be modulated over a wide range by changing the number of graphene layers of 3D-C.

List of Publications

Awards

1. **CPMT Student Travel Award Winner** (2016) for "Heat Dissipation Enhancement of 2.5D Package with 3D Graphene & 3D Boron Nitride Networks as Thermal Interface Material (TIM)" presented at the *ECTC 2016*.

Journals

Published/in press/accepted/submitted

1. **Loeblein, M.,** Tay, R. Y., Tsang, S. H., Ng, W. B. & Teo, E. H. T. (2014). Configurable Three-Dimensional Boron Nitride–Carbon Architecture and its Tunable Electronic Behavior with Stable Thermal Performances. *Small, 10*(15), 2992-2999. (Inside Front Cover)

2. Yang, Y.,¶ **Loeblein, M.,**¶ Tsang, S. H., Chow, K. K. & Teo, E. H. T. (2014). Three-Dimensional Graphene Based Passively Mode-Locked Fiber Laser. *Optics express, 22*(25), 31458-31465.

3. Tay, R. Y., Tsang, S. H., **Loeblein, M.,** Chow, W. L., Loh, G. C., Toh, J. W., Ang, S. L. & Teo, E. H. T. (2015). Direct Growth of Nanocrystalline Hexagonal Boron Nitride Films on Dielectric Substrates. *Applied Physics Letters, 106*(10), 101901.

4. Dabir, F., Sarraf-Mamoory, R., Riahi-Noori, N., **Loeblein, M.** & Teo, E. H. T. (2015) Synthesis and Electrical Properties Evaluation of Three-Dimensional Graphene. *Journal of Advanced Materials and Technologies, 4*(3), 17-23.

5. **Loeblein, M.,** Bolker, A., Tsang, S. H., Atar, N., Uzan-Saguy, C., Verker, R., Gouzman, I., Grossman, E. & Teo, E. H. T. (2015). 3D Graphene Infused Polyimide with Enhanced Electrothermal Performance for Long-Term Flexible Space Applications. *Small, 11*(48), 6425-6434. (Front Cover)

6. Dabir, F., Sarraf-Mamoory, R., **Loeblein, M.,** Tsang, S. H. & Teo, E. H. T. (2016) Effect of Titanium Nitride Coating on Physical Properties of Three-Dimensional Graphene. *Applied Surface Science, 356*, 399-407.

7. Dabir, F., Sarraf-Mamoory, R., **Loeblein, M.,** Tsang, S. H. & Teo, E. H. T. (2016) Effect of Annealing Temperature on Physical Properties of Nanostructured TiN/3DG Composite. *Materials and Design, 90,* 524-531.

8. **Loeblein, M.,**¶ Perry, G.,¶ Tsang, S. H., Xiao, W., Collard, D., Coquet, P., Sakai, Y. & Teo, E. H. T. (2016). Three-Dimensional Graphene: Biocompatible and Biodegradable Scaffold with Enhanced Oxygenation. *Advanced Healthcare Materials, 5*(10), 1177-1191.

9. Tay, R.,¶ Li, H.,¶ Tsang, S. H., Zhu, M., **Loeblein, M.,** Jing, L., Leong, F. & Teo, E. H. T. (2016) Trimethylamine Borane: A New Single-Source Precursor for Monolayer h-BN Single Crystals and h-BCN Thin Films. *Chemistry of Materials, 28*(7), 2180–2190.

10. **Loeblein, M.,** Tsang, S. H., Han, Y., Zhang, X. W. & Teo, E. H. T. (2016) Heat Dissipation Enhancement of 2.5D Package with 3D Graphene and 3D Boron Nitride Networks as Thermal Interface Material (TIM). *IEEE 66th Electronic Components and Technology Conference (ECTC)*, 707-713.

11. Verker, R., Ozeri, M., Bolker, A., **Loeblein, M.,** Teo, E. H. T. & Gouzman, I. (2016) Enhancement of Polyimide and 3D Graphene-Polyimide through Thermoforming and its Effect on Mechanical Properties and Associated Creep Phenomenon. *Polymer Degradation and Stability, 134*, 273-244.

12. **Loeblein, M.,** Tsang, S. H., Pawlik, M., Phua, E. J. R., Han, Y., Zhang, X. W., Gan, C. L. & Teo, E. H. T. (2017) High Density 3D-Boron Nitride & 3D-Graphene for High Performance Nano-Thermal Interface Material. *ACS Nano*, *11(2)*, 2033-2044.

13. **Loeblein, M.,** Jing, L., Liu, M., Cheah, J. J. W., Tsang, S. H. & Teo, E. H. T. (2017) A "Hairy" Polymer/3D-Foam Hybrid for Flexible High Performance Thermal Gap Filling Applications in Harsh Environment. *RSC Advances*, 7, 39292-39298.

14. **Loeblein, M.,** Bruno, A., Loh, G. C., Bolker, A., Uzan-Saguy, C., Antila, L., Tsang, S. H. & Teo, E. H. T. (2017) Investigation of electronic band structure and charge transfer mechanism of Oxidized Three-Dimensional Graphene as metal-free anodes material for Dye Sensitized Solar Cell application. *Chemical Physics Letters*, 685, 442-450.

15. Chen, B., Pawlik, M., Tay, R. Y., Zhu, M., **Loeblein, M.**, Tsang, S. H. & Teo, E. H.T. (2018) Flexible Thermal Rectifier Based on Macroscopic PDMS@Graphite Composite Film with Asymmetric Cone-Shape Interfaces. *Carbon*, 126, 464-471.

16. **Loeblein, M.,** Tsang, S. H., Huat, L. L., Teo, J. W. R. & Teo, E. H. T. (2017) Reliability studies of a super-durable 3D-foam based TIM for all environments. *(under revision).*

17. Nguyen, A.,¶ Mattiassi, S.,¶ **Loeblein, M.**, Chin, E., Ma, D. L., Coquet, P., Teo, E, Goh, E. & Yim, E. (2017) Human Rett-derived neuronal progenitor cells in 3D graphene scaffold as an in vitro platform to study the effect of electrical stimulation on neuronal differentiation. Invited submission to 'The Role of Biomaterials in Overcoming Barriers to Regeneration in the Central Nervous System' in *Biomedical Materials*, Guest Edited by Molly Shoichet. *(under revision)*

18. **Loeblein, M.,** Bolker, A., Ngoh, Z. L., Li, L., Tsang, S. H. Pawlik, M., Verker, R. & Teo, E. H. T. (2017) 3D-foam/shape memory polymer-hybrid with improved thermo-electrical performance and self-heating and timed actuation. *(in preparation)*

Patents

1. **Loeblein, M.,** Tsang, S. H., Teo, H. T. E., Bolker, A., Atar, N., Verker, R. & Grossman, E. (2014). *Technology Disclosure*, TD/281/14 – PAT/281/14/15/US PRV. PCT/IB2016/052570

2. **Loeblein, M.,** Tsang, S. H. & Teo, H. T. E. (2016). *Technology Disclosure*, TD/331/15 – PAT/331/15/16/SG PRV (Singapore provisional application number 10201601834U). PCT/SG2017/050113

3. **Loeblein, M.,** Tsang, S. H. & Teo, H. T. E. (2016). *Technology Disclosure*, TD/322/16 – PAT/322/16/16/SG PRV.

4. Pawlik, M., **Loeblein, M.,** Tsang, S. H., Teo, H. T. E., Coquet, P., Merlet, T. & Foncin, J. (2017). *Technology Disclosure*, TD/023/17.

Conferences

1. **Loeblein, M.,** Tay, R. Y., Tsang, S. H. & Teo, E. H. T. (2015). Three Dimensional Boron Nitride – Carbon Network Infused Polymer: High Thermal Conductivity with Tunable Electrical Behavior for the Next Generation Flexible Electronic. *MRS Spring 2015 Conference*, San Francisco, California, Oral presentation.

2. Silverman, I., Ron, G., Teo, E. H . T., Bolker, A., Grossman, E., **Loeblein, M.** & Tsang, S. H. (2015) Conceptual Design of a 3D-C High Intensity Positron Source. *AccApp15*, Washington, DC, Poster presentation.

3. **Loeblein, M.,** Bolker, A., Tsang, S. H., Atar, N., Uzan-Saguy, C., Verker, R., Gouzman, I., Grossman, E. & Teo, E. H. T. (2016) Studies of a New Class of High Electro-Thermal Performing Polyimide Embedded with 3D Scaffold in the Harsh Environment of Outer Space. *APS March Meeting 2016*, Baltimore, Maryland, Oral Presentation.

4. **Loeblein, M.,** Tsang, S. H., Yong, H., Zhang, X. W. & Teo, E. H. T. (2016) Heat Dissipation Enhancement of 2.5D Package with 3D Graphene & 3D Boron Nitride Networks as Thermal Interface Material (TIM). *Electronic Components and Technology Conference (ECTC), 2016 IEEE 66th*, Las Vegas, Nevada, Oral Presentation.

5. Leong, F. N., **Loeblein, M.,** Tsang, S. H. & Teo, E. H. T. (2016) Enhanced Thermal and Electrical Properties of Polymer by Infusion of 3D Graphene Foam. *International Symposium on Polymer Analysis and Characterization 2016*, Singapore, Oral Presentation.

6. Ngoh, Z. L., **Loeblein, M.,** Tsang, S. H. & Teo, E. H. T. (2016) Development of three-dimensional graphene (3D-C) infused shape memory polymer (SMP) for the application in satellite research. *International Symposium on Polymer Analysis and Characterization 2016*, Singapore, Poster Presentation.

7. Perry, G., **Loeblein, M.,** Tsang, S. H., Xiao, W., Collard, D., Coquet, P., Sakai, Y. & Teo, E. H. T. (2016) 3D Graphene Scaffold for Tissue Engineering and Regenerative Medicine. *MRS Fall 2016 Conference*, Poster Presentation.

(¶ equal contribution)

References

1. Novoselov, K. S.; Mishchenko, A.; Carvalho, A.; Castro Neto, A. H. *Science* **2016,** 353, (6298).
2. Novoselov, K. S.; Geim, A. K.; Morozov, S. V.; Jiang, D.; Zhang, Y.; Dubonos, S. V.; Grigorieva, I. V.; Firsov, A. A. *Science* **2004,** 306, (5696), 666-669.
3. Geim, A. K.; Novoselov, K. S. *Nat. Mater.* **2007,** 6, (3), 183-191.
4. Balandin, A. A.; Ghosh, S.; Bao, W.; Calizo, I.; Teweldebrhan, D.; Miao, F.; Lau, C. N. *Nano Lett.* **2008,** 8, (3), 902-907.
5. Novoselov, K. S.; Falko, V. I.; Colombo, L.; Gellert, P. R.; Schwab, M. G.; Kim, K. *Nature* **2012,** 490, (7419), 192-200.
6. Staley, N. E.; Wu, J.; Eklund, P.; Liu, Y.; Li, L.; Xu, Z. *Phys. Rev. B: Condens. Matter* **2009,** 80, (18), 184505.
7. Mak, K. F.; Lee, C.; Hone, J.; Shan, J.; Heinz, T. F. *Phys. Rev. Lett.* **2010,** 105, (13), 136805.
8. Li, L.; Yu, Y.; Ye, G. J.; Ge, Q.; Ou, X.; Wu, H.; Feng, D.; Chen, X. H.; Zhang, Y. *Nat Nano* **2014,** 9, (5), 372-377.
9. Dean, C. R.; Young, A. F.; Meric, I.; Lee, C.; Wang, L.; Sorgenfrei, S.; Watanabe, K.; Taniguchi, T.; Kim, P.; Shepard, K. *Nature nanotechnology* **2010,** 5, (10), 722-726.
10. Zhang, Y.; Zhang, L.; Zhou, C. *Acc. Chem. Res.* **2013,** 46, (10), 2329-2339.
11. Balandin, A. A. *Nat Mater* **2011,** 10, (8), 569-581.
12. Zurutuza, A.; Marinelli, C. *Nat Nano* **2014,** 9, (10), 730-734.
13. Li, X.; Cai, W.; An, J.; Kim, S.; Nah, J.; Yang, D.; Piner, R.; Velamakanni, A.; Jung, I.; Tutuc, E.; Banerjee, S. K.; Colombo, L.; Ruoff, R. S. *Science* **2009,** 324, (5932), 1312-1314.
14. Emtsev, K. V.; Bostwick, A.; Horn, K.; Jobst, J.; Kellogg, G. L.; Ley, L.; McChesney, J. L.; Ohta, T.; Reshanov, S. A.; Rohrl, J.; Rotenberg, E.; Schmid, A. K.; Waldmann, D.; Weber, H. B.; Seyller, T. *Nat Mater* **2009,** 8, (3), 203-207.
15. Tay, R. Y.; Griep, M. H.; Mallick, G.; Tsang, S. H.; Singh, R. S.; Tumlin, T.; Teo, E. H. T.; Karna, S. P. *Nano Lett.* **2014,** 14, (2), 839-846.
16. Tay, R. Y.; Park, H. J.; Ryu, G. H.; Tan, D.; Tsang, S. H.; Li, H.; Liu, W.; Teo, E. H. T.; Lee, Z.; Lifshitz, Y. *Nanoscale* **2016,** 8, (4), 2434-2444.
17. Chen, Z.; Ren, W.; Gao, L.; Liu, B.; Pei, S.; Cheng, H.-M. *Nat. Mater.* **2011,** 10, (6), 424-428.
18. Yin, J.; Li, X.; Zhou, J.; Guo, W. *Nano Lett.* **2013,** 13, (7), 3232-3236.
19. Fang, Q.; Shen, Y.; Chen, B. *Chem. Eng. J.* **2015,** 264, 753-771.
20. Pettes, M. T.; Ji, H.; Ruoff, R. S.; Shi, L. *Nano Lett.* **2012,** 12, (6), 2959-2964.
21. Chen, Z.; Xu, C.; Ma, C.; Ren, W.; Cheng, H.-M. *Adv. Mater.* **2013,** 25, (9), 1296-1300.
22. Ma, Y.; Chen, Y. *National Science Review* **2015,** 2, (1), 40-53.
23. Yan, Z.; Yao, W.; Hu, L.; Liu, D.; Wang, C.; Lee, C.-S. *Nanoscale* **2015,** 7, (13), 5563-5577.
24. Fan, X.; Chen, X.; Dai, L. *Current Opinion in Colloid & Interface Science* **2015,** 20, (5), 429-438.
25. Li, C.; Zhang, X.; Wang, K.; Zhang, H.-t.; Sun, X.-z.; Ma, Y.-w. *New Carbon Materials* **2015,** 30, (3), 193-206.
26. Mao, S.; Lu, G.; Chen, J. *Nanoscale* **2015,** 7, (16), 6924-6943.
27. Han, S.; Wu, D.; Li, S.; Zhang, F.; Feng, X. *Adv. Mater.* **2014,** 26, (6), 849-64.

28. Yavari, F.; Chen, Z.; Thomas, A. V.; Ren, W.; Cheng, H.-M.; Koratkar, N. *Sci. Rep.* **2011,** 1.
29. Li, N.; Zhang, Q.; Gao, S.; Song, Q.; Huang, R.; Wang, L.; Liu, L.; Dai, J.; Tang, M.; Cheng, G. *Sci. Rep.* **2013,** 3.
30. Crowder, S. W.; Prasai, D.; Rath, R.; Balikov, D. A.; Bae, H.; Bolotin, K. I.; Sung, H.-J. *Nanoscale* **2013,** 5, (10), 4171-4176.
31. Dong, X.-C.; Xu, H.; Wang, X.-W.; Huang, Y.-X.; Chan-Park, M. B.; Zhang, H.; Wang, L.-H.; Huang, W.; Chen, P. *ACS Nano* **2012,** 6, (4), 3206-3213.
32. Wang, M.; Duan, X.; Xu, Y.; Duan, X. *ACS Nano* **2016,** 10, (8), 7231-7247.
33. Moore, A. L.; Shi, L. *Mater. Today* **2014,** 17, (4), 163-174.
34. Choudhary, V.; Dhawan, S.; Saini, P., 4. Polymer based nanocomposites for electromagnetic interference (EMI) shielding.
35. Song, W.-L.; Cao, M.-S.; Lu, M.-M.; Bi, S.; Wang, C.-Y.; Liu, J.; Yuan, J.; Fan, L.-Z. *Carbon* **2014,** 66, (0), 67-76.
36. Liang, J.; Wang, Y.; Huang, Y.; Ma, Y.; Liu, Z.; Cai, J.; Zhang, C.; Gao, H.; Chen, Y. *Carbon* **2009,** 47, (3), 922-925.
37. Shehzad, K.; Xu, Y.; Gao, C.; Duan, X. *Chemical Society Reviews* **2016,** 45, (20), 5541-5588.
38. Zhou, M.; Lin, T.; Huang, F.; Zhong, Y.; Wang, Z.; Tang, Y.; Bi, H.; Wan, D.; Lin, J. *Adv. Funct. Mater.* **2013,** 23, (18), 2263-2269.
39. Cao, X.; Shi, Y.; Shi, W.; Lu, G.; Huang, X.; Yan, Q.; Zhang, Q.; Zhang, H. *Small* **2011,** 7, (22), 3163-3168.
40. Tao, O.; Yuanping, C.; Yuee, X.; Kaike, Y.; Zhigang, B.; Jianxin, Z. *Nanotechnology* **2010,** 21, (24), 245701 (6 pp.).
41. Song, L.; Ci, L.; Lu, H.; Sorokin, P. B.; Jin, C.; Ni, J.; Kvashnin, A. G.; Kvashnin, D. G.; Lou, J.; Yakobson, B. I.; Ajayan, P. M. *Nano Lett.* **2010,** 10, (8), 3209-3215.
42. Lipp, A.; Schwetz, K. A.; Hunold, K. *J. Eur. Ceram. Soc.* **1989,** 5, (1), 3-9.
43. Watanabe, K.; Taniguchi, T.; Kanda, H. *Nat. Mater.* **2004,** 3, (6), 404-9.
44. Rouquerol, J.; Avnir, D.; Fairbridge, C.; Everett, D.; Haynes, J.; Pernicone, N.; Ramsay, J.; Sing, K.; Unger, K. *Pure Appl. Chem.* **1994,** 66, (8), 1739-1758.
45. Deng, W.; Fang, Q. L.; Zhou, X. F.; Cao, H. L.; Liu, Z. P. *Rsc Advances* **2016,** 6, (25), 20843-20849.
46. Luo, J.; Lai, J. P.; Zhang, N.; Liu, Y. B.; Liu, R.; Liu, X. Y. *Acs Sustainable Chemistry & Engineering* **2016,** 4, (3), 1404-1413.
47. Li, J. H.; Zhang, G. P.; Sun, R.; Wong, C. P. *2016 China Semiconductor Technology International Conference (Cstic)* **2016**.
48. Zhang, L.; Zhang, F.; Yang, X.; Long, G.; Wu, Y.; Zhang, T.; Leng, K.; Huang, Y.; Ma, Y.; Yu, A. *Sci. Rep.* **2013,** 3.
49. Chen, W.; Yan, L. *Nanoscale* **2011,** 3, (8), 3132-3137.
50. Shi, Y. C.; Wang, A. J.; Wu, X. L.; Chen, J. R.; Feng, J. J. *J. Colloid Interface Sci.* **2016,** 484, 254-262.
51. Zhang, W. H.; Sun, Y. Y.; Liu, T. T.; Li, D. S.; Hou, C. L.; Gao, L.; Liu, Y. Q. *Applied Physics a-Materials Science & Processing* **2016,** 122, (3).
52. Worsley, M. A.; Pauzauskie, P. J.; Olson, T. Y.; Biener, J.; Satcher Jr, J. H.; Baumann, T. F. *J. Am. Chem. Soc.* **2010,** 132, (40), 14067-14069.
53. Wu, D.; Zhang, F.; Liang, H.; Feng, X. *Chemical Society Reviews* **2012,** 41, (18), 6160-6177.
54. Niu, Z.; Chen, J.; Hng, H. H.; Ma, J.; Chen, X. *Adv. Mater.* **2012,** 24, (30), 4144-4150.
55. Feng, B.; Xu, K.; Huang, A. *Desalination* **2016,** 394, 123-130.

56. Lv, L.; Zhang, P.; Cheng, H.; Zhao, Y.; Zhang, Z.; Shi, G.; Qu, L. *Small* **2016,** 12, (24), 3229-3234.
57. Vinod, S.; Tiwary, C. S.; Machado, L. D.; Ozden, S.; Vajtai, R.; Galvao, D. S.; Ajayan, P. M. *Nanoscale* **2016,** 8, (35), 15857-15863.
58. Xue, Y. M.; Dai, P. C.; Jiang, X. F.; Wang, X. B.; Zhang, C.; Tang, D. M.; Weng, Q. H.; Wang, X.; Pakdel, A.; Tang, C. C.; Bando, Y.; Golberg, D. *Journal of Materials Chemistry A* **2016,** 4, (4), 1469-1478.
59. Gautam, C.; Tiwary, C. S.; Machado, L. D.; Jose, S.; Ozden, S.; Biradar, S.; Galvao, D. S.; Sonker, R. K.; Yadav, B. C.; Vajtai, R.; Ajayan, P. M. *RSC Advances* **2016,** 6, (91), 87888-87896.
60. Zhao, H.; Song, X.; Zeng, H. *NPG Asia Mater* **2015,** 7, e168.
61. Cao, F.; Ding, Y.; Chen, L.; Chen, C.; Fang, Z. *Materials & Design* **2014,** 54, (0), 610-615.
62. Wang, X.; Zhang, Y.; Zhi, C.; Wang, X.; Tang, D.; Xu, Y.; Weng, Q.; Jiang, X.; Mitome, M.; Golberg, D. *Nat. Commun.* **2013,** 4.
63. Yuan, Y.; Ding, Y.; Wang, C.; Xu, F.; Lin, Z.; Qin, Y.; Li, Y.; Yang, M.; He, X.; Peng, Q.; Li, Y. *ACS Applied Materials & Interfaces* **2016,** 8, (26), 16852-16861.
64. Wei, W.; Sun, K.; Hu, Y. H. *Journal of Materials Chemistry A* **2016,** 4, (31), 12054-12057.
65. Zu, S.-Z.; Han, B.-H. *The Journal of Physical Chemistry C* **2009,** 113, (31), 13651-13657.
66. Xu, Y.; Wu, Q.; Sun, Y.; Bai, H.; Shi, G. *ACS Nano* **2010,** 4, (12), 7358-7362.
67. Huang, C.; Bai, H.; Li, C.; Shi, G. *Chem. Commun.* **2011,** 47, (17), 4962-4964.
68. Sui, Z.; Zhang, X.; Lei, Y.; Luo, Y. *Carbon* **2011,** 49, (13), 4314-4321.
69. Tynan, M. K.; Johnson, D. W.; Dobson, B. P.; Coleman, K. S. *Nanoscale* **2016,** 8, (27), 13303-13310.
70. Maiyalagan, T.; Dong, X.; Chen, P.; Wang, X. *J. Mater. Chem.* **2012,** 22, (12), 5286-5290.
71. Ashton, T. S.; Moore, A. L. *Journal of Materials Science* **2015,** 50, (18), 6220-6226.
72. Jiang, W.; Xin, H.; Li, W. *Mater. Lett.* **2016,** 162, 105-109.
73. Sha, J.; Gao, C.; Lee, S.-K.; Li, Y.; Zhao, N.; Tour, J. M. *ACS Nano* **2016,** 10, (1), 1411-1416.
74. Du, X.; Wu, W.; An, C.; Cheng, Y.; Zhang, X.; Sun, Y.; Liu, Y. *International Journal of Energy Research* **2016,** 40, (12), 1731-1738.
75. Zhang, L.; DeArmond, D.; Alvarez, N. T.; Zhao, D.; Wang, T.; Hou, G.; Malik, R.; Heineman, W. R.; Shanov, V. *Journal of Materials Chemistry A* **2016,** 4, (5), 1876-1886.
76. Drieschner, S.; Weber, M.; Wohlketzetter, J.; Vieten, J.; Makrygiannis, E.; Blaschke, B. M.; Morandi, V.; Colombo, L.; Bonaccorso, F.; Garrido, J. A. *2d Materials* **2016,** 3, (4).
77. Choi, B. G.; Yang, M.; Hong, W. H.; Choi, J. W.; Huh, Y. S. *ACS Nano* **2012,** 6, (5), 4020-4028.
78. Sun, L.; Tian, C.; Li, M.; Meng, X.; Wang, L.; Wang, R.; Yin, J.; Fu, H. *Journal of Materials Chemistry A* **2013,** 1, (21), 6462-6470.
79. Maleki, M.; Shokouhimehr, M.; Karimian, H.; Beitollahi, A. *Rsc Advances* **2016,** 6, (56), 51426-51434.
80. Xia, X.; Tu, J.; Zhang, Y.; Mai, Y.; Wang, X.; Gu, C.; Zhao, X. *The Journal of Physical Chemistry C* **2011,** 115, (45), 22662-22668.

81. Sivaprakash, S.; Sivaprakash, P. *Materials Research Express* **2016,** 3, (7), 075020.
82. Gutiérrez, M. C.; García-Carvajal, Z. Y.; Jobbágy, M.; Rubio, F.; Yuste, L.; Rojo, F.; Ferrer, M. L.; del Monte, F. *Adv. Funct. Mater.* **2007,** 17, (17), 3505-3513.
83. Gutiérrez, M. C.; Ferrer, M. L.; del Monte, F. *Chem. Mater.* **2008,** 20, (3), 634-648.
84. Wu, H.; Lu, L.; Zhang, Y.; Sun, Z.; Qian, L. *Colloids Surf. Physicochem. Eng. Aspects* **2016,** 502, 26-33.
85. Vickery, J. L.; Patil, A. J.; Mann, S. *Adv. Mater.* **2009,** 21, (21), 2180-2184.
86. Li, X.; Huang, X.; Liu, D.; Wang, X.; Song, S.; Zhou, L.; Zhang, H. *The Journal of Physical Chemistry C* **2011,** 115, (44), 21567-21573.
87. Xiao, L.; Wu, D.; Han, S.; Huang, Y.; Li, S.; He, M.; Zhang, F.; Feng, X. *ACS applied materials & interfaces* **2013,** 5, (9), 3764-3769.
88. Wu, Z.-S.; Sun, Y.; Tan, Y.-Z.; Yang, S.; Feng, X.; Müllen, K. *J. Am. Chem. Soc.* **2012,** 134, (48), 19532-19535.
89. Xue, Y.; Liu, J.; Chen, H.; Wang, R.; Li, D.; Qu, J.; Dai, L. *Angew. Chem. Int. Ed.* **2012,** 51, (48), 12124-12127.
90. Bi, H.; Huang, F.; Liang, J.; Tang, Y.; Lu, X.; Xie, X.; Jiang, M. *J. Mater. Chem.* **2011,** 21, (43), 17366-17370.
91. Lee, J.-S.; Ahn, H.-J.; Yoon, J.-C.; Jang, J.-H. *Phys. Chem. Chem. Phys.* **2012,** 14, (22), 7938-7943.
92. Roy-Mayhew, J. D.; Aksay, I. A. *Chem. Rev.* **2014**.
93. Tang, B.; Hu, G.; Gao, H.; Shi, Z. *J. Power Sources* **2013,** 234, (0), 60-68.
94. Wang, H.; Sun, K.; Tao, F.; Stacchiola, D. J.; Hu, Y. H. *Angew. Chem.* **2013,** 125, (35), 9380-9384.
95. Han, S.; Wu, D.; Li, S.; Zhang, F.; Feng, X. *Advanced Materials* **2014,** 26, (6), 849-864.
96. Liu, J.; Wang, J.; Wang, T.; Li, D.; Xi, F.; Wang, J.; Wang, E. *Biosens. Bioelectron.* **2015,** 65, (0), 281-286.
97. Xu, R.; Lu, Y.; Jiang, C.; Chen, J.; Mao, P.; Gao, G.; Zhang, L.; Wu, S. *ACS applied materials & interfaces* **2014,** 6, (16), 13455-13460.
98. Samad, Y. A.; Li, Y.; Schiffer, A.; Alhassan, S. M.; Liao, K. *Small* **2015,** 11, (20), 2380-2385.
99. Jeong, Y. R.; Park, H.; Jin, S. W.; Hong, S. Y.; Lee, S. S.; Ha, J. S. *Adv. Funct. Mater.* **2015,** 25, (27), 4228-4236.
100. Chen, M.; Zhang, L.; Duan, S.; Jing, S.; Jiang, H.; Li, C. *Adv. Funct. Mater.* **2014,** 24, (47), 7548-7556.
101. Samad, Y. A.; Li, Y.; Alhassan, S. M.; Liao, K. *ACS applied materials & interfaces* **2015,** 7, (17), 9195-9202.
102. Chen, M.; Duan, S.; Zhang, L.; Wang, Z.; Li, C. *Chem. Commun.* **2015,** 51, (15), 3169-3172.
103. Zhang, X.; Liu, D.; Yang, L.; Zhou, L.; You, T. *Journal of Materials Chemistry A* **2015,** 3, (18), 10031-10037.
104. Shen, Y.; Fang, Q.; Chen, B. *Environ. Sci. Technol.* **2014,** 49, (1), 67-84.
105. Zhang, X.; Yeung, K. K.; Gao, Z.; Li, J.; Sun, H.; Xu, H.; Zhang, K.; Zhang, M.; Chen, Z.; Yuen, M. M. *Carbon* **2014,** 66 201-209.
106. Li, M.; Sun, Y.; Xiao, H.; Hu, X.; Yue, Y. *Nanotechnology* **2015,** 26, (10), 105703.
107. Hu, C.; Xue, J.; Dong, L.; Jiang, Y.; Wang, X.; Qu, L.; Dai, L. *ACS Nano* **2016,** 10, (1), 1325-1332.

108. Ahn, H. S.; Kim, J. M.; Park, C.; Jang, J.-W.; Lee, J. S.; Kim, H.; Kaviany, M.; Kim, M. H. *Scientific reports* **2013,** 3.
109. Thiyagarajan, P.; Oh, M.-W.; Yoon, J.-C.; Jang, J.-H. *Appl. Phys. Lett.* **2014,** 105, (3), 033905.
110. Zhao, Y.-H.; Wu, Z.-K.; Bai, S.-L. *Composites Part A: Applied Science and Manufacturing* **2015,** 72, 200-206.
111. Liu, Z.; Shen, D.; Yu, J.; Dai, W.; Li, C.; Du, S.; Jiang, N.; Li, H.; Lin, C.-T. *RSC Advances* **2016,** 6, (27), 22364-22369.
112. Zhao, Y.-H.; Zhang, Y.-F.; Bai, S.-L. *Composites Part A: Applied Science and Manufacturing* **2016,** 85, 148-155.
113. Zhao, Y.-H.; Wu, Z.-K.; Bai, S.-L. *Int. J. Heat Mass Transfer* **2016,** 101, 470-475.
114. Fedden, A.; Franke, M. In *Graphitized carbon foam with phase change material for thermal energy storage*, Proceedings of the Ninth AIAA/ASME Joint Thermophysics and Heat Transfer Conference, 2006.
115. Yang, J.; Qi, G.-Q.; Liu, Y.; Bao, R.-Y.; Liu, Z.-Y.; Yang, W.; Xie, B.-H.; Yang, M.-B. *Carbon* **2016,** 100, 693-702.
116. Yang, J.; Zhang, E.; Li, X.; Zhang, Y.; Qu, J.; Yu, Z.-Z. *Carbon* **2016,** 98, 50-57.
117. Zhang, L.; Li, R.; Tang, B.; Wang, P. *Nanoscale* **2016,** 8, (30), 14600-14607.
118. Paul, R.; Voevodin, A.; Hu, J.; Amama, P.; Ganguli, S.; Roy, A.; Zemlyanov, D.; Fisher, T. S. *Thin Solid Films* **2013,** 528, 187-193.
119. Loeblein, M.; Tay, R. Y.; Tsang, S. H.; Ng, W. B.; Teo, E. H. T. *Small* **2014,** 10, (15), 2992-2999.
120. Min, S.; Blumm, J.; Lindemann, A. *Thermochim. Acta* **2007,** 455, (1–2), 46-49.
121. van der PAUYV, L. **1958**.
122. Tay, R. Y.; Wang, X.; Tsang, S. H.; Loh, G. C.; Singh, R. S.; Li, H.; Mallick, G.; Teo, E. *Journal of Materials Chemistry C* **2013**.
123. Li, X.; Yin, J.; Zhou, J.; Guo, W. *Nanotechnology* **2014,** 25, (10), 105701.
124. Kim, K. K.; Hsu, A.; Jia, X.; Kim, S. M.; Shi, Y.; Hofmann, M.; Nezich, D.; Rodriguez-Nieva, J. F.; Dresselhaus, M.; Palacios, T. *Nano Lett.* **2011,** 12, (1), 161-166.
125. Kim, S. M.; Hsu, A.; Araujo, P. T.; Lee, Y.-H.; Palacios, T.; Dresselhaus, M.; Idrobo, J.-C.; Kim, K. K.; Kong, J. *Nano Lett.* **2013,** 13, (3), 933-941.
126. Ferrari, A. C.; Meyer, J. C.; Scardaci, V.; Casiraghi, C.; Lazzeri, M.; Mauri, F.; Piscanec, S.; Jiang, D.; Novoselov, K. S.; Roth, S.; Geim, A. K. *Phys. Rev. Lett.* **2006,** 97, (18), 187401.
127. Hwang, J.-S.; Lin, Y.-H.; Hwang, J.-Y.; Chang, R.; Chattopadhyay, S.; Chen, C.-J.; Chen, P.; Chiang, H.-P.; Tsai, T.-R.; Chen, L.-C. *Nanotechnology* **2013,** 24, (1), 015702.
128. Reich, S.; Ferrari, A.; Arenal, R.; Loiseau, A.; Bello, I.; Robertson, J. *Phys. Rev. B: Condens. Matter* **2005,** 71, (20), 205201.
129. Gorbachev, R. V.; Riaz, I.; Nair, R. R.; Jalil, R.; Britnell, L.; Belle, B. D.; Hill, E. W.; Novoselov, K. S.; Watanabe, K.; Taniguchi, T.; Geim, A. K.; Blake, P. *Small* **2011,** 7, (4), 465-468.
130. Ci, L.; Song, L.; Jin, C.; Jariwala, D.; Wu, D.; Li, Y.; Srivastava, A.; Wang, Z. F.; Storr, K.; Balicas, L.; Liu, F.; Ajayan, P. M. *Nat Mater* **2010,** 9, (5), 430-435.
131. Chang, C.-K.; Kataria, S.; Kuo, C.-C.; Ganguly, A.; Wang, B.-Y.; Hwang, J.-Y.; Huang, K.-J.; Yang, W.-H.; Wang, S.-B.; Chuang, C.-H.; Chen, M.; Huang, C.-I.; Pong, W.-F.; Song, K.-J.; Chang, S.-J.; Guo, J.-H.; Tai, Y.; Tsujimoto, M.; Isoda, S.; Chen, C.-W.; Chen, L.-C.; Chen, K.-H. *ACS Nano* **2012,** 7, (2), 1333-1341.

132. Shi, Y.; Hamsen, C.; Jia, X.; Kim, K. K.; Reina, A.; Hofmann, M.; Hsu, A. L.; Zhang, K.; Li, H.; Juang, Z.-Y.; Dresselhaus, M. S.; Li, L.-J.; Kong, J. *Nano Lett.* **2010,** 10, (10), 4134-4139.
133. Pop, E.; Varshney, V.; Roy, A. K. *MRS Bull.* **2012,** 37, (12), 1273-1281.
134. Bresnehan, M. S.; Hollander, M. J.; Wetherington, M.; Wang, K.; Miyagi, T.; Pastir, G.; Snyder, D. W.; Gengler, J. J.; Voevodin, A. A.; Mitchel, W. C.; Robinson, J. A. **2013**, 1-13.
135. Huang, H.; Liu, C.; Wu, Y.; Fan, S. *Adv. Mater.* **2005,** 17, (13), 1652-1656.
136. Shahil, K. M.; Balandin, A. A. *Nano Lett.* **2012,** 12, (2), 861-867.
137. Michel, K. H.; Verberck, B. *physica status solidi (b)* **2009,** 246, (11-12), 2802-2805.
138. Sevin√ßli, H.; Li, W.; Mingo, N.; Cuniberti, G.; Roche, S. *Phys. Rev. B: Condens. Matter* **2011,** 84, (20), 205444.
139. Jiang, J.-W.; Wang, J.-S. *EPL (Europhysics Letters)* **2011,** 96, (1), 16003.
140. Schuetz, M.; Glicksman, L. *Journal of Cellular Plastics* **1984,** 20, (2), 114-121.
141. Balandin, A. A. In *In-plane and cross-plane thermal conductivity of graphene: Applications in thermal interface materials*, Carbon Nanotubes, Graphene, and Associated Devices IV, 23-24 Aug. 2011, USA, 2011; SPIE - The International Society for Optical Engineering: USA, p 810107 (8 pp.).
142. Koh, Y. K.; Bae, M.-H.; Cahill, D. G.; Pop, E. *Nano Lett.* **2010,** 10, (11), 4363-4368.
143. Jo, I.; Pettes, M. T.; Kim, J.; Watanabe, K.; Taniguchi, T.; Yao, Z.; Shi, L. *Nano Lett.* **2013,** 13, (2), 550-554.
144. Zhou, T.; Bobal, T.; Oud, M.; Songliang, J., Au/Sn Solder Alloy and Its Applications in Electronics Packaging. In *Coining Inc*.
145. Zhang, X.; Yeung, K. K.; Gao, Z.; Li, J.; Sun, H.; Xu, H.; Zhang, K.; Zhang, M.; Chen, Z.; Yuen, M. M. F.; Yang, S. *Carbon*, (0).
146. Xu, S.; Rezvanian, O.; Peters, K.; Zikry, M. *Nanotechnology* **2013,** 24, (15), 155706.
147. Pang, H.; Chen, T.; Zhang, G.; Zeng, B.; Li, Z.-M. *Mater. Lett.* **2010,** 64, (20), 2226-2229.
148. Collaboration *IEEE standard method for measuring the effectiveness of electromagnetic shielding enclosures*; Inst. Electr. & Electron. Eng., New York, NY, USA: USA, 1998; p v+39.
149. Markham, D. *Materials & Design* **1999,** 21, (1), 45-50.
150. Förch, R.; Schönherr, H.; Jenkins, A. T. A., *Surface design: Applications in bioscience and nanotechnology*. John Wiley & Sons: 2009.
151. Due, J.; Robinson, A. J. *Appl. Therm. Eng.* **2013,** 50, (1), 455-463.
152. Goel, N.; Anoop, T.; Bhattacharya, A.; Cervantes, J.; Mongia, R. K.; Machiroutu, S. V.; Lin, H.-L.; Huang, Y.-C.; Fan, K.-C.; Denq, B.-L. In *Technical review of characterization methods for thermal interface materials (TIM)*, Thermal and Thermomechanical Phenomena in Electronic Systems, 2008. ITHERM 2008. 11th Intersociety Conference on, 2008; IEEE: pp 248-258.
153. O'neill Michael, J., Differential microcalorimeter. Google Patents: 1966.
154. Loeblein, M.; Perry, G.; Tsang, S. H.; Xiao, W.; Collard, D.; Coquet, P.; Sakai, Y.; Teo, E. H. *Adv. Healthcare Mater.* **2016,** 5, (10), 1177-91.
155. Bello, A.; Fabiane, M.; Dodoo-Arhin, D.; Ozoemena, K. I.; Manyala, N. *J. Phys. Chem. Solids* **2014,** 75, (1), 109-114.
156. Shin, Y. J.; Wang, Y.; Huang, H.; Kalon, G.; Wee, A. T. S.; Shen, Z.; Bhatia, C. S.; Yang, H. *Langmuir* **2010,** 26, (6), 3798-3802.

157. You, S. A.; Kwon, O. S.; Jang, J. *J. Mater. Chem.* **2012,** 22, (34), 17805-17812.
158. Ovejero, G.; Sotelo, J.; Romero, M.; Rodríguez, A.; Ocana, M.; Rodríguez, G.; Garcia, J. *Ind. Eng. Chem. Res.* **2006,** 45, (7), 2206-2212.
159. Wang, G.; Wang, B.; Wang, X.; Park, J.; Dou, S.; Ahn, H.; Kim, K. *J. Mater. Chem.* **2009,** 19, (44), 8378-8384.
160. Muszynski, R.; Seger, B.; Kamat, P. V. *The Journal of Physical Chemistry C* **2008,** 112, (14), 5263-5266.
161. Chen, Q.; Zhang, L.; Chen, G. *Anal. Chem.* **2011,** 84, (1), 171-178.
162. Hwang, J.; Yoon, T.; Jin, S. H.; Lee, J.; Kim, T. S.; Hong, S. H.; Jeon, S. *Adv. Mater.* **2013,** 25, (46), 6724-9.
163. Ramanath, G.; Cui, G.; Ganesan, P.; Guo, X.; Ellis, A. V.; Stukowski, M.; Vijayamohanan, K.; Doppelt, P.; Lane, M. *Appl. Phys. Lett.* **2003,** 83, (2), 383-385.
164. Gandhi, D. D.; Lane, M.; Zhou, Y.; Singh, A. P.; Nayak, S.; Tisch, U.; Eizenberg, M.; Ramanath, G. *Nature* **2007,** 447, (7142), 299-302.
165. Witucki, G. L. *Journal of coatings technology* **1993,** 65, 57-57.
166. Kaur, S.; Raravikar, N.; Helms, B. A.; Prasher, R.; Ogletree, D. F. *Nat. Commun.* **2014,** 5.
167. Pasternack, R. M.; Rivillon Amy, S.; Chabal, Y. J. *Langmuir* **2008,** 24, (22), 12963-12971.
168. Xu, R.; Lu, Y.; Jiang, C.; Chen, J.; Mao, P.; Gao, G.; Zhang, L.; Wu, S. *ACS Applied Materials & Interfaces* **2014,** 6, (16), 13455-13460.
169. Jeong, Y. R.; Park, H.; Jin, S. W.; Hong, S. Y.; Lee, S.-S.; Ha, J. S. *Adv. Funct. Mater.* **2015,** 25, (27), 4228-4236.
170. Oh, W.; Shin, T. J.; Ree, M.; Jin, M. Y.; Char, K. *Macromol. Chem. Phys.* **2002,** 203, (5-6), 801-811.
171. Ratta, V. Crystallization, morphology, thermal stability and adhesive properties of novel high performance semicrystalline polyimides. Virginia Polytechnic Institute and State University, 1999.
172. Feger, C., *Advances in polyimide: science and technology*. CRC Press: 1993.
173. Atar, N.; Grossman, E.; Gouzman, I.; Bolker, A.; Hanein, Y. *ACS applied materials & interfaces* **2014,** 6, (22), 20400-20407.
174. Pimenta, M.; Dresselhaus, G.; Dresselhaus, M. S.; Cancado, L.; Jorio, A.; Saito, R. *Phys. Chem. Chem. Phys.* **2007,** 9, (11), 1276-1290.
175. Grossman, E.; Lifshitz, Y.; Wolan, J. T.; Mount, C. K.; Hoflund, G. B. *Journal of Spacecraft and Rockets* **1999,** 36, (1), 75-78.
176. Xiao, X.; Xie, T.; Cheng, Y.-T. *J. Mater. Chem.* **2010,** 20, (17), 3508-3514.
177. Rousseau, I. A. *Polym. Eng. Sci.* **2008,** 48, (11), 2075-2089.
178. Jia, J.; Sun, X.; Lin, X.; Shen, X.; Mai, Y. W.; Kim, J. K. *ACS Nano* **2014,** 8, (6), 5774-83.
179. http://www.businesswire.com/news/home/20151216005646/en/IDTechEx-Research-More-than-Moore-electronics-packaging, retrieved 16 December 2015
180. Tong, X. C., *Advanced materials for thermal management of electronic packaging*. Springer Science & Business Media: 2011; Vol. 30.
181. Viswanath, R.; Wakharkar, V.; Watwe, A.; Lebonheur, V. *Intel Technology Journal Q3* **2000**.
182. Prasher, R. *Proc. IEEE* **2006,** 94, (8), 1571-1586.
183. Schulz, M., The Challenging Task of Thermal Management. In *PCIM, Nürnberg 2011*, 2011.
184. Prasher, R.; Chiu, C.-P., Thermal Interface Materials. In *Materials for Advanced Packaging*, Lu, D.; Wong, C. P., Eds. Springer US: 2009; pp 437-458.

185. Nath, P.; Chopra, K. *Thin Solid Films* **1974,** 20, (1), 53-62.
186. Green, R. E., *Machinery's handbook*. Industrial Press: 1992; Vol. 24.
187. Farhad, S.; Whalley, D. C.; Conway, P. P. In *Thermal Interface Materials - A Review of the State of the Art*, Electronics Systemintegration Technology Conference, 2006. 1st, 5-7 Sept. 2006, 2006; pp 1292-1302.
188. Liu, J.; Michel, B.; Rencz, M.; Tantolin, C.; Sarno, C.; Miessner, R.; Schuett, K.-V.; Tang, X.; Demoustier, S.; Ziaei, A. In *Recent progress of thermal interface material research-an overview*, Thermal Inveatigation of ICs and Systems, 2008. THERMINIC 2008. 14th International Workshop on, 2008; IEEE: pp 156-162.
189. Li, Y.; Wong, C. P. *Mater. Sci. Eng. R Rep.* **2006,** 51, (1–3), 1-35.
190. Fu, J.; Shi, L.; Zhang, D.; Zhong, Q.; Chen, Y. *Polym. Eng. Sci.* **2010,** 50, (9), 1809-1819.
191. Zhu, B.; Ma, J.; Wu, J.; Yung, K.; Xie, C. *J. Appl. Polym. Sci.* **2010,** 118, (5), 2754-2764.
192. Huang, X.; Jiang, P.; Tanaka, T. *IEEE Elect. Insul. Mag.* **2011,** 27, (4), 8-16.
193. Goyal, V.; Balandin, A. A. *Appl. Phys. Lett.* **2012,** 100, (7), 073113.
194. King, J., *Materials handbook for hybrid microelectronics*. Artech House Inc: 685 Canton Street, Norwood, Massachusetts 02062, USA, 1988.
195. Garimella, S. V.; Singhal, V.; Dong, L. *Proc. IEEE* **2006,** 94, (8), 1534-1548.
196. http://www.extremetech.com/extreme/222590-an-end-to-scaling-intels-next-generation-chips-will-sacrifice-speed-to-reduce-power, retrieved 20th May 2016
197. https://www.pugetsystems.com/labs/articles/Impact-of-Temperature-on-Intel-CPU-Performance-606/ , retrieved 20th May 2016
198. http://www.anandtech.com/show/9550/understanding-intels-dynamic-power-and-thermal-framework-smarter-throttling, retrieved 20th May 2016
199. Garimella, S. V.; Fleischer, A. S.; Murthy, J. Y.; Keshavarzi, A.; Prasher, R.; Patel, C.; Bhavnani, S. H.; Venkatasubramanian, R.; Mahajan, R.; Joshi, Y. *IEEE Trans. Compon. Packag. Technol.* **2008,** 31, (4), 801-815.
200. Dreslinski, R. G.; Wieckowski, M.; Blaauw, D.; Sylvester, D.; Mudge, T. *Proceedings of the IEEE* **2010,** 98, (2), 253-266.
201. Bar-Cohen, A.; Matin, K.; Narumanchi, S. *J. Electron. Packag.* **2015,** 137, (4), 040803.
202. Lim, K.-H.; Kim, S.-K.; Chung, M.-K. *Thermochim. Acta* **2009,** 494, (1), 71-79.
203. Nag, A.; Raidongia, K.; Hembram, K. P. S. S.; Datta, R.; Waghmare, U. V.; Rao, C. N. R. *ACS Nano* **2010,** 4, (3), 1539-1544.
204. Sevik, C.; Kinaci, A.; Haskins, J. B.; Çağın, T. *Phys. Rev. B: Condens. Matter* **2011,** 84, (8), 085409.
205. Lindsay, L.; Broido, D. *Phys. Rev. B: Condens. Matter* **2011,** 84, (15), 155421.
206. Sevik, C.; Kinaci, A.; Haskins, J. B.; Çağın, T. *Phys. Rev. B: Condens. Matter* **2012,** 86, (7), 075403.
207. Che, J.; Çağın, T.; Deng, W.; Goddard III, W. A. *J. Chem. Phys.* **2000,** 113, (16), 6888-6900.
208. Sichel, E.; Miller, R.; Abrahams, M.; Buiocchi, C. *Phys. Rev. B: Condens. Matter* **1976,** 13, (10), 4607.
209. Simpson, A.; Stuckes, A. *J. Phys. C: Solid State Phys.* **1971,** 4, (13), 1710.
210. Delhaes, P., *Graphite and precursors*. CRC Press: 2000; Vol. 1.
211. Wu, H.; Drzal, L. T. *Carbon* **2012,** 50, (3), 1135-1145.
212. Xin, G.; Sun, H.; Hu, T.; Fard, H. R.; Sun, X.; Koratkar, N.; Borca-Tasciuc, T.; Lian, J. *Adv. Mater.* **2014,** 26, (26), 4521-4526.

213. Zhu, H.; Li, Y.; Fang, Z.; Xu, J.; Cao, F.; Wan, J.; Preston, C.; Yang, B.; Hu, L. *ACS Nano* **2014,** 8, (4), 3606-3613.
214. Song, W.-L.; Wang, P.; Cao, L.; Anderson, A.; Meziani, M. J.; Farr, A. J.; Sun, Y.-P. *Angew. Chem. Int. Ed.* **2012,** 51, (26), 6498-6501.
215. Yao, Y.; Zeng, X.; Wang, F.; Sun, R.; Xu, J.-b.; Wong, C.-P. *Chem. Mater.* **2016,** 28, (4), 1049-1057.
216. Meziani, M. J.; Song, W.-L.; Wang, P.; Lu, F.; Hou, Z.; Anderson, A.; Maimaiti, H.; Sun, Y.-P. *ChemPhysChem* **2015,** 16, (7), 1339-1346.
217. Malekpour, H.; Chang, K. H.; Chen, J. C.; Lu, C. Y.; Nika, D. L.; Novoselov, K. S.; Balandin, A. A. *Nano Lett.* **2014,** 14, (9), 5155-5161.
218. Li, Q.; Guo, Y.; Li, W.; Qiu, S.; Zhu, C.; Wei, X.; Chen, M.; Liu, C.; Liao, S.; Gong, Y.; Mishra, A. K.; Liu, L. *Chem. Mater.* **2014,** 26, (15), 4459-4465.
219. Zeng, X.; Yao, Y.; Gong, Z.; Wang, F.; Sun, R.; Xu, J.; Wong, C. P. *Small* **2015,** 11, (46), 6205-6213.
220. Sato, K.; Horibe, H.; Shirai, T.; Hotta, Y.; Nakano, H.; Nagai, H.; Mitsuishi, K.; Watari, K. *J. Mater. Chem.* **2010,** 20, (14), 2749-2752.
221. Casalegno, V.; Vavassori, P.; Valle, M.; Ferraris, M.; Salvo, M.; Pintsuk, G. *J. Nucl. Mater.* **2010,** 407, (2), 83-87.
222. Leroy, B.; Plougonven, C. *J. Electrochem. Soc.* **1980,** 127, (4), 961-970.
223. Draney, N. R.; Liu, J. J.; Jiang, T. In *Experimental investigation of bare silicon wafer warp*, Microelectronics and Electron Devices, 2004 IEEE Workshop on, 2004; IEEE: pp 120-123.
224. Zhang, H. Y.; Zhang, X. W.; Lau, B.; Lim, S.; Ding, L.; Yu, M. *IEEE Trans. Compon. Packag. Manuf. Technol.* **2014,** 4, (5), 807-816.
225. Lau, J. H., TSV Interposers: The Most Cost-Effective Integrator for 3D IC Integration. In *Chip Scale Rev*, 2011; Vol. 15, pp 23-27.
226. Hoe, Y. Y. G.; Yue, T. G.; Damaruganath, P.; Chong, C. T.; Lau, J. H.; Xiaowu, Z.; Vaidyanathan, K. In *Effect of TSV interposer on the thermal performance of FCBGA package*, Electronics Packaging Technology Conference, 2009. EPTC'09. 11th, 2009; IEEE: pp 778-786.
227. Heng Yun, Z.; Xiao Wu, Z.; Lau, B. L.; Lim, S.; Liang, D.; Yu, M. B. *IEEE Trans. Compon. Packag. Manuf. Technol.* **2014,** 4, (5), 807-816.
228. Yan, Z.; Liu, G.; Khan, J. M.; Balandin, A. A. *Nat. Commun.* **2012,** 3, 827.
229. Gao, Z.; Zhang, Y.; Fu, Y.; Yuen, M. M.; Liu, J. *Carbon* **2013,** 61, 342-348.
230. Sun, S.; Bao, J.; Mu, W.; Fu, Y.; Zhang, Y.; Ye, L.; Liu, J. In *Cooling hot spots by hexagonal boron nitride heat spreaders*, Electronic Components and Technology Conference (ECTC) , 2015 IEEE 65th, 26-29 May 2015, 2015; pp 1658-1663.
231. Zhang, Y.; Han, H.; Wang, N.; Zhang, P.; Fu, Y.; Murugesan, M.; Edwards, M.; Jeppson, K.; Volz, S.; Liu, J. *Adv. Funct. Mater.* **2015,** 25, (28), 4430-4435.
232. McLachlan, D. S. *J. Phys. C: Solid State Phys.* **1985,** 18, (9), 1891.
233. Love, J. C.; Estroff, L. A.; Kriebel, J. K.; Nuzzo, R. G.; Whitesides, G. M. *Chem. Rev.* **2005,** 105, (4), 1103-1170.
234. Prasher, R. *Appl. Phys. Lett.* **2009,** 94, (4), 1905.
235. Hu, L.; Zhang, L.; Hu, M.; Wang, J.-S.; Li, B.; Keblinski, P. *Phys. Rev. B: Condens. Matter* **2010,** 81, (23), 235427.
236. Sun, F.; Zhang, T.; Jobbins, M. M.; Guo, Z.; Zhang, X.; Zheng, Z.; Tang, D.; Ptasinska, S.; Luo, T. *Adv. Mater.* **2014,** 26, (35), 6093-6099.
237. Swartz, E. T.; Pohl, R. O. *Reviews of modern physics* **1989,** 61, (3), 605.
238. Losego, M. D.; Grady, M. E.; Sottos, N. R.; Cahill, D. G.; Braun, P. V. *Nat. Mater.* **2012,** 11, (6), 502-506.

239. Han, H.; Zhang, Y.; Wang, N.; Samani, M. K.; Ni, Y.; Mijbil, Z. Y.; Edwards, M.; Xiong, S.; Sääskilahti, K.; Murugesan, M. *Nat. Commun.* **2016,** 7.
240. Liang, Z.; Evans, W.; Desai, T.; Keblinski, P. *Appl. Phys. Lett.* **2013,** 102, (6), 061907.
241. Ni, Y.; Le Khanh, H.; Chalopin, Y.; Bai, J.; Lebarny, P.; Divay, L.; Volz, S. *Appl. Phys. Lett.* **2012,** 100, (19), 193118.
242. Lin, W.; Zhang, R.; Moon, K.-S.; Wong, C. *Carbon* **2010,** 48, (1), 107-113.
243. Taphouse, J. H.; Smith, O. N. L.; Marder, S. R.; Cola, B. A. *Adv. Funct. Mater.* **2014,** 24, (4), 465-471.
244. O'Brien, P. J.; Shenogin, S.; Liu, J.; Chow, P. K.; Laurencin, D.; Mutin, P. H.; Yamaguchi, M.; Keblinski, P.; Ramanath, G. *Nat Mater* **2013,** 12, (2), 118-122.
245. Boday, D. J.; Kuczynski, J.; Wertz, J. T.; Zhang, J., Thermal interface material (tim) with thermally conductive integrated release layer. Google Patents: 2012.
246. Liang, Q.; Yao, X.; Wang, W.; Liu, Y.; Wong, C. P. *ACS Nano* **2011,** 5, (3), 2392-2401.
247. Wang, R. Y.; Segalman, R. A.; Majumdar, A. *Appl. Phys. Lett.* **2006,** 89, (17), 173113.
248. Segal, D.; Nitzan, A.; Hänggi, P. *The Journal of chemical physics* **2003,** 119, (13), 6840-6855.
249. Markussen, T. *The Journal of chemical physics* **2013,** 139, (24), 244101.
250. Meier, T.; Menges, F.; Nirmalraj, P.; Hölscher, H.; Riel, H.; Gotsmann, B. *Phys. Rev. Lett.* **2014,** 113, (6), 060801.
251. Ameen, J. G.; Korleski, J. E.; Mortimer Jr, W. P.; Yokimcus, V. P., Thermally conductive adhesive interface. Google Patents: 1997.
252. Hattori, M. In *Needs and applications of high temperature LSIs for automotive electronic systems*, High Temperature Electronics, 1999. HITEN 99. The Third European Conference on, 1999; IEEE: pp 37-43.
253. Fairchild, M. R.; Snyder, R. B.; Berlin, C. W.; Sarma, D. *Emerging substrate technologies for harsh-environment automotive electronics applications*; 0148-7191; SAE Technical Paper: 2002.
254. Watson, J.; Castro, G. *Analog Dialogue* **2012,** 46, (2), 3-9.
255. Ohadi, M.; Jianwei, Q. In *Thermal management of harsh-environment electronics*, Semiconductor Thermal Measurement and Management Symposium, 2004. Twentieth Annual IEEE, 9-11 Mar 2004, 2004; pp 231-240.
256. Myers, B. A. *Electronics cooling* **2003,** 9, 24-31.
257. Patterson, D. *COTS Journal* **2002**, 45-48.
258. Nakajima, A.; Shoji, A.; Yonemori, K.; Seo, N. *Jpn. J. Appl. Phys.* **2016,** 55, (2), 027101.
259. Lee, S. H.; Jung, J. H.; Oh, I. K. *Small* **2014,** 10, (19), 3880-3886.
260. Kuilla, T.; Bhadra, S.; Yao, D.; Kim, N. H.; Bose, S.; Lee, J. H. *Prog. Polym. Sci.* **2010,** 35, (11), 1350-1375.
261. Nieto, A.; Boesl, B.; Agarwal, A. *Carbon* **2015,** 85, 299-308.
262. Liu, F.; Ming, P.; Li, J. *Phys. Rev. B: Condens. Matter* **2007,** 76, (6), 064120.
263. Mata, A.; Fleischman, A. J.; Roy, S. *Biomedical microdevices* **2005,** 7, (4), 281-293.
264. Hong, J.-Y.; Yun, S.; Wie, J. J.; Zhang, X.; Dresselhaus, M. S.; Kong, J.; Park, H. S. *Nanoscale* **2016**.
265. Song, B.; Wu, Z.; Zhu, Y.; Moon, K.-s.; Wong, C. In *Three-dimensional graphene-based composite for flexible electronic applications*, 2015 IEEE 65th

Electronic Components and Technology Conference (ECTC), 2015; IEEE: pp 1803-1807.
266. http://retra.co.uk/life-expectancy-of-electronic-equipment/, retrieved 17th September 2016
267. Vieira, C.; da Silva, P.; da Silva, F.; Capitaneo, J.; Monteiro, S. *Rev. Mater.* **2005,** 10, (4), 526-536.
268. Mo, L.; Leong, K. K. M.; Kawi, S. *Catal. Sci. Tech.* **2014,** 4, (7), 2107-2114.
269. Pang, L. S. K.; Saxby, J. D.; Chatfield, S. P. *J. Phys. Chem.* **1993,** 97, (27), 6941-6942.
270. Xie, S.-Y.; Wang, W.; Fernando, K. A. S.; Wang, X.; Lin, Y.; Sun, Y.-P. *Chem. Commun.* **2005**, (29), 3670-3672.
271. Tummala, R. R., *Fundamentals of microsystems packaging*. McGraw-Hill New York: 2001.
272. Tansley, T.; Maddison, D. *J. Appl. Phys.* **1991,** 69, (11), 7711-7713.
273. http://www.mt.com/sg/en/home/supportive_content/matchar_apps/MatChar_UC281.html, retrieved December 6 2016
274. Pecht, M.; Palmer III, M.; Naft, J. **1986**.
275. http://www.sigmaaldrich.com/catalog/CertOfAnalysisPage.do?symbol=281778&LotNo=bcbk2912v&brandTest=ALDRICH
276. http://www.evilmadscientist.com/2013/solder-expire/
277. Yoshida, K.; Kamada, K.; Atsuta, M. *The Journal of prosthetic dentistry* **2001,** 85, (2), 184-189.
278. Ritter, J. E.; Huseinovic, A. *J. Electron. Packag.* **2000,** 123, (4), 401-404.
279. Suganuma, K.; Kim, S.-J.; Kim, K.-S. *JOM* **2009,** 61, (1), 64-71.
280. George, E.; Osterman, M.; Pecht, M.; Coyle, R.; Parker, R.; Benedetto, E. *Journal of Microelectronics and Electronic Packaging* **2014,** 11, (4), 137-145.
281. Camino, G.; Lomakin, S. M.; Lazzari, M. *Polymer* **2001,** 42, (6), 2395-2402.
282. Grassie, N.; Macfarlane, I. G. *Eur. Polym. J.* **1978,** 14, (11), 875-884.
283. Lu, D.; Wong, C., *Materials for advanced packaging*. Springer: 2009; Vol. 181.
284. Watanabe, T.; Ooba, N.; Hayashida, S.; Kurihara, T.; Imamura, S. *J. Lightwave Technol.* **1998,** 16, (6), 1049.
285. Minges, M. L., *Electronic materials handbook: packaging*. Asm International: 1989; Vol. 1.
286. Guenther, T.; Lovell, N. H.; Suaning, G. J. *Expert Rev. Med. Devices* **2012,** 9, (1), 33-48.
287. Lane, S. S.; Kuppermann, B. D.; Fine, I. H.; Hamill, M. B.; Gordon, J. F.; Chuck, R. S.; Hoffman, R. S.; Packer, M.; Koch, D. D. *Am. J. Ophthalmol.* **2004,** 137, (6), 993-1001.
288. Liu, P.; Sherman, E.; Jacobsen, A. *J. Power Sources* **2009,** 189, (1), 646-650.
289. Minhun, J.; Jaeyoung, K.; Jinsoo, N.; Namsoo, L.; Chaemin, L.; Gwangyong, L.; Junseok, K.; Hwiwon, K.; Kyunghwan, J.; Leonard, A. D.; Tour, J. M.; Gyoujin, C. *Electron Devices, IEEE Transactions on* **2010,** 57, (3), 571-580.
290. Radivojevic, Z.; Beecher, P.; Bower, C.; Haque, S.; Andrew, P.; Hasan, T.; Bonaccorso, F.; Ferrari, A. C.; Henson, B., Electrotactile touch surface by using transparent graphene. In *Proceedings of the 2012 Virtual Reality International Conference*, ACM: Laval, France, 2012; pp 1-3.
291. Bae, S.; Kim, H.; Lee, Y.; Xu, X.; Park, J.-S.; Zheng, Y.; Balakrishnan, J.; Lei, T.; Ri Kim, H.; Song, Y. I.; Kim, Y.-J.; Kim, K. S.; Ozyilmaz, B.; Ahn, J.-H.; Hong, B. H.; Iijima, S. *Nat Nano* **2010,** 5, (8), 574-578.

292. Ghosh, M., *Polyimides: fundamentals and applications*. CRC Press: 1996.
293. Sun, Y.; Rogers, J. A. *Adv. Mater.* **2007,** 19, (15), 1897-1916.
294. Glassbrenner, C. J.; Slack, G. A. *Physical Review* **1964,** 134, (4A), A1058-A1069.
295. Cahill, D. G.; Pohl, R. O. *Phys. Rev. B: Condens. Matter* **1987,** 35, (8), 4067-4073.
296. Du, J.; Cheng, H.-M. *Macromol. Chem. Phys.* **2012,** 213, (10-11), 1060-1077.
297. Marconnet, A. M.; Panzer, M. A.; Goodson, K. E. *Reviews of Modern Physics* **2013,** 85, (3), 1295-1326.
298. Byrne, M. T.; Gun'ko, Y. K. *Adv. Mater.* **2010,** 22, (15), 1672-1688.
299. Nazempour, H. E.-D. a. M., *Thermal Conductivity of Nanoparticles Filled Polymers*. Intech; 1ST edition: April 18, 2012.
300. Godet, C. *J. Non-Cryst. Solids* **2002,** 299, 333-338.
301. Godet, C. *Diamond Relat. Mater.* **2003,** 12, (2), 159-165.
302. Godet, C. *Philos. Mag. B* **2001,** 81, (2), 205-222.
303. Gan, L.; Bolker, A.; Saguy, C.; Kalish, R.; Tan, D.; Tay, B.; Gruen, D.; Bruno, P. *Diamond Relat. Mater.* **2009,** 18, (9), 1118-1122.
304. Li, Q.; Li, Y.; Zhang, X.; Chikkannanavar, S. B.; Zhao, Y.; Dangelewicz, A. M.; Zheng, L.; Doorn, S. K.; Jia, Q.; Peterson, D. E. *Adv. Mater.* **2007,** 19, (20), 3358-3363.
305. Smith Jr, J.; Connell, J.; Delozier, D.; Lillehei, P.; Watson, K.; Lin, Y.; Zhou, B.; Sun, Y.-P. *Polymer* **2004,** 45, (3), 825-836.
306. Smith Jr, J. G.; Delozier, D. M.; Connell, J. W.; Watson, K. A. *Polymer* **2004,** 45, (18), 6133-6142.
307. Dai, W.; Yu, J.; Liu, Z.; Wang, Y.; Song, Y.; Lyu, J.; Bai, H.; Nishimura, K.; Jiang, N. *Composites Part A: Applied Science and Manufacturing* **2015,** 76, (0), 73-81.
308. Dai, W.; Yu, J.; Wang, Y.; Song, Y.; Alam, F. E.; Nishimura, K.; Lin, C.-T.; Jiang, N. *Journal of Materials Chemistry A* **2015,** 3, (9), 4884-4891.
309. Yan, W.; Zhang, Y.; Sun, H.; Liu, S.; Chi, Z.; Chen, X.; Xu, J. *Journal of Materials Chemistry A* **2014,** 2, (48), 20958-20965.
310. Murakami, T.; Ebisawa, K.; Miyao, K.; Ando, S. *J. Photopolym. Sci. Technol.* **2014,** 27, (2), 187-191.
311. Li, T.-L.; Hsu, S. L.-C. *The Journal of Physical Chemistry B* **2010,** 114, (20), 6825-6829.
312. Xie, S.-H.; Zhu, B.-K.; Li, J.-B.; Wei, X.-Z.; Xu, Z.-K. *Polym. Test.* **2004,** 23, (7), 797-801.
313. Irwin, P. C.; Cao, Y.; Bansal, A.; Schadler, L. S. In *Thermal and mechanical properties of polyimide nanocomposites*, Electrical Insulation and Dielectric Phenomena, 2003. Annual Report. Conference on, 19-22 Oct. 2003, 2003; pp 120-123.
314. Kozako, M.; Okazaki, Y.; Hikita, M.; Tanaka, T. In *Preparation and evaluation of epoxy composite insulating materials toward high thermal conductivity*, 2010 10th IEEE International Conference on Solid Dielectrics, 2010; IEEE: pp 1-4.
315. Procter, P.; Solc, J. In *Improved thermal conductivity in microelectronic encapsulants*, Electronic Components and Technology Conference, 1991. Proceedings., 41st, 1991; IEEE: pp 835-842.
316. Lee, W. S.; Yu, J. *Diamond Relat. Mater.* **2005,** 14, (10), 1647-1653.
317. Varlow, B.; Robertson, J.; Donnelly, K. *IET Science, Measurement & Technology* **2007,** 1, (2), 96-102.
318. Xu, Y.; Chung, D.; Mroz, C. *Composites Part A: Applied science and manufacturing* **2001,** 32, (12), 1749-1757.

319. Furuya, K.; Munakata, F.; Matsuo, K.; Akimune, Y.; Ye, J.; Okada, A. *J. Therm. Anal. Calorim.* **2002,** 69, (3), 873-879.
320. Zhang, B.; Li, J.; Sun, J.; Zhang, S.; Zhai, H.; Du, Z. *J. Eur. Ceram. Soc.* **2002,** 22, (1), 93-99.
321. Wang, S.; Tambraparni, M.; Qiu, J.; Tipton, J.; Dean, D. *Macromolecules* **2009,** 42, (14), 5251-5255.
322. Zhang, Y.; Hu, X.; Zhao, J. H.; Sheng, K.; Cannon, W. R.; Wang, X.; Fursin, L. *IEEE Trans. Compon. Packag. Technol.* **2009,** 32, (4), 716-723.
323. Huang, X.; Xie, L.; Jiang, P.; Wang, G.; Liu, F. *J. Phys. D: Appl. Phys.* **2009,** 42, (24), 245407.
324. Li, T. L.; Hsu, S. L. C. *J. Appl. Polym. Sci.* **2011,** 121, (2), 916-922.
325. Tseng, I.; Chiang, J.; Lin, H.; Tsai, M. *Chemistry* **2012,** 70, 31-38.
326. Tsai, M.-H.; Tseng, I.-H.; Chiang, J.-C.; Li, J.-J. *ACS applied materials & interfaces* **2014,** 6, (11), 8639-8645.
327. Pramoda, K. P.; Chung, T. S.; Liu, S. L.; Oikawa, H.; Yamaguchi, A. *Polym. Degrad. Stab.* **2000,** 67, (2), 365-374.
328. Goo, Y.-S.; Lee, Y.-I.; Kim, N.; Lee, K.-J.; Yoo, B.; Hong, S.-J.; Kim, J.-D.; Choa, Y.-H. *Surf. Coat. Technol.* **2010,** 205, Supplement 1, S369-S372.
329. Ghosh, M.; Mittal, K., *Polyimides: Fundamentals and Applications*. Marcel Dekker: New York, NY, 1996.
330. Arnold, G. S.; Peplinski, D. R. *AIAA J.* **1985,** 23, (10), 1621-1626.
331. Pater, R. H.; Curto, P. A. *Acta Astronaut.* **2007,** 61, (11), 1121-1129.
332. Megusar, J. *J. Nucl. Mater.* **1997,** 245, (2), 185-190.
333. Materials, D. H. P., Kapton MT thermally conductive substrate polyimide film.
334. Finckenor, M.; Dooling, D. *Multilayer Insulation Material Guidelines*; NASA/TP-1999-209263; National Aeronautics and Spcae Administration: Washington, D.C., 1999.
335. Finckenor, M., *Multilayer insulation material guidelines*. Marshall Space Flight Center: 1999.
336. Tribble, A. C., *The space environment: implications for spacecraft design (revised and expanded edition)*. Princeton University Press, Princeton: 2003.
337. Tribble, A. C., *The Space Environment*. Princeton University Press: Princetone, NJ, 1995.
338. Peplinski, D. R.; Arnold, G. S.; Borson, E. N. In *Introduction to simulation of upper atmosphere oxygen satellite exposed to atomic oxygen in low Earth orbit*, 13th Space Simulation Conf., 1984; pp 133-145.
339. Reddy, M. R. *Journal of Materials Science* **1995,** 30, (2), 281-307.
340. Townsend, L.; Fry, R. *Adv. Space Res.* **2002,** 30, (4), 957-963.
341. Tripathi, R. K.; Wilson, J. W.; Youngquist, R. C. *Adv. Space Res.* **2008,** 42, (6), 1043-1049.
342. Spillantini, P. *Adv. Space Res.* **2010,** 45, (7), 900-916.
343. Ounaies, Z.; Park, C.; Wise, K.; Siochi, E.; Harrison, J. *Compos. Sci. Technol.* **2003,** 63, (11), 1637-1646.
344. Purvis, C. K.; Garrett, H. B.; Whittlesey, A.; Stevens, N. J. *Design guidelines for assessing and controlling spacecraft charging effects*; NASA Tech. Paper 2361; National Aeronautics and Spcae Administration: 1984.
345. Angirasa, D.; Ayyaswamy, P. S. *Journal of spacecraft and rockets* **2014,** 51, (3), 750-761.

346. Banks, B. A.; de Groh, K. K.; Miller, S. K. *Low Earth Orbital Atomic Oxygen Interactions with Spacecraft Materials*; NASA/TM-2004-213400; National Aeronautics and Spcae Administration: November, 2004.
347. Reddy, M. R.; Srinivasamurthy, N.; Agrawal, B. *Surf. Coat. Technol.* **1993,** 58, (1), 1-17.
348. Cairns, D. R.; Witte, R. P.; Sparacin, D. K.; Sachsman, S. M.; Paine, D. C.; Crawford, G. P.; Newton, R. *Appl. Phys. Lett.* **2000,** 76, (11), 1425-1427.
349. Banks, B. A.; Snyder, A.; Miller, S. K.; De Groh, K. K.; Demko, R. *Journal of spacecraft and rockets* **2004,** 41, (3), 335-339.
350. De Groh, K. K.; Banks, B. A. *Journal of spacecraft and rockets* **1994,** 31, (4), 656-664.
351. Luong, N. D.; Hippi, U.; Korhonen, J. T.; Soininen, A. J.; Ruokolainen, J.; Johansson, L.-S.; Nam, J.-D.; Sinh, L. H.; Seppälä, J. *Polymer* **2011,** 52, (23), 5237-5242.
352. Koo, M.; Bae, J.-S.; Shim, S. E.; Kim, D.; Nam, D.-G.; Lee, J.-W.; Lee, G.-W.; Yeum, J. H.; Oh, W. *Colloid. Polym. Sci.* **2011,** 289, (13), 1503-1509.
353. Wu, H.; Wang, K.; Meng, Y.; Lu, K.; Wei, Z. *Journal of Materials Chemistry A* **2013,** 1, (21), 6366-6372.
354. Tang, L.-C.; Wan, Y.-J.; Yan, D.; Pei, Y.-B.; Zhao, L.; Li, Y.-B.; Wu, L.-B.; Jiang, J.-X.; Lai, G.-Q. *Carbon* **2013,** 60, 16-27.
355. Nicholson, K. T.; Minton, T. K.; Sibener, S. *Prog. Org. Coat.* **2003,** 47, (3), 443-447.
356. ECSS-Q-70-02A, 2000
357. Poinas, P. In *Satellite Thermal Control Engineering*, The ESA initiative training courses, Small and Medium Sized Enterprises SME04, June, 2004.
358. Standard Solar Constant and Zero Air Mass Solar Spectral Irradiance Tables. ASTM International: West Conshohocken, PA, 2002.
359. Atar, N.; Grossman, E.; Gouzman, I.; Bolker, A.; Murray, V. J.; Marshall, B. C.; Qian, M.; Minton, T. K.; Hanein, Y. *ACS applied materials & interfaces* **2015,** 7, 12047-12056.
360. Smith, J.; Connell, J.; Delozier, D.; Lillehei, P.; Watson, K.; Lin, Y.; Zhou, B.; Sun, Y. P. *Polymer* **2004,** 45, (3), 825-836.
361. Association, E., Packaging Materials for ESD Sensitive Items. ESD Association: USA, 2008.
362. Standardization, E. C. f. S. **2000**.
363. Vered, R.; Matlis, S.; Nahor, G.; Lempert, G. D.; Grossman, E.; Marom, G.; Lifshitz, Y. *Surf. Interface Anal.* **1994,** 22, (1-12), 532-537.
364. Zhang, J.; Lindholm, N. F.; Brunsvold, A. L.; Upadhyaya, H. P.; Minton, T. K.; Tagawa, M. *ACS applied materials & interfaces* **2009,** 1, (3), 653-660.
365. Minton, T. K.; Garton, D. J. *Chemical dynamics in extreme environments* **2001,** 11, 420-489.
366. Shpilman, Z.; Gouzman, I.; Lempert, G.; Grossman, E.; Hoffman, A. *Rev. Sci. Instrum.* **2008,** 79, (2), -.
367. http://Outgassing.Nasa.Gov/
368. Berg, G. J.; McBride, M. K.; Wang, C.; Bowman, C. N. *Polymer*, (0).
369. Leng, J.; Lan, X.; Liu, Y.; Du, S. *Prog. Mater Sci.* **2011,** 56, (7), 1077-1135.
370. Zhao, Q.; Qi, H. J.; Xie, T. *Prog. Polym. Sci.* **2015,** 49-50, (0), 79-120.
371. Meng, H.; Li, G. *Polymer* **2013,** 54, (9), 2199-2221.
372. Wu, Y.; Hu, J.; Zhang, C.; Han, J.; Wang, Y.; Kumar, B. *Journal of Materials Chemistry A* **2015,** 3, (1), 97-100.

373. Lu, H.; Liang, F.; Yao, Y.; Gou, J.; Hui, D. *Composites Part B: Engineering* **2014,** 59, (0), 191-195.
374. Du, F.-P.; Ye, E.-Z.; Yang, W.; Shen, T.-H.; Tang, C.-Y.; Xie, X.-L.; Zhou, X.-P.; Law, W.-C. *Composites Part B: Engineering* **2015,** 68, (0), 170-175.
375. Luo, H.; Li, Z.; Yi, G.; Zu, X.; Wang, H.; Wang, Y.; Huang, H.; Hu, J.; Liang, Z.; Zhong, B. *Mater. Lett.* **2014,** 134, (0), 172-175.
376. Lu, H.; Liang, F.; Gou, J.; Leng, J. *J. Intell. Mater. Syst. Struct.* **2014**, 1045389X14535015.
377. Wang, W.; Liu, D.; Liu, Y.; Leng, J.; Bhattacharyya, D. *Compos. Sci. Technol.* **2015,** 106, (0), 20-24.
378. Lu, H.; Liu, Y.; Gou, J.; Leng, J.; Du, S. *International Journal of Smart and Nano Materials* **2010,** 1, (1), 2-12.
379. Zheng, Y.; Li, J.; Lee, E.; Yang, S. *RSC Advances* **2015,** 5, (39), 30495-30499.
380. Lu, H.; Yao, Y.; Huang, W. M.; Leng, J.; Hui, D. *Composites Part B: Engineering* **2014,** 62, (0), 256-261.
381. Lendlein, A.; Jiang, H.; Junger, O.; Langer, R. *Nature* **2005,** 434, (7035), 879-882.
382. Liu, Y.; Li, Y.; Chen, H.; Yang, G.; Zheng, X.; Zhou, S. *Carbohydr. Polym.* **2014,** 104, (0), 101-108.
383. Yang, B.; Huang, W. M.; Li, C.; Li, L. *Polymer* **2006,** 47, (4), 1348-1356.
384. Chae Jung, Y.; Hwa So, H.; Whan Cho, J. *Journal of Macromolecular Science, Part B* **2006,** 45, (4), 453-461.
385. Lv, H.; Leng, J.; Liu, Y.; Du, S. *Adv. Eng. Mater.* **2008,** 10, (6), 592-595.
386. Heuchel, M.; Razzaq, M. Y.; Kratz, K.; Behl, M.; Lendlein, A. *Polymer* **2015,** 65, (0), 215-222.
387. Mohr, R.; Kratz, K.; Weigel, T.; Lucka-Gabor, M.; Moneke, M.; Lendlein, A. *Proc. Natl. Acad. Sci. U. S. A.* **2006,** 103, (10), 3540-3545.
388. Schmidt, A. M. *Macromol. Rapid Commun.* **2006,** 27, (14), 1168-1172.
389. Yakacki, C. M.; Satarkar, N. S.; Gall, K.; Likos, R.; Hilt, J. Z. *J. Appl. Polym. Sci.* **2009,** 112, (5), 3166-3176.
390. Yu, K.; Liu, Y.; Leng, J. *RSC Advances* **2014,** 4, (6), 2961-2968.
391. Hornbogen, E. *Adv. Eng. Mater.* **2006,** 8, (1-2), 101-106.
392. Huang, W. *Materials & design* **2002,** 23, (1), 11-19.
393. Otsuka, K.; Wayman, C. M., *Shape memory materials*. Cambridge university press: 1999.
394. Lendlein, A.; Langer, R. *Science* **2002,** 296, (5573), 1673-1676.
395. Metcalfe, A.; Desfaits, A.-C.; Salazkin, I.; Yahia, L. H.; Sokolowski, W. M.; Raymond, J. *Biomaterials* **2003,** 24, (3), 491-497.
396. Wache, H.; Tartakowska, D.; Hentrich, A.; Wagner, M. *J. Mater. Sci. Mater. Med.* **2003,** 14, (2), 109-112.
397. Wong, Y.; Kong, J.; Widjaja, L.; Venkatraman, S. *Sci. China Chem.* **2014,** 57, (4), 476-489.
398. Bao, M.; Lou, X.; Zhou, Q.; Dong, W.; Yuan, H.; Zhang, Y. *ACS Applied Materials & Interfaces* **2014,** 6, (4), 2611-2621.
399. Ji, F.; Zhu, Y.; Hu, J.; Liu, Y.; Yeung, L.-Y.; Ye, G. *Smart Mater. Struct.* **2006,** 15, (6), 1547.
400. Hu, J.-l.; Ding, X.-m.; Tao, X.-m.; Yu, J.-m. *JOURNAL-DONG HUA UNIVERSITY-ENGLISH EDITION-* **2002,** 19, (3), 89-93.
401. Browne, A. L.; Johnson, N. L., Shape memory polymer seat assemblies. Google Patents: 2007.

402. Buravalla, V. R.; Browne, A. L.; Johnson, N. L., Tunable vehicle structural members and methods for selectively changing the mechanical properties thereto. Google Patents: 2010.
403. Browne, A. L.; Johnson, N. L., Hood assembly utilizing active materials based mechanisms. Google Patents: 2011.
404. Liu, Y.; Du, H.; Liu, L.; Leng, J. *Smart Mater. Struct.* **2014,** 23, (2), 023001.
405. Arzberger, S. C.; Munshi, N. A.; Lake, M. S.; Barrett, R.; Tupper, M. L.; Keller, P. N.; Francis, W.; Campbell, D.; Gall, K. *Lafayette, Colorado: Composite Technology Development Inc* **2004**.
406. Mohd Jani, J.; Leary, M.; Subic, A.; Gibson, M. A. *Materials & Design* **2014,** 56, (0), 1078-1113.
407. Behl, M.; Lendlein, A. *Mater. Today* **2007,** 10, (4), 20-28.
408. Yoonessi, M.; Shi, Y.; Scheiman, D. A.; Lebron-Colon, M.; Tigelaar, D. M.; Weiss, R.; Meador, M. A. *ACS Nano* **2012,** 6, (9), 7644-7655.
409. Xie, T. *Polymer* **2011,** 52, (22), 4985-5000.
410. Gojny, F. H.; Wichmann, M. H. G.; Fiedler, B.; Kinloch, I. A.; Bauhofer, W.; Windle, A. H.; Schulte, K. *Polymer* **2006,** 47, (6), 2036-2045.
411. Chen, Y.-M.; Ting, J.-M. *Carbon* **2002,** 40, (3), 359-362.
412. Chen, X.; Lu, Y.; Zhang, X.; Zhao, F. *Materials & Design* **2012,** 40, (0), 497-501.
413. Teng, C.-C.; Ma, C.-C. M.; Lu, C.-H.; Yang, S.-Y.; Lee, S.-H.; Hsiao, M.-C.; Yen, M.-Y.; Chiou, K.-C.; Lee, T.-M. *Carbon* **2011,** 49, (15), 5107-5116.
414. Buckley, P. R.; McKinley, G. H.; Wilson, T. S.; Small, W.; Benett, W. J.; Bearinger, J. P.; McElfresh, M. W.; Maitland, D. J. *Biomedical Engineering, IEEE Transactions on* **2006,** 53, (10), 2075-2083.
415. Cao, F.; Jana, S. C. *Polymer* **2007,** 48, (13), 3790-3800.
416. Ohki, T.; Ni, Q.-Q.; Ohsako, N.; Iwamoto, M. *Composites Part A: Applied Science and Manufacturing* **2004,** 35, (9), 1065-1073.
417. Razzaq, M. Y.; Frormann, L. *Polym. Compos.* **2007,** 28, (3), 287-293.
418. Weidenfeller, B.; Höfer, M.; Schilling, F. R. *Composites Part A: Applied Science and Manufacturing* **2004,** 35, (4), 423-429.
419. Hager, M. D.; Bode, S.; Weber, C.; Schubert, U. S. *Prog. Polym. Sci.* **2015,** 49-50, (0), 3-33.
420. Bai, M.; Chung, J. *International Journal of Thermal Sciences* **2011,** 50, (6), 869-880.
421. Bellin, I.; Kelch, S.; Langer, R.; Lendlein, A. *Proceedings of the National Academy of Sciences* **2006,** 103, (48), 18043-18047.
422. Kolesov, I.; Radusch, H. *Express Polym Lett* **2008,** 2, (7), 461-473.
423. Xie, T.; Xiao, X.; Cheng, Y. T. *Macromol. Rapid Commun.* **2009,** 30, (21), 1823-1827.
424. Qin, H.; Mather, P. T. *Macromolecules* **2009,** 42, 273-280.
425. Yang, Z.; Wang, Q.; Wang, T. *Macromol. Chem. Phys.* **2016**.
426. Luo, X.; Mather, P. T. *Adv. Funct. Mater.* **2010,** 20, (16), 2649-2656.
427. Ge, Q.; Qi, H. J.; Dunn, M. L. *Appl. Phys. Lett.* **2013,** 103, (13), 131901.
428. Liu, Z.; Song, L.; Zhao, S.; Huang, J.; Ma, L.; Zhang, J.; Lou, J.; Ajayan, P. M. *Nano Lett.* **2011,** 11, (5), 2032-2037.
429. Liu, Y.; Boyles, J. K.; Genzer, J.; Dickey, M. D. *Soft Matter* **2012,** 8, (6), 1764-1769.
430. He, Z.; Satarkar, N.; Xie, T.; Cheng, Y. T.; Hilt, J. Z. *Adv. Mater.* **2011,** 23, (28), 3192-3196.

431. Zhao, Q.; Behl, M.; Lendlein, A. *Soft Matter* **2013,** 9, (6), 1744-1755.
432. Wang, C.; Zhang, C.; Chen, S. *Carbon* **2016,** 109, 666-672.
433. Coopersmith, J. *Issues in Science and Technology* **2012,** 29, (1).
434. Das, A.; Cobb, R., TechSat 21 - Space Missions Using Collaboratig Constellations of Satellites. In *12th AIAA/USU Conference on Small Satellites*, Air Force Research Laboratory, Space Vehicles Directorate, Kirtland Airforce Base, NM 87117, 1998.
435. National Aeronautics and Space Administration MISSE: Testing materials in space. http://www.nasa.gov/centers/langley/news/factsheets/MISSE.html
436. Brown, C. D., *Elements of Spacecraft Design*. 2002; p 2.
437. Menaa, F.; Abdelghani, A.; Menaa, B. *J. Tissue Eng. Regen. Med.* **2015,** 9, 1321.
438. Krontiras, P.; Gatenholm, P.; Hägg, D. A. *J. Biomed. Mater. Res. B* **2015,** 103, 195.
439. Shen, H.; Niu, Y.; Hu, X.; Yang, F.; Wang, S.; Wu, D. *J. Mater. Chem. B* **2015,** 3, 4417.
440. Frydrych, M.; Román, S.; MacNeil, S.; Chen, B. *Acta Biomater.* **2015,** 18, 40.
441. Song, Q.; Jiang, Z.; Li, N.; Liu, P.; Liu, L.; Tang, M.; Cheng, G. *Biomaterials* **2014,** 35, 6930.
442. Zhi, J.; Cui, H.; Chen, A.; Xie, Y.; Huang, F. *J. Power Sources* **2015,** 281, 404.
443. Sun, Y.; Cao, Y.; Huang, W.; Zhu, Y.; Heng, L.; Tang, B. *Mater. Lett.* **2016,** 165, 178.
444. Loeblein, M.; Bruno, A.; Loh, G. C.; Bolker, A.; Uzan-Saguy, C.; Antila, L.; Tsang, S. H.; Teo, E. H. T. *Chemical Physics Letters* 2017, 685, 442-450.
445. Yang, Y.; Loeblein, M.; Tsang, S. H.; Chow, K. K.; Teo, E. H. T. *Optics express* **2014,** 22(25), 31458-31465.
446. Bonaccorso, F.; Lombardo, A.; Hasan, T.; Sun, Z.; Colombo, L.; Ferrari, A.C. *Mater. Today* **2012,** 15(12), 564–589.
447. Geim A. K.; Novoselov, K.S. *Nat. Mater.* **2007,** 6(3), 183–191.
448. Tang, D. Y.; Zhang, H.; Bao, Q. L.; Loh, K. P. *Fiber Lasers VIII: Technology, Systems, and Applications, Proc. SPIE* **2011,** 7914, 79141H.
449. Song, Y. W.; Jang, S. Y.; Han, W. S.; Bae, M. K. *Appl. Phys. Lett.* **2010,** 96(5), 051122.
450. Bao, Q. L.; Zhang, H.; Wang, Y.; Ni, Z. H.; Yan, Y. L.; Shen, Z. X.; Loh, K. P.; Tang, D. Y. *Adv. Funct. Mater.* **2009,** 19(19), 3077–3083.
451. Sun, Z.; Hasan, S.; Torrisi, F.; Popa, D.; Privitera, G.; Wang, F.; Bonaccorso, F.; Basko, D. M.; Ferrari, A.C. *ACS Nano* **2010,** 4(2), 803–810.
452. Lagatsky, A. A.; Sun, Z.; Kulmala, T. S.; Sundaram, R. S.; Milana, S.; Torrisi, F.; Antipov, O. L.; Lee, Y.; Ahn, J. H.; Brown, C. T. A.; Sibbett, W.; Ferrari, A. C. *Appl. Phys. Lett.* **2013,** 102(1), 013113.